

# University of Wollongong - Research Online

## Thesis Collection

Title: Exploring novel radiotherapy techniques with Monte Carlo simulation and measurement

Author: Heidi Nettelbeck

Year: 2009

Repository DOI:

### Copyright Warning

You may print or download ONE copy of this document for the purpose of your own research or study. The University does not authorise you to copy, communicate or otherwise make available electronically to any other person any copyright material contained on this site.

You are reminded of the following: This work is copyright. Apart from any use permitted under the Copyright Act 1968, no part of this work may be reproduced by any process, nor may any other exclusive right be exercised, without the permission of the author. Copyright owners are entitled to take legal action against persons who infringe their copyright. A reproduction of material that is protected by copyright may be a copyright infringement. A court may impose penalties and award damages in relation to offences and infringements relating to copyright material.

Higher penalties may apply, and higher damages may be awarded, for offences and infringements involving the conversion of material into digital or electronic form.

**Unless otherwise indicated, the views expressed in this thesis are those of the author and do not necessarily represent the views of the University of Wollongong.**

Research Online is the open access repository for the University of Wollongong. For further information contact the UOW Library: [research-pubs@uow.edu.au](mailto:research-pubs@uow.edu.au)

## **NOTE**

This online version of the thesis may have different page formatting and pagination from the paper copy held in the University of Wollongong Library.

## **UNIVERSITY OF WOLLONGONG**

### **COPYRIGHT WARNING**

You may print or download ONE copy of this document for the purpose of your own research or study. The University does not authorise you to copy, communicate or otherwise make available electronically to any other person any copyright material contained on this site. You are reminded of the following:

Copyright owners are entitled to take legal action against persons who infringe their copyright. A reproduction of material that is protected by copyright may be a copyright infringement. A court may impose penalties and award damages in relation to offences and infringements relating to copyright material. Higher penalties may apply, and higher damages may be awarded, for offences and infringements involving the conversion of material into digital or electronic form.

# Exploring novel radiotherapy techniques with Monte Carlo simulation and measurement

Heidi Nettelbeck

A thesis submitted in fulfilment of the  
requirements for the award of the degree

Doctor of Philosophy



School of Engineering Physics

University of Wollongong

Australia

2009

Thesis supervisors: Doctor George J. Takacs and Professor Anatoly B.  
Rosenfeld

## ABSTRACT

This work is the first comprehensive investigation of potential changes in the radiobiological effectiveness of clinical photon beams caused by a redistribution of electrons in a magnetic field. It is also a fundamental study of both the influence of magnetic fields on the peak-to-valley dose ratio of microbeams and the accuracy of theoretical modelling for dose planning in Microbeam Radiation Therapy (MRT).

The application of a strong transverse magnetic field to a volume undergoing irradiation by a photon beam can produce localised regions of dose enhancement and dose reduction. Results from Monte Carlo PENELOPE simulation show regions of enhancement and reduction of as much as 111% and 77% respectively for magnetic fields of 1 to 100 T applied to  $\text{Co}^{60}$ , 6, 10, 15, and 24 MV photon beams. The dose redistribution is shown to occur predominantly through an alteration in the lower energy electron population, which may correspond to a change in the relative biological effectiveness.

In MRT, an experimental and theoretical investigation of the influence of transverse and longitudinal magnetic fields on the lateral dose profile and peak-to-valley dose ratio (PVDR) of microbeams is presented. Results show that longitudinal magnetic fields greater than 10 T are needed to produce an effect. Strong transverse magnetic fields, on the other hand, have no influence on microbeam profiles. The radiation response of the edge-on MOSFET and its ability to measure dose profiles of monoenergetic and polyenergetic microbeams are also investigated.

Simulations investigating the dependence of microbeam dose profiles on the accuracy of beamline modelling (i.e. synchrotron source, multislit collimator, and beam divergence) are also presented. Results show the asymmetric collimator construction is responsible for a 10% variation in the full-width at half-maximum of microbeams which affects the PVDR. Modelling the distributed source and beam divergence increases the penumbral dose by almost 30%. The influence of the collimator alignment, interaction medium, and the height of scoring regions on the PVDR are also investigated.

## **CERTIFICATION**

I, Heidi Nettelbeck, declare that this thesis, submitted in fulfilment of the requirements for the award of Doctor of Philosophy, in School of Engineering Physics, University of Wollongong, is wholly my own work unless otherwise referenced or acknowledged. The document has not been submitted for qualifications at any other academic institution.

---

Heidi Nettelbeck

April 14, 2009

## ACKNOWLEDGEMENTS

I would like to acknowledge my supervisors, Doctor George Takacs and Professor Anatoly Rosenfeld and thank them for their guidance throughout the course of this project. In particular, I thank George for his assistance with the Monte Carlo aspects of this work, and Anatoly for sharing his in-depth knowledge of radiation dosimetry.

My appreciation also extends to Doctor Michael Lerch at the Centre for Medical Radiation Physics, University of Wollongong, and the scientists on the ID-17 biomedical beamline at the European Synchrotron Radiation Facility in Grenoble, France, for their assistance with the magneto-MRT experiments. I would also like to acknowledge Terry Braddock and Brad Oborn for constructing the magnet devices used in these experiments, and Doctor José Fernández-Varea for identifying the origin of a spurious peak in the simulated electron spectra.

I also thank the postgraduate students and staff in the School of Physics for their lively discussions and friendship over the years. I have fond memories of mountain and beach runs with George and Neil, and music sessions in the lab. Finally, I thank my friends and family for their ongoing encouragement. A special thank you to Daniel for his unfailing patience and support, and God for carrying me to the end.



## TABLE OF CONTENTS

	Page
LIST OF TABLES . . . . .	vii
LIST OF FIGURES . . . . .	viii
PUBLICATION LIST . . . . .	xix
CHAPTER	
1 Introduction . . . . .	1
1.1 Background and motivation . . . . .	1
1.2 Objectives and scope of this research . . . . .	4
1.3 Thesis outline . . . . .	5
2 Radiation transport and the Monte Carlo PENELOPE code . . . . .	7
2.1 Interactions of radiation with matter . . . . .	7
2.1.1 Photon interactions . . . . .	7
2.1.2 Electron interactions . . . . .	13
2.2 Monte Carlo PENELOPE code . . . . .	14
2.2.1 Brief outline of code structure and operation . . . . .	14
2.2.2 Particle transport . . . . .	15
2.2.3 Electron transport in magnetic fields . . . . .	16
3 Influence of a transverse magnetic field on the dose distribution in photon beam radiotherapy . . . . .	19
3.1 Introduction . . . . .	19
3.2 Simulation methods . . . . .	23
3.3 Simulation results . . . . .	29
3.3.1 Effect of the magnetic field strength . . . . .	29
3.3.2 Effect of the photon beam energy . . . . .	33
3.3.3 Effect of the depth and thickness of magnetic field . . . . .	34
3.4 Discussion . . . . .	40
3.5 Conclusion . . . . .	45
4 Effect of a transverse magnetic field on the electron distribution of high-energy photon beams . . . . .	47
4.1 Introduction . . . . .	47
4.2 Simulation methods . . . . .	50
4.3 Simulation results and discussion . . . . .	55
4.3.1 Influence of a magnetic field on electron spectra below 1 MeV . . . . .	58
4.3.2 Influence of a magnetic field on electron spectra below 10 keV . . . . .	61
4.3.3 Influence of a magnetic field on electron spectra below 1 keV . . . . .	65
4.3.4 Effect of magnetic field on the $w$ -values of electrons . . . . .	72
4.3.5 Effect of magnetic field on the spatial distribution of electrons . . . . .	78



4.4	Conclusion . . . . .	94
5	MOSFET dosimetry in Microbeam Radiation Therapy (MRT) . . . . .	97
5.1	Introduction . . . . .	97
5.1.1	Microbeam Radiation Therapy (MRT) . . . . .	97
5.1.2	MOSFET dosimetry in MRT . . . . .	102
5.1.3	MRT at the ESRF ID-17 biomedical beamline . . . . .	106
5.2	Experimental and simulation methods . . . . .	109
5.3	Results and discussion . . . . .	114
5.3.1	Radiation response of MOSFET dosimeters . . . . .	114
5.3.2	Measured and simulated dose profiles of microbeams . . . . .	117
5.3.3	Measured and simulated peak-to-valley dose ratios (PVDRs) . . . . .	127
5.4	Conclusion . . . . .	136
6	Magneto-MRT: influence of a magnetic field on microbeam profiles . . . . .	139
6.1	Introduction . . . . .	139
6.2	Materials and methods . . . . .	142
6.2.1	Magneto-MRT with a transverse magnetic field . . . . .	142
6.2.2	Magneto-MRT with a longitudinal magnetic field . . . . .	144
6.2.3	Magneto-MRT Monte Carlo simulations . . . . .	154
6.3	Results and Discussion . . . . .	155
6.3.1	Effect of a transverse magnetic field on microbeam profiles . . . . .	155
6.3.2	Effect of a longitudinal magnetic field on microbeam profiles . . . . .	161
6.4	Conclusion . . . . .	169
7	A Monte Carlo study of the influence of MRT beamline components on microbeam profiles . . . . .	171
7.1	Introduction . . . . .	171
7.2	Materials and Methods . . . . .	174
7.3	Results and discussion . . . . .	178
7.3.1	Effect of the beam divergence . . . . .	178
7.3.2	Effect of the multislit collimator . . . . .	179
7.3.3	Effect of the source model . . . . .	181
7.3.4	Effect of the multislit collimator lateral offset . . . . .	184
7.3.5	Effect of the simulation model . . . . .	187
7.3.6	Effect of the multislit collimator alignment . . . . .	195
7.3.7	Effect of the collimator design . . . . .	203
7.3.8	Effect of the interaction medium . . . . .	205
7.3.9	Effect of the height of scoring regions . . . . .	209
7.4	Conclusion . . . . .	211
8	Conclusion . . . . .	215
APPENDICES		
A	High current pulser for the magnet coil in magneto-MRT experiments . . . . .	223
REFERENCES . . . . .		227

## LIST OF TABLES

Table		Page
3.1	Range of electrons in water as a function of energy. . . . .	22
3.2	Comparison of the maximum DPF for a 15 MV beam with $B = 1$ to 100 T. . . . .	31
3.3	Comparison of the minimum DPF for a 15 MV beam with $B = 1$ to 100 T. . . . .	31
3.4	Comparison of the maximum DPF for a 15 MV beam with $B = 1$ to 100 T using bin depths of 0.1 and 0.2 cm. . . . .	32
3.5	Comparison of the minimum DPF for a 15 MV beam with $B = 1$ to 100 T, and bin depths of 0.1 and 0.2 cm. . . . .	33
3.6	Comparison of the maximum DPF for different photon beams with $B = 5$ T. . . . .	33
3.7	Comparison of the minimum DPF for different photon beams with $B = 5$ T. . . . .	34
4.1	Binding energies of hydrogen and oxygen. . . . .	50
4.2	Energies and probabilities of Auger electron production in water. . . . .	71
6.1	Peak and valley doses and PVDR of the central peak (peak 2) in an ar- ray of three microbeams. Peak and valley doses were measured with Gafchromic film at 0.1 and 0.2 cm depth (in perspex) in the presence and absence of a 1 T longitudinal magnetic field, $B$ . . . . .	163



## LIST OF FIGURES

Figure	Page
2.1 Cross sections for photon interactions in water. Data extracted from the NIST XCOM Photon Cross Sections database. . . . .	8
2.2 Angular distribution of Compton scattered photons calculated from the Klein-Nishina cross section. A plot of the intensity of a scattered photon of 0.1, 0.5, 1, 5, 10, and 15 MeV interacting with a free electron at the centre of this graph. . . . .	11
2.3 Angular distribution of Compton scattered electrons calculated from the Klein-Nishina cross section. A plot of the intensity of the electrons produced from Compton scattered photons of 0.1, 0.5, 1, 5, 10, and 15 MeV. . . . .	11
3.1 Energy dependence of the range, mean free path, and radius of curvature of an electron moving in magnetic field. The range of an electron (in water) as a function of energy is based on the data in table 3.1. . . . .	21
3.2 Effect of a slice of 5 T transverse magnetic field (7 to 9 cm depth) on the: (a) depth-dose, and (b) dose perturbation factor (DPF) of a 10 MV beam (direction of magnetic field is out of the page). . . . .	24
3.3 Figure (a) and (b) show the input photon beam spectrum used for simulations with 6 and 10 MV beams, respectively. . . . .	26
3.3 Figure (c) and (d) show the input photon beam spectrum used for simulations with 15 and 24 MV beams, respectively. . . . .	27
3.4 Dose distribution of a 15 MV beam (in water) subjected to a slice of 1, 2, 5, 10, 20 and 100 T transverse magnetic field (7 to 9 cm depth), using bin depths of: (a) 0.2 cm, and (b) 0.1 cm. . . . .	30
3.5 Effect of the elastic scattering parameters $C_1$ and $C_2$ ( $C = C_1 = C_2$ ) on the dose deposition of a 15 MV beam (in water) subjected to a 2 T transverse magnetic field (7 to 9 cm depth). . . . .	32
3.6 Dose distribution of $\text{Co}^{60}$ , 6, 10, 15 and 24 MV photon beams (in water) subjected to a slice of 5 T transverse magnetic field (7 to 9 cm depth). . . . .	34
3.7 Dose distribution of a 15 MV beam with a slice of 5 T transverse magnetic field (2 cm thick) applied at different depths in the water phantom. . . . .	35
3.8 Effect of the magnetic field thickness. Figures (a) and (b) show the effect on the depth-dose of a 15 MV beam when a 2, 5 and 10 T transverse magnetic field is applied at 7.5 to 8.5 cm and 7 to 9 cm depth (i.e. 1 cm and 2 cm thick) in water, respectively. . . . .	36
3.8 Effect of the magnetic field thickness. Figures (c) and (d) show the effect on the depth-dose of a 15 MV beam when a 2, 5 and 10 T transverse magnetic field is applied at 6.5 to 9.5 cm and 6 to 10 cm depth (i.e. 3 cm and 4 cm thick) in water, respectively. . . . .	37
3.9 Effect of the magnetic field thickness. Figures (a) and (b) compare the effect of a 5 T transverse magnetic field of different thicknesses (1 to 4 cm) on the depth-dose (in water) of a 6 and 10 MV beam respectively. . . . .	38

3.9	Effect of the magnetic field thickness. Figures (c) and (d) compare the effect of a 5 T transverse magnetic field of different thicknesses (1 to 4 cm) on the depth-dose (in water) of a 15 and 24 MV beam respectively.	39
3.10	Influence of a magnetic field on the mean distance an electron travels along the beam direction from its origin at 6.9 cm depth.	41
3.11	Secondary electron spectrum of a 15 MV photon beam at different depths (5.5 to 10.5 cm) in water.	42
4.1	Relationship between relative biological effectiveness (RBE) and mean linear energy transfer (LET) for cell killing, where the three curves correspond to different levels of cell survival, or surviving fraction (SF).	48
4.2	Figure (a) plots the absorption and scattering contributions towards the total attenuation of water. Figure (b) plots the PENELOPE atomic photo-electric cross sections of hydrogen (K shell) and oxygen (K, L <sub>1</sub> , L <sub>2</sub> , and L <sub>3</sub> shells).	51
4.3	First generation electron spectra for polyenergetic and monoenergetic photon beams (in water). Figure (a) plots the first generation electron spectra for Co <sup>60</sup> , 6, 10, and 15 MV beams. Corresponding electron spectra for 1, 5, 10, and 15 MeV monoenergetic photon beams are shown in figure (b).	56
4.4	Secondary electron spectra (all generations) for a 15 MV beam with depth (in water). Figures (a) and (b) plot the electron spectra in the presence and absence of a slice of 5 T transverse magnetic field (7 to 9 cm depth), respectively.	57
4.5	Normalised electron spectra (below 1 MeV) for a 15 MV beam. Figures (a) and (b) plot a ratio of the electron population in the presence and absence of a 2 and 5 T transverse magnetic field (7 to 9 cm depth), respectively.	59
4.5	Normalised electron spectra (below 1 MeV) for a 15 MV beam. Figures (c) and (d) plot a ratio of the electron population in the presence and absence of a 10 and 20 T transverse magnetic field (7 to 9 cm depth), respectively.	60
4.6	Secondary electron spectra (below 10 keV) for a 15 MV beam. Figures (a) and (b) plot the electron spectra in five depth regions in the presence and absence of a 5 T transverse magnetic field (7 to 9 cm depth), respectively.	63
4.7	Normalised electron spectra (below 10 keV) for a 15 MV beam. A ratio of the electron population in five depth regions in the presence and absence of a 5 T transverse magnetic field (7 to 9 cm depth).	64
4.8	Ratio of electron spectra (below 10 keV) for a 15 MV beam as a function of magnetic field. A ratio of the electron population in five depth regions in the presence and absence of a 1, 2, 3, 4, 5, 10, and 20 T transverse magnetic field (7 to 9 cm depth).	64
4.9	Photon spectra (below 10 keV) for a 15 MV beam. Figures (a) and (b) plot the photon spectra with and without a 5 T transverse magnetic field (7 to 9 cm depth), respectively.	66
4.10	Electron spectra (below 1 keV) for a 15 MV beam. Figures (a) and (b) plot the electron spectra with and without a 5 T transverse magnetic field (7 to 9 cm depth), respectively.	67

4.11	Normalised electron spectra (below 1 keV) for a 15 MV beam. Figures (a) and (b) plot a ratio of the electron population in the presence and absence of a 2 and 5 T transverse magnetic field (7 to 9 cm depth), respectively. . . . .	68
4.11	Normalised electron spectra (below 1 keV) for a 15 MV beam. Figures (c) and (d) plot a ratio of the electron population in the presence and absence of a 10 and 20 T transverse magnetic field (7 to 9 cm depth), respectively. . . . .	69
4.12	Spectra of atomic relaxation electrons and photons (in water) for a 15 MV beam. Figures (a) and (b) plot the spectra of atomic relaxation electrons with and without a 5 T transverse magnetic field (7 to 9 cm depth), respectively. Atomic relaxation photons are plotted in figure (c). . . . .	70
4.13	Mean $w$ -values of first generation electrons of the following photon beams: (a) Co <sup>60</sup> , 6, 10, and 15 MV, and (b) 0.1, 0.5, 1, 5, 10, and 15 MeV. . . . .	73
4.14	Distance travelled by electrons before they are deviated from their initial trajectory by a given angle. . . . .	74
4.15	Distance electrons travel in water before the angle of deviation from their initial trajectory exceeds 25.8, 45.6, 60, and 90 degrees (i.e. $w = 0.9, 0.7, 0.5$ , and zero). A plot of the accumulative electron population as a function of distance travelled from the origin is shown in figures (a), (b), and (c) for 0.1, 0.5, and 1 MeV electrons, respectively. . . . .	75
4.15	Distance electrons travel in water before the angle of deviation from their initial trajectory exceeds 25.8, 45.6, 60, and 90 degrees (i.e. $w = 0.9, 0.7, 0.5$ , and zero). A plot of the accumulative electron population as a function of distance travelled from the origin is shown in figures (d), (e), and (f) for 5, 10, and 15 MeV electrons, respectively. . . . .	76
4.16	Population and mean $w$ -values of first generation electrons for 15 MV beam beyond 6.9 cm depth (in water). . . . .	77
4.17	Magnetic field's influence on the interaction depths of electrons starting at 6.9 cm depth. Figure (a) plots the electrons' mean $z$ -ranges as a function of magnetic field. A ratio of the mean $z$ -ranges with and without magnetic field is shown in figure (b), and a ratio of electrons with final positions downstream of their initial position ( $z > z_{start}$ ) to those with final positions upstream ( $z < z_{start}$ ) is plotted in figure (c). . . . .	80
4.17	Magnetic field's influence on the lateral ranges of electrons starting at 6.9 cm depth. Figure (d) plots the mean $y$ -ranges of electrons as a function of magnetic field. A ratio of the mean $y$ -ranges with and without magnetic field is shown in figure (e), and a ratio of electrons with negative final $y$ -positions ( $y < 0$ ) to those with positive final $y$ -positions ( $y > 0$ ) is plotted in figure (f). . . . .	81
4.18	Magnetic field's influence on the interaction depths of electrons starting at 7.5 cm depth. Figure (a) plots the electrons' mean $z$ -ranges as a function of magnetic field. A ratio of the mean $z$ -ranges with and without magnetic field is shown in figure (b), and a ratio of electrons with final positions downstream of their initial position ( $z > z_{start}$ ) to those with final positions upstream ( $z < z_{start}$ ) is plotted in figure (c). . . . .	84

4.18	Magnetic field's influence on the lateral ranges of electrons starting at 7.5 cm depth. Figure (d) plots the mean $y$ -ranges of electrons as a function of magnetic field. A ratio of the mean $y$ -ranges with and without magnetic field is shown in figure (e), and a ratio of electrons with negative final $y$ -positions ( $y < 0$ ) to those with positive final $y$ -positions ( $y > 0$ ) is plotted in figure (f). . . . .	85
4.19	Magnetic field's influence on the interaction depths of electrons starting at 8.5 cm depth. Figure (a) plots the electrons' mean $z$ -ranges as a function of magnetic field. A ratio of the mean $z$ -ranges with and without magnetic field is shown in figure (b), and a ratio of electrons with final positions downstream of their initial position ( $z > z_{start}$ ) to those with final positions upstream ( $z < z_{start}$ ) is plotted in figure (c). . . . .	88
4.19	Magnetic field's influence on the lateral ranges of electrons starting at 8.5 cm depth. Figure (d) plots the mean $y$ -ranges of electrons as a function of magnetic field. A ratio of the mean $y$ -ranges with and without magnetic field is shown in figure (e), and a ratio of electrons with negative final $y$ -positions ( $y < 0$ ) to those with positive final $y$ -positions ( $y > 0$ ) is plotted in figure (f). . . . .	89
4.20	Magnetic field's influence on the interaction depths of electrons starting at 8.9 cm depth. Figure (a) plots the electrons' mean $z$ -ranges as a function of magnetic field. A ratio of the mean $z$ -ranges with and without magnetic field is shown in figure (b), and a ratio of electrons with final positions downstream of their initial position ( $z > z_{start}$ ) to those with final positions upstream ( $z < z_{start}$ ) is plotted in figure (c). . . . .	91
4.20	Magnetic field's influence on the lateral ranges of electrons starting at 8.9 cm depth. Figure (d) plots the mean $y$ -ranges of electrons as a function of magnetic field. A ratio of the mean $y$ -ranges with and without magnetic field is shown in figure (e), and a ratio of electrons with negative final $y$ -positions ( $y < 0$ ) to those with positive final $y$ -positions ( $y > 0$ ) is plotted in figure (f). . . . .	92
5.1	Schematic diagram of a $p$ -MOSFET (Metal-Oxide-Semiconductor Field Effect Transistor) dosimeter. . . . .	103
5.2	Schematic diagram of the MOSFET reader. The MOSFET dosimeter is read out under a constant current $I_D$ with the gate and source grounded. The threshold voltage, $V_{th}$ , measured across the MOSFET is proportional to the dose deposited in the $\text{SiO}_2$ gate oxide. . . . .	104
5.3	The dose response of MOSFET dosimeters to effective radiation energy. The dose response (in free-air geometry) was normalised to that obtained with 6 MV X-rays from a medical linear accelerator. . . . .	106
5.4	X-ray energy spectrum for MRT measured at the ESRF ID-17 biomedical beamline. . . . .	107
5.5	Schematic diagram of the MRT setup at the ESRF ID-17 beamline. . . . .	108
5.6	Scanning electron microscope image of the REM TOT500 RADFET chip ( $1 \times 1 \times 0.5 \text{ mm}^3$ ), which shows the two low-sensitive MOSFETs, Q2 and Q3, and two high-sensitive MOSFETs, Q1 and Q4. The direction of the X-ray microbeam is indicated by the arrows. . . . .	110
5.7	Illustration of the MOSFET configuration used to scan the dose profiles of monoenergetic microbeams, where the beam direction is into the page. . . . .	112

5.8	Radiation response of MOSFET dosimeters. Figure (a) plots the normalised response of a MOSFET(H) dosimeter subjected to $43 \times 0.15$ s pulses of white beam radiation. The response of a MOSFET(L) dosimeter to $19 \times 0.03$ s irradiations with a 50 keV beam is shown in figure (b).	115
5.8	Radiation response of MOSFET dosimeters. Figure (c) plots the normalised response of a MOSFET(H) dosimeter subjected to $20 \times 0.15$ s pulses of irradiation with a 50 keV beam. The response of a MOSFET(H) dosimeter to $25 \times 10$ s irradiations with a 100 keV beam is shown in figure (d).	116
5.9	Dose profiles of monoenergetic microbeams measured at 1.1 cm depth (in perspex) with a MOSFET(L) dosimeter. Figures (a) and (b) show the dose profile of the central peak in an array of 24 microbeams (peak 12) for 30 and 50 keV beams, respectively.	118
5.9	Dose profiles of monoenergetic microbeams measured at 1.1 cm depth (in perspex) with a MOSFET(L) dosimeter. Figures (c) and (d) show the dose profile of the central peak in an array of 24 microbeams (peak 12) for 70 and 100 keV beams, respectively.	119
5.10	Dose profile of the central peak in an array of 24 microbeams (peak 12) obtained with the ESRF white beam and measured with a MOSFET(H) dosimeter at 1.1 cm depth (in perspex).	120
5.11	Comparison of the dose profile of the central peak in an array of 24 microbeams (peak 12) measured with a MOSFET at 1.1 cm depth (in perspex) for the white beam and monoenergetic beams of 30, 50, 70, and 100 keV.	121
5.12	Simulated dose profile of the central microbeam in an array of 24 microbeams (peak 12) obtained at 1.1 cm depth (in perspex) for the white beam and monoenergetic beams of 30, 50, 70, and 100 keV.	122
5.13	Simulated penumbral and valley dose of a single microbeam, and the central microbeam (peak 12) in an array of 24 microbeams. Figures (a) and (b) plot the dose profile of a single microbeam and peak 12, respectively, at 1.1 cm depth (in perspex) for the white beam and monoenergetic beams of 30, 50, 70, and 100 keV.	123
5.14	Simulated microbeam profile showing the dose distribution according to the type of initial photon interaction. Figures (a) and (b) plot the dose contributions of a single microbeam at 1.1 cm depth (in perspex) for monoenergetic beams of 30 and 50 keV, respectively.	124
5.14	Simulated microbeam profile showing the dose distribution according to the type of initial photon interaction. Figures (c) and (d) plot the dose contributions of a single microbeam at 1.1 cm depth (in perspex) for monoenergetic beams of 70 and 100 keV, respectively.	125
5.15	Comparison of the Continuous Slowing Down Approximation (CSDA) range of electrons in silicon and perspex.	126
5.16	Photon interaction cross sections in silicon.	128
5.17	Measured PVDR of the central microbeam in an array of 24 (peak 12) calculated from peak and valley doses obtained at 1.1 cm depth (in perspex) for 30, 50, and 70 keV beams and the white beam (maximum intensity of 83 keV).	129



5.18	Simulated PVDR of the central microbeam in an array of 24 (peak 12) calculated from the theoretical dose profiles at 1.1 cm depth (in perspex) for 30, 50, 70, and 100 keV beams and the white beam (maximum intensity of 83 keV). . . . .	130
5.19	Measured PVDRs of microbeams 12, 17, and 22 (in an array of 24 microbeams) for the 50 keV and white beams, calculated from peak and valley dose measurements obtained with a MOSFET at 1.1 cm depth (in perspex). . . . .	132
5.20	Simulated PVDRs of microbeams 12, 17, and 22 (in an array of 24 microbeams) for the 50 keV and white beams, calculated from the theoretical dose profiles obtained at 1.1 cm depth (in perspex). The 50 keV measured PVDRs (meas 50 keV) are also shown for comparison. . . . .	133
5.21	Simulated PVDRs for an array of 24 microbeams, calculated from the theoretical dose profiles obtained at 1.1 cm depth (in perspex) with the white beam and 30, 50, 70, and 100 keV monoenergetic beams. . . . .	134
5.22	Measured and simulated PVDRs with depth (in perspex) for the central peak in an array of three microbeams (peak 2) produced with a white beam. The measured PVDRs were obtained at 0.9, 1.9, and 2.8 cm depth, and the theoretical PVDRs at various depths up to 1.2 cm. . . . .	134
5.23	Simulated peak and valley doses for the central peak in an array of three microbeams (peak 2) up to 2.8 cm depth (in perspex). Peak and valley doses have been normalised to their maximum values. . . . .	135
6.1	Impact of different types of interaction on the lateral dose profile of a single microbeam (25 $\mu\text{m}$ wide) obtained with the ESRF white beam. Curve 1 plots the microbeam profile comprising all interaction contributions. Curves 2, 3, and 4 plot the profile with suppression of the photoelectric effect, Compton scattering, and electron tracking, respectively. . . . .	140
6.2	Simulated first generation electron spectrum of the ESRF white beam (in perspex). . . . .	141
6.3	Photos of the 1 T transverse magnetic field device used for magneto-MRT experiments (direction of magnetic field is towards the handle). The magnet device (right) was mounted on the goniometer stage, where a perspex phantom containing a MOSFET was wedged between the magnet poles (left). . . . .	143
6.4	Illustration of the 1 T longitudinal magnetic field device used for magneto-MRT experiments. A 0.3 cm diameter hole was drilled through the centre of the permanent magnets to allow the passage of microbeams parallel to the direction of magnetic field. . . . .	144
6.5	Scatter contributions from different magnet materials. Figure (a) plots the depth-dose profile of a pencil beam simulated with different magnet materials (NdFeB, perspex, and air) in three regions along central axis: air cavity 1, perspex phantom, and air cavity 2. Figure (b) plots the depth-dose profile with perspex replacing the air in cavity 2. . . . .	147
6.6	Effect of magnet scatter contributions on the radial dose. Figure (a) plots a ratio of the radial dose with and without NdFeB magnets, at the following depths: 2.48 cm (exit of air cavity 1), 2.60 and 2.90 cm (1 and 4 mm depth in perspex), and 3.02 cm (entrance to air cavity 2). Figures (b) and (c) plots the corresponding radial dose with perspex magnets instead of NdFeB, and perspex replacing the air in cavity 2. . . . .	148

6.7	Photo of the 2 T longitudinal magnetic field device used for magneto-MRT experiments. The device comprises a pair of cylindrical NdFeB permanent magnets with steel focus cones and a U-shaped iron circuit to maximise magnetic flux. . . . .	150
6.8	MATLAB simulation of the magnetic flux produced by the longitudinal magnetic field device. A maximum field of 2.2 T was calculated between the focus cones, which were separated by 1 cm. . . . .	151
6.9	Photos of the magnet coil used for magneto-MRT experiments. The 828-turn copper coil was mounted on the goniometer (left), where the cylindrical perspex phantom (housing the MOSFET) was inserted into the air core and secured to a perspex block behind the coil (right). . . . .	153
6.10	Oscilloscope output verifying the synchronisation of the current pulse (i.e. pulsed magnetic field) and the rectangular diode pulse (i.e. beam delivery). . . . .	153
6.11	Oscilloscope output verifying the coincidence of the pulsed current (i.e. discharge of capacitors) and magnetic field. Delay between the current and diode pulses was adjusted to provide a maximum magnetic field during irradiation of the target. . . . .	154
6.12	Lateral dose profile of an array of three microbeams measured with a MOSFET at 0.9 cm depth (in perspex) in the presence of a 1 T transverse magnetic field. . . . .	156
6.13	Effect of a 1 T transverse magnetic field on the valley dose of an array of three microbeams. Figures (a) and (b) plot the dose profiles of valley regions $V_{12}$ and $V_{23}$ (i.e. left and right of the central microbeam, peak 2) respectively, measured with a MOSFET at 0.9 cm depth (in perspex) in the presence and absence of magnetic field. . . . .	157
6.14	Valley dose for an an array of three microbeams measured with a MOSFET at 0.9, 1.9, and 2.8 cm depth (in perspex). Figures (a) and (b) plot the dose at the centre of valleys $V_{12}$ and $V_{23}$ (i.e. left and right of the central microbeam, peak 2) respectively, in the presence and absence of a 1 T transverse magnetic field. . . . .	158
6.14	Peak dose and PVDR for the central microbeam in an array of three microbeams (peak 2) measured with a MOSFET at 0.9, 1.9, and 2.8 cm depth (in perspex), in the presence and absence of a 1 T transverse magnetic field, is shown in figures (c) and (d) respectively. The PVDR was calculated using the dose at the centre of peak 2 and valleys $V_{12}$ and $V_{23}$ on either side. . . . .	159
6.15	Simulated effect of a transverse magnetic field on the dose profile of an array of three microbeams. A plot of the microbeam array scored between 0.8 and 1.0 cm depth (in perspex) in the presence and absence of a 2 and 100 T transverse magnetic field. . . . .	161
6.16	Dose profile of an array of three microbeams measured with Gafchromic film at 0.1, 0.2, 0.7, 1.1, and 1.2 cm depths (in perspex) in the absence of magnetic field. . . . .	162
6.17	Peak dose of the central microbeam in an array of three microbeams (peak 2) with depth. A plot of the peak dose measured with Gafchromic film at depths (in perspex) of 0.1, 0.2, 0.3, and 0.4 cm in the presence of a 1 T longitudinal magnetic field, and 0.1, 0.2, 0.7, 1.1, and 1.2 cm in the absence of magnetic field. . . . .	163

6.18	Effect of a 1 T longitudinal magnetic field on the peak and valley doses of an array of three microbeams. Figures (a) and (b) show the peak and valley dose profiles, respectively, measured with Gafchromic film at 0.2 cm depth (in perspex) in the presence and absence of magnetic field. . . . .	164
6.19	Simulated effect of a longitudinal magnetic field on the dose profile of a single microbeam. A plot of the profile scored between 1.0 and 1.2 cm depth (in perspex) in the presence and absence of a 2, 10, 20, 50, and 100 T magnetic field. . . . .	166
6.20	Simulated effect of a longitudinal magnetic field on the dose profile of an array of three microbeams. Figure (a) shows the dose profile of the array scored between 1.0 and 1.2 cm depth (in perspex) in the presence and absence of a 2, 10, 20, 50, and 100 T magnetic field. A ratio of the dose profile with and without magnetic field is plotted in figure (b). . . . .	168
6.21	Simulated effect of a longitudinal magnetic field on the PVDR of an array of three microbeams. A plot of the PVDR of the central microbeam against magnetic field strength, using the dose profiles scored between 1.0 and 1.2 cm depth (in perspex). . . . .	169
7.1	Photo of the Tecomet <sup>®</sup> multislit collimator (left) which comprises two identical tungsten air stacks mounted in an aluminum frame. Each stack (right) contains 125 parallel, 100 $\mu\text{m}$ wide, 8 mm deep apertures with 400 $\mu\text{m}$ centre-to-centre spacing. . . . .	173
7.2	Illustration of the lateral offset of the multislit collimator stacks. Figure (a) illustrates the adjustment of microbeam width by laterally moving one stack relative to the other (as indicated by arrows). Figure (b) shows an enlargement of a single collimator element, comparing the photon transmission through the central collimator aperture (C) and the fifth apertures to the left and right of centre (L5 and R5 respectively). . . . .	176
7.3	Illustration of the effect of multislit collimator alignment. Figure (a) shows the multislit collimator rotated through a small positive angle (with respect to the beam). Figure (b) shows an enlargement of a single collimator element, comparing the photon transmission through the central aperture (C) and the fifth apertures to the left and right of centre (L5 and R5 respectively). . . . .	178
7.4	The influence of the beam divergence (i.e. source to target distance). Figure (a) compares the dose profile of a single microbeam scored between 1 and 2 cm depth (in water) with and without beam divergence (Diverge and On Phantom, respectively). A ratio of the Diverge and On Phantom profiles is shown in figure (b). . . . .	180
7.5	The effect of the multislit collimator. Figure (a) plots a ratio of the dose profile of a single microbeam obtained with and without the multislit collimator (MSC and NoMSC, respectively) and a point source (Pt src). A ratio of the corresponding MSC and NoMSC profiles obtained with a distributed source (Dist src) is plotted in figure (b). All dose profiles were scored between 1 and 2 cm depth in water. . . . .	182
7.6	The effect of the source model. Figure (a) compares the dose profile of a single microbeam obtained with a point source (Pt src) to that produced by a distributed source (Dist src), using the multislit collimator (MSC). The dose profiles were scored between 1 and 2 cm depth (in water), where a ratio of the profiles is plotted in figure (b). . . . .	183

7.7	The effect of the multislit collimator (MSC) lateral offset. Figures (a) and (b) compare the dose profile of the central microbeam (C single) with those obtained for the 5th and 12th microbeams to the left and right of centre, respectively (i.e. in LHS array and RHS array). . . . .	185
7.7	The effect of the multislit collimator (MSC) lateral offset. Figures (c) and (d) compare the dose profiles of the 5th and 12th microbeams on either side of centre, respectively (i.e. L5 single with R5 single and L12 single with R12 single). . . . .	186
7.8	The effect of the simulation model. Figure (a) compares the dose profile of the central microbeam simulated with the single-beam and full array models (C single and C full, respectively) and scored between 1 and 2 cm depth in water. A ratio of these C profiles, and those obtained for the L12 and R12 microbeams at either edge of the array, are shown in figure (b). . . . .	189
7.9	Effect of the simulation model. Figure (a) shows the dose profile of a single microbeam used by the superposition model. Figure (b) plots the dose profile of the sup and full arrays obtained with the superposition and full array models, respectively, where a ratio of these profiles is shown in figure (c). All profiles were scored between 1 and 2 cm depth (in water). . . . .	191
7.10	The effect of the simulation model. Figure (a) plots a ratio of the sup and full array dose profiles of the L12 and R12 microbeams at the left and right edges of the array, respectively. Figure (b) compares the central microbeam profile in the full array (C full) with those at the left and right edges of the array (L12 full and R12 full, respectively). . . . .	193
7.11	The effect of the simulation model. Figure (a) compares the PVDRs of microbeams in the sup array and full array. A ratio of the peak and valley doses and PVDRs of microbeams in the sup and full arrays is plotted in figure (b). . . . .	194
7.12	The effect of the multislit collimator alignment on the dose profile of an array of 25 microbeams. Figures (a), (b), and (c) compare the dose profile of the full array with and without collimator rotations of $\pm 0.05^\circ$ , $\pm 0.1^\circ$ , and $\pm 0.2^\circ$ respectively. . . . .	196
7.13	The effect of the multislit collimator alignment on the dose profile of the central microbeam. Figures (a), (b), and (c) compare the dose profile of the central microbeam (C) produced with and without collimator rotations of $\pm 0.05^\circ$ , $\pm 0.1^\circ$ , and $\pm 0.2^\circ$ respectively. . . . .	197
7.14	The effect of positive angles of collimator rotation on the dose profiles of microbeams. Figures (a), (b), and (c) compare the dose profile of the central microbeam (C full) with those at the left and right edges of the array (L12 full and R12 full) for collimator rotations of 0.05, 0.1, and 0.2° respectively. . . . .	198
7.15	The effect of negative angles of collimator rotation on the dose profiles of microbeams. Figures (a), (b), and (c) compare the dose profile of the central microbeam (C full) with those at the left and right edges of the array (L12 full and R12 full) for collimator rotations of -0.05, -0.1, and -0.2° respectively. . . . .	200

7.16	The effect of the multislit collimator alignment on the peak and valley doses of microbeams. Figures (a) and (b) respectively compare the peak and valley doses of a microbeam array (normalised to dose in the central microbeam) with and without collimator rotations of $\pm 0.05^\circ$ , $\pm 0.1^\circ$ , and $0.2^\circ$ . The dose profile obtained with a $-0.2^\circ$ rotation is not shown owing to poor statistics. . . . .	201
7.17	The effect of the multislit collimator alignment on the PVDRs of microbeams. Figure (a) compares the PVDRs of a microbeam array obtained with collimator rotations of $\pm 0.05^\circ$ , $\pm 0.1^\circ$ , and $\pm 0.2^\circ$ . A ratio of the PVDRs with and without collimator rotation is plotted in figure (b). . . . .	202
7.18	The effect of the multislit collimator design on microbeam profiles. Figure (a) compares the dose profile of the central microbeam produced with the dual stack collimator (C full) with those at the left and right edges of array (L12 full and R12 full). The corresponding microbeam profiles obtained with a single stack collimator are shown in figure (b). . . . .	204
7.19	Effect of the alignment of the single stack collimator on the dose profiles of microbeams. Figures (a) and (b) plot the dose profiles of the central microbeam (C full) and the L12 full and R12 full microbeams (at the left and right edges of the array) produced with the single stack collimator rotated through $0.05^\circ$ and $-0.05^\circ$ , respectively. . . . .	206
7.20	Effect of the interaction medium on microbeam profiles. Figure (a) compares the dose profile of the central peak in an array of 25 microbeams (C full) scored between 1 and 2 cm depth in water ( $H_2O$ ) and polymethyl methacrylate (PMMA). A ratio of the dose profiles is shown in figure (b). . . . .	208
7.21	Single microbeam profile showing the dose distribution according to the type of initial photon interaction in water ( $H_2O$ ) and polymethyl methacrylate (PMMA) for a 100 keV beam, where CS = Compton scattering, PE = Photoelectric effect, and Total = contributions from CS, PE, and Rayleigh scattering. . . . .	209
7.22	Effect of the height of scoring regions on the valley dose of microbeams. Comparison of the valley dose of the central microbeam (C full) in five lateral slices (each 0.2 cm high) to the total valley dose in all slices (i.e. 0 to 1 cm). . . . .	210
7.23	Effect of the height of scoring regions on the PVDR of microbeams. A ratio of the PVDR in five individual lateral slices (each 0.2 cm high) to the total PVDR integrated over all slices (i.e. 0 to 1 cm). . . . .	210
A.24	Circuit diagram of the pulse time delay. Discharge of the capacitor bank was initiated with a trigger signal generated from either a manual trigger button on the control panel or by an external transistor-transistor logic (TTL) input pulse. . . . .	224
A.25	Circuit diagram of current pulser. When a current of 200 A was pulsed through the coil, a magnetic field of about 2.5 T was estimated at the centre of the coil's air core. . . . .	225
A.26	Test results for the magnet coil. Charging the capacitor bank to 300 V enabled a discharge current of around 200 A to be pulsed through the coil. This corresponded to a peak flux of 1.3 T at the centre of the coil's surface. . . . .	226

## PUBLICATION LIST

The following publications are by the author, several of which are used in this work:

1. H. Nettelbeck, G. J. Takacs, M. L. F. Lerch and A. B. Rosenfeld, “Microbeam radiation therapy: A Monte Carlo study of the influence of the source, multislit collimator and beam divergence on microbeams,” *Medical Physics*, vol. 36(2), pp. 447–456, 2009.
2. H. Nettelbeck, G. J. Takacs and A. B. Rosenfeld, “Effect of transverse magnetic fields on dose distribution and RBE of photon beams: comparing PENELOPE and EGS4 Monte Carlo codes,” *Physics in Medicine and Biology*, vol. 53, pp. 5123–5137, 2008.
3. E. A. Siegbahn, H. Nettelbeck, E. Bräuer-Krisch, M. L. F. Lerch, A. B. Rosenfeld and A. Bravin, “MOSFET dosimetry with high spatial resolution in intense synchrotron-generated x-ray microbeams,” *Medical Physics*, vol. 36(4), pp. 1128–1127, 2009.
4. A. B. Rosenfeld, E. A. Siegbahn, E. Bräuer-Krish, A. Holmes-Siedle, M. L. F. Lerch, A. Bravin, I. M. Cornelius, G. J. Takacs, N. Painuly, H. Nettelbeck and T. Kron, “Edge-on face-to-face MOSFET for synchrotron microbeam dosimetry: MC modeling,” *IEEE Transactions on Nuclear Science*, vol. 52(6)1, pp. 2562–2569, Dec. 2005.
5. H. Nettelbeck, M. Lerch, G. Takacs and A. Rosenfeld, “Magneto-Radiotherapy: Making the electrons conform,” *Australasian Physical & Engineering Sciences in Medicine*, vol. 31(1), pp. 77–78, Mar. 2008.

6. H. Nettelbeck, M. Lerch, G. Takacs and A. Rosenfeld, “Magneto-Radiotherapy: Using magnetic fields to ‘guide’ dose-deposition,” *Australasian Physical & Engineering Sciences in Medicine*, vol. 29(4), p. 359, Dec. 2006.
7. H. Nettelbeck, A. Rosenfeld, G. Takacs and M. Lerch, “Magneto-Radiotherapy: Effect of magnetic field on dose distribution and RBE,” *Australasian Physical & Engineering Sciences in Medicine*, vol. 28(4), pp. 276–277, Dec. 2005.
8. H. Nettelbeck, M. Lerch, G. Takacs and A. Rosenfeld, “Microbeam Radiation Therapy (MRT): Monte Carlo modelling of microbeams,” *Australasian Physical & Engineering Sciences in Medicine*, accepted for publication.

## CONFERENCES

The author has presented work at the following conferences:

1. Australasian College of Physical Scientists and Engineers in Medicine symposium (MedPhys08), Sydney, Australia, Dec. 2008. Presentation: “Microbeam Radiation Therapy (MRT): Monte Carlo modelling of microbeams.”
2. Australasian High Energy Physics and Medical Physics conference (AUSHEP08), Adelaide, Australia, Dec. 2008. Presentation: “Microbeam Radiation Therapy: Application of magnetic fields and the accuracy of Monte Carlo in MRT.”
3. New Prospects for Brain Tumour Radiotherapy: Synchrotron Light and Microbeam Radiation Therapy conference (SYRAD 2008), European Synchrotron Radiation Facility (ESRF), Grenoble, France, June 2-4, 2008. Presentation: “Modelling the source and multislit collimator geometry and their influence on MRT microbeam profiles.”
4. Australasian College of Physical Scientists and Engineers in Medicine symposium (MedPhys07), Sydney, Aust., Dec. 2007. Presentation: “Magneto-Radiotherapy: Making the electrons conform.”
5. Engineering and Physical Sciences in Medicine (EPSM06), Noosa, Australia, Sep. 17-21, 2006. Presentation: “Magneto-Radiotherapy: Using magnetic fields to ‘guide’ dose-deposition.”
6. Australasian College of Physical Scientists and Engineers in Medicine symposium (MedPhys06), Sydney, Aust., Dec. 2006. Presentation: “Magneto-Radiotherapy: Using magnetic fields to ‘guide’ dose-deposition.”



7. Australian Institute of Nuclear Science and Engineering 18th Radiation Biology conference (AINSE Radiation 2006), Sydney, Australia, April 20-21, 2006. Presentation: “Magneto-Radiotherapy: Effect of a magnetic field on dose-deposition and RBE.”
8. World Congress on Medical Physics and Biomedical Engineering 2006 (WC 2006), Seoul, Korea, Aug. 27 - Sep. 1 “Magneto-Radiotherapy: effect of magnetic field on dose distribution” (presented by A. B. Rosenfeld on author’s behalf).
9. Engineering and Physical Sciences in Medicine (EPSM05), Adelaide, Australia, Oct. 23-27, 2006. Presentation: “Magneto-Radiotherapy: Effect of a magnetic field on dose-deposition and RBE.”
10. Australian Experimental High Energy Physics Consortium (AEHEPC05), Melbourne, Australia, Dec. 12-14, 2005. Presentation: “Magneto-Radiotherapy: Enhancement of dose distribution in radiotherapy and synchrotron MRT.”
11. Experimental Radiation Oncology workshop (ERO 2004), Newcastle, Australia, Dec. 2004. Presentation: “Magneto-Radiotherapy: Effect of a magnetic Field on physical absorbed dose distribution and RBE.”

# **CHAPTER 1**

## **INTRODUCTION**

### **1.1 Background and motivation**

The prevalence of cancer worldwide continues to drive scientists to search for a cure. While this thesis makes no attempt at finding a cure, it does constitute another step towards the research and development of current radiotherapy techniques for improving cancer treatment.

Cancer is a group of diseases characterised by the uncontrolled growth and spread of abnormal cells. It is a leading cause of death worldwide, with 7.9 million deaths being attributed to it in 2007 [1]. Globally, over 22 million people are burdened by the disease which impinges on the lives of tens of millions every year [2]. In Australia, 1 in 3 men and 1 in 4 women will be diagnosed with cancer before the age of 75 [3]. Of the people who develop cancer, about one half will undergo some form of radiation treatment [2, 4].

Radiation therapy, or radiotherapy, is the medical use of ionising radiation to treat a variety of diseases. The ultimate goal of radiotherapy is to deliver a high dose of radiation to a well-defined target volume with minimal radiation toxicity to surrounding healthy tissues. Radiotherapy can be administered curatively for eradication of the disease, or palliatively for localised tumour control or symptomatic relief to prolong and improve the quality of life. Treatment can be delivered from outside the body via external beam radiotherapy, or from inside the body via brachytherapy (i.e. sealed sources are placed inside or close to the tumour) or systemic radiation (i.e. unsealed sources ingested or injected into the body). The type of radiation and dose delivery technique depends on the tumour type as well as its progression and location within the body (e.g. deep-seated tumours benefit from deep-penetrating radiation, whilst short-range radiation is suitable

for tumours that are localised or near to radiation-sensitive tissue). Today radiotherapy is used to treat most types of solid tumours such as cancer of the bladder, brain, breast, cervix, larynx, lung, prostate, skin, soft tissue, spine, stomach, and uterus.

Over the last century, following the discovery of X-rays by Wilhelm Röntgen in 1895 and shortly afterwards natural radioactivity by Henry Becquerel, the discipline of radiotherapy has progressed from experimental application of X-rays with rudimentary equipment to more accurate and efficient treatment procedures that use sophisticated technologies. Radiotherapy began towards the close of the 19th century, within two months of Röntgen's discovery of X-rays. It was pioneered by Emil Grubbé when he used X-rays to irradiate a patient with advanced breast cancer [5]. A couple of years later, in 1898, Marie Curie's discovery of radium as a natural source of high-energy X-rays (i.e.  $\gamma$ -rays) led to its use in the treatment of deep-seated tumours [6]. By 1910, the use of brachytherapy emerged with the implantation of radium tubes directly into the diseased region of the body. In 1913, William Coolidge's invention of the hot-cathode tube (to thermally emit electrons) revolutionised radiotherapy in that it allowed the control of radiation quality and quantity (dose) [7]. During the 1940s, with the introduction of particle accelerators and the betatron, megavoltage X-ray treatment became available for deep-seated tumours. Less than a decade later, the first clinical linear accelerator (linac) was built [8] and, in 1953, the first patient treatment was recorded [9].

The availability of computers in the early 1960s paved the way for a new era in cancer therapy and diagnosis. In the late 1970s treatment planning profited enormously with the development of diagnostic imaging technologies such as computerised tomography (CT) and, less than a decade later, magnetic resonance imaging (MRI). This technology, which provides detailed patient-specific anatomical data, has enabled the determination of the size and location of the tumour as well as any nearby radiation-sensitive healthy tissues. Treatment planning uses this data to optimise the size and direction of radiation beams in such a way to maximise dose to the tumour while minimising the damage to surrounding healthy tissues.

Over the years, numerous 3-D dose-calculation algorithms have been developed for treatment planning in radiotherapy. Generally, these algorithms can be classified into two groups; i) analytical correction-based methods, which predict dose deposition using data collected in water, and ii) model-based methods, which use the physical principles of photon and electron transport to simulate patient treatment [10]. The primary difference between the two is that model-based methods do not rely on measured dose data to correct patient treatment [11]. Of these algorithms, those based on Monte Carlo modelling are considered to be the most accurate [10, 12–14]. Its superior accuracy over other dose calculation algorithms stems from its ability to model complex radiation transport in heterogeneous geometries for any incident beam, where the selection of particle positions and interaction types is made using random numbers. Monte Carlo also has the ability to directly simulate particle transport through the geometry of beam delivery devices, such as those in the treatment-head of a linac. It can also be used to estimate dose quantities from individual particle types and sources that are difficult or not amenable to measurement [13]. These abilities, coupled with increased computer processing power, have led to Monte Carlo becoming increasingly available in commercial radiation therapy planning systems.

There is no universal method of cancer treatment. Although conventional external beam radiotherapy is one of the most common modalities, it can be unsuitable for some types of tumours. Studies have shown that broad-beam conventional radiotherapy treatment of infantile brain tumours can be irretrievably damaging to the developing brain, especially for children less than three years of age [15–19]. Considering brain tumours are among the most common forms of cancer in children [17], a safe alternative treatment method is desirable. Microbeam Radiation Therapy (MRT) is a promising alternative.

MRT is an innovative experimental technique that uses a synchrotron and multislit collimator to produce an array of parallel, rectangular, micron-sized X-ray beams (microbeams) [19–28] analogous to the parallel panels of open vertical blinds. Aimed at the tumour volume, the microbeams interact in tissue, delivering a lethal radiation dose

to cells in their path (i.e. peak regions) whilst sparing cells lying in the fraction of a millimeter spacing between adjacent microbeams, called valley regions. The advantage of MRT over broad-beam radiotherapy is the ability of normal tissue to tolerate large amounts of radiation in small volumes whilst preserving the tissue's architecture, which has been demonstrated in a number of small-animal MRT studies [18, 20, 21, 24, 28–30]. This high resistivity of normal tissue to radiation damage from microscopically thin ionising radiation beams was first observed by Curtis at the Brookhaven National Laboratory (BNL), in 1967, when investigating the hazards of cosmic radiation on astronauts [31]. Almost 40 years later, the development of MRT began at the National Synchrotron Light Source (NSLS) in Upton, New York, USA [32] and a few years later at the European Synchrotron Radiation Facility (ESRF) in Grenoble, France. Today, MRT is in its final stages of development. At the ESRF, preparations are in place for clinical MRT trials on dogs which, if successful, could lead to the availability of MRT to humans.

## **1.2 Objectives and scope of this research**

A primary objective of this thesis is to explore the potential therapeutic benefits that may arise with the application of magnetic fields during external photon beam and Microbeam Radiation Therapy (MRT) treatments. This work is based on the premise that magnetic fields can alter the trajectory of charged particles and the distribution of their dose.

In radiobiology, or the study of ionising radiation on biological systems, the principle target for radiation-induced biological effects is the DNA of cells. Strand breaks in DNA from charged particle tracks and chemical species (free-radicals) can bring about cell death, carcinogenesis and mutation [33–35]. Successful cell-killing occurs when a sufficient number of breaks in the DNA occur within close proximity. This begs the question of whether magnetic fields can be used to alter the paths of charged particles (electrons) in such a way to bring about a change in their relative biological effectiveness. The influence of a magnetic field on the electron spectrum of a clinical 15 MV photon beam,

typically used in conventional external beam radiotherapy, will be discussed.

The use of magnetic fields in radiotherapy, or magneto-radiotherapy, will also be investigated for MRT with the aim of improving the peak-to-valley dose ratio (PVDR) by reducing the lateral scatter of electrons out of the peak regions and into the valleys. This will be investigated with a combination of Monte Carlo simulation and physical measurement. Since the advent of MRT, there has been an ongoing quest to find a radiation detector suitable for measuring dose in micrometer-sized volumes. The MOSFET detector has shown potential with its small sensitive volume and micron resolution. Measurements will be performed to characterise the radiation response of the MOSFET for multiple use in MRT. Its ability to measure the lateral dose profiles of monoenergetic and polyenergetic microbeams, and hence estimate PVDRs, will also be investigated.

An ongoing challenge in MRT is the resolution of discrepancies between the absorbed dose calculated by Monte Carlo and that measured experimentally. The need to resolve these discrepancies is driven by the desirability of making MRT available to humans, and hence the demand for an accurate dose planning system. This work addresses the importance of modelling beamline components by using PENELOPE Monte Carlo simulation to investigate the influence of the source, multislit collimator, and beam divergence on the dose profiles of microbeams.

### **1.3 Thesis outline**

Monte Carlo simulation is used extensively throughout this thesis for the calculation of dose and other physical quantities that may be difficult or not amenable to measurement. An introduction to the Monte Carlo method and a description of the Monte Carlo PENELOPE toolkit are provided in chapter 2.

Chapter 3 uses Monte Carlo PENELOPE to explore the influence of a transverse magnetic field on the dose distribution of high-energy photon beams, such as those typically used in radiotherapy. A comparative study is made between the dose distributions

obtained with the Monte Carlo PENELOPE and EGS4 codes for the purpose of benchmarking PENELOPE's charged particle transport algorithm in static electromagnetic field applications. The optimal width of the magnetic field and depth at which it is applied to achieve maximum therapeutic benefit is also presented. Chapter 4 extends this work by investigating potential changes in the relative biological effectiveness from the redistribution of electrons in a transverse magnetic field.

Chapter 5 investigates the performance of edge-on MOSFET dosimeters for use in MRT at the European Synchrotron Radiation Facility in Grenoble, France. A study of the MOSFET's radiation response and ability to measure the dose profiles of monoenergetic and polyenergetic microbeams with micron-sized resolution is presented. The measured dose profiles and PVDRs of microbeams are supplemented with theoretical results obtained by the means of Monte Carlo PENELOPE simulation.

Chapter 6 explores the potential use of magnetic fields in MRT to alter the electron distribution, and hence, the PVDR of microbeams. This is investigated for transverse and longitudinal magnetic fields using a combination of Monte Carlo simulations and physical experiments, with three different magnet devices.

Chapter 7 addresses the importance of accurately modelling beam delivery and microbeam transport in MRT by challenging simplifications commonly made in Monte Carlo studies. Simulations with the Monte Carlo PENELOPE code are used to investigate the influence of the source, multislit collimator and beam divergence (from the source to detector) on the dose profiles and PVDRs of microbeams. Also investigated is the effect of the collimator alignment, height of scoring bins, and type of interaction medium. A comparison of the dose profile of a microbeam array obtained with a full model of the beamline to that generated from the superposition of a single microbeam profile is also presented.

## **CHAPTER 2**

### **RADIATION TRANSPORT AND THE MONTE CARLO PENELOPE CODE**

This chapter provides a review of the different principles of radiation transport in matter. It concentrates on photon and electron transport, as the bulk of this thesis is concerned with photon beam irradiation. The implementation of radiation transport in Monte Carlo is also discussed for the PENELOPE toolkit, which was used extensively in this work.

#### **2.1 Interactions of radiation with matter**

##### **2.1.1 Photon interactions**

When a photon traverses a medium, it undergoes interactions with the atomic nuclei and electrons that comprise the medium. A primary photon is the term used to describe a photon which has not interacted with the medium. When such a photon undergoes an interaction it is referred to as a scattered photon. The probability of primary or scattered photon interactions depends on the energy of the photon and the composition of the medium with which it interacts. The dominant photon interaction processes; coherent (Rayleigh) scattering, incoherent (Compton) scattering, photoelectric absorption and electron-positron pair production, are outlined below. Figure 2.1 shows the cross sections for photon interactions<sup>1</sup> in water, where Compton scattering can be seen to dominate between about 30 keV and several MeV, which is the energy range of most photons in this study.

---

<sup>1</sup>Interaction cross section data extracted from the National Institute of Standards and Technology (NIST) XCOM Photon Cross Sections database [36]



Please see print copy for image

Figure 2.1: Cross sections for photon interactions in water. Data extracted from the NIST XCOM Photon Cross Sections database [36].

#### 2.1.1.1 Coherent (Rayleigh) scattering

Coherent or Rayleigh scattering is the process by which a photon interacts with atomic electrons but does not excite or ionise the target atom. While the direction of the photon may change, resulting in a transfer of momentum to the atom, the energy of the photon remains the same. A coherent scattering event can be described by considering the photon as an electromagnetic wave. The incident wave causes the atomic electrons to oscillate with the same frequency and in phase with one another, resulting in the interference of electromagnetic waves scattered from different parts of the atomic-charge cloud. Thus, the scattered photon emerges with the same frequency (energy) but different direction of motion. From the conservation of energy and momentum, the photon is predominantly scattered in the forward direction.

Rayleigh scattering mainly occurs at low photon energies for large  $Z$  values. In water, it is important at photon energies below about 10 keV (refer to figure 2.1). The cross section for this process,  $d\sigma_{Ra}/d\theta$ , is given by

$$\frac{d\sigma_{Ra}}{d\theta} = \frac{r_o^2}{2}(1 + \cos^2\theta)[F(x, Z)]^2 2\pi \sin\theta \quad (2.1)$$

where  $r_o$  is the classical electron radius,  $\theta$  is the scattering angle,  $x$  is the magnitude of momentum transfer in the collision ( $x = (\sin\theta/2)/\lambda$ ),  $Z$  is the atomic number of the target atom, and  $F(x, Z)$  is called the atomic form factor [37]. This factor is a monotonically decreasing function of the momentum transfer, where  $F(x, Z)$  approaches  $Z$  for a small  $\theta$  value, while for a large  $\theta$  value it tends toward zero. For low photon energies and small momentum transfers, the cross section for Rayleigh scattering,  $d\sigma_{Ra}$ , can be approximated by [38]

$$d\sigma_{Ra} \simeq \frac{8}{3}\pi r_o^2 Z^2 \quad (2.2)$$

#### 2.1.1.2 Incoherent (Compton) scattering

Compton scattering is the predominant mode of photon interaction in water and soft tissue between energies of about 30 keV and 2 MeV (refer to figure 2.1). In Compton scattering, the incident photon collides inelastically with an atomic electron. As a result, some of the photon energy,  $h\nu$ , is scattered and some is transferred to the electron as kinetic energy,  $E_k$ . By conservation of energy, assuming the electron is free or unbound (as the binding energies are a small fraction of the photon energy), the scattered photon will retain an energy  $h\nu' = h\nu - E_k$ . Applying conservation of momentum leads to the following relation between the energy of the scattered photon and its scattering angle,  $\theta$ ,

$$h\nu' = \frac{h\nu}{1 + \left(\frac{h\nu}{m_o c^2}\right)(1 - \cos\theta)} \quad (2.3)$$

where  $h$  is Planck's constant,  $\nu$  is the photon frequency,  $m_o$  is the electron rest mass and  $c$  is the speed of light.

This equation shows that the maximum energy transferred to an electron is when the incident photon makes a direct hit with the electron and is scattered through  $180^\circ$  (i.e. back along its incoming path). In this case, the electron will travel forward in the direction of the incident photon ( $\theta = 0$ ). In such a collision, the scattered photon will retain its minimum energy. However, when a photon instead makes a grazing hit with the electron, it scatters in the forward direction ( $\theta \sim 0$ ) while the electron is set in motion at almost  $90^\circ$ . In this type of collision, the scattered photon retains a maximum energy (essentially the full incident photon energy) whilst the electron receives almost no energy. Collisions between these two extremes are possible.

The differential cross section for a photon interacting with a free electron at rest is given by the Klein-Nishina equation:

$$\frac{d\sigma}{d\Omega} \sim \left( \frac{E}{E'} + \frac{E'}{E} - 1 + \cos^2\varphi \right) \quad (2.4)$$

where  $E'$  is the energy of the scattered photon given by

$$E' = \frac{E}{1 + [E/(m_o c^2)](1 - \cos\varphi)} \quad (2.5)$$

The angle of the Compton electron,  $\phi_{e-}$ , is therefore defined as

$$\cot\phi_{e-} = \left( 1 + \frac{E}{m_o c^2} \right) \tan\left(\frac{\varphi}{2}\right) \quad (2.6)$$

Figure 2.2 shows the angular distribution of Compton scattered photons of energies 0.1, 0.5, 1, 5, 10, and 15 MeV calculated from the Klein-Nishina cross section (equation 2.4). The corresponding angular distribution of Compton electrons (calculated from equation 2.6) is plotted in figure 2.3.

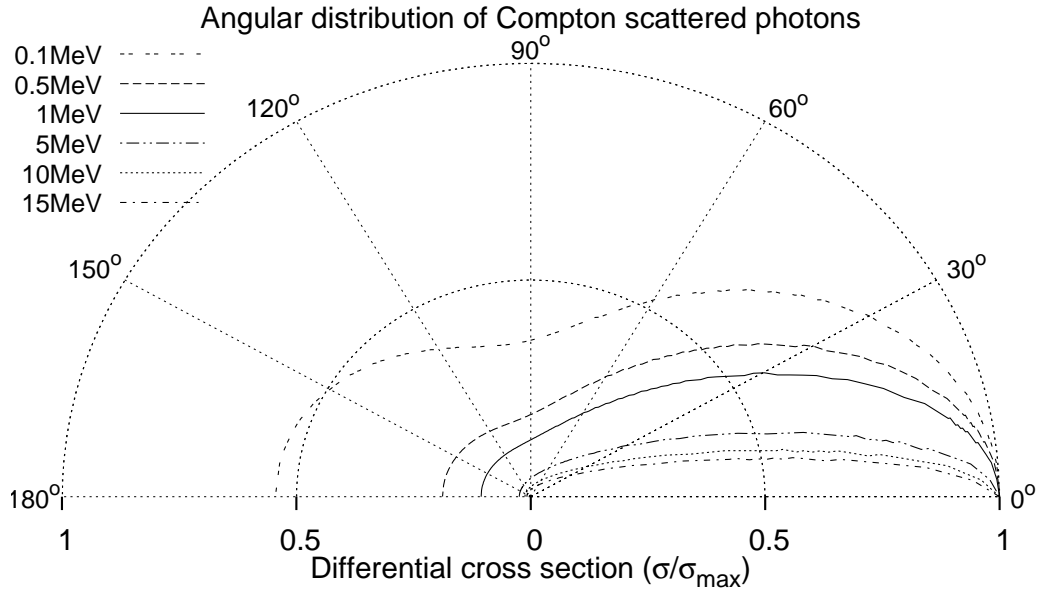


Figure 2.2: Angular distribution of Compton scattered photons calculated from the Klein-Nishina cross section (equation 2.4). A plot of the intensity of a scattered photon of 0.1, 0.5, 1, 5, 10, and 15 MeV interacting with a free electron at the centre of the graph.

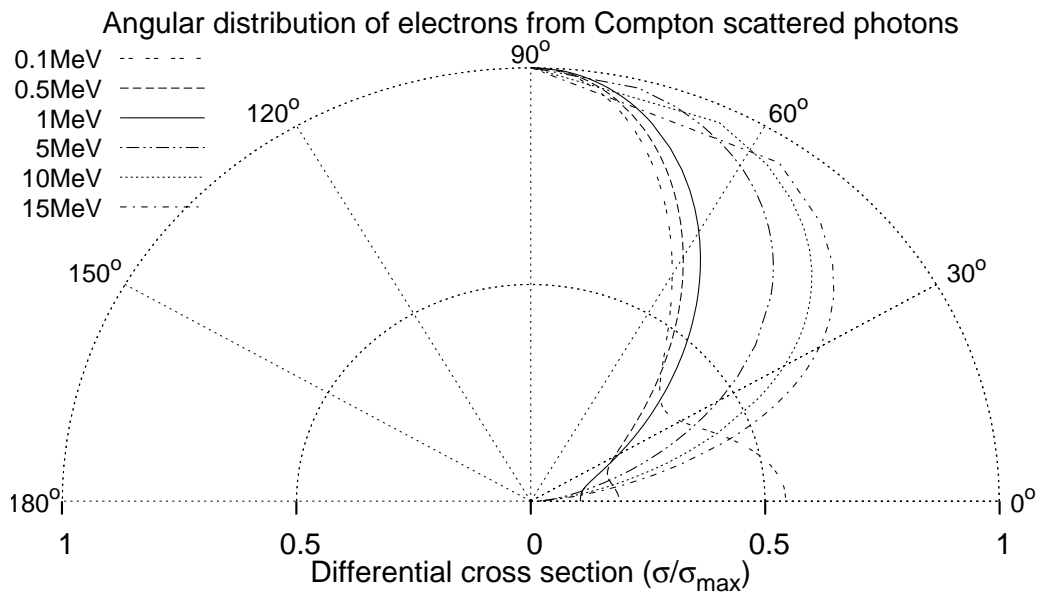


Figure 2.3: Angular distribution of Compton scattered electrons calculated from the Klein-Nishina cross section (equation 2.6). A plot of the intensity of the electrons produced from Compton scattered photons of 0.1, 0.5, 1, 5, 10, and 15 MeV.

### 2.1.1.3 Photoelectric absorption

In the photoelectric process, a photon of energy  $h\nu$  is absorbed by an atom resulting in the ejection of a bound electron from one of the K, L, M, or N shells. The ejected electron receives almost all of the photon energy, emerging with a kinetic energy  $E_k = h\nu - E_s$ , where  $E_s$  is the binding energy of the electron. Such an ionisation leaves the atom in an excited state. As the atom returns to the ground state it emits characteristic radiation, either as X-rays or Auger electrons, whose energy depends on the shell from which the electron was ejected.

The probability of photoelectric interaction increases rapidly with decreasing energy, particularly for high  $Z$  materials, where it is the predominant mode of interaction at low photon energies. In water and soft tissue, this corresponds to photon energies below about 30 keV, as shown in figure 2.1. Photoelectric interaction is most likely to occur with a K-shell electron (of the target atom), providing the photon energy is greater than the K-shell binding energy.

### 2.1.1.4 Electron-positron pair production

For a pair production event to occur, the energy of the incident photon,  $h\nu$ , must be at least twice the rest mass energy of an electron (1.022 MeV). In these interactions, a photon passes near the nucleus of an atom where its energy is converted to form an electron-positron pair. The excess energy of the photon ( $h\nu - 1.022$  MeV) is shared between the electron and positron as kinetic energy.

The electron and positron travel through matter ionising and exciting particles until they are brought to rest. When the positron nears the end of its path, it combines with an electron and they undergo annihilation to produce two 0.511 MeV photons which are emitted in opposite directions.

### 2.1.2 Electron interactions

The interaction of photons with matter gives rise to secondary electrons. Unlike photons which lose their energy in a few collisions, electrons can undergo a very large number of collisions before all of their energy is absorbed. The types of interactions whereby electrons lose energy include collisions with atomic electrons (collision energy loss) and encounters with the Coulomb force of atomic nuclei (radiative energy loss). Both types of interactions are inelastic as they involve the loss of incident electron energy. Elastic interactions can occur when an electron passes by a nucleus at a large distance. In these types of Coulomb force interactions, the electron suffers a change in direction but no loss in kinetic energy since the mass of the electron is substantially smaller than that of the atom.

In radiobiology, cell damage is primarily attributed to the processes of ionisation and excitation that result from collision energy loss [10]. Ionisation occurs when the incident electron strips the atom of a bound electron. Excitation is the process whereby the incident electron excites an atomic electron by temporarily elevating it to a higher energy level (which results in the emission of characteristic radiation). Both of these processes change the chemical reactivity of the molecule involved, thereby contributing to radiation damage. Most encounters involving collision energy losses result in small energy transfers between the incident and atomic electrons. However, it is also possible for large collision energy losses to occur when an incident electron transfers a higher proportion of its energy to an atomic electron. In this case, the electron that is knocked out of the atom will have sufficient energy to produce a track of its own. Such electrons are known as delta rays, or  $\delta$ -rays.

Radiative energy losses may occur when an electron passes very close to the nucleus of an atom, where the electromagnetic force sends the electron in a partial orbit around the positive nucleus. As a result, the electron recedes from the interaction with reduced energy. This loss in energy appears as a bremsstrahlung photon in order to conserve energy. The probability of such an interaction increases with increasing electron

energy and decreasing distance between the electron and the nucleus. It is also dependent on the density, or atomic number of the absorber atoms, where bremsstrahlung production is more prevalent in media of higher atomic number (i.e. lead) than in media of low atomic number (i.e. water or soft tissue), where energy loss is predominantly through ionisation events.

## 2.2 Monte Carlo PENELOPE code

Monte Carlo is a numerical technique that uses a class of computational algorithms to solve complex physical and mathematical problems. It is based on the generation of random numbers which are used to sample values for the problem variables from known Probability Density Functions (PDF) [39, 40]. In the case of radiation transport in matter, a set of Differential Cross Sections (DCS) for the relevant interaction mechanisms are used to determine the PDFs of random variables that characterise a particle track [38]. These variables may be quantities such as the distance travelled between successive interaction events, the type of interaction and target particle, or the energy loss and angular deflection in an event (and the initial state of any secondary particles produced). Monte Carlo is therefore a popular theoretical tool used to evaluate radiation transport in complex target geometries and material compositions.

The Monte Carlo PENELOPE code is a computational algorithm used for the simulation of coupled electron-photon transport [38]. The algorithm simulates different interaction mechanisms using a combination of numerical databases and analytical cross section models for particles with an energy between 100 eV and 1 GeV.

### 2.2.1 Brief outline of code structure and operation

The kernel of the code system is the FORTRAN 77 subroutine package PENELOPE [38]. It uses a collection of subprograms and relevant subroutines to simulate electron-photon showers in arbitrary material systems. Photon histories are simulated individually in chronological succession, while the generation of electron and positron

tracks are simulated using the mixed simulation method (discussed in section 2.2.2). Secondary particles generated with an initial energy above a specified absorption energy are stored on a ‘secondary stack’ and simulated in chronological order following the completion of each primary track. The processes whereby secondary particles are emitted are described in section 2.1.

The PENELOPE subroutine is steered by a MAIN program written by the user for their particular problem. This program controls the evolution of particle tracks and scoring of relevant quantities (i.e. energy distribution within arbitrary geometries), leaving PENELOPE to do most of the simulation work. Physical information for each interaction medium (i.e. physical composition, interaction cross sections, relaxation data, etc) are read from material data files, which are extracted from the relevant atomic interaction databases. In the case of material systems with complex geometries, operations to determine the active medium and change it when the particle crosses into another one can be performed automatically by the subroutine package PENGEO. For applications involving static external magnetic fields, PENELOPE uses a subroutine package PENFIELD, which is linked to PENELOPE and PENGEO, to track particle transport in a given field and material configuration [38].

### 2.2.2 Particle transport

In PENELOPE, photon transport is simulated individually (i.e. event by event). Electron and positron transport, on the other hand, are described by means of mixed simulation procedures [41]. This is because individual simulation of electron or positron transport may be infeasible owing to the large number of interactions that these particles can experience. The mixed simulation method therefore combines the individual simulation of hard collisions (i.e. events with scattering angle  $\theta$  or energy loss  $W$  larger than preselected cutoff values  $\theta_c$  and  $W_c$ ) with grouped simulation of multiple soft collisions (i.e. events where  $\theta < \theta_c$  or  $W < W_c$ ). Hard collisions are simulated with the appropriate



DCSs, while multiple soft collisions along a step of the particle's path (between two consecutive hard events) are simulated in a single artificial soft scattering event by means of the random hinge method [41]. In this case, the simulation detail is dependent on the user defined parameters  $C_1$  and  $C_2$ . The average angular deflection is related to  $C_1$  such that  $C_1 \simeq 1 - \langle \cos\theta \rangle$ , and the maximum average fractional energy loss in a single step (i.e. along the mean free path between consecutive hard elastic events) is defined by  $C_2$ . For hard collisions, the cutoff energies for inelastic collisions and bremsstrahlung emission,  $W_{cc}$  and  $W_{cr}$  respectively, are defined by the user.

The cross section data used by PENELOPE are obtained from a number of sources. For photoelectric absorption and pair production (ranging from 100 eV to 1 GeV), the DCSs are sourced from the Evaluated Photon Data Library (EPDL) database [42] and the XCOM Photon Cross Sections program [43], respectively. The DCSs for Compton scattering events are described by means of the relativistic impulse approximation [44], and the transition probabilities for atomic relaxation events (i.e. emission of characteristic radiation and Auger electrons) from vacancies produced in the K-shell and L-subshells are extracted from the Evaluated Atomic Data Library (EADL) [45]. In the case of elastic electron scattering, the DCSs are derived from a modified Wentzel distribution with parameters obtained from relativistic partial-wave analysis [38]. Note that for low energy photons below the K absorption edge, the reduced form of the Rayleigh scattering cross section (equation 2.2) does not incorporate anomalous scattering factors [46, 47] that would otherwise lead to a general reduction in the cross section [38].

### 2.2.3 Electron transport in magnetic fields

Radiation transport in static uniform magnetic fields is implemented in PENELOPE by the means of a robust tracking algorithm [38]. When a charged particle interacts in a static external magnetic field its loss in kinetic energy and change in direction of motion are determined by the means of this tracking algorithm. In the absence of a magnetic field, an electron will move in a straight line between consecutive interaction events.

In the presence of a magnetic field, however, this straight trajectory segment will be divided into macroscopic lengths (of maximum allowed step length) to account for the effect of the magnetic force. In such simulations, the accuracy of generated trajectories is controlled by the smallness of the user-defined delta simulation parameters  $\delta_B$ ,  $\delta_E$  and  $\delta_v$  (i.e. relative changes in magnetic field, kinetic energy and velocity, and direction of motion respectively). In the case of a uniform magnetic field, the tracking algorithm is exact and independent of step length.



## **CHAPTER 3**

### **INFLUENCE OF A TRANSVERSE MAGNETIC FIELD ON THE DOSE DISTRIBUTION IN PHOTON BEAM RADIOTHERAPY**

#### **3.1 Introduction**

In this chapter, the influence of a transverse magnetic field on the dose distribution of photon beams is investigated with Monte Carlo PENELOPE simulation. A comparison is made between the dose distributions obtained with Monte Carlo PENELOPE and EGS4 codes in order to benchmark the performance of PENELOPE's charged particle transport algorithm in applications involving static electromagnetic fields. The optimal width of magnetic field and the depth at which it is applied to achieve maximum therapeutic benefit is also investigated. Many of the results appearing in this chapter have been published previously in a peer-reviewed journal article [48].

Since the advent of radiotherapy as a means of tumour control an ongoing challenge has been to reduce the radiation dose delivered to normal tissue. Conformal radiotherapy, intensity modulated radiotherapy, and brachytherapy are three methods in current use. Magneto-radiotherapy, or the use of magnetic fields to produce a favourable redistribution of dose, despite being suggested over half a century ago, is still not in use. This is primarily due to the practical difficulty of applying magnetic fields of sufficient strength to bring about a significant alteration of the dose deposition. A secondary consideration is the incorporation of the effects of the magnetic fields on the dose distribution into the treatment planning process. A third consideration is the potential for any change in radiobiological effectiveness of the radiation through physical, chemical, or biological means.

Changes in technology mean that the ability to apply sufficiently strong magnetic

fields will soon be at hand. Therefore it is desirable to extend earlier studies to allow further progress to be made in the second and third areas referred to above. The work in both the current and succeeding chapters constitutes another step on that path.

The concept of applying magnetic fields to alter the dose deposition of scattered electrons from radiotherapy beams was suggested by Bostick in 1950. He proposed that a longitudinal magnetic field applied during electron beam therapy would reduce the lateral scattering of secondary electrons, thereby reducing the penumbral broadening of the beam with depth [49]. Since then a number of Monte Carlo studies have investigated the potential for transverse and longitudinal magnetic fields to alter the dose distribution from radiotherapy beams [50–63].

An electron travelling in a magnetic field experiences a Lorentz-force which bends its trajectory, between scattering events, into a helical-shaped path (the entire trajectory will not be a perfect helical shape due to scattering). The radius of curvature of an electron,  $R_e$ , depends on the electron's kinetic energy,  $E_k$ , and the strength of the external magnetic field,  $B$ , in which it is travelling. This dependence is given by

$$R_e = \frac{M_e c}{e B} \sqrt{\left(\frac{E_k}{E_o}\right)^2 + \frac{2E_k}{E_o}} \quad (3.1)$$

where  $M_e$ ,  $e$ , and  $E_o$  are the mass, charge, and rest energy of an electron respectively, and  $c$  is the speed of light.

The mean free path of an electron between scattering events is also strongly energy dependent. This is shown in figure 3.1 with a plot of the mean free path of an electron (in water) and its radius of curvature when subject to a 1, 2, 5 and 20 T magnetic field. Naively, one might expect to see an effect of the magnetic field on the dose deposition only if these two characteristic lengths are comparable in size. We will see later that an effect exists even when the radius of curvature is orders of magnitude larger than the mean free path. This occurs because of the large number of interactions that an electron needs to undergo before its trajectory is significantly altered.

Also shown in the figure is the range of an electron in water as a function of energy. A magnetic field will influence an electron's trajectory when this distance is larger than or comparable with its radius of curvature. For a 1 T magnetic field, this is satisfied by electrons with an energy of 1 MeV and above. For electrons below 1 MeV, these distances become comparable at stronger magnetic fields (e.g. 100 T for 0.01 MeV electrons).

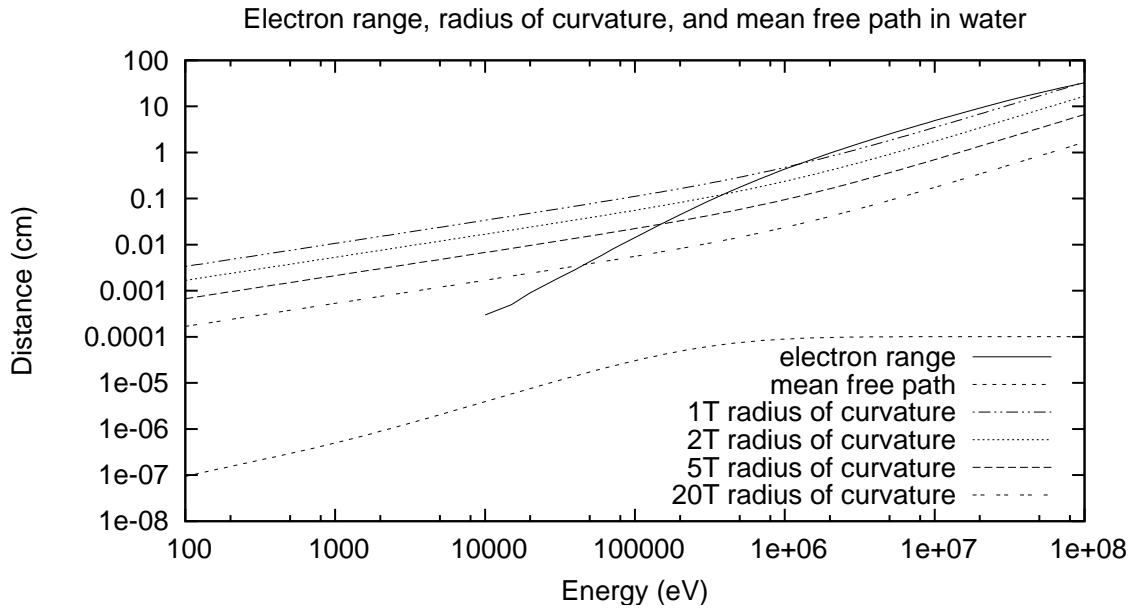


Figure 3.1: Energy dependence of the range, mean free path, and radius of curvature of an electron moving in magnetic field. The range of an electron (in water) as a function of energy is based on the data in table 3.1.

Studies concentrating on the alteration of dose deposition with a transverse magnetic field (i.e. perpendicular to beam direction) began in 1975 with a Monte Carlo study by Shih [50]. They found that a 6 T transverse magnetic field applied to a 70 MeV electron beam reduced the lateral spread of electrons, forming a localised maximum dose region at the end of their range analogous to the well-known ‘Bragg peak’. Since then, a number of studies have investigated the dose redistribution obtained with transverse magnetic fields applied to radiotherapy beams. Whitmire and Bernard [51, 52] measured surface dose reductions of up to 40% in polystyrene and cork phantoms when magnetic fields of 0.9 to 1.8 T were applied to betatron accelerator energies of 10-45 MeV. A Monte

Table 3.1: Range of electrons in water as a function of energy [37].

Energy (MeV)	Range (cm)
0.01	0.0003
0.05	0.0043
0.10	0.0143
0.20	0.0447
0.50	0.1759
1.00	0.4359
2.00	0.9720
5.00	2.524
10.0	4.917
20.0	9.237

Carlo study by Nardi and Barnea [54] showed up to 50% reduction in the surface to peak dose (a ratio used to monitor skin sparing) with a 3 T uniform field applied to a 15 MeV electron beam beyond 4 cm depth (in tissue). A later Monte Carlo study by Lee and Ma [57] also found transverse magnetic fields applied to electron beams to significantly reduce the surface to peak dose and cause steeper dose fall-offs in the maximum dose.

Fewer studies have investigated the effect of a magnetic field on the dose distribution from photon beams. Recognising this gap in the literature, Jette performed Monte Carlo simulations to study changes in the dose distribution for 15, 30, and 45 MV photon beams when non-uniform transverse magnetic fields of up to 5 T (central strength) were applied [56]. For all three beams, a 2 T field produced a significant enhancement in the maximum dose and a slightly larger enhancement with 3 T, where these regions of dose enhancement were immediately followed by a region of dose reduction. A further enhancement in the maximum dose with stronger magnetic fields was only observed with the 45 MV beam.

Localised regions of dose enhancement and dose reduction were also observed by Li *et al.* in a Monte Carlo study with EGS4 investigating the effect of transverse magnetic fields on the dose distribution from photon beams, using different strength magnetic fields (1 to 20 T) and photon beam energies ( $\text{Co}^{60}$ , 6, 10, 15, 24, and 50 MV) [58]. The

slice of uniform transverse magnetic field was applied between 7 and 9 cm depth in a water phantom, and zero magnetic field was applied to the remainder of the volume. The application of different strength magnetic fields to a 15 MV beam produced dose enhancements and dose reductions of up to 97% and 79% respectively (these were obtained with a 5 T magnetic field). Li *et al.* also studied the effect of photon beam energy on the dose distribution of Co<sup>60</sup>, 6, 10, 15, 24, and 50 MV photon beams with a 5 T magnetic field and observed an increase in the maximum dose and a reduction in the minimum dose when the beam energy was increased. Li *et al.* quantifies this dose perturbation effect by calculating a Dose Perturbation Factor (DPF) which is a ratio of dose obtained with magnetic field to that obtained without magnetic field as a function of depth along the axis of the beam. Hence, a  $DPF < 1.0$  is a dose reduction, while a  $DPF > 1.0$  is a dose enhancement.

Localised regions of dose enhancement and dose reduction could benefit the treatment of tumours near radiation-sensitive structures by aligning the region of dose enhancement with the tumour volume and the region of dose reduction with the critical structure. This is shown in figure 3.2 with Monte Carlo PENELOPE simulation of the effect on the depth-dose and DPF of a 10 MV beam when a slice of 5 T transverse magnetic field,  $B$ , is applied between 7 and 9 cm depth (in water).

### 3.2 Simulation methods

The accurate low-energy electron and photon cross sections gives PENELOPE a superiority over other Monte Carlo codes for applications involving low-energy transport. For example, PENELOPE can transport electrons and photons with energies as low as 100 eV [38] which is much lower than the EGS4 transport cutoff of 1 keV for photons and tens of keV for charged particles [64]. Another key difference between EGS4 and PENELOPE lies in the electron transport algorithms. While both codes use exact tracking algorithms for charged particle transport in a magnetic field, the implementation of their



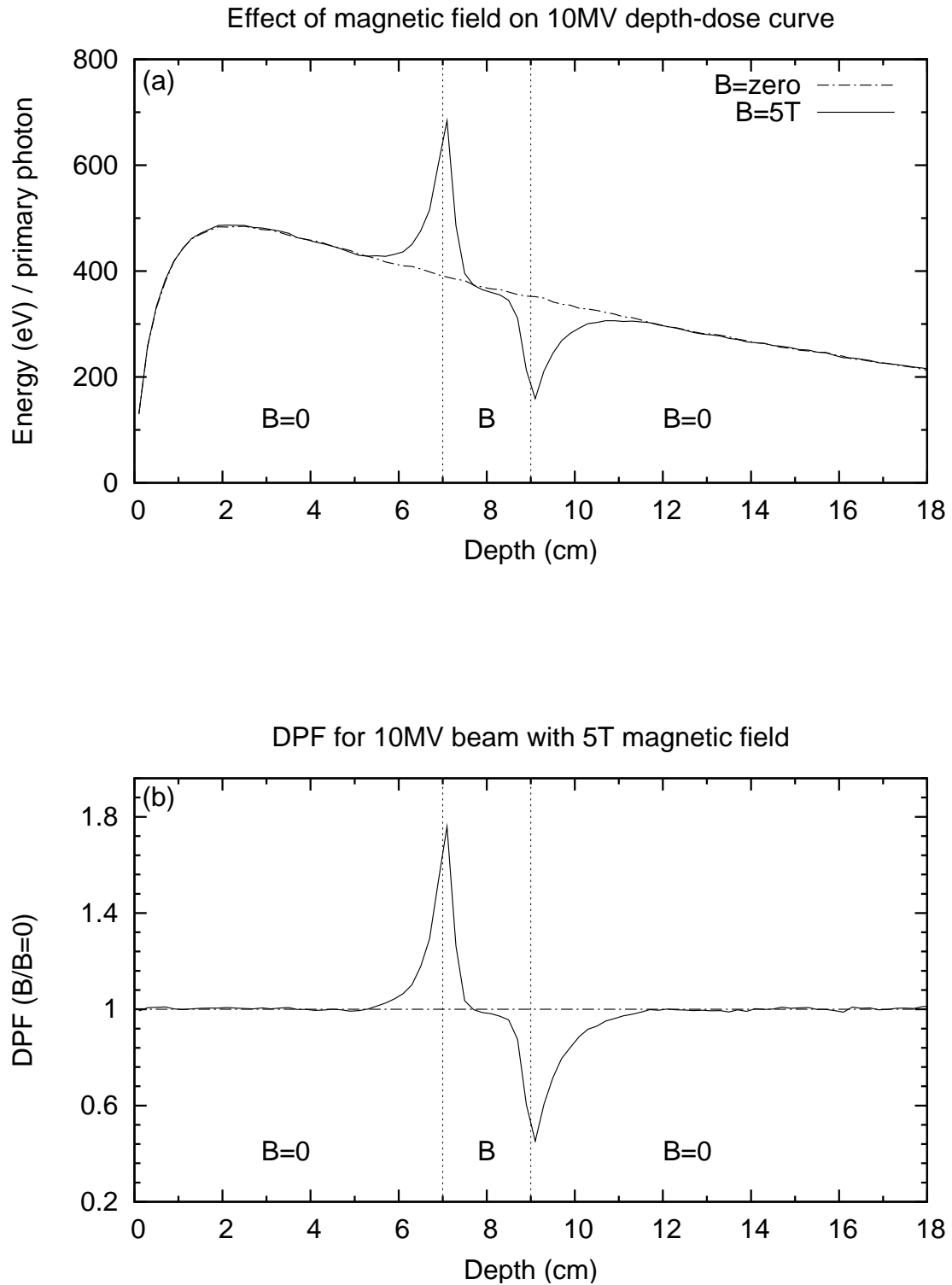


Figure 3.2: Effect of a slice of 5 T transverse magnetic field (7 to 9 cm depth) on the: (a) depth-dose, and (b) dose perturbation factor (DPF) of a 10 MV beam (direction of magnetic field is out of the page).

condensed history methods varies significantly. Hence, it is logical to examine whether the two codes make similar predictions about the effect of a magnetic field on the dose deposition.

This present work compares the dose enhancement and dose reduction obtained with Monte Carlo PENELOPE and EGS4 codes for different strength magnetic fields and photon beam energies, based on the EGS4 study by Li *et al.* [58] which used input energy spectra for the 6, 10, 15, 24 and 50 MV photon beams from Mohan *et al.* [65]. The photon beam was incident on a  $30 \times 30 \times 20 \text{ cm}^3$  (width  $\times$  height  $\times$  depth) water phantom with a  $4 \times 4 \text{ cm}^2$  field at 100 cm source to surface distance (SSD). A slice of uniform transverse magnetic field was applied between 7 and 9 cm depth in the phantom, and the remaining volume outside of this region was set to zero magnetic field. Cylindrical scoring bins of 0.5 cm radius  $\times$  0.2 cm depth were used to tally the energy deposition from particle interactions. The electron and photon transport cutoffs were 10 keV and the total number of histories were  $10^8$  to ensure the relative uncertainty (98% confidence level) of energy deposition in each bin did not exceed 2%.

PENELOPE simulations were carried out with identical combinations of magnetic field strength and photon beam energy as those used in the EGS4 study with the exception of the 50 MV beam (i.e.  $\text{Co}^{60}$ , 6, 10, 15, and 24 MV). The Mohan photon beam input spectra used in Monte Carlo simulation of the 6, 10, 15, and 24 MV beams is plotted in figures 3.3 (a), (b), (c) and (d), respectively. The PENELOPE simulation parameters, unless otherwise stated, were identical to those used in the EGS4 study (i.e. electron and photon energy cutoffs, number of histories, and bin volumes). Statistical uncertainties of three standard deviations were calculated for each bin. Due to a discrepancy with the EGS4 results for 15 MV and 2 T, the simulations were repeated using photon beam input spectra determined by Sheikh-Bagheri and Rogers [66] for 6, 10, and 15 MV beams (24 MV spectrum was not available) to compare with the DPFs obtained with the spectra of Mohan *et al.* [65].

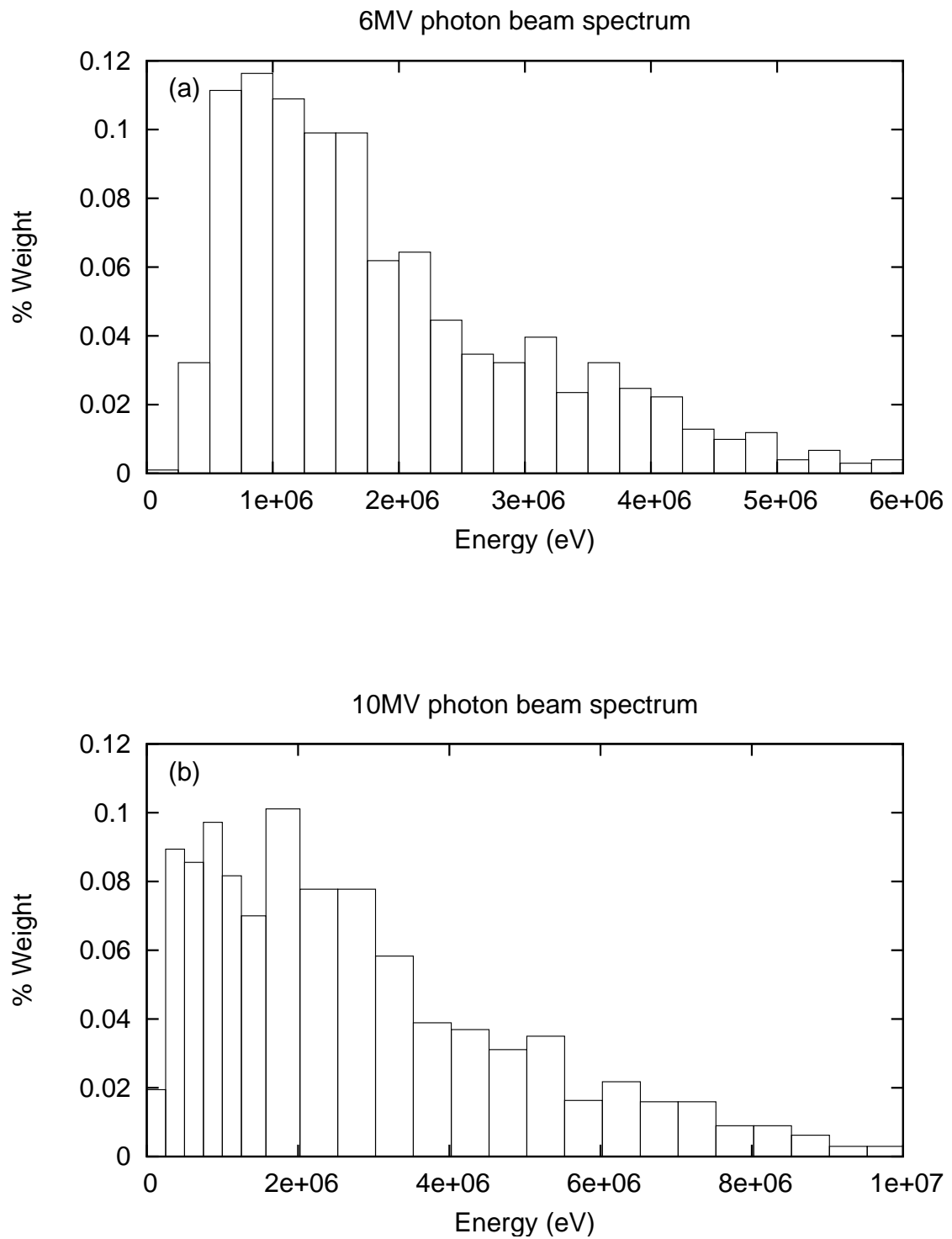


Figure 3.3: Figure (a) and (b) show the input photon beam spectrum (based on the Mohan spectra [65]) used for simulations with 6 and 10 MV beams respectively.

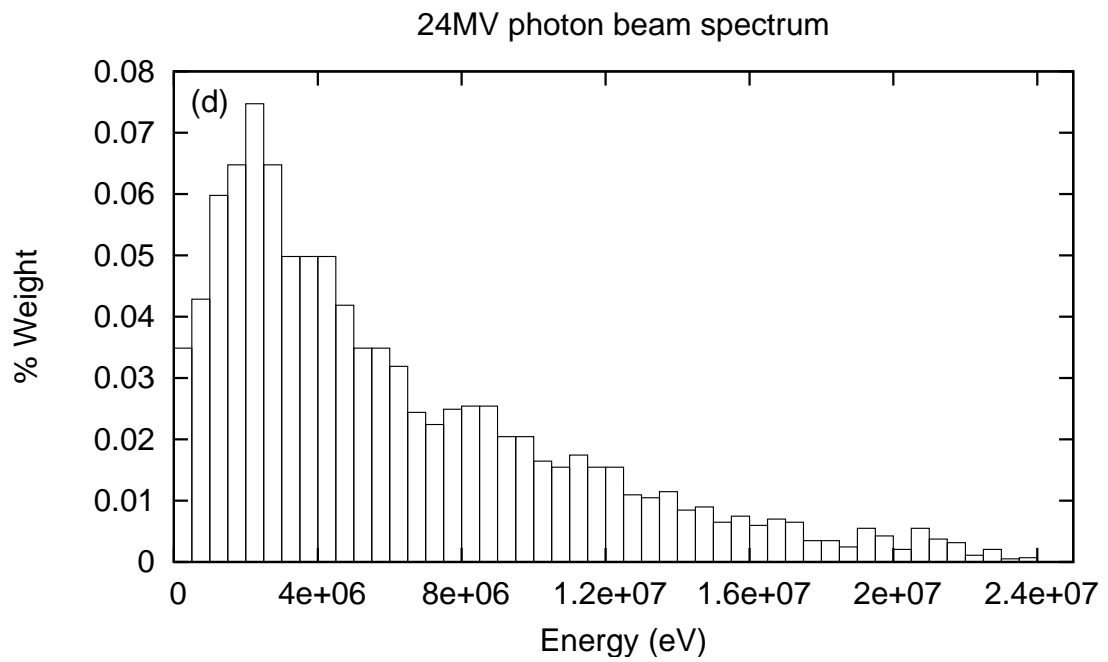
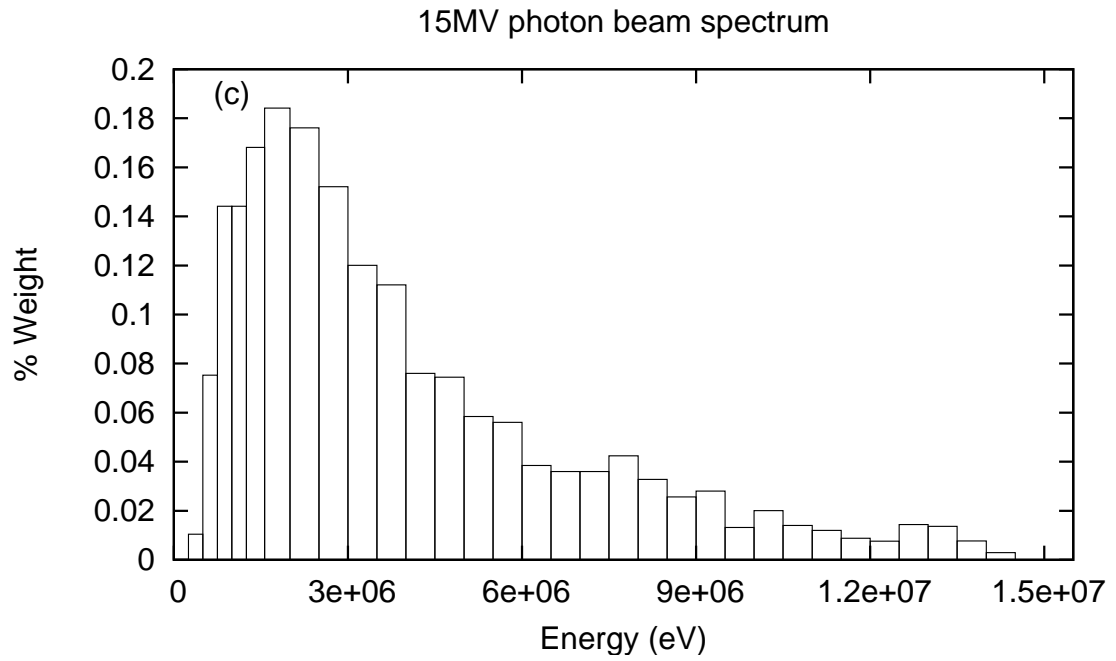


Figure 3.3: Figure (c) and (d) show the input photon beam spectrum (based on the Mohan spectra [65]) used for simulations with 15 and 24 MV beams respectively.

Further PENELOPE simulations were performed with twice the number of scoring bins (i.e. the bin depth was halved from 0.2 cm to 0.1 cm depth) to improve the DPF resolution, particularly around the magnetic field boundaries where the DPF rapidly increases or decreases. These simulations were performed with the Mohan *et al.* photon beam spectra and identical simulation parameters to those used above, apart from the smaller bin volume.

In the course of comparing the PENELOPE and EGS4 dose distributions, a persistent discrepancy in one set of the results led to an investigation of the effect of PENELOPE elastic scattering parameters  $C_1$  and  $C_2$  on the accuracy of the simulations. Limited to the interval of (0,0.2), Salvat *et al.* recommends setting  $C_1$  and  $C_2$  to a conservative value of 0.05, indicating that using smaller values is at the expense of increased simulation time whilst larger values may reduce accuracy. In this study, the values of  $C_1$  and  $C_2$  inside the region of magnetic field were both varied from 0.05 to a value of 0.02, 0.1, 0.2 and 0.5 (in regions beyond the magnetic field,  $C_1$  and  $C_2$  remained at 0.05). The influence of electron and photon low-energy transport cutoffs on the DPF were also investigated for 2 and 5 T magnetic fields applied to a 15 MV beam.

Simulations were also performed to study the dose distribution of a photon beam with the 2 cm slice of transverse magnetic field applied at different depths. This was investigated for a 15 MV photon beam and 5 T magnetic field at depths of 0 to 2 cm, 0.5 to 2.5 cm, 2 to 4 cm, 4 to 6 cm, and 7 to 9 cm in the water phantom.

Investigations were also carried out to determine the optimal magnetic field thickness for producing maximum dose enhancements and reductions. Simulations were performed with transverse magnetic fields of 2, 5 and 10 T with thicknesses ranging from 1 to 4 cm and applied to 6, 10, 15 and 24 MV photon beams. The width of each slice was centred at 8 cm depth in the water phantom.

### 3.3 Simulation results

#### 3.3.1 Effect of the magnetic field strength

The effect of magnetic field strength on a 15 MV beam is shown in figure 3.4 with a plot of the DPF as a function of depth along the central axis. Tables 3.2 and 3.3 compare the maximum and minimum DPFs obtained with PENELOPE and EGS4 (using identical bin volumes) for a 15 MV beam subjected to different magnetic fields, where PENELOPE(Mo) and PENELOPE(SBR) are the results obtained with Mohan *et al.* and Sheikh-Bagheri and Rogers spectra, respectively. Also included in the tables and figure 3.5 are the DPFs obtained with a 2 T field using different elastic scattering values  $C_1$  and  $C_2$ , demonstrating clearly that these have no effect on the results.

The largest dose enhancement (91%) was obtained with a 5 T magnetic field, which was more than double that obtained with 2 T and 8 times larger than that obtained with 1 T. Further increases in field strength failed to yield larger dose enhancements where values of 79%, 82%, and 80% were obtained with 10, 20, and 100 T respectively.

Almost all of the PENELOPE DPF results were within 4% of those obtained with EGS4. The exceptions were the 2 T maximum DPF and the 2 and 20 T minimum DPFs, yielding respective discrepancies of 24%, 15%, and 10% for PENELOPE(Mo) and 24%, 14%, and 5% for PENELOPE(SBR). All PENELOPE(Mo) and PENELOPE(SBR) results were within 4% of each other. Reducing the PENELOPE electron and photon low-energy transport cutoffs from 10 keV to 1 keV had no effect on the DPFs of a 15 MV beam subjected to 2 and 5 T magnetic fields.

Figure 3.4 shows the improved resolution in DPF with smaller bin volumes (0.1 cm instead of 0.2 cm depth), particularly in the dose enhancement and dose reduction regions at the magnetic field boundaries. A comparison of the maximum and minimum DPFs obtained with PENELOPE and EGS4 are presented in tables 3.4 and 3.5, where the results labelled PENELOPE(A) and PENELOPE(B) correspond to a bin depth of 0.2 cm (i.e. same bin volume as that used by EGS4 study) and 0.1 cm, respectively.

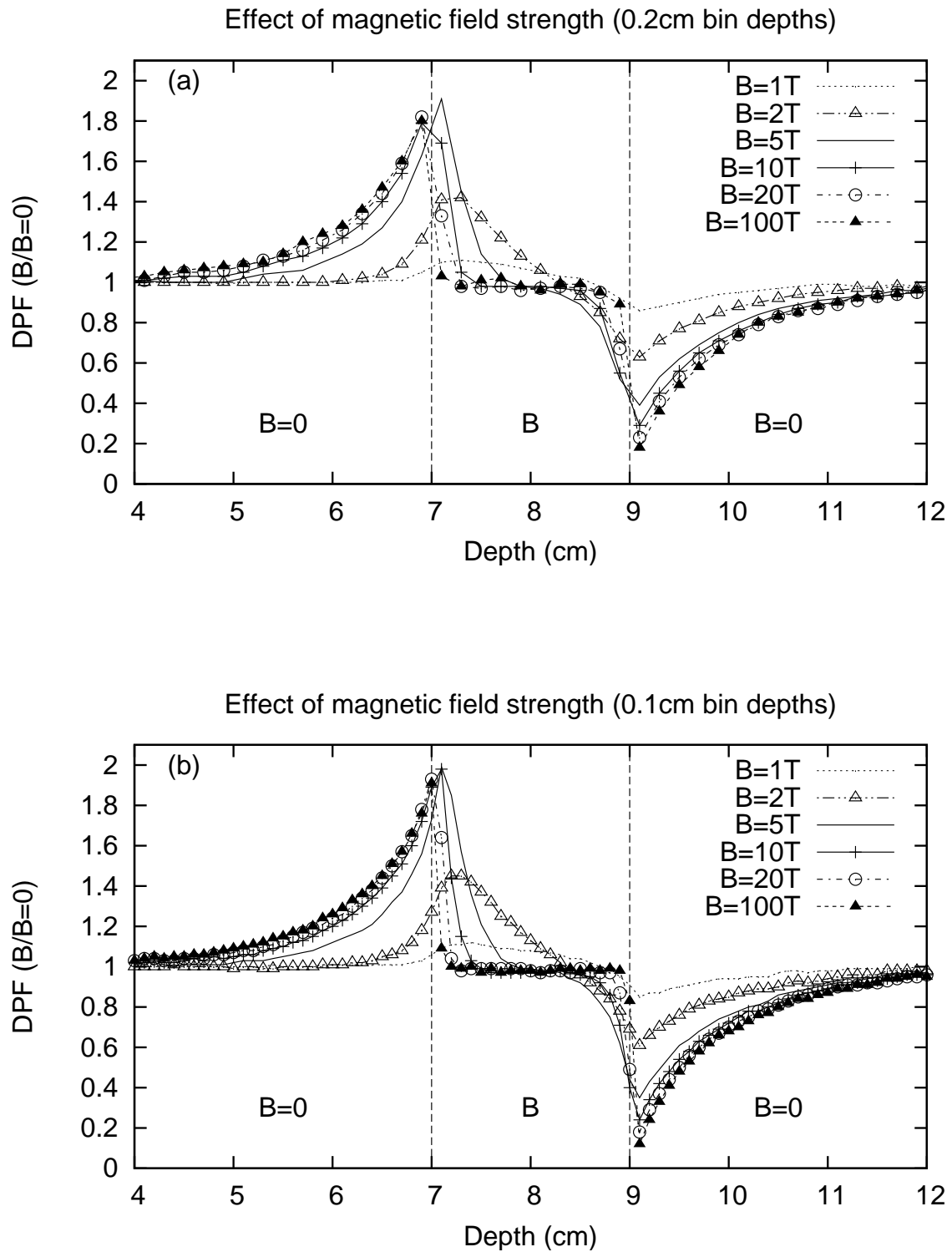


Figure 3.4: Dose distribution of a 15 MV beam (in water) subjected to a slice of 1, 2, 5, 10, 20 and 100 T transverse magnetic field (7 to 9 cm depth), using bin depths of: (a) 0.2 cm, and (b) 0.1 cm.

Table 3.2: Comparison of the maximum DPF for a 15 MV beam with B = 1 to 100 T.

B(T)	EGS4	PENELOPE(Mo)		PENELOPE(SBR)		
	DPF	DPF	Mo:EGS4	DPF	SBR:EGS4	SBR:Mo
1	1.08	$1.11 \pm 0.02$	1.03	$1.11 \pm 0.02$	1.03	1.00
2	1.67	$1.42 \pm 0.02$	0.85	$1.43 \pm 0.02$	0.86	1.01
2(C=0.02)	-	$1.41 \pm 0.02$	-	-	-	-
2(C=0.1)	-	$1.40 \pm 0.02$	-	-	-	-
2(C=0.2)	-	$1.41 \pm 0.02$	-	-	-	-
2(C=0.5)	-	$1.41 \pm 0.02$	-	-	-	-
3	-	$1.71 \pm 0.03$	-	$1.73 \pm 0.03$	-	1.01
4	-	$1.87 \pm 0.01$	-	$1.87 \pm 0.02$	-	1.00
5	1.97	$1.91 \pm 0.03$	0.97	$1.92 \pm 0.04$	0.98	1.01
10	1.81	$1.79 \pm 0.02$	0.99	$1.81 \pm 0.06$	1.00	1.01
20	1.85	$1.82 \pm 0.05$	0.98	$1.85 \pm 0.06$	1.00	1.02
100	-	$1.80 \pm 0.05$	-	-	-	-

Table 3.3: Comparison of the minimum DPF for a 15 MV beam with B = 1 to 100 T.

B(T)	EGS4	PENELOPE(Mo)		PENELOPE(SBR)		
	DPF	DPF	Mo:EGS4	DPF	SBR:EGS4	SBR:Mo
1	0.84	$0.86 \pm 0.01$	1.02	$0.86 \pm 0.01$	1.02	1.00
2	0.51	$0.63 \pm 0.01$	1.24	$0.63 \pm 0.01$	1.24	1.00
2(C=0.02)	0.51	$0.64 \pm 0.01$	1.25	-	-	-
2(C=0.1)	-	$0.63 \pm 0.01$	-	-	-	-
2(C=0.2)	-	$0.64 \pm 0.01$	-	-	-	-
2(C=0.5)	-	$0.64 \pm 0.01$	-	-	-	-
3	-	$0.51 \pm 0.01$	-	$0.50 \pm 0.01$	-	0.98
4	-	$0.44 \pm 0.01$	-	$0.43 \pm 0.01$	-	0.98
5	0.39	$0.39 \pm 0.01$	1.00	$0.39 \pm 0.01$	1.00	1.00
10	0.28	$0.29 \pm 0.01$	1.04	$0.28 \pm 0.02$	1.00	0.97
20	0.21	$0.23 \pm 0.05$	1.10	$0.22 \pm 0.05$	1.05	0.96
100	-	$0.18 \pm 0.11$	-	-	-	-

According to the ratio of PEN(B) to PEN(A), the maximum and minimum DPFs for the 0.1 cm bins are as much as 11% larger and 33% smaller than those obtained with 0.2 cm bins. This difference is attributed to the higher resolution of the smaller bins, particularly at the magnetic field boundaries where the dose gradients are steep.



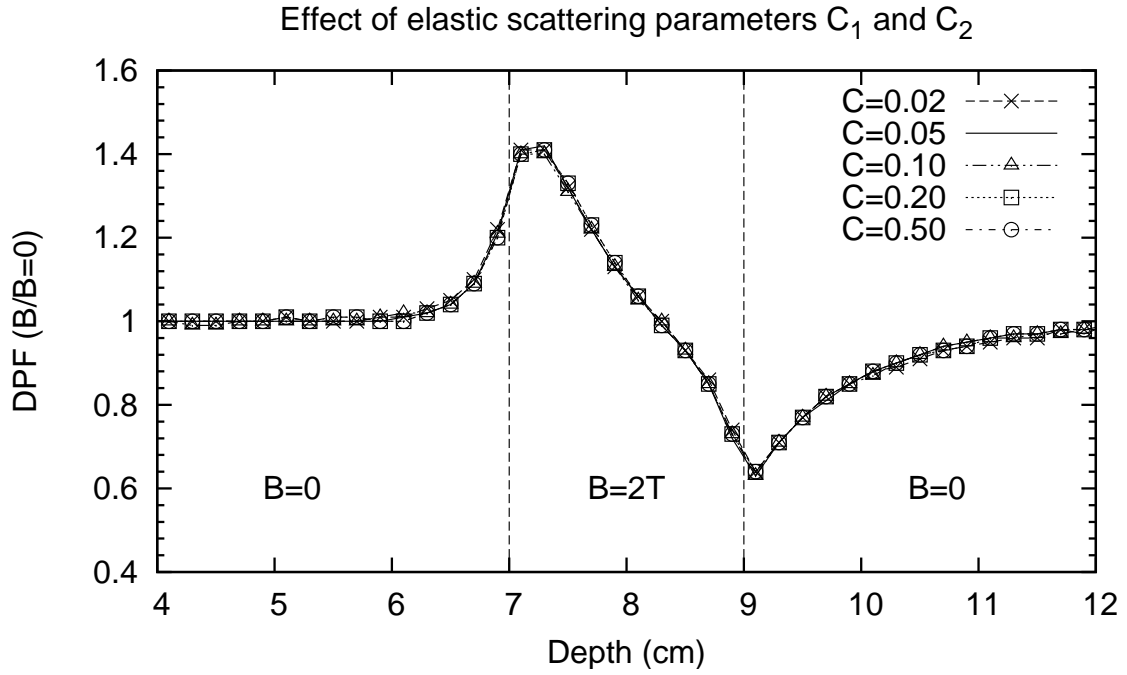


Figure 3.5: Effect of the elastic scattering parameters  $C_1$  and  $C_2$  ( $C = C_1 = C_2$ ) on the dose deposition of a 15 MV beam (in water) subjected to a 2 T transverse magnetic field (7 to 9 cm depth).

Table 3.4: Comparison of the maximum DPF for a 15 MV beam with  $B = 1$  to 100 T using bin depths of 0.1 and 0.2 cm.

B(T)	EGS4	PENELOPE(A) (0.2cm bins)		PENELOPE(B) (0.1cm bins)		
	DPF	DPF	PEN(A):EGS4	DPF	PEN(B):EGS4	PEN(B):PEN(A))
1	1.08	$1.11 \pm 0.02$	1.03	$1.12 \pm 0.03$	1.04	1.01
2	1.67	$1.42 \pm 0.02$	0.85	$1.45 \pm 0.02$	0.87	1.02
3	-	$1.71 \pm 0.03$	-	$1.73 \pm 0.02$	-	1.01
4	-	$1.87 \pm 0.01$	-	$1.88 \pm 0.03$	-	1.01
5	1.97	$1.91 \pm 0.03$	0.97	$1.99 \pm 0.02$	1.01	1.04
10	1.81	$1.79 \pm 0.02$	0.99	$1.98 \pm 0.07$	1.09	1.11
20	1.85	$1.82 \pm 0.05$	0.98	$1.93 \pm 0.03$	1.04	1.06
100	-	$1.80 \pm 0.05$	-	$1.91 \pm 0.14$	-	1.06

Table 3.5: Comparison of the minimum DPF for a 15 MV beam with  $B = 1$  to 100 T, and bin depths of 0.1 and 0.2 cm.

B(T)	EGS4	PENELOPE(A) (0.2cm bins)		PENELOPE(B) (0.1cm bins)		
	DPF	DPF	PEN(A):EGS4	DPF	PEN(B):EGS4	PEN(B):PEN(A)
1	0.84	$0.86 \pm 0.01$	1.02	$0.85 \pm 0.01$	1.01	0.99
2	0.51	$0.63 \pm 0.01$	1.24	$0.61 \pm 0.01$	1.20	0.97
3	-	$0.51 \pm 0.01$	-	$0.48 \pm 0.01$	-	0.94
4	-	$0.44 \pm 0.01$	-	$0.41 \pm 0.01$	-	0.93
5	0.39	$0.39 \pm 0.01$	1.00	$0.35 \pm 0.01$	0.90	0.90
10	0.28	$0.29 \pm 0.01$	1.04	$0.24 \pm 0.01$	0.86	0.83
20	0.21	$0.23 \pm 0.05$	1.10	$0.18 \pm 0.03$	0.86	0.78
100	-	$0.18 \pm 0.11$	-	$0.12 \pm 0.11$	-	0.67

### 3.3.2 Effect of the photon beam energy

Figure 3.6 shows the dose perturbation obtained with a slice of 5 T transverse magnetic field (7 to 9 cm depth) applied to  $\text{Co}^{60}$ , 6, 10, 15, and 24 MV photon beams. Tables 3.6 and 3.7 compare the maximum and minimum DPFs obtained with PENELOPE and EGS4, where PENELOPE(Mo) and PENELOPE(SBR) are the results obtained with Mohan *et al.* spectra and Sheikh-Bagheri and Rogers spectra, respectively. The PENELOPE(Mo) maximum and minimum DPFs were within 6% of those obtained with EGS4. Apart from a 9% discrepancy between the 10 MV minimum DPFs, the PENELOPE(Mo) and PENELOPE(SBR) DPFs were within 5% of each other. Repeating the 10 MV simulations with different random seed values had no effect on the minimum DPF result.

Table 3.6: Comparison of the maximum DPF for different photon beams with  $B = 5$  T.

Beam	EGS4	PENELOPE(Mo)		PENELOPE(SBR)		
	DPF	DPF	DPF(Mo:EGS4)	DPF	DPF(SBR:EGS4)	DPF(SBR:Mo)
$\text{Co}^{60}$	1.16	$1.23 \pm 0.03$	1.06	$1.23 \pm 0.03$	1.06	1.00
6MV	1.56	$1.56 \pm 0.07$	1.00	$1.59 \pm 0.08$	1.02	1.02
10MV	1.82	$1.76 \pm 0.06$	0.97	$1.85 \pm 0.05$	1.02	1.05
15MV	1.97	$1.91 \pm 0.04$	0.97	$1.92 \pm 0.04$	0.98	1.01
24MV	2.08	$2.11 \pm 0.01$	1.01	-	-	-

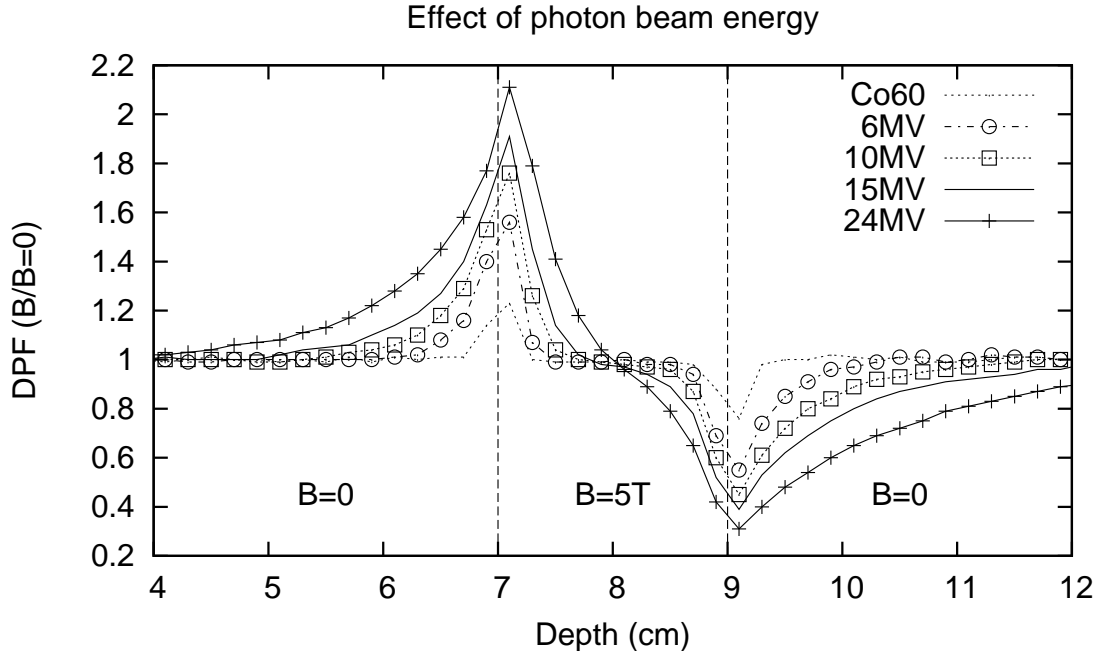


Figure 3.6: Dose distribution of  $\text{Co}^{60}$ , 6, 10, 15 and 24 MV photon beams (in water) subjected to a slice of 5 T transverse magnetic field (7 to 9 cm depth).

Table 3.7: Comparison of the minimum DPF for different photon beams with  $B = 5$  T.

Beam	EGS4	PENELOPE(Mo)		PENELOPE(SBR)		
	DPF	DPF	DPF(Mo:EGS4)	DPF	DPF(SBR:EGS4)	DPF(SBR:Mo)
$\text{Co}^{60}$	0.78	$0.76 \pm 0.02$	0.97	$0.76 \pm 0.02$	0.97	1.00
6MV	0.55	$0.55 \pm 0.01$	1.00	$0.54 \pm 0.01$	0.98	0.98
10MV	0.44	$0.45 \pm 0.01$	1.02	$0.41 \pm 0.01$	0.93	0.91
15MV	0.39	$0.39 \pm 0.01$	1.00	$0.39 \pm 0.01$	1.00	1.00
24MV	0.31	$0.31 \pm 0.01$	1.00	-	-	-

### 3.3.3 Effect of the depth and thickness of magnetic field

The effect of a 5 T magnetic field (2 cm thick) applied to a 15 MV beam at various depths in a water phantom is shown in figure 3.7. Positioning the slice of magnetic field below the surface (0 to 2 cm depth) produced a maximum DPF of about 2.85. Moving the position of the field from the surface to a depth of 0.5 to 2.5 cm yielded a DPF of 1.9 at the surface of the phantom, which dropped to 1.65 at 0.3 cm depth before rising to a

maximum DPF of 1.95 at 0.5 cm depth. No change in either the maximum or minimum DPF was observed with the field positioned at greater depths.

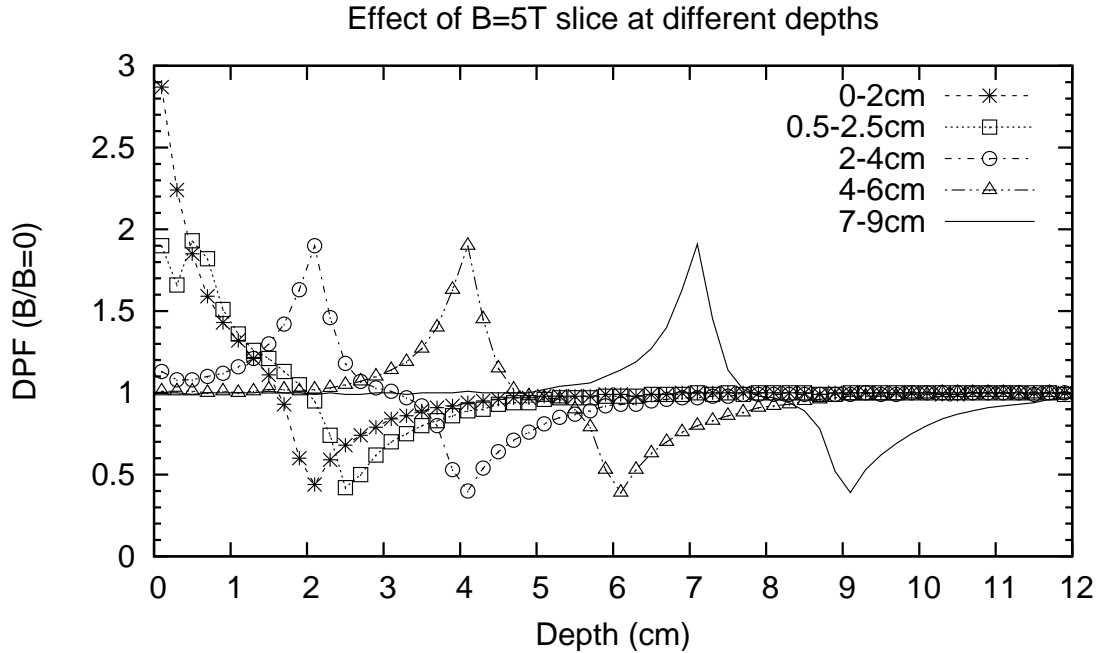


Figure 3.7: Dose distribution of a 15 MV beam with a slice of 5 T transverse magnetic field (2 cm thick) applied at different depths in the water phantom.

Also investigated was the effect of different thicknesses of a uniform magnetic field on the depth-dose of a 15 MV beam (in water). Figures 3.8 (a), (b), (c), and (d) plot the DPFs obtained in the presence of a 2, 5, and 10 T magnetic field slice of thickness 1, 2, 3, and 4 cm (centred at 8 cm depth), respectively. The maximum and minimum DPFs were neither affected by an increase or reduction in the magnetic field thickness (from 2 cm), nor were the widths of the dose enhancement and dose reductions. The only effect from varying the field thickness was an alteration in the range over which unity DPF is maintained between maximum and minimum DPF. While reducing the field thickness from 2 cm to 1 cm eliminated the region of unity DPF, increasing the thickness from 2 cm to 3 or 4 cm expanded the region of unity DPF. Similar trends were observed for 6, 10, and 24 MV photon beams subjected to a 5 T magnetic field of different thicknesses, as shown in figures 3.9 (a), (b), (c), and (d) respectively.

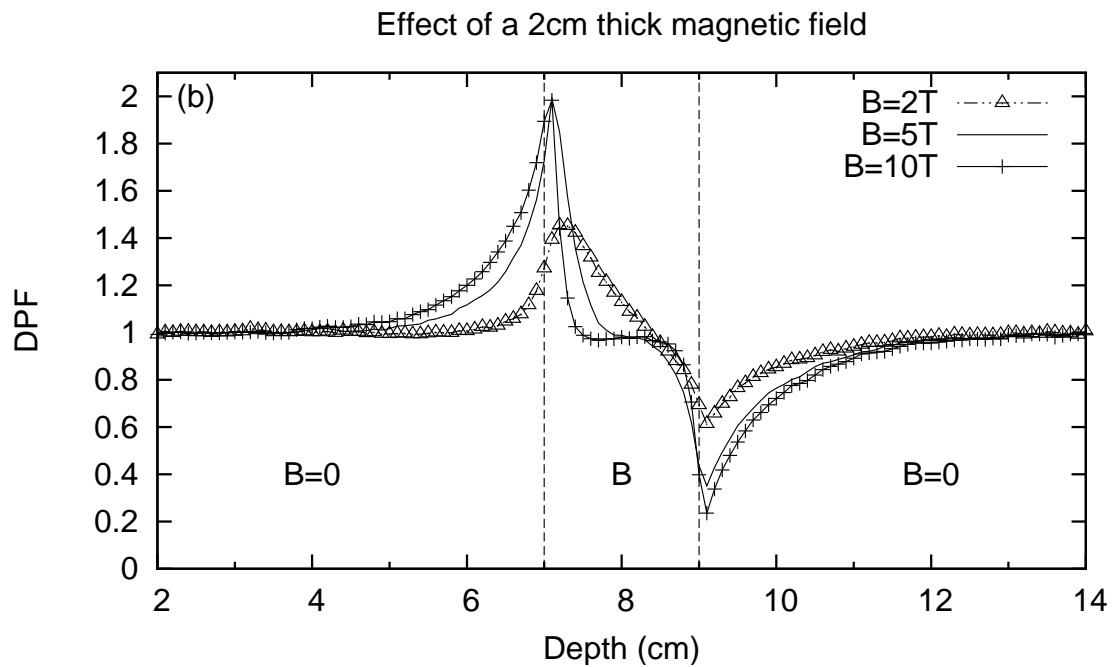
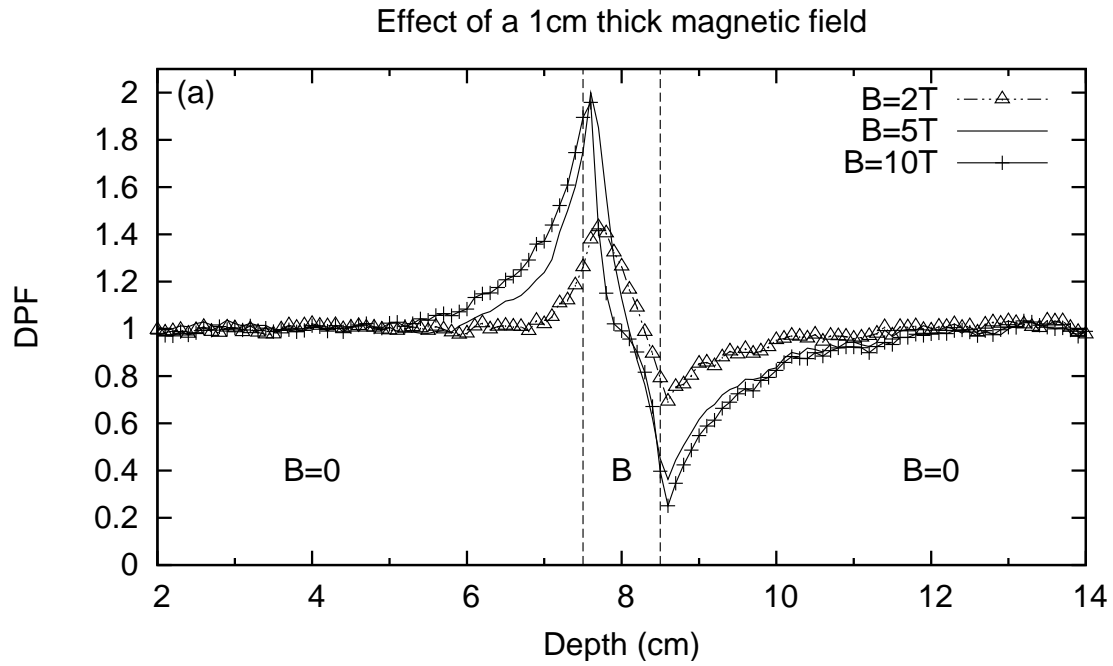


Figure 3.8: Effect of the magnetic field thickness. Figures (a) and (b) show the effect on the depth-dose of a 15 MV beam when a 2, 5 and 10 T transverse magnetic field is applied at 7.5 to 8.5 cm and 7 to 9 cm depth (i.e. 1 cm and 2 cm thick) in water, respectively.

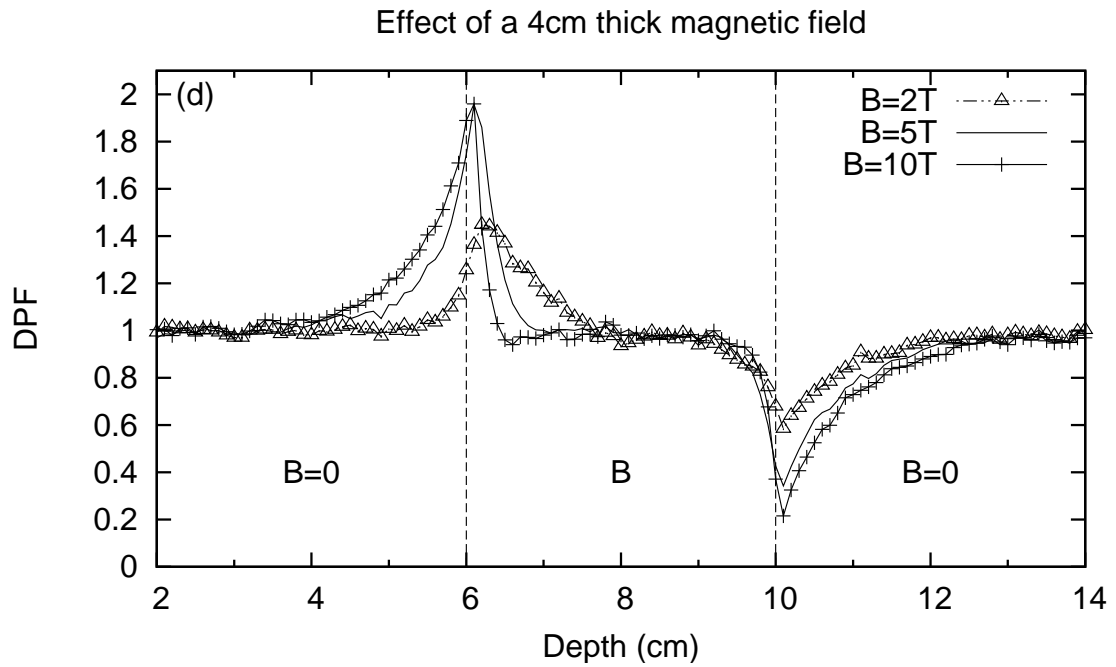
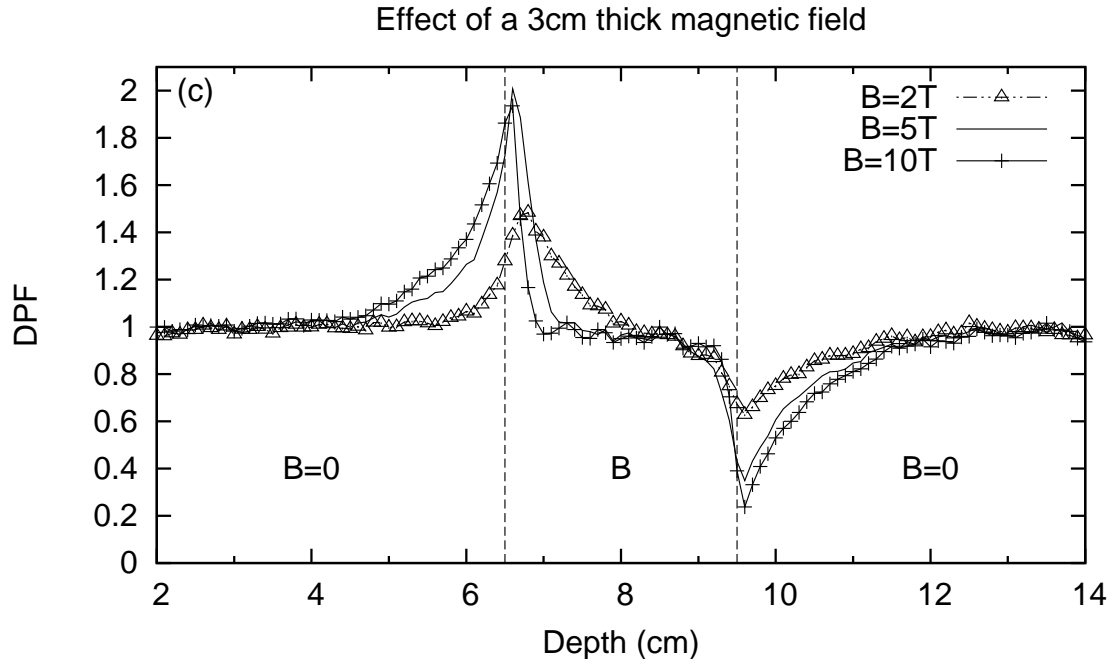


Figure 3.8: Effect of the magnetic field thickness. Figures (c) and (d) show the effect on the depth-dose of a 15 MV beam when a 2, 5 and 10 T transverse magnetic field is applied at 6.5 to 9.5 cm and 6 to 10 cm depth (i.e. 3 cm and 4 cm thick) in water, respectively.

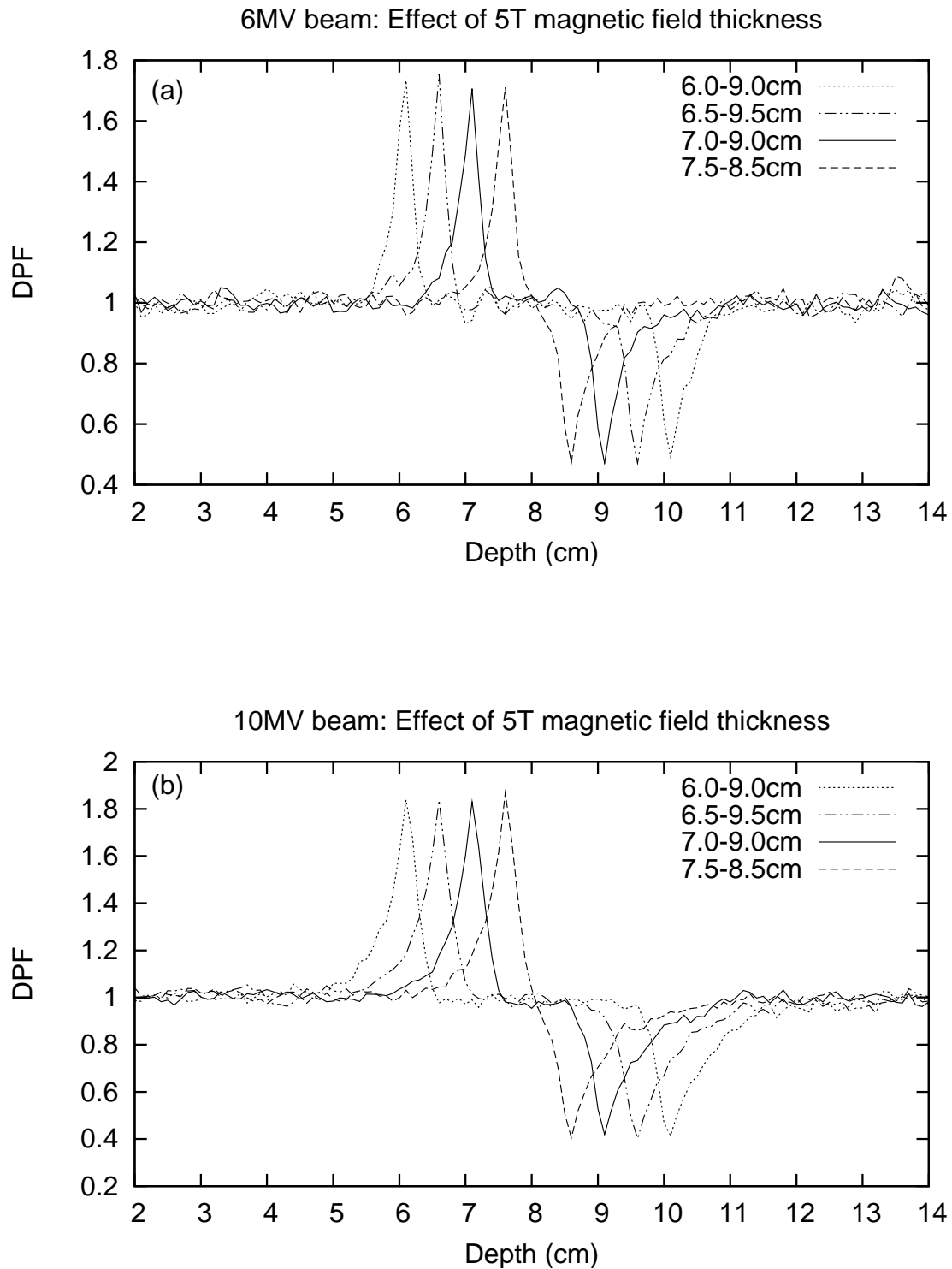


Figure 3.9: Effect of the magnetic field thickness. Figures (a) and (b) compare the effect of a 5 T transverse magnetic field of different thicknesses (1 to 4 cm) on the depth-dose (in water) of a 6 and 10 MV beam respectively.

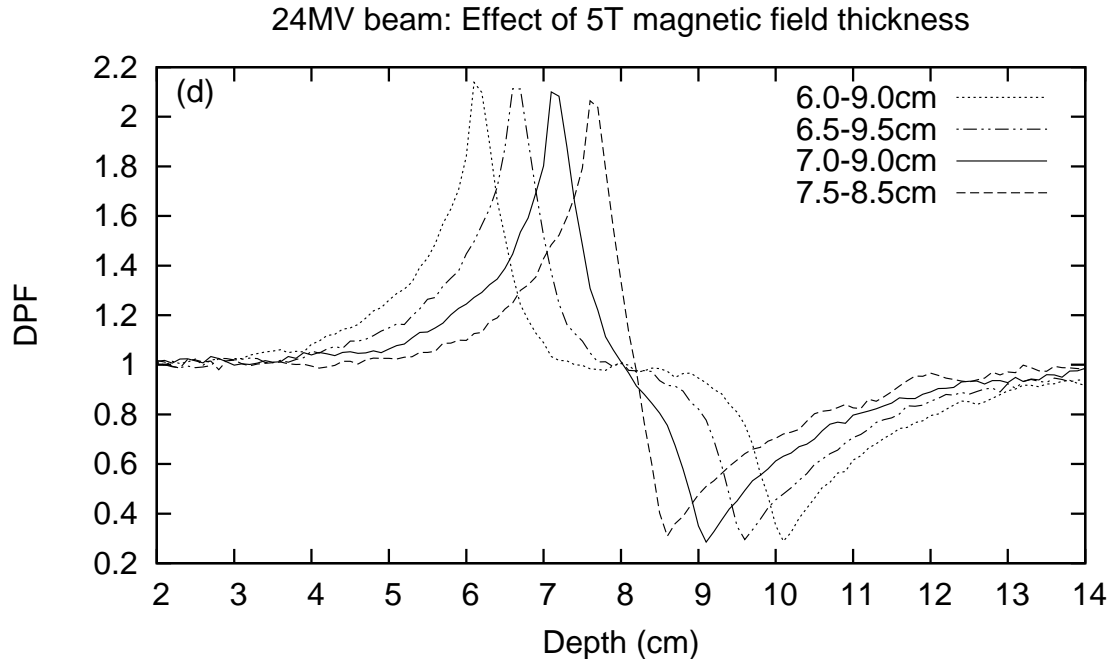
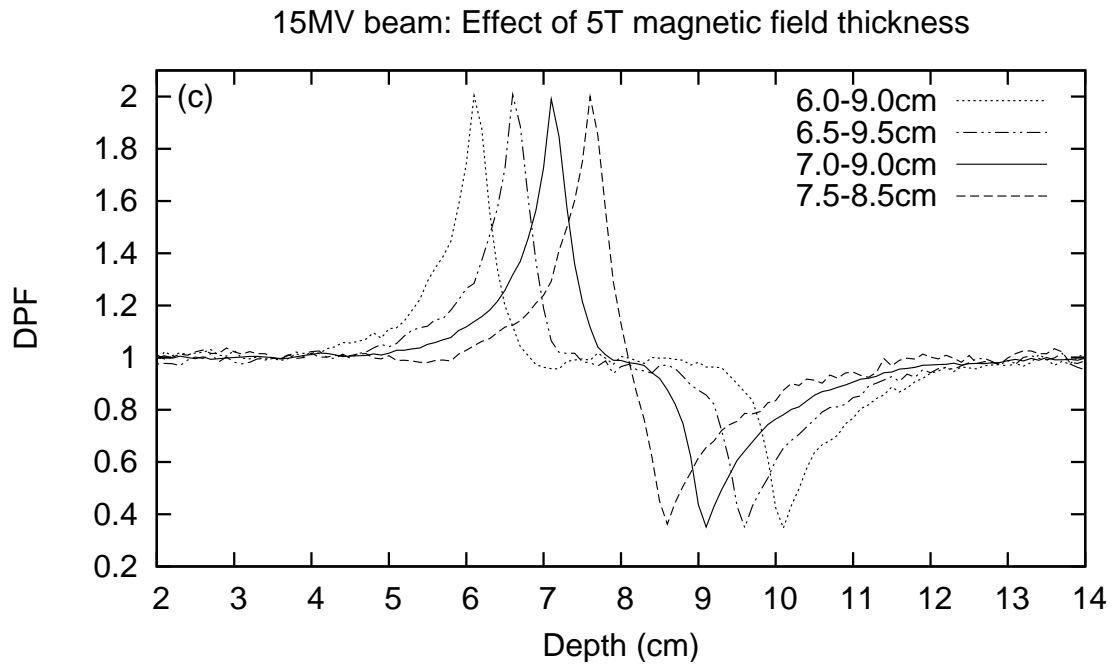


Figure 3.9: Effect of the magnetic field thickness. Figures (c) and (d) compare the effect of a 5 T transverse magnetic field of different thicknesses (1 to 4 cm) on the depth-dose (in water) of a 15 and 24 MV beam respectively.



### 3.4 Discussion

The effect of a transverse magnetic field on the dose distribution of high-energy photon beams was a dose enhancement (increase in DPF) at depths approaching and entering the magnetic field (i.e. between 5.5 and 7.5 cm). This dose perturbation was followed by a region of dose reduction (decrease in DPF) at depths exiting and beyond the magnetic field (i.e. between 8.5 and 10.5 cm), where the DPF returned to unity at about 12 cm depth.

The region of dose enhancement arises from secondary electrons on average having an initial direction downstream (as shown in the following chapter). In the absence of a magnetic field, this leads to dose being deposited some distance downstream. The effect of the transverse magnetic field is to reduce the average distance between the depth at which an electron originates and the depth at which most of its energy gets deposited. This could be pictured as due to the electrons spiraling around the transverse magnetic field vector which reduces their depth of interaction and the depth of any secondary particles they produce.

As shown in figure 3.1, the radius of curvature of an electron subjected to a magnetic field, and its mean free path (in water) between interactions, are both energy dependent. The figure also shows the cyclotron radius of an electron to be several orders of magnitude greater than its mean free path. This might lead to the erroneous conclusion that it is not possible for the magnetic field to influence the dose distribution. It must be remembered however that most electron interactions produce negligible change in the electron trajectory. Therefore, more significant than the mean free path is the mean distance an electron must travel before its trajectory is altered from its original path by one radian. As long as this distance is not significantly smaller than the radius of curvature we expect to see an effect. Alternatively, one could follow the approach of Bielajew, who compared the radius of an electron in a magnetic field to its range, and derived a ‘rule of thumb’ showing these lengths become comparable in water at a magnetic field strength of approximately two thirds of a Tesla for relativistic energies [53]. Note that this result

is independent of electron kinetic energy as both the range and the radius are linearly dependent on kinetic energy for relativistic electrons. This rule of thumb does not apply at lower energies where the radius becomes proportional to the square root of the kinetic energy (refer to figure 3.1).

This is reflected in figure 3.10 which shows the mean distance travelled along the beam direction by electrons (of different energies) as a function of magnetic field. It can be seen that electrons with an energy less than 1 MeV are not significantly affected. According to the secondary electron spectrum of a 15 MV beam as shown in figure 3.11, around 40% of secondary electrons have energies of 1 MeV or higher. Thus, it is primarily these electrons which are responsible for the effects observed. It is also apparent from this figure that magnetic field strengths beyond 5 T will not produce significantly different dose enhancements, since it is at 5 T that the minimum distance an electron travels in the beam direction from its origin is observed. (A comprehensive study of the effect of magnetic field strength on the range of different energy electrons appears in the subsequent chapter.)

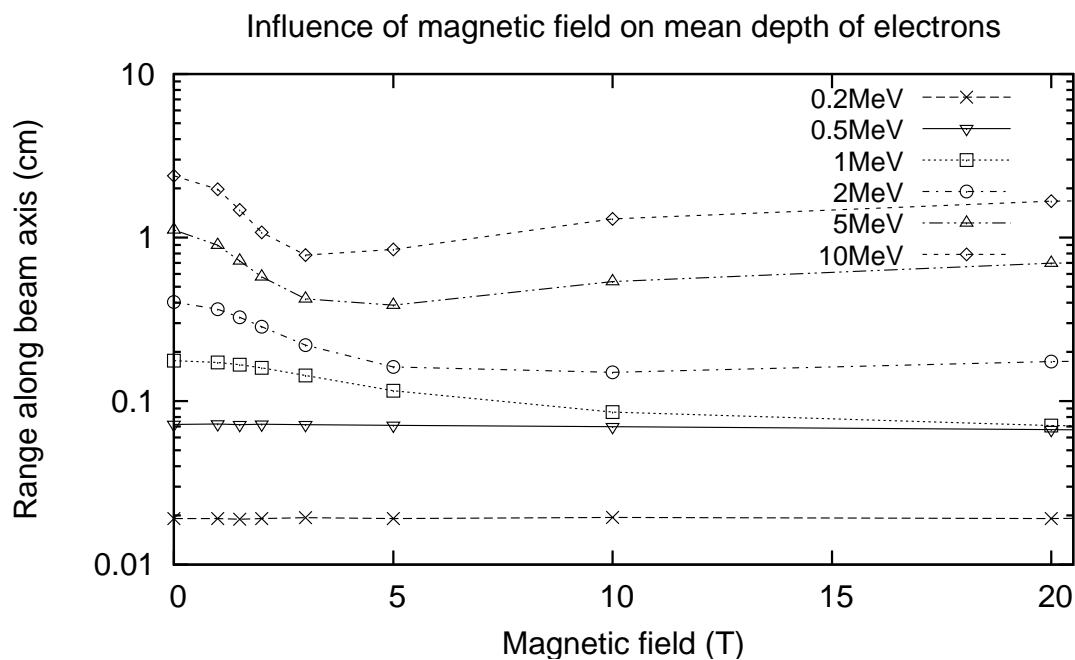


Figure 3.10: Influence of a magnetic field on the mean distance an electron travels along the beam direction from its origin at 6.9 cm depth.

Consequently, higher energy electrons suffer a greater deviation in their path due to the magnetic field than lower energy electrons, resulting in shallower depths of interaction and production of any secondary particles. This increase in dose at shallower depths gives rise to the dose enhancement observed in the region approaching the magnetic field, where the distribution of particle energies, depths of interaction, and ranges give rise to its breadth.

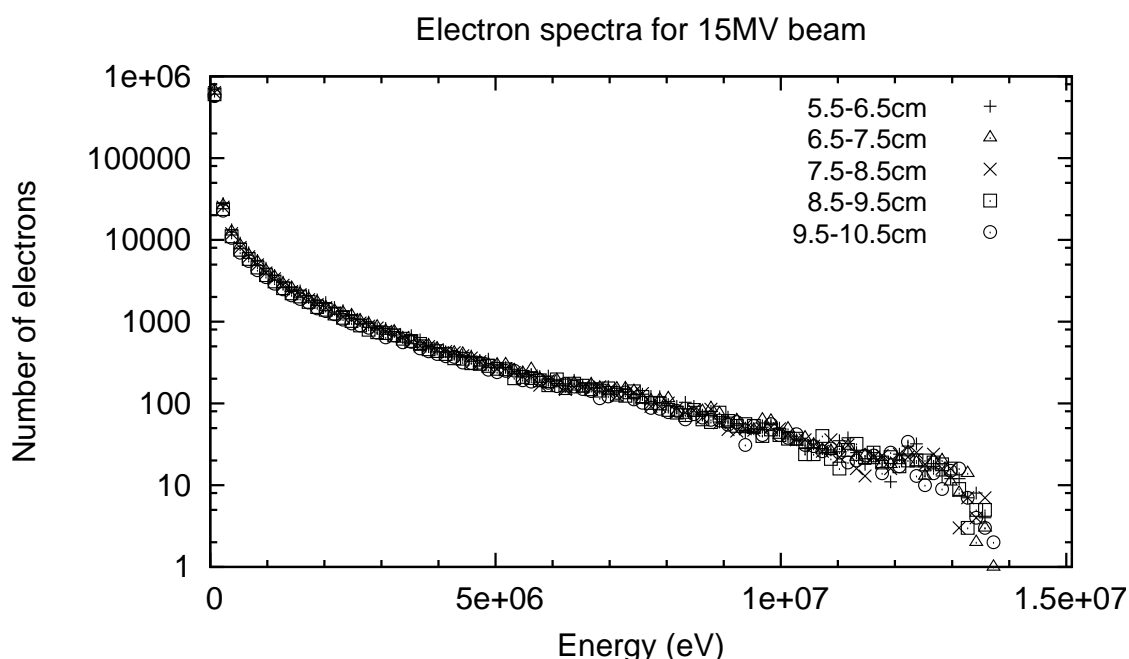


Figure 3.11: Secondary electron spectrum of a 15 MV photon beam at different depths (5.5 to 10.5 cm) in water.

The largest maximum DPF (1.91) occurred with a field strength of 5 T, where stronger magnetic fields failed to yield larger maximum DPFs due to fewer low-energy electrons being able to escape the magnetic field as their radii of curvature became too confined. This also explains the steep fall-off in the DPF between the maximum and minimum value inside the magnetic field. The region of dose reduction corresponds to the absence of electrons, and any secondary particles they produce, that would otherwise be present in the absence of magnetic field. Thus, the primary dose contributors in this

region are photons (since they are unaffected by the magnetic field) and any secondary particles they produce. The reduction in minimum DPF yield with increasing magnetic field strength is due to fewer electrons escaping the magnetic field since their smaller radii of curvature reduces their depth of interaction.

The PENELOPE elastic scattering parameters  $C_1$  and  $C_2$  had no influence on the results, owing to the code's improved modelling of soft energy losses [38]. Decreasing the PENELOPE electron and photon low-energy transport cutoffs from 10 keV to 1 keV also had no effect on the DPF or the low-energy electron spectrum.

Doubling the number of scoring bins (by halving their depth) had an effect on the maximum and minimum DPFs. The small enhancement in the maximum DPF with smaller bins is attributed to the improved resolution of the position of maximum DPF. For example, an enhancement in the maximum DPF of 11% was observed for the 15 MV and 10 T combination, which shifted from a depth of 6.9 cm to 7.1 cm. Enhancements of up to 6% were observed for all other magnetic field combinations with 15 MV, some resulting in minor shifts in the maximum DPF to greater depths (e.g. 20 and 100 T maximum DPF shifted from 6.9 to 7.0 cm depth). Conversely, the minimum DPF exhibited a reduction, especially at higher magnetic fields. For example, a reduction in the minimum DPF of 33% was observed for the 15 MV and 100 T combination.

Despite an additional bin at the 9 cm boundary (i.e. bins at 8.9, 9.0, and 9.1 cm instead of 8.9 and 9.1 cm), the position of the minimum DPF remained fixed at 9.1 cm depth. The reduction in the minimum DPF arises from the presence of the extra bin at 9 cm depth. It scores any dose depositions immediately beyond the magnetic field that would have otherwise been deposited in the 9.1 cm bin (for the case of 0.2 cm bins). This gives rise to the steeper fall-off in the dose reduction at the 9 cm field boundary. The lower minimum DPFs exhibited by higher magnetic fields is due to the electrons' smaller cyclotron radii (and hence, shallower depths of interaction), which results in fewer electrons escaping the magnetic field.

Higher energy photon beams subjected to a 5 T magnetic field exhibit larger maximum and smaller minimum DPFs, owing to their longer ranges and correspondingly greater yields of secondary electrons at these depths. Of the electrons generated within the vicinity of the magnetic field, those with a range sufficiently larger than their cyclotron radius have a higher probability of escaping the magnetic field. This leads to a broadening in the dose enhancement and dose reduction at the magnetic field boundaries, which is wider for higher energy photon beams due to the larger range of secondary electrons set into motion.

The 185% increase in the maximum DPF of a 15 MV photon beam subjected to the slice of 5 T transverse magnetic field at the phantom's surface is due to the large population of low-energy electrons in the build-up region (i.e. distance from the surface to the depth at which maximum dose occurs), which is about 3 cm for a  $4 \times 4 \text{ cm}^2$  field. As the ranges of these electrons (in water) are only fractions of a centimeter (e.g. a 100 keV electron has a 0.01 cm range in water), the presence of a magnetic field reduces their depth of interaction, thereby leading to an increase in DPF. This also explains the consistent maximum and minimum DPFs obtained with the slice of magnetic field applied beyond the build-up region. The DPF realised in this study will be greater than those attainable with a more realistic magnetic field distribution as demonstrated in the work by Jette [67].

Altering the thickness of the magnetic field (i.e. depth over which it is applied) had no affect on the maximum and minimum DPFs. According to the 15 MV secondary electron spectrum in figure 3.11, the majority of electrons at these depths have energies less than 1 MeV, which corresponds to a range (in water) of less than 0.4 cm. When subjected to a 5 T magnetic field, these electrons have a cyclotron radius of less than 0.1 cm, and therefore remain trapped within the field unless they are near to one of its boundaries.

### 3.5 Conclusion

The application of a slice of uniform transverse magnetic field to high-energy photon beams results in localised regions of dose enhancement and dose reduction. The region of dose enhancement occurs at depths approaching and entering the slice of magnetic field, while the region of dose reduction is present at depths exiting and beyond the slice.

The dose enhancement arises from a reduction in the depth of interaction of electrons and any secondary particles they produce, as they travel through the transverse magnetic field. The largest enhancement (maximum DPF of 1.91) was observed with 5 T, where further increments in magnetic field (up to 100 T) failed to produce higher maximum DPFs. The breadth of this dose enhancement region is attributed to the spread of energy, depth of interaction, and range of the electrons. Correspondingly, there is a region of dose reduction immediately beyond the magnetic field slice caused by a deficiency of electrons in this region (since photons are unaffected by the magnetic field). The decreasing minimum DPF with increasing magnetic field is due to the smaller cyclotron radii of electrons, which reduces their depth of interaction and probability of escaping the magnetic field.

The PENELOPE maximum and minimum DPFs were 91% enhancement and 77% reduction respectively, which are slightly smaller than Li's respective EGS4 results of 97% and 79%. The PENELOPE DPFs were mostly within 4% of those obtained with EGS4, where the minor discrepancies between the codes were not resolved. Reducing the PENELOPE photon and electron low-energy transport cutoff to 1 keV and altering the elastic scattering parameters  $C_1$  and  $C_2$  had no effect on the results. Increasing the bin resolution (by halving the depth of the scoring bins from 0.2 to 0.1 cm) produced a small increase in the maximum DPFs and a corresponding reduction in the minimum DPFs. It did not, however, resolve the discrepancies between the PENELOPE and EGS4 results.

The application of a 5 T magnetic field to different energy photon beams revealed larger maximum and smaller minimum DPFs with higher beam energies. This is because

higher energy photons interact at greater depths, resulting in the presence of more electrons within the vicinity of magnetic field. The electron deficiency beyond the magnetic field gives rise to the reduction in the minimum DPF, which was more severe for higher energy beams.

Applying a slice of 5 T magnetic field at the surface of the water phantom produced a substantial 185% increase in the maximum DPF for the 15 MV beam. Altering the thickness of the magnetic field had no effect on the maximum and minimum DPFs, although it did produce wider regions of unity DPF inside the slice of magnetic field. This could be therapeutically beneficial for the treatment of tumours close to radiation-sensitive structures in the body, where the magnetic field thickness (chosen according to the distance between the tumour and critical structure) would be aligned in such a way to maximise dose to the tumour whilst sparing critical tissue.

## **CHAPTER 4**

### **EFFECT OF A TRANSVERSE MAGNETIC FIELD ON THE ELECTRON DISTRIBUTION OF HIGH-ENERGY PHOTON BEAMS**

#### **4.1 Introduction**

In chapter 3, the application of a transverse magnetic field to high-energy photon beams was shown to alter the dose deposition in such a way as to produce localised regions of dose enhancement and dose reduction. The current chapter investigates the influence of a transverse magnetic field on the spatial distribution of secondary electrons produced from these photon beams. It also explores the potential of a magnetic field to alter the corresponding relative biological effectiveness of this radiation through a change in the low-energy secondary electron spectrum. Results appearing in sections 4.3.1 and 4.3.5 of this chapter have been published in a peer-reviewed journal article [48].

When radiation traverses matter, it can deposit its energy via the processes of ionisation or excitation of absorber atoms. In tissue, these energy depositions can induce lesions in the DNA of cells, which if incompletely or incorrectly repaired may result in lethal or mutagenic radiobiological effects [33–35]. It is commonly accepted that the initiation of these effects depends on the spatial distribution of lesions [68]. Isolated DNA damage such as single-strand breaks (SSBs) are generally repaired efficiently [35], while closely spaced lesions such as double-strand breaks (DSBs), where two or more SSBs occur on opposing strands within 10 to 20 base pairs [69], may lead to irreparable DNA damage. It has also been postulated that substantial biological damage results from clusters of DNA lesions (formed when low-energy electrons produced from electron inelastic collisions interact in close proximity to one another) as they are more prone to misrepair [70–72].



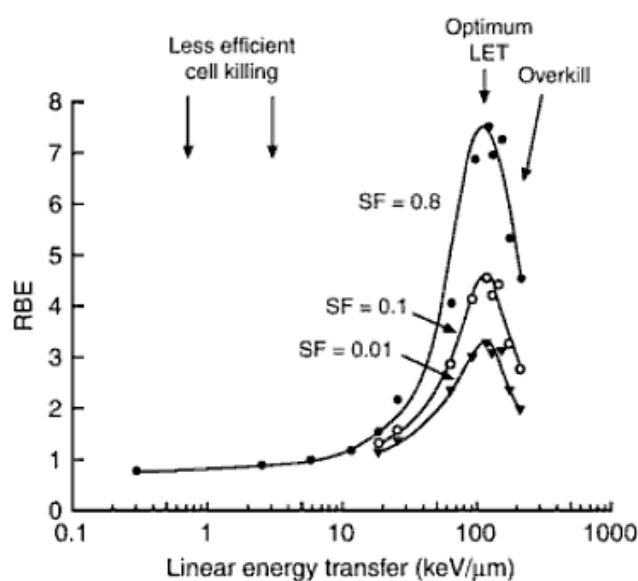


Figure 4.1: Relationship between relative biological effectiveness (RBE) and mean linear energy transfer (LET) for cell killing, where the three curves correspond to different levels of cell survival, or surviving fraction (SF) [74, 75].

For the same absorbed dose, or average energy deposited per unit mass, it is well known that different radiation types can induce different biological effects. This is quantified by the term relative biological effectiveness (RBE), or the ratio of the absorbed dose of a reference radiation to the absorbed dose of a test radiation to produce the same biological effect. Thus, for an equivalent radiation exposure, a higher RBE results in greater biological damage. Generally, RBE increases with increasing linear energy transfer (LET), which is the rate of energy loss per unit distance along the path of a charged particle [73]. This is shown in figure 4.1 with a plot of RBE as a function of LET for three different levels of cell survival, or surviving fraction (SF) [74, 75], where a maximum RBE occurs at an LET between 100 and 200 keV/ $\mu$ m.

As an electron loses energy its LET increases, and generally, so does its RBE. Therefore short-range low-energy electrons have a higher probability of inducing lethal damage to the DNA of cells (via strand breaks) than more energetic electrons. A 20 keV electron, for example, has a 9  $\mu$ m range in tissue which is roughly the diameter of a typical human cell.

When an electron is subjected to a magnetic field, the Lorentz force confines its trajectory, and hence its energy deposition, to a smaller volume. Since the radius of curvature of an electron is known to decrease with decreasing energy, it is possible that the application of a magnetic field will not only affect the macroscopic absorbed dose distribution, but that it will also affect the distribution of ionisation clusters on a nanometre scale - in DNA.

While the effect of a magnetic field on the absorbed dose distribution has been examined, and the potential for magnetic fields to alter the RBE has been mentioned [51, 53, 61, 76], absent from the literature is the study of a magnetic field's influence on the electron distribution from high-energy photon beams and any related change to their RBE. Considering the implementation of magnetic fields into radiotherapy has become practically feasible with the recent development of an integrated 1.5 T MRI scanner and 6 MV linear accelerator (for soft-tissue tumour imaging, position verification, and treatment monitoring in image-guided radiotherapy [60, 62, 77]), these effects should be studied to ascertain their importance in treatment planning. This chapter endeavours to explore these effects by using Monte Carlo PENELOPE simulation to investigate the influence of a transverse magnetic field on the secondary electron spectrum of various photon beams.

In the course of obtaining secondary electron spectra with and without a magnetic field, several peaks consistently featured at energies below 700 eV. Since their origin is most likely related to atomic relaxation events, a number of simulations were performed to determine the energies of characteristic radiation in water (i.e. hydrogen and oxygen atoms). According to the plot of absorption and scattering contributions towards the total attenuation (in water) in figure 4.2 (a), the predominant mode of interaction of photons with relatively low energies is the photoelectric process. In this process, the incident photon undergoes an interaction with an absorber atom in which the photon transfers its energy,  $h\nu$ , to one of the orbital electrons of the bound shells of the atom. This photoelectron, whose most probable origin is the K shell of the atom, is ejected from the atom

with an energy,  $E_{e^-}$ , given by

$$E_{e^-} = h\nu - E_b \quad (4.1)$$

where  $E_b$  is the binding energy of the photoelectron in its original shell. The vacancy created by the ejected photoelectron is filled through the capture of a free electron from the medium and/or rearrangement of electrons from other shells that have a lower binding energy. This process generates characteristic X-ray photons and/or Auger electrons. The energy of the characteristic radiation is the surplus energy liberated when an electron drops from its outer shell to a shell closer to the nucleus (i.e. difference in their binding energies). The binding energies for hydrogen and oxygen are shown in table 4.1. The PENELOPE atomic photoelectric cross sections of hydrogen (K shell) and oxygen (K,  $L_1$ ,  $L_2$ , and  $L_3$  shells) are shown in figure 4.2 (b).

Table 4.1: Binding energies of hydrogen and oxygen [78].

Element	Shell	Electronic level	Binding energy (eV)
H	K	1s	13.6
O	K	1s	543.1
	$L_1$	2s	41.6

## 4.2 Simulation methods

As photon trajectories are unaltered by the presence of a magnetic field, the location of any first generation secondary electrons (i.e. descendants from primary photons) is also unaffected. Simulations were performed to obtain the first generation secondary electron spectra in water (in the absence of a magnetic field) for  $\text{Co}^{60}$ , 6, 10, and 15 MV and 1, 5, 10, and 15 MeV photon beams. These simulations used electron and photon energy cutoffs of 10 keV and a total of  $10^8$  primary histories.

Simulations were also performed to obtain the secondary electron spectrum (all generations) for a 15 MV beam with and without a slice of transverse magnetic field

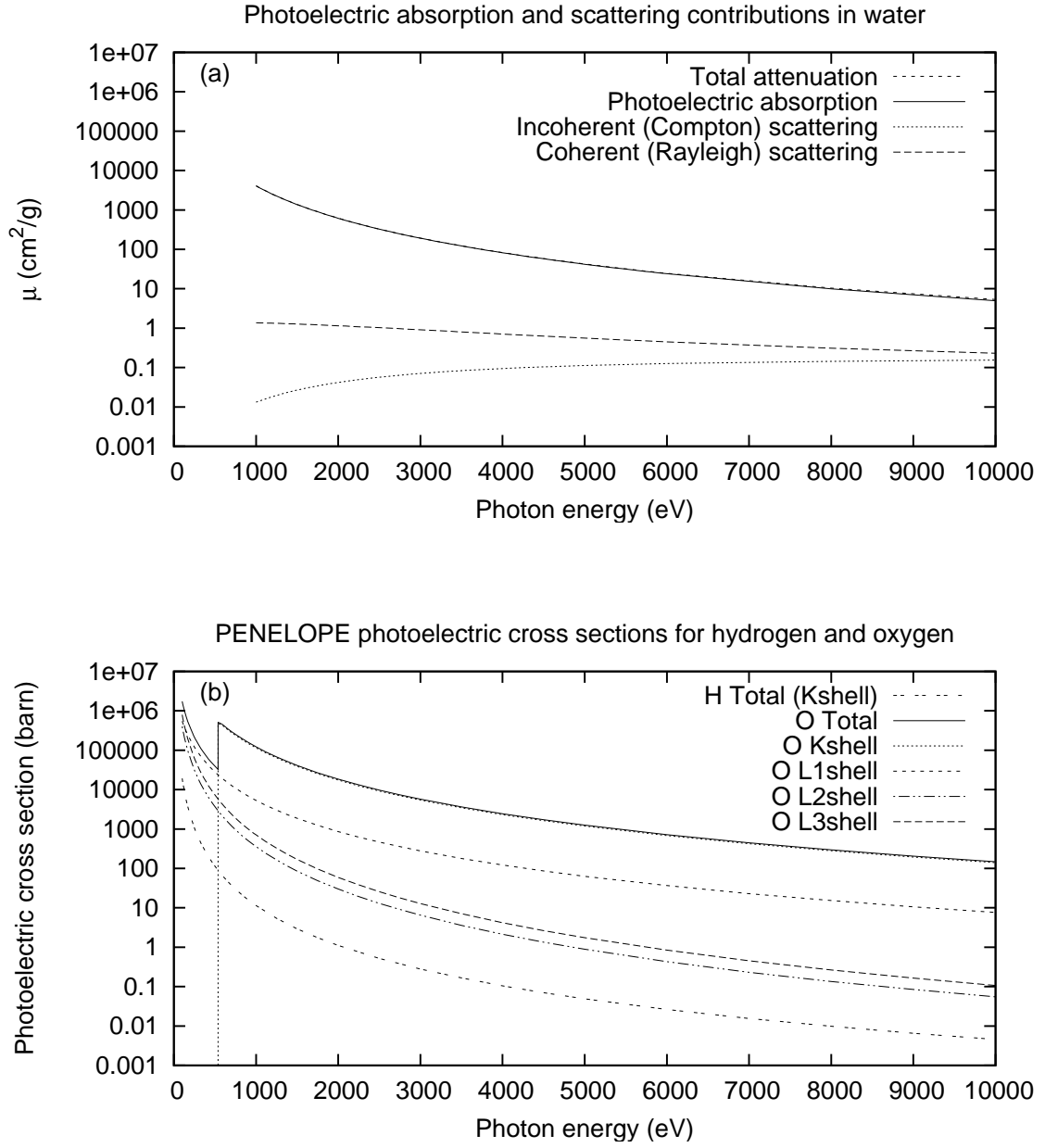


Figure 4.2: Figure (a) plots the absorption and scattering contributions towards the total attenuation of water using data obtained from NIST [36]). Figure (b) plots the PENELOPE atomic photoelectric cross sections for hydrogen (K shell) and oxygen (K,  $L_1$ ,  $L_2$ , and  $L_3$  shells) [38].

(between 7 and 9 cm depth). Magnetic fields of 2, 5, 10, and 20 T were chosen for this study. The total number of primary photon histories was  $10^8$  to ensure a statistical uncertainty within 98% confidence level. These simulations used the same water phantom and field size as those used to obtain the depth-dose curves in chapter 3. That is, a water

phantom  $30 \times 30 \times 20 \text{ cm}^3$  (width  $\times$  height  $\times$  depth) and a field size  $4 \times 4 \text{ cm}^2$  at 100 cm source to surface distance (SSD). Transport cutoffs were 10 keV for electron and photon transport and 1 keV for the parameters for  $W_{cc}$ ,  $W_{cr}$ , and the elastic scattering parameters  $C_1$  and  $C_2$  were set to 0.05. The electrons were binned along central axis according to their energy (up to 1 MeV) and depth using bin intervals of 10 keV and 0.2 cm respectively. Electron spectra were plotted for five different regions of interest within the vicinity of the magnetic field: 5.5 to 6.5 cm depth (before the magnetic field slice), 6.5 to 7.5 cm (entering the magnetic field), 7.5 to 8.5 cm (inside the magnetic field), 8.5 to 9.5 cm (exiting the magnetic field), and 9.5 to 10.5 cm (beyond the magnetic field).

The simulations were repeated with bin intervals of 100 eV to obtain an electron spectrum up to 10 keV. These simulations used transport cutoffs of 100 eV for electrons and photons, and the parameters  $W_{cc}$  and  $W_{cr}$ . The ratio of spectra obtained with and without magnetic field was constant over most of the energy range. Additional simulations were performed with 1, 3, and 4 T magnetic fields to produce a plot of the (constant) ratio of electron population with and without magnetic field as a function of field strength.

In the course of obtaining the secondary electron spectra (up to 10 keV), several peaks were observed at energies below 700 eV. The unresolved peak between 450 and 550 eV prompted simulations with smaller energy bins of 10 eV (rather than 100 eV) in attempt to resolve it. As the PENELOPE interaction models and the associated databases for particle interaction are limited to an energy of 100 eV (i.e. particles with an energy below 100 eV are no longer transported), a variable named *ecut* (set to 1 keV) was used to force all electrons with an energy below 1 keV to be put onto the secondary stack prior to absorption. This stack is used to store the information of secondary particles (emitted from primary particle interactions), which are simulated in chronological succession after completion of each primary track. These simulations were performed with  $10^7$  (rather than  $10^8$ ) primary histories, owing to longer simulation times with lower energy cutoffs.

Additional simulations were performed in order to establish whether the spectral

peaks are the result of atomic relaxation events in water (as they occur at typical energies for characteristic radiation in oxygen). These simulations used the PENELOPE ILB(4) label to track particles emitted from atomic relaxation and identify the shell from which they were released. The transport parameters used in these simulations were identical to those used to obtain the electron spectrum up to 1 keV. Electrons retrieved from the stack with a non-zero ILB(4) label (i.e. emitted from atomic relaxation) were binned in cylindrical scoring volumes of 0.5 cm radius  $\times$  0.2 cm depth according to their energy and position along central axis.

In PENELOPE, the direction of a particle is defined by  $u$ ,  $v$  and  $w$  which corresponds to the projection of its direction on the  $x$ ,  $y$ , and  $z$  axes, respectively. Since the effect of a transverse magnetic field on electron trajectories is greatest for those moving perpendicular to the field and least for those travelling parallel to it, a number of simulations were performed to study the angles by which electron paths deviate from their initial direction ( $u, v, w = 0, 0, 1$ ) as they travel through water. These simulations focused on the change in an electron's  $w$ -value, where a value of zero corresponds to an electron deviated 90 degrees from the beam axis, while a value of unity describes an electron moving parallel to the beam. The mean  $w$ -values of first generation electrons were investigated with Co<sup>60</sup>, 6, 10, and 15 MV and 0.1, 0.5, 1, 5, 10, and 15 MeV photon beams (in the absence of a magnetic field). The simulations were performed with  $10^6$  primary histories and  $C_1$  and  $C_2$  values of 0.05, and made use of the PENELOPE ILB(1) and ILB(2) labels to identify first generation electrons and the type of parent particle respectively. When a secondary electron with an ILB(1)  $> 1$  and an ILB(2) = 2 (i.e. descendant of a photon) was taken off the secondary stack, its  $w$ -value was binned (according to energy) and its transport terminated.

Also investigated was the mean distance that an electron travels (in the absence of a magnetic field) before the  $w$ -value of its initial trajectory ( $u, v, w = 0, 0, 1$ ) is deviated by a given angle up to 90 degrees (i.e.  $w = 0$ ). This study used monoenergetic electron beams of 0.1, 0.5, 1, 5, 10, and 15 MeV, and a total of 10 bins to score  $w$ -values between 1.0 and

zero. The simulations were performed with a total of  $10^6$  primary histories and energy cutoffs of 0.1 MeV for electron beams with an energy of 1 MeV and higher, and cutoffs of 0.01 MeV for lower energy electrons. The electrons were transported until their energy reached half of its initial value, where its  $w$ -value was binned prior to its termination. Additional simulations were performed for each of the electron beams to determine the mean range of electrons in water as a function of energy. These simulations used transport cutoffs of 0.01 MeV for all beam energies.

A detailed investigation of the effect of a transverse magnetic field on the range and spatial distribution of electrons was also performed to better understand the changes observed in the depth-dose curves of chapter 3. In this study, monoenergetic electron beams of 0.01, 0.05, 0.1, 0.5, 1, 5, 10, and 15 MeV (i.e. typical electrons produced from the interaction of a 15 MV photon beam) were subjected to a slice of 1, 1.5, 2, 3, 5, 10, 20, 30, 40, 50, 75, and 100 T magnetic field between 7 and 9 cm depth (in water). Five simulations were performed for each electron beam, where the primary electrons were started from a depth of: 6.9 cm (immediately before the magnetic field); 7.5, 8.5, and 8.9 cm (inside the magnetic field); and 9.1 cm (immediately beyond the magnetic field). The initial direction of primary electrons was along the  $z$ -axis ( $w = 1$ ), and perpendicular to the transverse magnetic field, which was in the direction of the positive  $x$ -axis. The simulations used low-energy electron and photon cutoffs of 100 eV and a total of  $10^5$  primary electron histories.

For each simulation, the electron's  $y$  and  $z$ -range was calculated as the distance between its origin and endpoint (prior to absorption), and a mean of these ranges was determined at the completion of the simulation. Since a magnetic field along the positive  $x$ -axis exerts a Lorentz force on electrons in the direction of the negative  $y$ -axis, its influence on the electron spatial distribution was investigated by tallying electron populations on either side of the plane  $y = 0$  (according to the  $y$ -coordinate of their final position). The ratio of electrons with a negative  $y$ -endpoint ( $y < 0$ ) to those with a positive  $y$ -endpoint ( $y > 0$ ) was calculated for the five different starting depths. The effect of a magnetic

field on the electron distribution along the  $z$ -axis (beam axis) was also investigated by calculating a ratio of the number of electrons with a final position downstream of their start position ( $z > z_{start}$ ) to those with an end position upstream of the start ( $z < z_{start}$ ).

### 4.3 Simulation results and discussion

Figures 4.3 (a) and (b) plot the first generation electron spectra (in water) for polyenergetic photon beams of  $\text{Co}^{60}$ , 6, 10, and 15 MV and monoenergetic photon beams of 1, 5, 10, and 15 MeV, respectively. Most of these electrons are produced in Compton scattering events, as this is the dominant photon interaction mechanism (in water) between about 30 keV and several MeV. The large population of low-energy electrons stems from the higher Klein-Nishina cross section that photons undergo small angle Compton scattering (refer to figure 2.2). The electron spectra of monoenergetic photon beams exhibit a peak just below the photon energy, which corresponds to the maximum energy transferred to a Compton electron (i.e. when the photon is backscattered  $180^\circ$  from the initial direction of its motion). This peak does not appear in the electron spectra of polyenergetic photon beams as there are fewer high-energy electrons owing to the small probability of high-energy photons.

Figures 4.4 (a) and (b) show the spectra of secondary electrons of all generations for a 15 MV beam obtained with and without a 5 T transverse magnetic field (between 7 and 9 cm depth) respectively. These spectra show the electron population in five 1 cm-deep regions within the vicinity of the magnetic field: 5.5 to 6.5 cm depth (before the magnetic field slice), 6.5 to 7.5 cm (entering the magnetic field), 7.5 to 8.5 cm (inside the magnetic field), 8.5 to 9.5 cm (exiting the magnetic field), and 9.5 to 10.5 cm (beyond the magnetic field). The spectra obtained with magnetic field exhibit differences in the electron population below about 1 MeV which are not present in the corresponding spectra obtained without magnetic field.



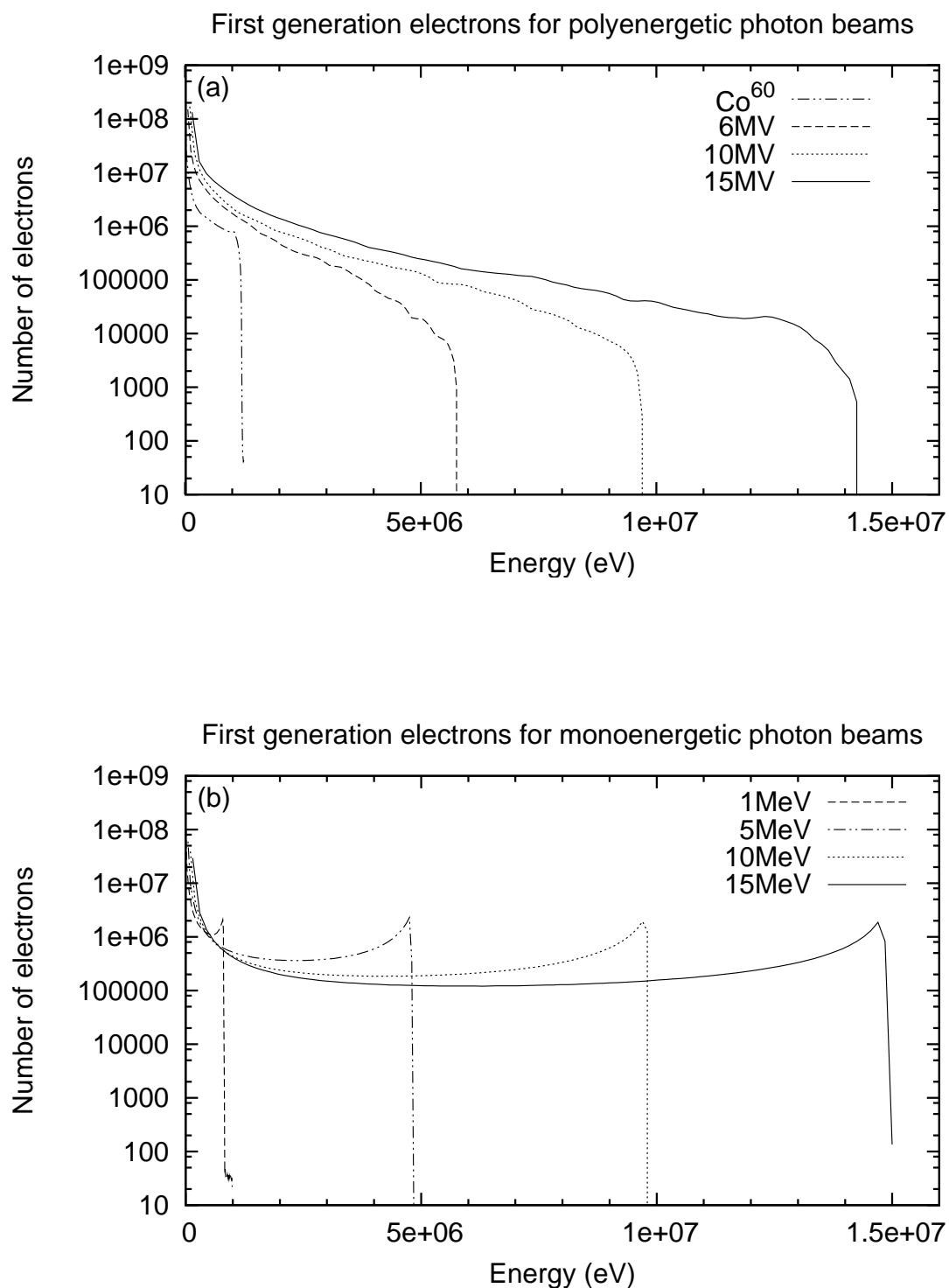


Figure 4.3: First generation electron spectra for polyenergetic and monoenergetic photon beams (in water). Figure (a) plots the first generation electron spectra for  $\text{Co}^{60}$ , 6, 10, and 15 MV beams. Corresponding electron spectra for 1, 5, 10, and 15 MeV monoenergetic photon beams are shown in figure (b).

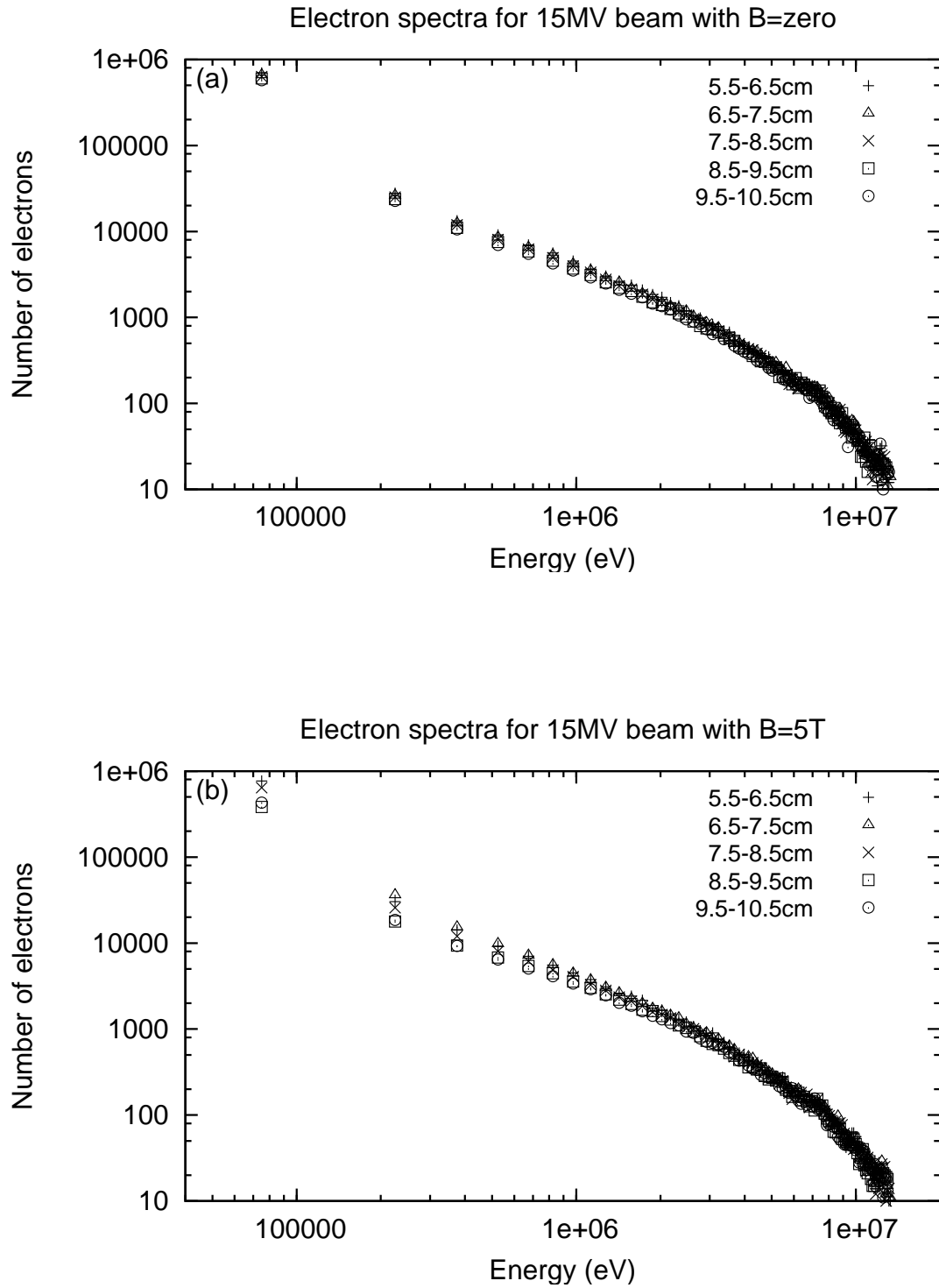


Figure 4.4: Secondary electron spectra (all generations) for a 15 MV beam with depth (in water). Figures (a) and (b) plot the electron spectra in the presence and absence of a slice of 5 T transverse magnetic field (7 to 9 cm depth), respectively.

#### 4.3.1 Influence of a magnetic field on electron spectra below 1 MeV

Figures 4.5 (a), (b), (c), and (d) plot a ratio of the electron population (below 1 MeV) in the presence and absence of a 2, 5, 10, and 20 T transverse magnetic field (7 to 9 cm depth), respectively. For all magnetic fields investigated, a maximum electron population (below 1 MeV) occurred in the region entering the magnetic field (6.5 to 7.5 cm depth) and a minimum population in the region exiting the field (8.5 to 9.5 cm depth).

The presence of a 5 T magnetic field produced the largest augmentation in electron population between 6.5 and 7.5 cm, which was 54% higher than that obtained in the absence of field. It also yielded the smallest electron population between 8.5 and 9.5 cm, which was 48% lower than that obtained without magnetic field. Reducing the magnetic field from 5 to 2 T resulted in reductions of 30% and 22% in the maximum and minimum electron populations respectively. However, increasing the magnetic field beyond 5 T failed to produce larger maximum and minimum electron populations in these regions, although variations were observed in the populations of other regions. In the region before the magnetic field (5.5 to 6.5 cm) the electron population increased with stronger magnetic fields, while in the region beyond the field (9.5 to 10.5 cm) it decreased. Inside the magnetic field (7.5 to 8.5 cm), the ratio of electron population was unity for all magnetic fields except 2 T, which exhibited a 14% increase.

The regions of maximum and minimum electron population correspond with the regions of maximum dose enhancement and dose reduction in the depth-dose profiles of chapter 3 (refer to figure 3.4). This suggests that the effect of a magnetic field on the dose deposition is associated with a change in the secondary electron spectrum.

For an electron moving in a transverse magnetic field, its depth of interaction is reduced when its range is comparable to or greater than its cyclotron radius. This in effect causes an upstream migration of electrons (with sufficient range), and hence, any secondary electrons they produce from interactions within the medium (water). Of the

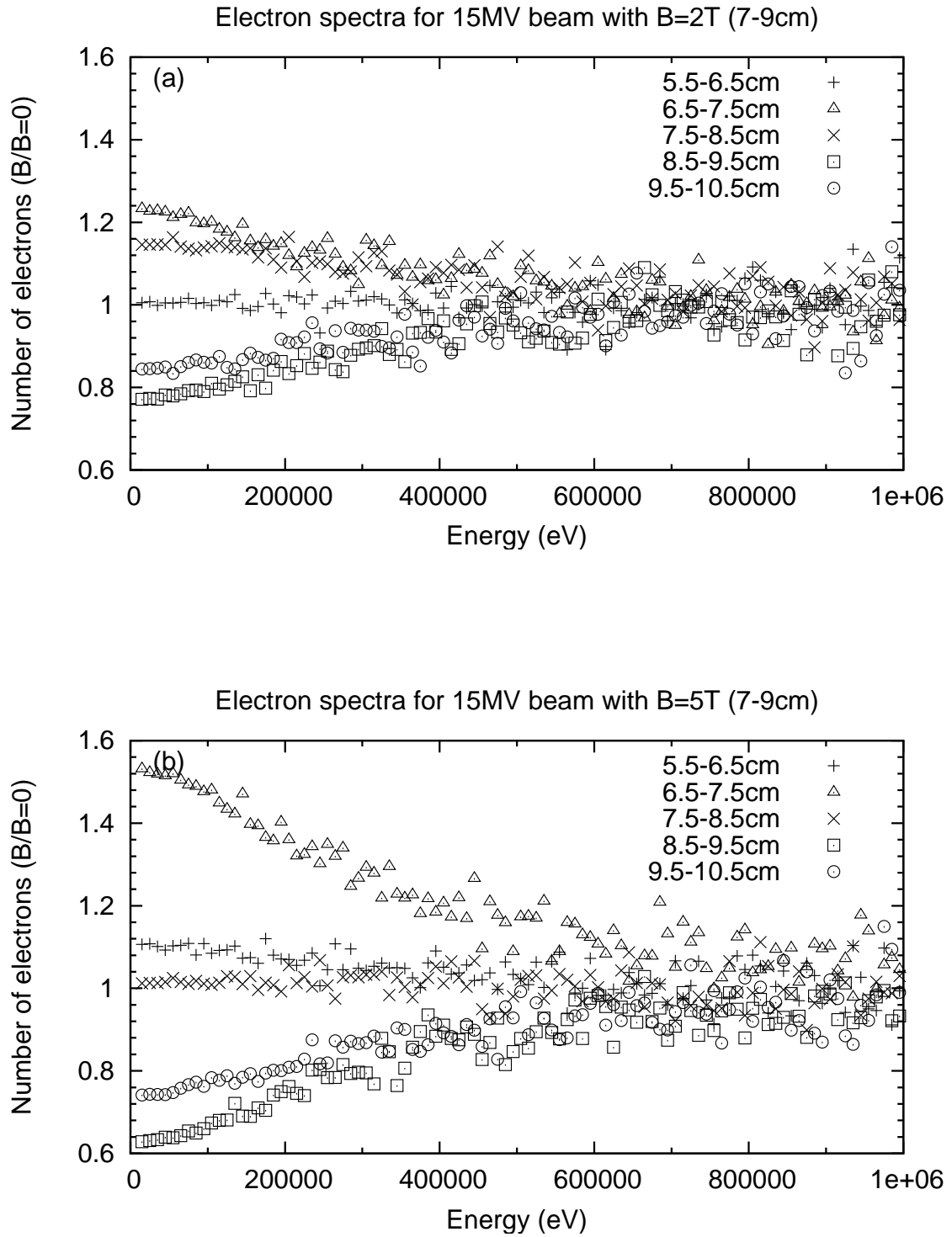


Figure 4.5: Normalised electron spectra (below 1 MeV) for a 15 MV beam. Figures (a) and (b) plot a ratio of the electron population in the presence and absence of a 2 and 5 T transverse magnetic field (7 to 9 cm depth), respectively.

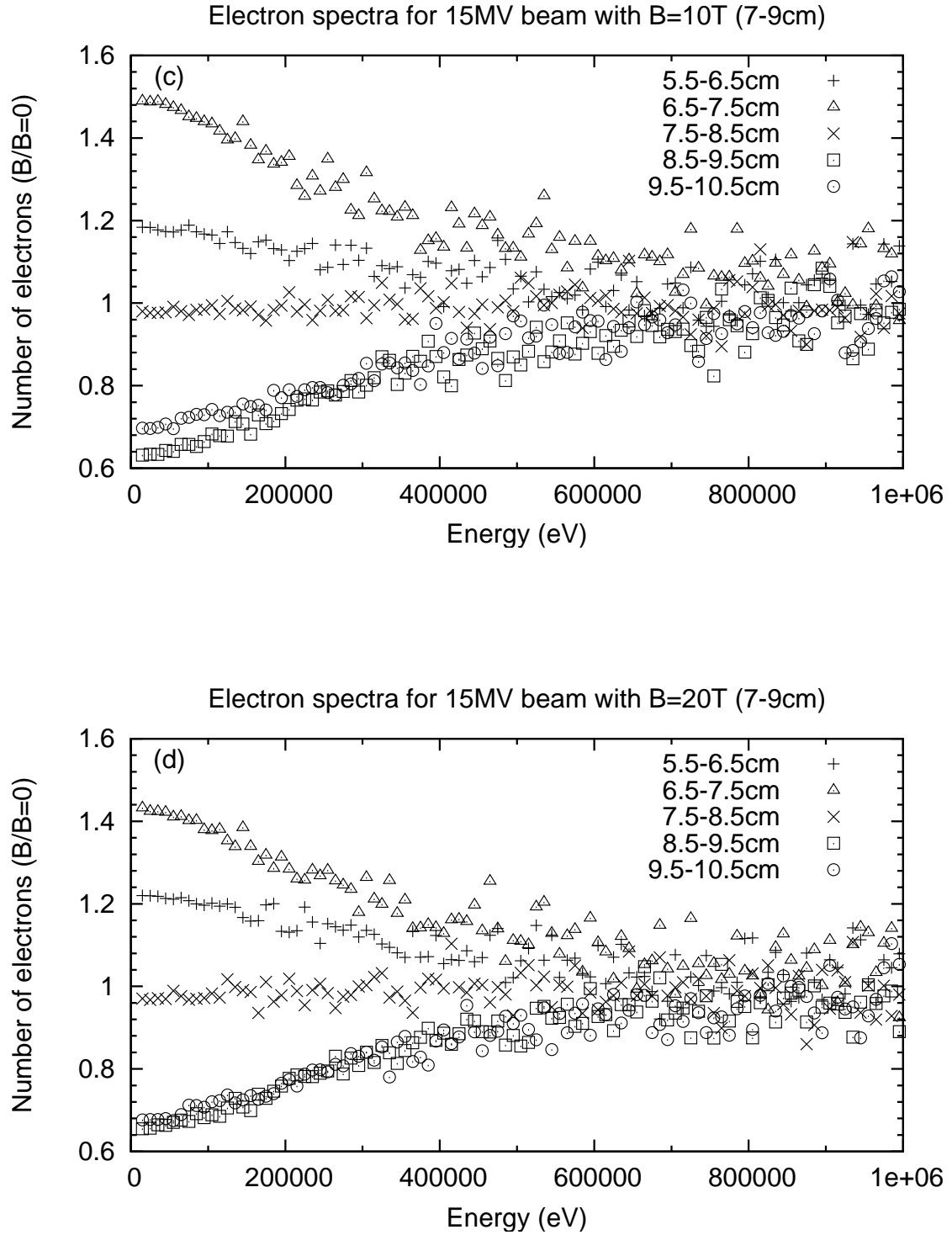


Figure 4.5: Normalised electron spectra (below 1 MeV) for a 15 MV beam. Figures (c) and (d) plot a ratio of the electron population in the presence and absence of a 10 and 20 T transverse magnetic field (7 to 9 cm depth), respectively.

descendant electrons, those with an energy of 0.5 MeV or lower will deposit their energy locally since their ranges are less than the 0.2 cm depth of the scoring bins. It is therefore the upstream migration of electrons that gives rise to the population increase in the regions before and entering the magnetic field (5.5 to 6.5 cm and 6.5 to 7.5 cm), and the subsequent depletion of electrons (minimum population) further downstream in the regions exiting and beyond the magnetic field (8.5 to 9.5 cm and 9.5 to 10.5 cm). The smaller variations in electron population observed with 2 T as opposed to 5, 10, and 20 T are attributed to the electrons' larger cyclotron radii in weaker magnetic fields, and hence, lower probability of depositing their energy further upstream.

Inside the magnetic field (7.5 to 8.5 cm), there was little change in the electron population with and without a magnetic field of 5 T or stronger. (A similar observation was made in the depth-dose profiles in chapter 3). This is because the electron population in this region is maintained by an upstream migration of electrons (i.e. shallower depths of interaction) which would have otherwise, in the absence of a magnetic field, deposited dose further downstream. The increase in electron population exhibited by the 2 T field is attributed to the electrons' larger radii of curvature, and hence, deeper depths of interaction (i.e. fewer electrons can escape the magnetic field to deposit their energy upstream). In the region beyond the magnetic field (9.5 to 10.5 cm), a depletion of electrons (resulting from the upstream migration) gives rise to the comparatively smaller population. Here, the majority of electrons are of first generation (i.e. produced from photon interactions) as photon trajectories are not influenced by a magnetic field.

#### 4.3.2 Influence of a magnetic field on electron spectra below 10 keV

As an electron loses energy its LET increases and so does its relative biological effectiveness (RBE). It is therefore possible that the increase in low-energy electron population in the region entering the magnetic field (6.5 to 7.5 cm) may correspond to an increase in RBE, and conversely, the reduction in population in the region exiting the magnetic field (8.5 to 9.5 cm) may correspond to a reduction in RBE.

The larger differences in the electron population with decreasing energy led to a study of the electron spectra below 10 keV (smallest bin in the electron spectra below 1 MeV). Figures 4.6 (a) and (b) show the resulting spectra obtained with and without a 5 T magnetic field, respectively, using bin intervals and energy cutoffs of 100 eV. These spectra reveal an unresolved peak between 450 and 550 eV (i.e. centres of 100 eV bins) superimposed on a Compton continuum. In the absence of a magnetic field, the electron distribution appears to be approximately the same in all five regions. However, when subjected to a 5 T magnetic field the spectra disperse in a similar fashion to that exhibited by the electron spectra in figure 4.4, where the largest and smallest populations are observed in the regions 6.5 to 7.5 cm and 8.5 to 9.5 cm respectively.

A ratio of the electron population obtained with and without a 5 T magnetic field, as shown in figure 4.7, reveals a constant ratio between about 600 and 10000 eV. This is also apparent in the ratio of electron spectra obtained with and without a 1, 2, 3, 4, 10, and 20 T transverse magnetic field. A plot of the mean ratio as a function of magnetic field (in the five different regions) is shown in figure 4.8.

In the region before the slice of magnetic field (5.5 to 6.5 cm depth), the ratio of electron population rises above unity and continues to increase with magnetic fields greater than 2 T. In the region entering the magnetic field (6.5 to 7.5 cm depth), the electron population augments with increasing field strength, reaching a maximum increase of 52% at 5 T before decreasing by up to 10% at stronger fields. Inside the slice of magnetic field (7.5 to 8.5 cm depth), the ratio of electron population is approximately unity for magnetic fields beyond about 4 T, while at weaker field strengths it rises above unity by as much as 8%. In the region exiting the magnetic field (8.5 to 9.5 cm depth), the ratio rapidly decreases with increasing field up to about 4 T where the ratio is 36% below unity. There is little change in the ratio between field strengths of 4 to 20 T. Sub-unity ratios are observed in the region beyond the magnetic field (9.5 to 10.5 cm depth), where the ratio can be seen to decrease with increasing magnetic field by as much as 32% at 20 T.

While the presence of magnetic field has no affect on the trajectories of photons, it

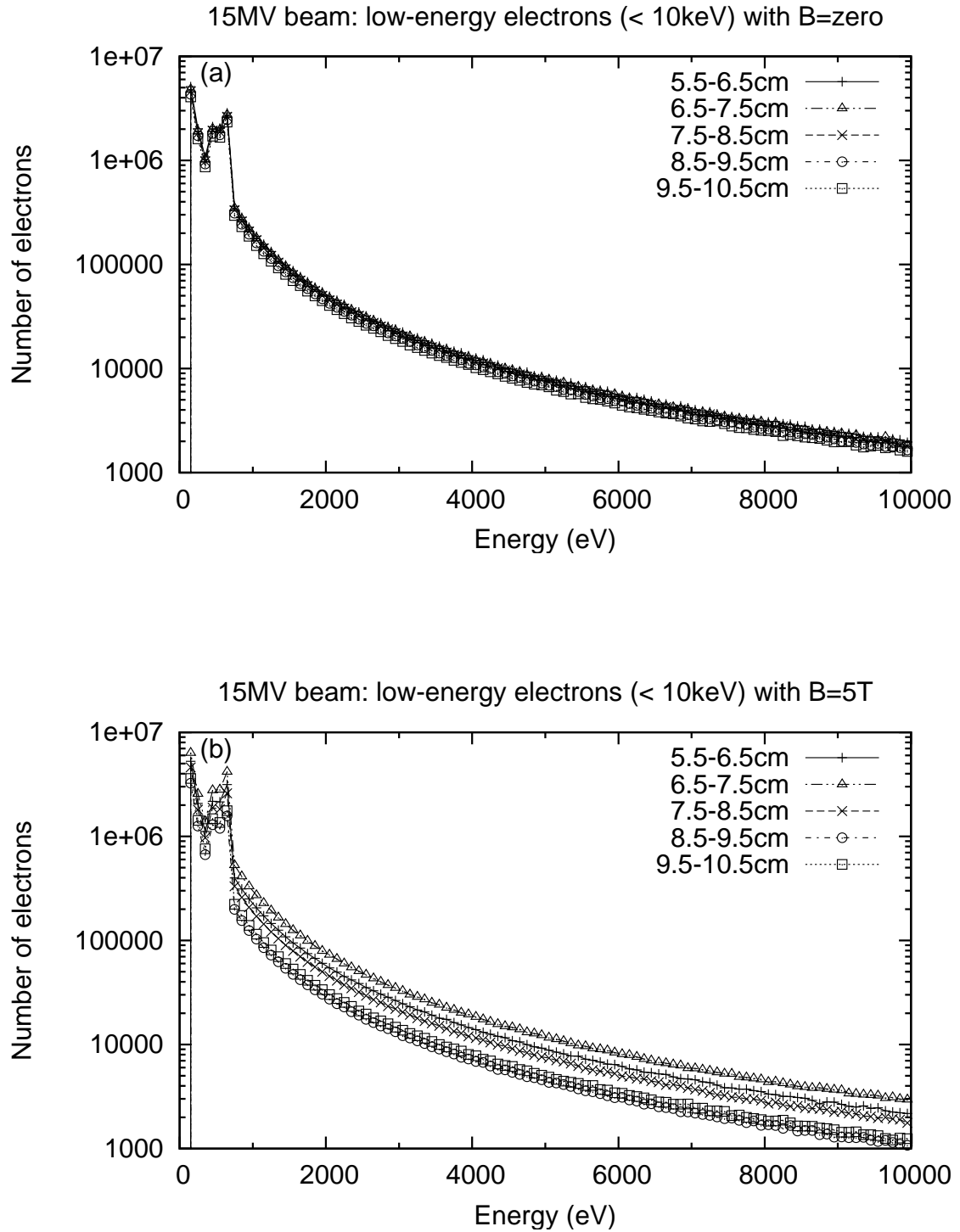


Figure 4.6: Secondary electron spectra (below 10 keV) for a 15 MV beam. Figures (a) and (b) plot the electron spectra in five depth regions in the presence and absence of a 5 T transverse magnetic field (7 to 9 cm depth), respectively.



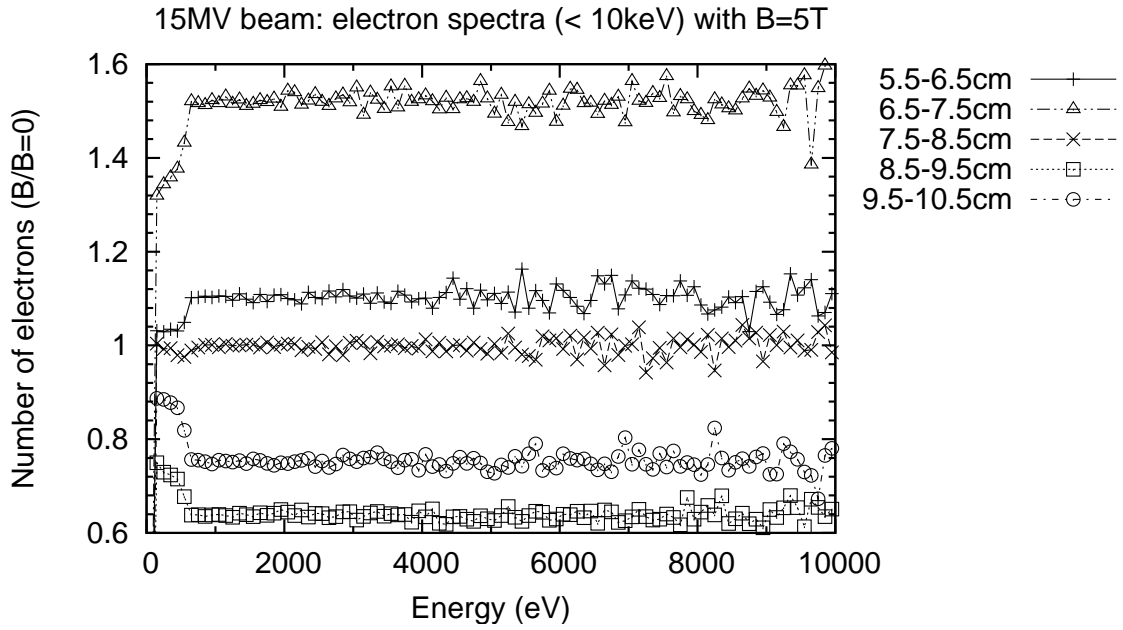


Figure 4.7: Normalised electron spectra (below 10 keV) for a 15 MV beam. A ratio of the electron population in five depth regions in the presence and absence of a 5 T transverse magnetic field (7 to 9 cm depth).

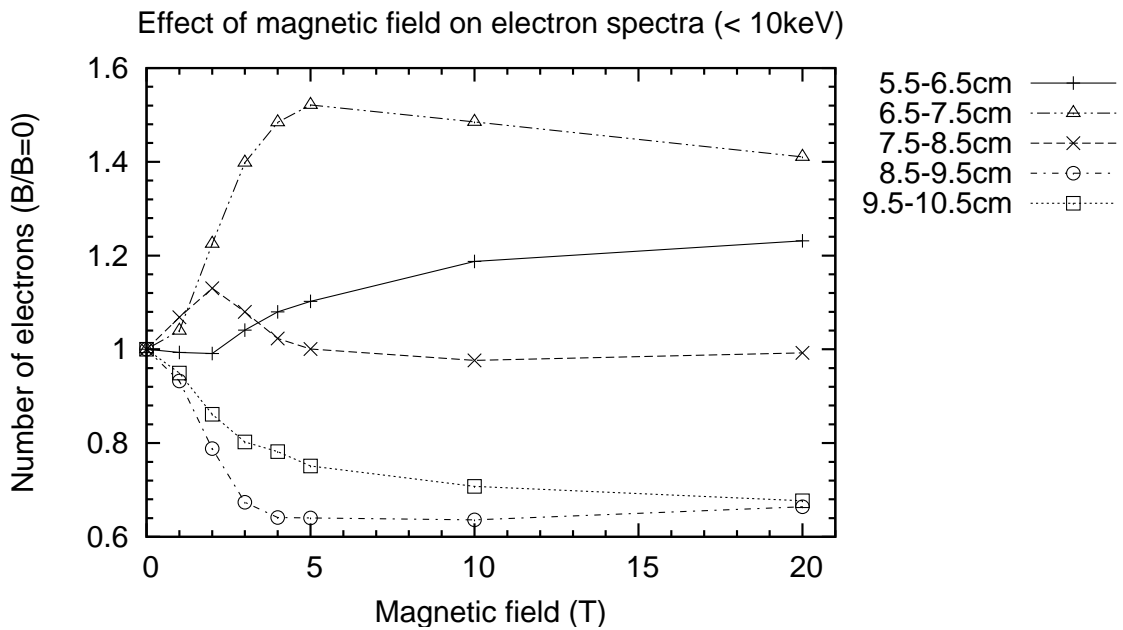


Figure 4.8: Ratio of electron spectra (below 10 keV) for a 15 MV beam as a function of magnetic field. A ratio of the electron population in five depth regions in the presence and absence of a 1, 2, 3, 4, 5, 10, and 20 T transverse magnetic field (7 to 9 cm depth).

can influence their spatial distribution. This occurs when the photon is a descendant of an electron whose range is comparable to or greater than its cyclotron radius, leading to an alteration in its depth of interaction, and hence that of the secondary photon. Simulations were therefore performed to obtain the secondary photon spectra (below 10 keV) for a 15 MV beam in the presence and absence of magnetic field. Figures 4.9 (a) and (b) show the resulting photon spectra with and without a 5 T transverse magnetic field, respectively. Common to both spectra is a peak at 550 eV (centre of 100 eV bin) which has a higher intensity in the regions before and entering the magnetic field (5.5 to 6.5 cm and 6.5 to 7.5 cm) and a lower intensity in the regions exiting and beyond the field (8.5 to 9.5 cm and 9.5 to 10.5 cm). On either side of the peak, the comparatively smaller populations and insufficient statistics render it difficult to ascertain any influence of the magnetic field.

#### 4.3.3 Influence of a magnetic field on electron spectra below 1 keV

The unresolved peaks between 450 and 550 eV in the electron spectra of figure 4.6 led to additional simulations of electron spectra (below 1 keV) using a finer bin resolution of 10 eV as opposed to 100 eV. Figures 4.10 (a) and (b) show the electron spectra (below 1 keV) for a 15 MV beam in the presence and absence of a slice of 5 T transverse magnetic field (7 to 9 cm depth), respectively. The corresponding ratio of electron population with and without magnetic field is shown in figures 4.11 (a), (b), (c), and (d) for 2, 5, 10, and 20 T magnetic fields, respectively.

The 550 eV peak in the photon spectra (below 10 keV) and appearance of several peaks between 475 and 685 eV in the electron spectra (below 1 keV) prompted further simulations to establish their identity and origin. As the K shell binding energy of oxygen (543.1 eV) is within this range, the simulations targeted electrons and photons produced from atomic relaxation events in water (i.e. hydrogen and oxygen atoms). Figures 4.12 (a) and (b) show the resulting spectra of atomic relaxation electrons in the presence and absence of a 5 T magnetic field, respectively. A plot of atomic relaxation photons is shown in figure 4.12 (c).

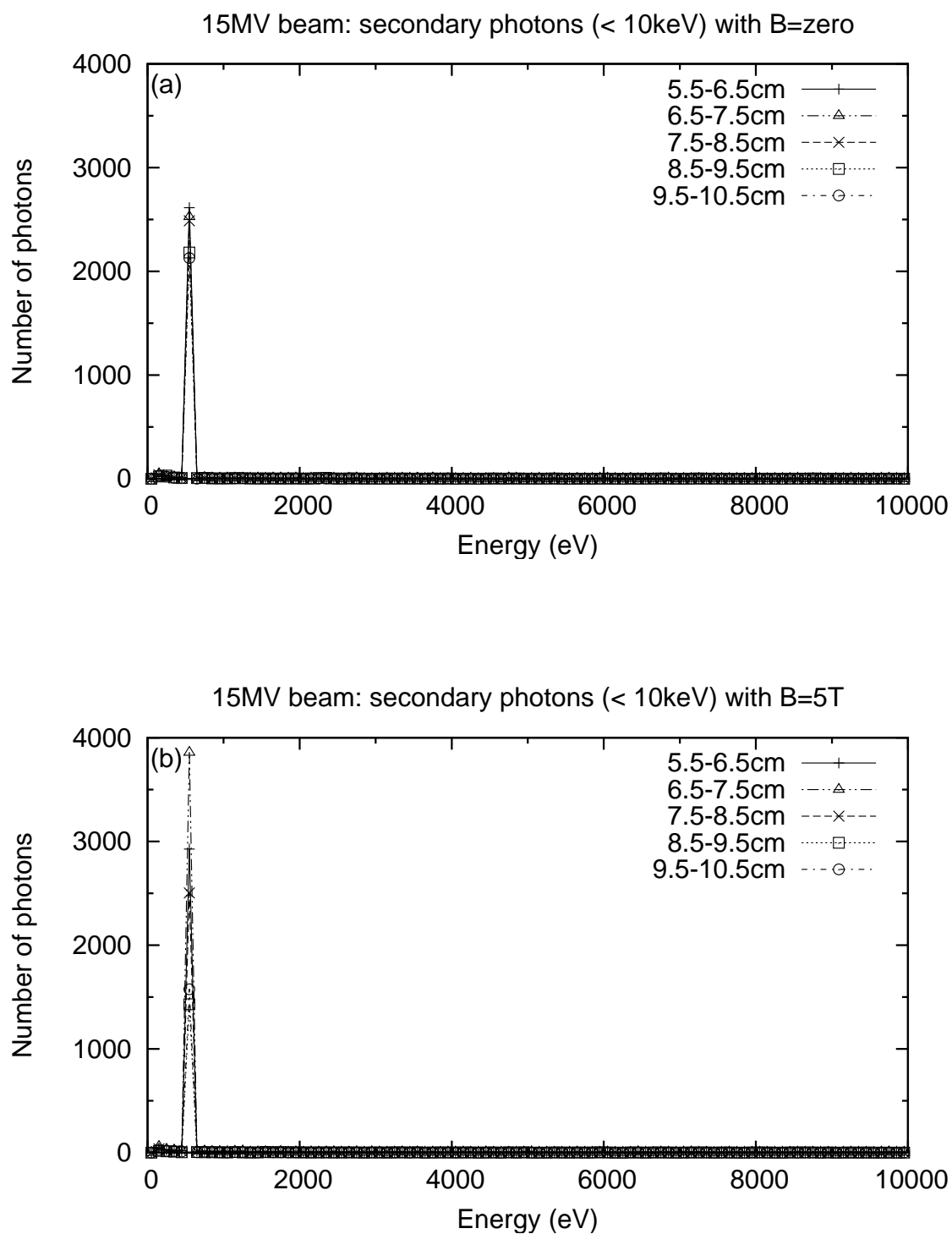


Figure 4.9: Photon spectra (below 10 keV) for a 15 MV beam. Figures (a) and (b) plot the photon spectra with and without a 5 T transverse magnetic field (7 to 9 cm depth), respectively.

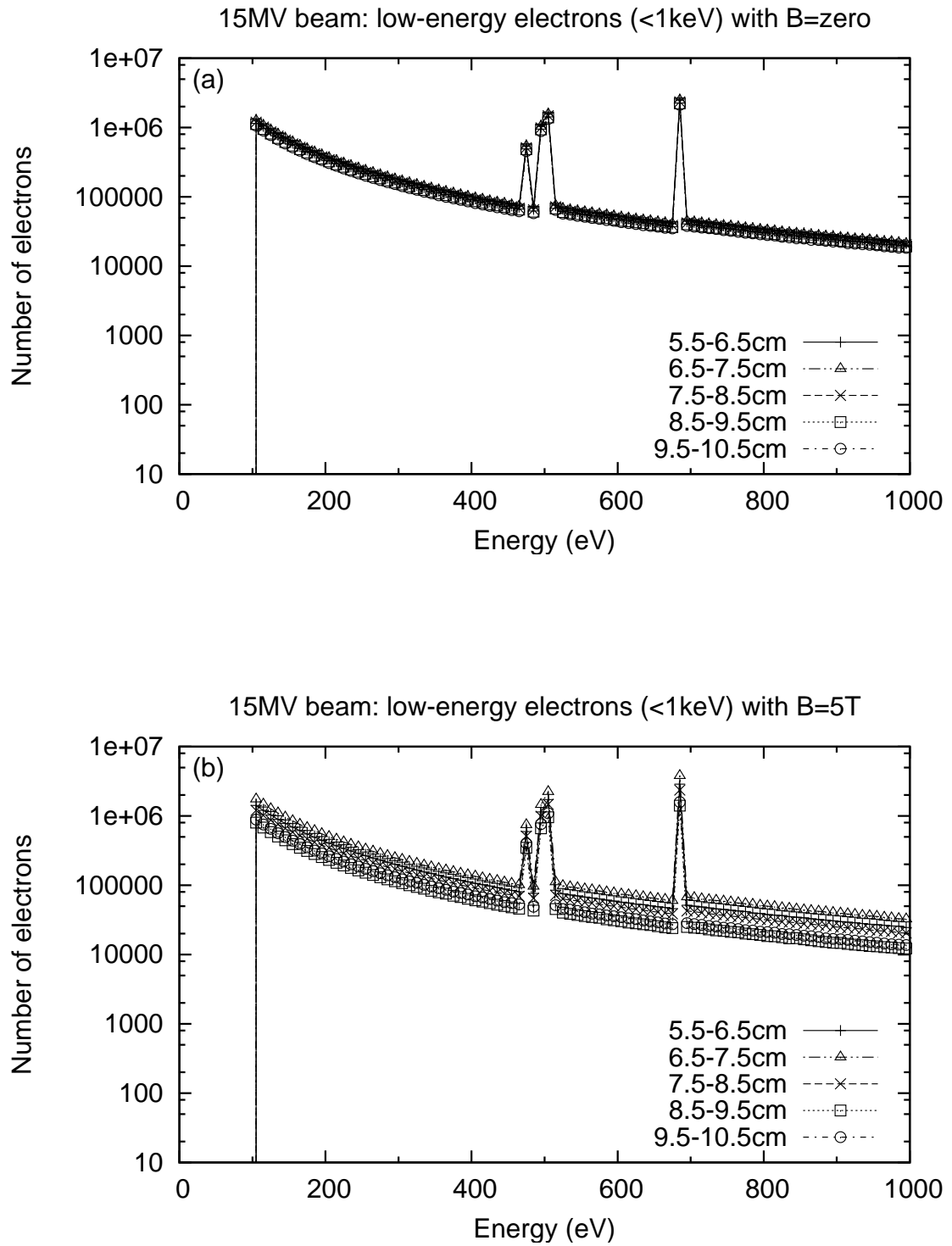


Figure 4.10: Electron spectra (below 1 keV) for a 15 MV beam. Figures (a) and (b) plot the electron spectra with and without a 5 T transverse magnetic field (7 to 9 cm depth), respectively.

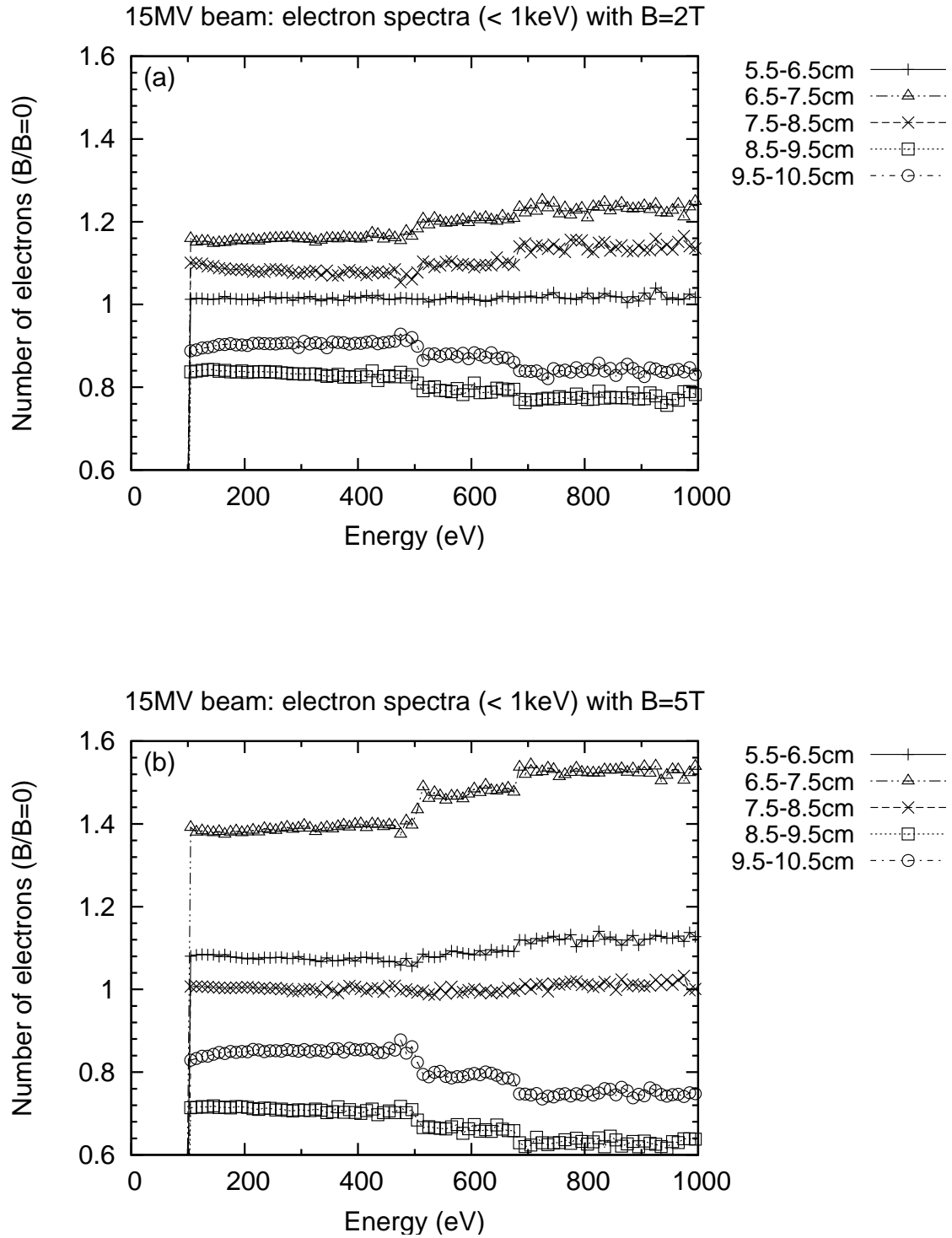


Figure 4.11: Normalised electron spectra (below 1 keV) for a 15 MV beam. Figures (a) and (b) plot a ratio of the electron population in the presence and absence of a 2 and 5 T transverse magnetic field (7 to 9 cm depth), respectively.

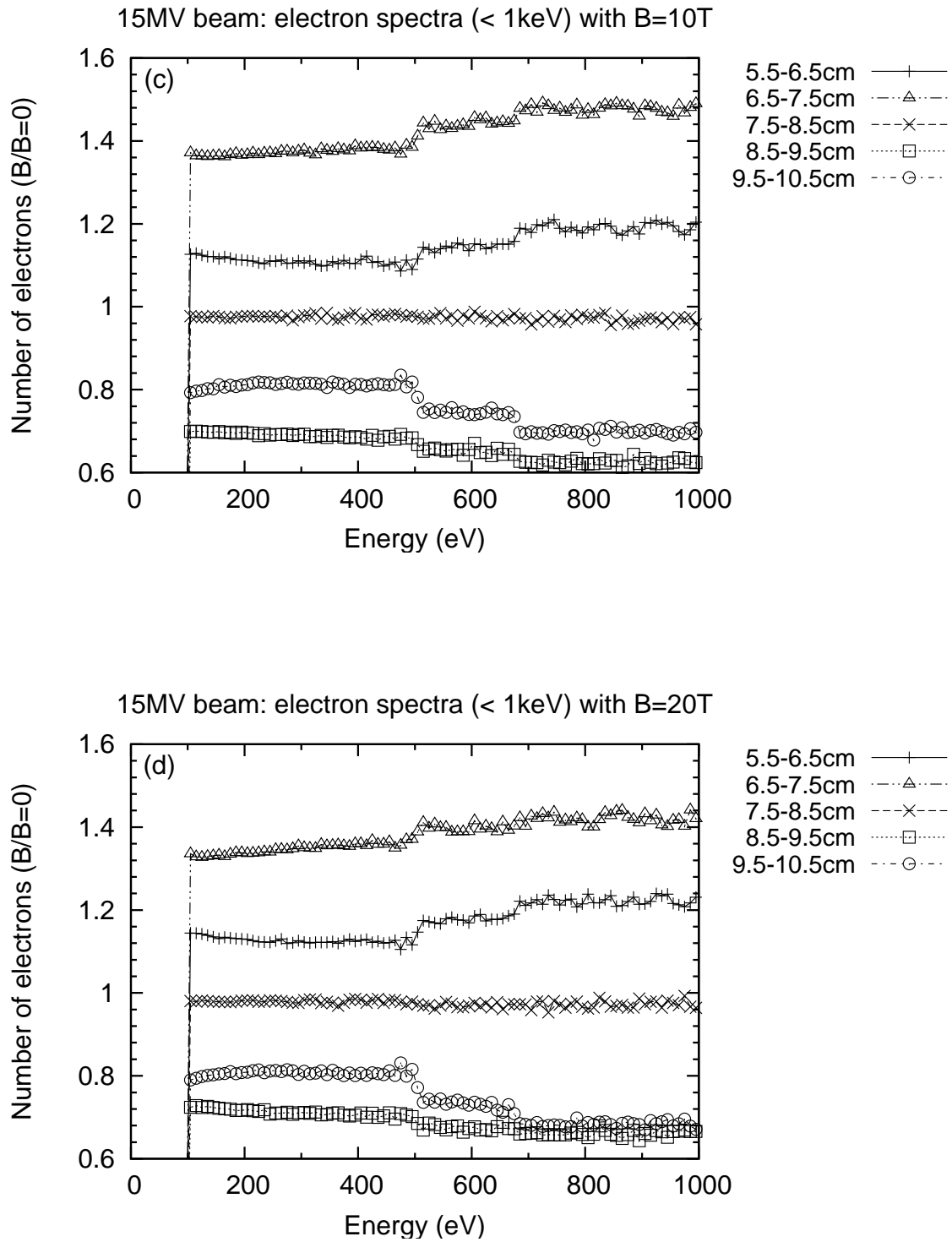


Figure 4.11: Normalised electron spectra (below 1 keV) for a 15 MV beam. Figures (c) and (d) plot a ratio of the electron population in the presence and absence of a 10 and 20 T transverse magnetic field (7 to 9 cm depth), respectively.

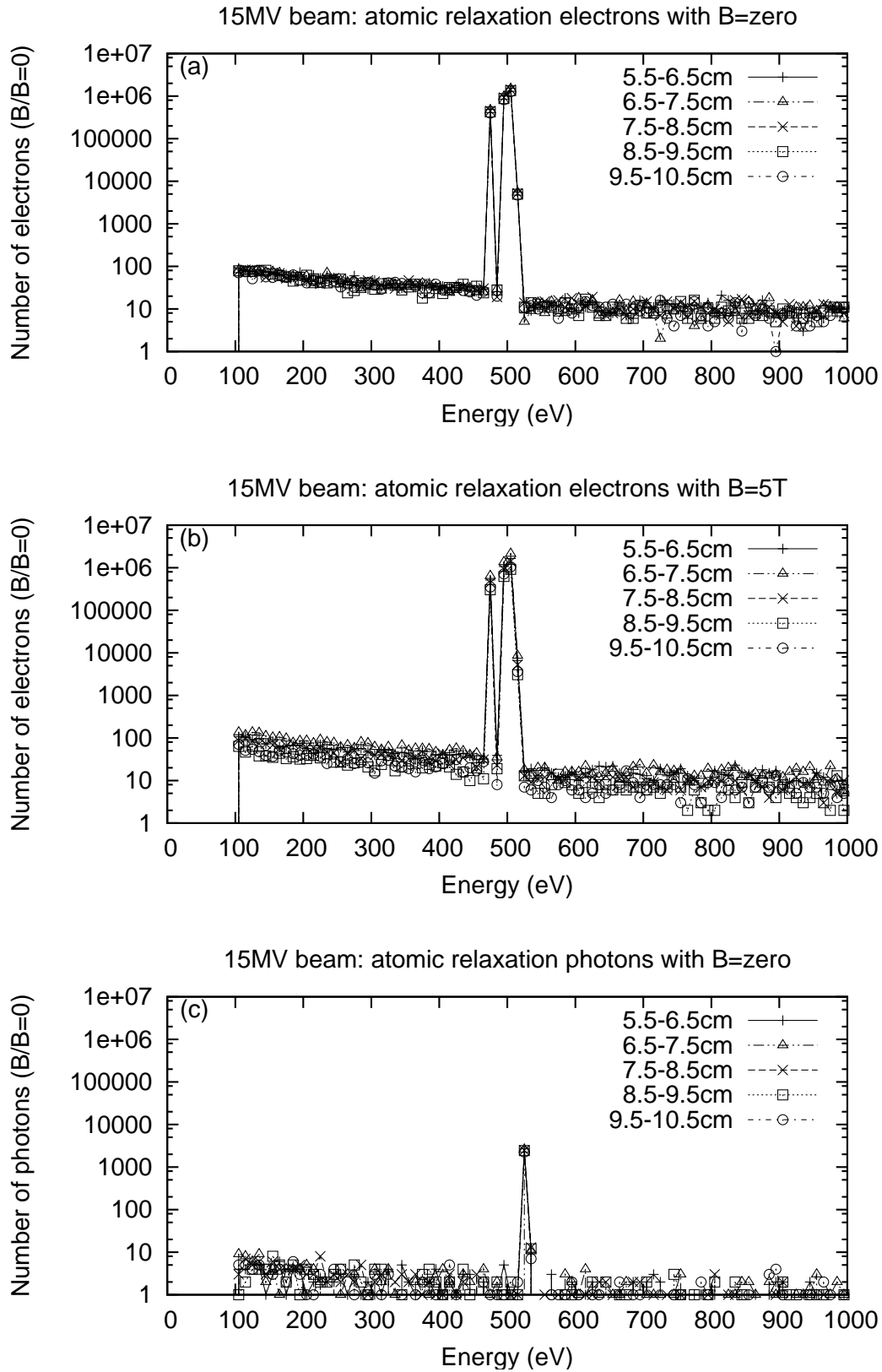


Figure 4.12: Spectra of atomic relaxation electrons and photons (in water) for a 15 MV beam. Figures (a) and (b) plot the spectra of atomic relaxation electrons with and without a 5 T transverse magnetic field (7 to 9 cm depth), respectively. Atomic relaxation photons are plotted in figure (c).

Common to both the electron and atomic relaxation electron spectra are peaks at 475 eV and between 495 and 505 eV, whose origin is thus from atomic relaxation in oxygen. The PENELOPE binding energies for the K, L<sub>1</sub>, L<sub>2</sub>, and L<sub>3</sub> shells of oxygen are 543, 24, 14, and 14 eV, respectively [38], where the transition probabilities and energies of Auger electron production (in water) are given in table 4.2.

Table 4.2: Energies and probabilities of Auger electron production in water [38].

Auger e-	Energy (eV)	Probability
KL1L1	4.788E+02	1.786E-01
KL1L2	4.938E+02	1.162E-01
KL1L3	4.939E+02	2.304E-01
KL2L2	5.089E+02	1.108E-02
KL2L3	5.089E+02	2.911E-01
KL3L3	5.090E+02	1.668E-01

The spectral peaks at 475, 495, and 505 eV in the secondary electron spectra therefore result from Auger electron emission. The peak at 475 eV is produced from KL1L1 Auger electrons, while the broad peak around 500 eV arises from the emission of Auger electrons following atomic relaxations to the K shell from the L<sub>3</sub> and L<sub>2</sub> shells. The prominent peak at 685 eV, however, is not the result of Auger electron emission but an artefact of the Sternheimer-Liljequist model used to simulate soft inelastic collisions (refer to subsection 3.2.5.4 of the 2006 PENELOPE manual [79]).

The single peak at 525 eV, which features in both the low-energy photon and atomic relaxation photon spectra, corresponds with the K<sub>α</sub> characteristic X-ray emission from the excitation and relaxation of electrons within the atomic shells of oxygen. It occurs when an incident photon transfers sufficient energy to a K shell electron (in oxygen) to excite it into an outer, less-tightly bound shell, leaving a vacancy in the K shell. When this vacancy is filled by an electron dropping from either the L<sub>2</sub> or L<sub>3</sub> shell, a 529 eV photon is emitted (i.e. the difference between their binding energies).



#### 4.3.4 Effect of magnetic field on the $w$ -values of electrons

The effect of a transverse magnetic field on electron trajectories is greatest for those moving perpendicular to the magnetic field and least for those travelling parallel to it. This observation prompted a series of simulations to gather information about the angles through which electron paths deviate from their initial direction (in water) in the absence of a magnetic field. These simulations focused on the distribution of  $w$ -values since it is this component of the electron's path which is parallel with the incident beam ( $z$ -axis) and perpendicular to the magnetic field ( $x$ -axis). A  $w$ -value of zero describes an electron travelling perpendicular to the field, while a  $w$ -value of unity describes an electron moving parallel to it.

Figures 4.13 (a) and (b) plot the mean  $w$ -values of first generation electrons as a function of energy for  $\text{Co}^{60}$ , 6, 10, and 15 MV and 0.05, 0.10, 0.50, 1, 2, 5, 10, and 15 MeV photon beams, respectively. As shown in figure 2.2, the higher the energy of the Compton scattered photon the smaller its angle of deviation from its initial direction ( $w = 1$ ), and the larger the angular deviation of the Compton electron (refer to figure 2.3).

The mean  $w$ -values of first generation electrons for monoenergetic and polyenergetic photon beams are shown in figure 4.13. Generally, for a given energy photon beam, the higher the electron energy the less it is deviated from the beam direction ( $w = 1$ ), except first generation electrons of 0.1, 0.5, and 1 MeV beams, which exhibit a rapid drop in  $w$ -value at about 0.028, 0.33, and 0.8 MeV respectively. The maximum  $w$ -value corresponds to the maximum kinetic energy that can be transferred to a free electron from a Compton scattered photon. This occurs when the photon is scattered 180 degrees, where the electron moves in the forward direction in order to conserve momentum. Beyond the drop-off, the  $w$ -value increases with increasing energy, reaching a final value of about 0.5, 0.8, and 0.9 for 0.1, 0.5, and 1 MeV photon beams respectively. The final  $w$ -value results from photoelectric interactions where the incident photon loses all of its energy in ejecting an orbital electron within the absorber atom. The kinetic energy given to this electron is the surplus from that required to free the electron (i.e. minus the binding energy).

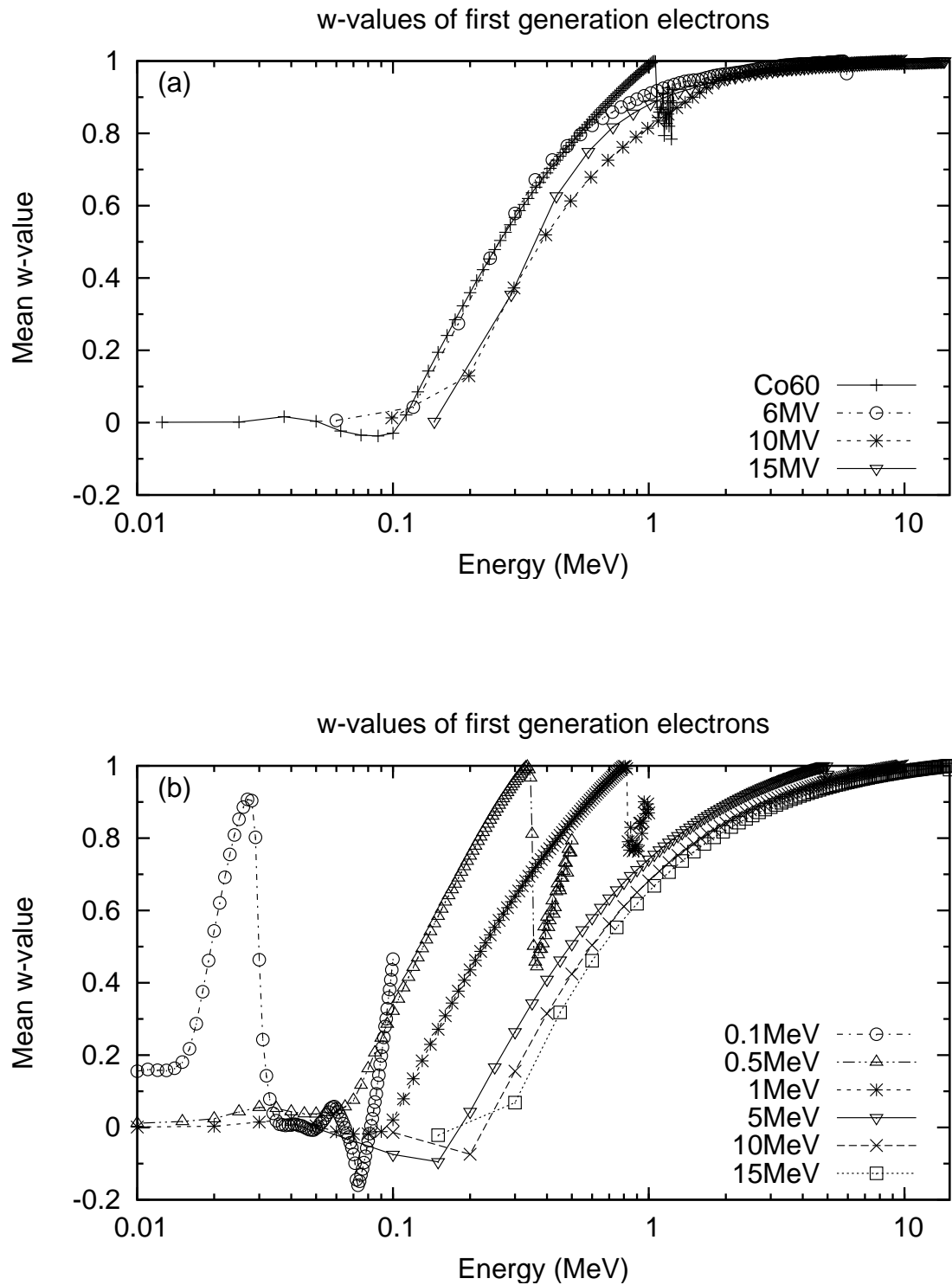


Figure 4.13: Mean  $w$ -values of first generation electrons for the following photon beams: (a)  $\text{Co}^{60}$ , 6, 10, and 15 MV, and (b) 0.1, 0.5, 1, 5, 10, and 15 MeV.

Electrons moving parallel to a magnetic field are unaffected by its presence. Simulations were therefore performed to determine the mean distance that an electron travels (in the absence of a magnetic field) before its initial direction ( $u, v, w = 0, 0, 1$ ) is altered by 90 degrees. Figure 4.14 plots the mean distance travelled (in water) by 0.1, 0.5, 1, 5, 10, and 15 MeV electrons before their initial trajectory is deviated by a given angle. Figures 4.15 (a), (b), (c), (d), (e), and (f) show the populations of 0.1, 0.5, 1, 5, 10, and 15 MeV electrons as functions of the mean distance travelled before their paths are deviated by more than 25.8, 45.6, 60, and 90 degrees (i.e.  $w = 0.9, 0.7, 0.5$ , and zero), respectively.

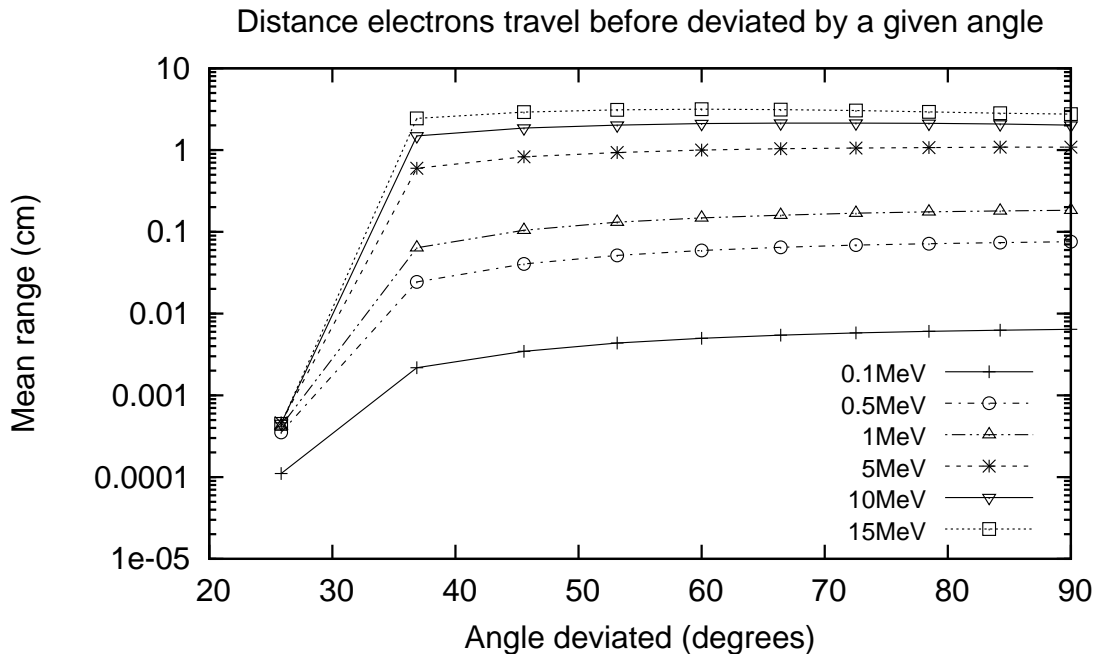


Figure 4.14: Distance travelled by electrons before they are deviated from their initial trajectory by a given angle.

Simulations were also performed to determine the mean  $w$ -values of first generation electrons beyond a depth of 6.9 cm in the water phantom. Figure 4.16 plots the population and mean  $w$ -values as a function of energy for first generation electrons of a 15 MV beam beyond 6.9 cm depth. This spectrum is almost identical to that obtained within the entire water phantom in figure 4.13 (a). The main difference between the current spectrum

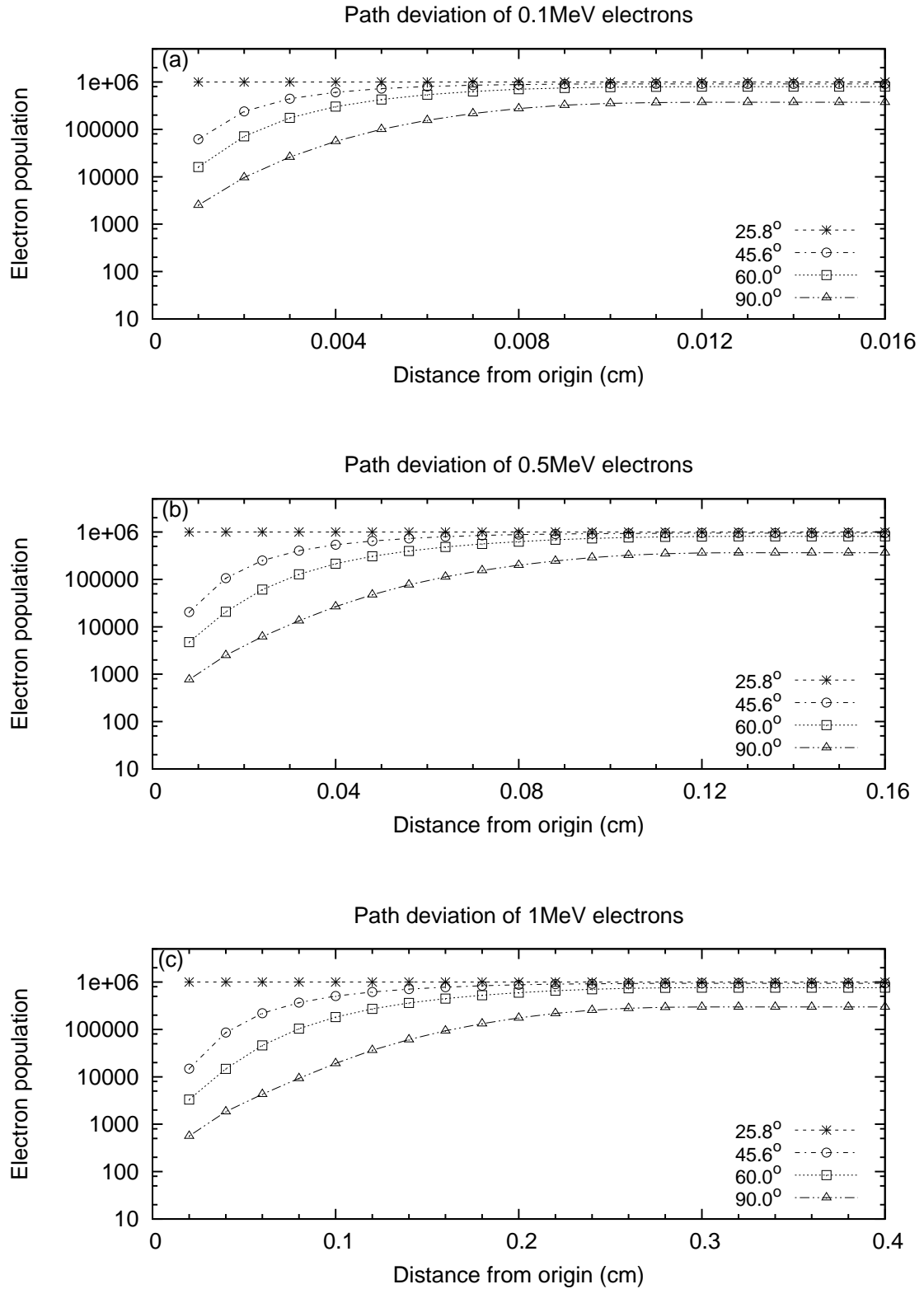


Figure 4.15: Distance electrons travel in water before the angle of deviation from their initial trajectory exceeds 25.8, 45.6, 60, and 90 degrees (i.e.  $w = 0.9, 0.7, 0.5$ , and zero). A plot of the accumulative electron population as a function of distance travelled from the origin is shown in figures (a), (b), and (c) for 0.1, 0.5, and 1 MeV electrons, respectively.

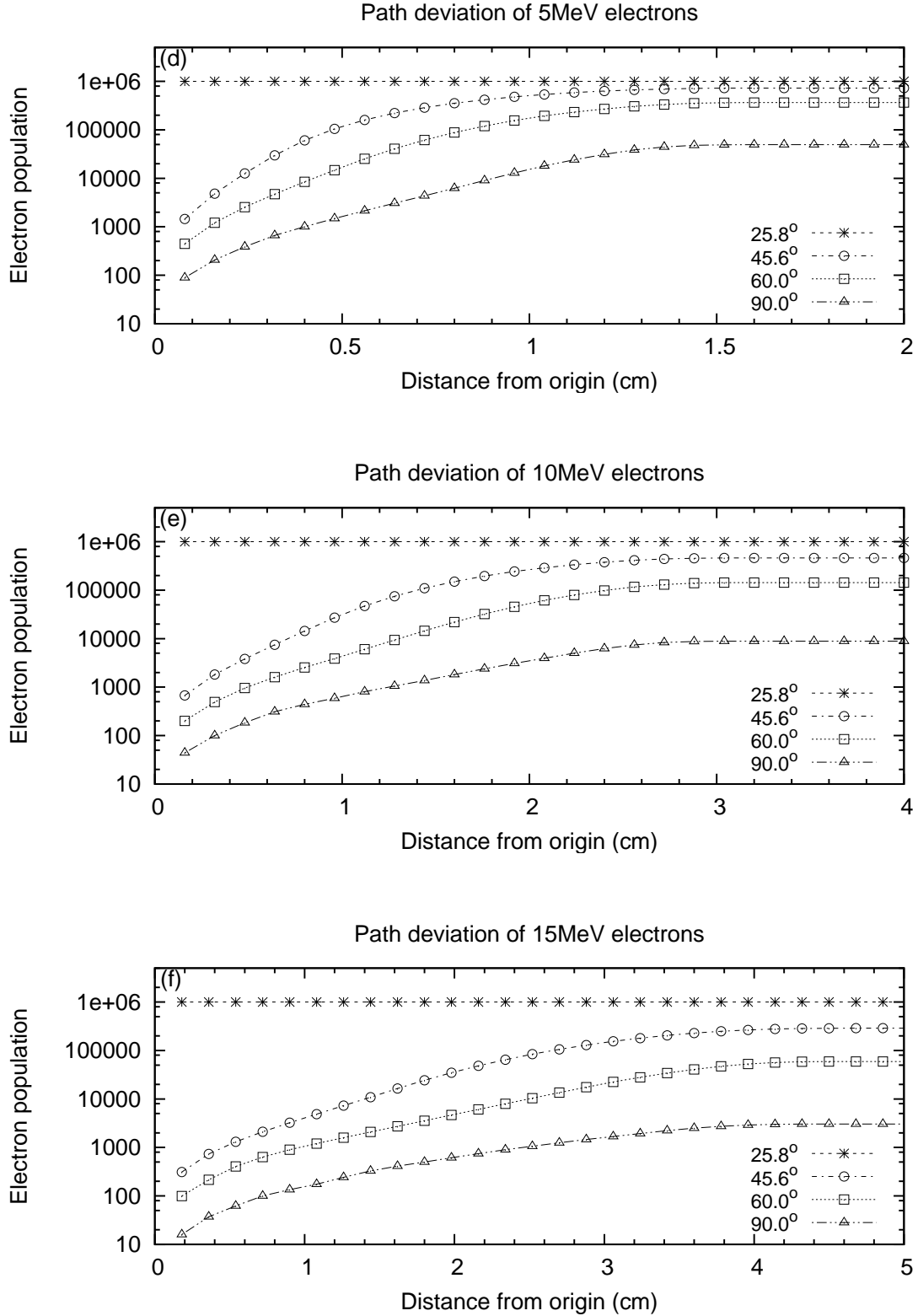


Figure 4.15: Distance electrons travel in water before the angle of deviation from their initial trajectory exceeds 25.8, 45.6, 60, and 90 degrees (i.e.  $w = 0.9, 0.7, 0.5$ , and zero). A plot of the accumulative electron population as a function of distance travelled from the origin is shown in figures (d), (e), and (f) for 5, 10, and 15 MeV electrons, respectively.

and the former is the inclusion of the  $w$ -values between 0.1 and 0.01 MeV. According to figure 4.16, about 50% electrons have an energy less than 0.15 MeV and  $w$ -values less than 0.25 (i.e. less than 76 degrees deviation from the  $z$ -axis). The figure also shows that about 30% of electrons have a  $w$ -value greater than 0.707 (i.e. deviated less than 45 degrees), indicating that the dominant component of their range is along the  $z$ -axis.

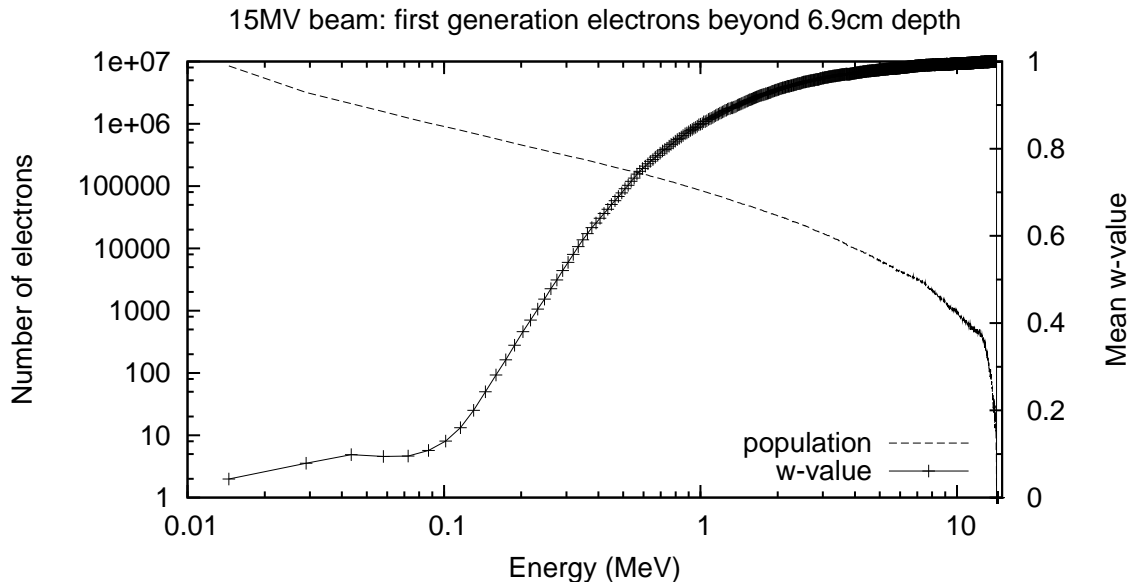


Figure 4.16: Population and mean  $w$ -values of first generation electrons for 15 MV beam beyond 6.9 cm depth (in water).

According to the secondary electron spectra for a 15 MV beam (figure 4.4), about 40% of secondary electrons have an energy of 1 MeV or higher. As shown in figure 4.16, this corresponds to a  $w$ -value greater than 0.8 (beyond 6.9 cm depth), where most of these electrons maintain a  $w$ -value above 0.7 over their range (refer to figure 4.15). Lower energy electrons, on the other hand, exhibit substantial alterations in their direction, particularly near the end of their range. Most of these electrons have a  $w$ -value below 0.7, which equates to a deviation of more than 45 degrees from their initial direction. It is therefore a combination of larger ranges and  $w$ -values that renders the paths of higher energy electrons more susceptible to alteration by the magnetic field.

#### 4.3.5 Effect of magnetic field on the spatial distribution of electrons

For the path of an electron to be affected by a magnetic field, its cyclotron radius must be comparable to or smaller than its range. For the case of a transverse magnetic field applied along the  $x$ -axis, electrons moving perpendicular to the field along the  $y$  or  $z$  axes will experience the largest deviation, while those moving parallel to the field will be unperturbed. When an electron has a  $w$ -value greater than 0.7 (i.e. deviated less than 45 degrees), the dominant component of its range is along the  $z$ -axis (i.e. depth direction). According to the secondary electron spectra for a 15 MV photon beam (figure 4.4), this occurs at electron energies of 0.5 MeV or higher. Considering the range of these electrons is comparable to or larger than their cyclotron radii at most magnetic field strengths, their trajectories and depths of interaction will be affected, and so will the spatial distribution of any secondary particles they produce.

A detailed examination of how the range and spatial distribution of electrons is affected by the presence of a transverse magnetic field (7 to 9 cm depth) is shown in figures 4.17 to 4.20, where electrons are tracked from five different starting depths within the vicinity of a magnetic field: 6.9, 7.5, 8.5, 8.9, and 9.1 cm. The study was performed with monoenergetic electron beams of 0.01, 0.05, 0.1, 0.5, 1, 5, 10, and 15 MeV subjected to magnetic fields of 1, 1.5, 2, 3, 5, 10, 20, 30, 40, 50, 75, and 100 T, where the mean  $y$ -range,  $z$ -range, and spatial distribution of these electrons as a function of magnetic field strength was investigated for each of the five starting depths.

Figure 4.17 shows the mean range and spatial distribution of monoenergetic electrons starting at 6.9 cm depth (immediately before the slice of magnetic field). The depth of interaction of electrons subjected to different magnetic fields is shown in figure 4.17 (a). In the absence of magnetic field, the mean  $z$ -ranges of 1, 5, 10, and 15 MeV electrons were determined to be 0.2, 1.1, 2.4, and 3.6 cm respectively. For 5, 10, and 15 MeV electrons, the mean  $z$ -range can be seen to decrease to a minimum between 3 and 5 T before recovering to almost its initial value by 100 T. A reduction in mean  $z$ -range with increasing magnetic field is also apparent with 1 MeV electrons, although,

unlike higher energy electrons it does not recover at stronger magnetic fields. The mean depth of interaction of electrons below 1 MeV appears unaltered. Similar trends are exhibited by the ratios of mean  $z$ -range with and without a magnetic field in figure 4.17 (b), where a minimum ratio can be seen between 3 and 5 T for 5, 10, and 15 MeV electrons. The plot also reveals a decrease in the ratio with increasing magnetic field for 0.5 and 1 MeV electrons, and ratios of unity are observed for electrons below 0.5 MeV.

Figure 4.17 (c) shows the influence of a transverse magnetic field on the depth of interaction of electrons starting at 6.9 cm depth by plotting a ratio of electrons with a final position downstream of their starting position ( $z > z_{start}$ ) to those with a final position upstream of the start ( $z < z_{start}$ ). For electrons with an energy below 1 MeV, the ratios are constant and greater than unity. At higher electron energies, on the other hand, the ratio decreases with increasing magnetic field and drops below unity between about 5 and 10 T for 5, 10, and 15 MeV electrons.

As shown in figure 4.17, an electron's depth of interaction is altered by the magnetic field when its range becomes comparable to or larger than its cyclotron radius. According to figure 3.1, this occurs at magnetic fields of approximately 2, 10, 20, and 100 T for 0.5, 0.1, 0.05, and 0.01 MeV electrons respectively. At magnetic fields between 1 and 100 T, electrons with an energy of 1 MeV or higher exhibit variations in their mean  $z$ -range as their total range becomes comparable to or larger than their cyclotron radii. Lower energy electrons, on the other hand, exhibit only minor changes in their mean  $z$ -range at these magnetic fields as stronger fields are required to sufficiently reduce their radii to values less than or comparable with their ranges.

When electrons start at 6.9 cm depth, only those with a  $z$ -range greater than 0.1 cm will reach the magnetic field (between 7 and 9 cm depth). Since 1 MeV electrons have a mean  $z$ -range of 0.2 cm, those entering the magnetic field will become trapped unless their radii of curvature is sufficiently smaller than their range to allow escape (1 MeV electrons subjected to a 5 T field have a 0.1 cm radius). The electrons that do escape (via the upstream boundary) have insufficient range to return to their starting depth, which



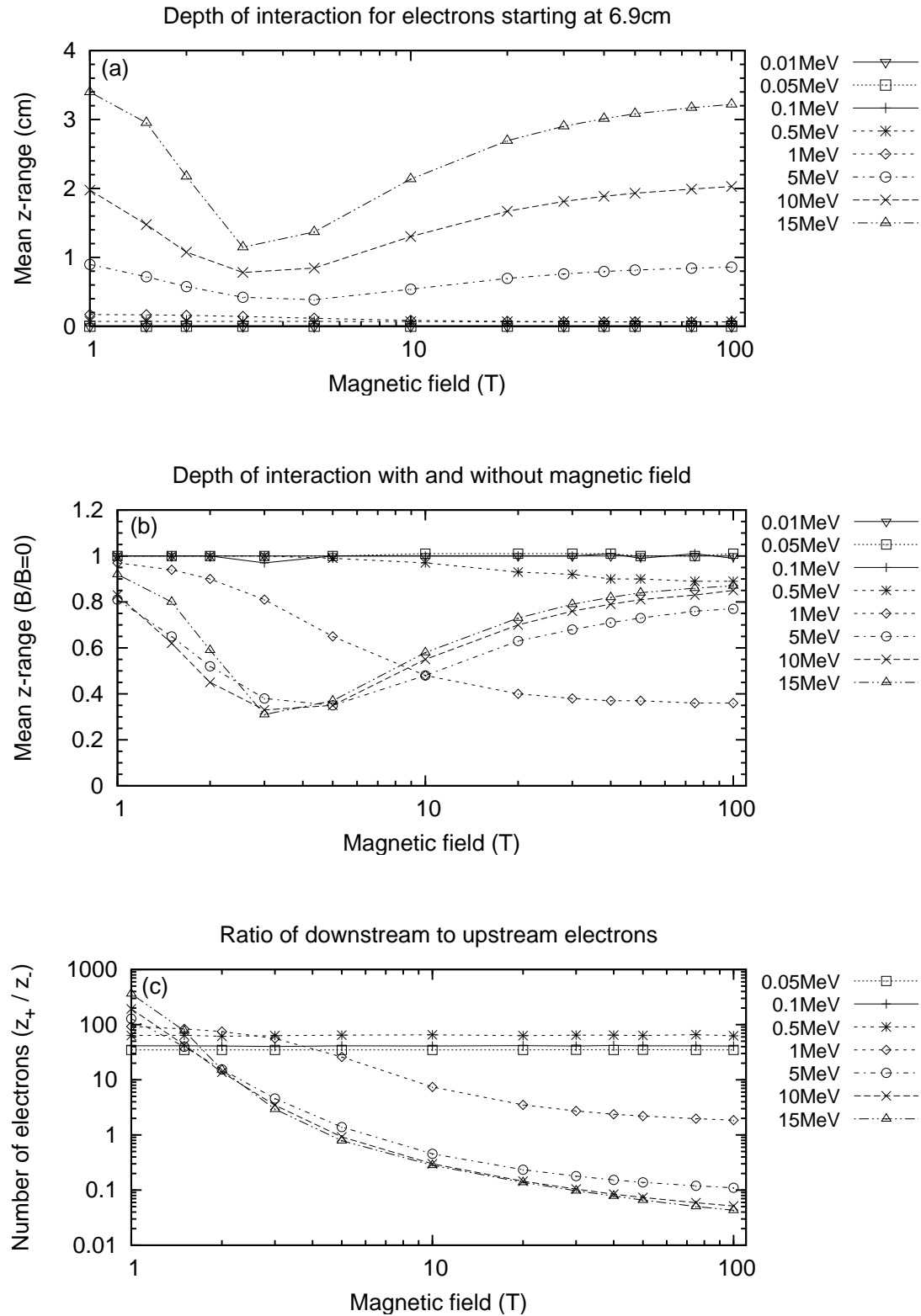


Figure 4.17: Magnetic field's influence on the interaction depths of electrons starting at 6.9 cm depth. Figure (a) plots the electrons' mean  $z$ -ranges as a function of magnetic field. A ratio of the mean  $z$ -ranges with and without magnetic field is shown in figure (b), and a ratio of electrons with final positions downstream of their initial position ( $z > z_{start}$ ) to those with final positions upstream ( $z < z_{start}$ ) is plotted in figure (c).

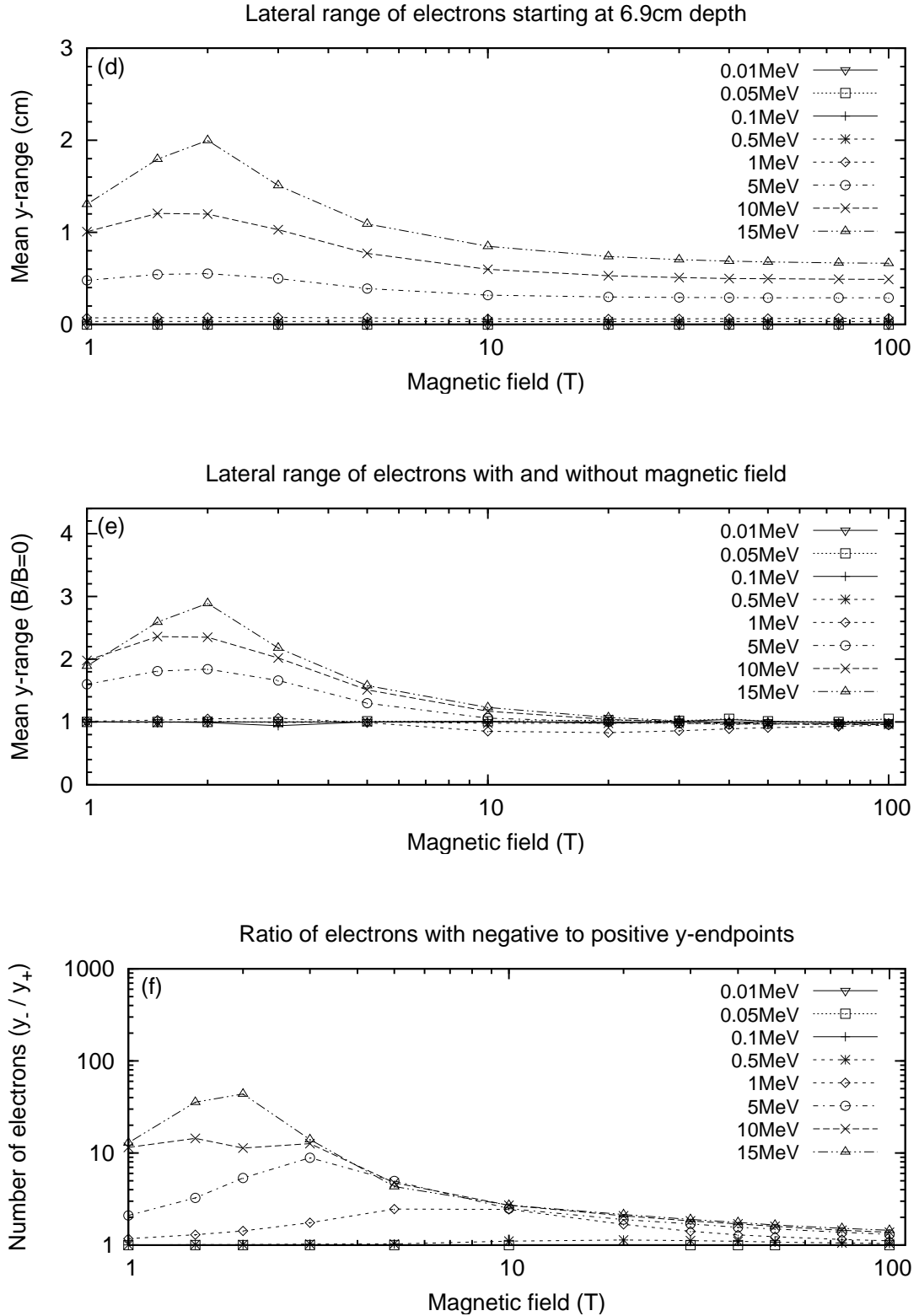


Figure 4.17: Magnetic field's influence on the lateral ranges of electrons starting at 6.9 cm depth. Figure (d) plots the mean y-ranges of electrons as a function of magnetic field. A ratio of the mean y-ranges with and without magnetic field is shown in figure (e), and a ratio of electrons with negative final y-positions ( $y < 0$ ) to those with positive final y-positions ( $y > 0$ ) is plotted in figure (f).

results in smaller mean  $z$ -ranges with increasing magnetic fields.

Electrons with an energy of 5 MeV or higher reveal an initial reduction in mean  $z$ -range up until about 5 T, at which a minimum  $z$ -range is observed. This is attributed to the range of these electrons being sufficiently larger than their radii as to enable their trajectories to be bent upstream by the magnetic field. These electrons therefore have an increased probability of escaping the magnetic field (via the 7 cm boundary), leading to shallower depths of interaction. The magnetic field at which the minimum mean  $z$ -range occurs (between 3 and 5 T) is also where the ratio of upstream to downstream electrons drops below unity, which suggests that electrons are depositing their energy in close proximity to their initial position ( $z_{start}$ ). When these electrons are subjected to stronger magnetic fields, their smaller radii enable them to escape the field region sooner, resulting in energy depositions further upstream. This upstream migration of electrons gives rise to the increase in mean  $z$ -range (beyond the minimum) with increasing magnetic field.

The lateral range of electrons is also affected by the presence of a transverse magnetic field. As shown in figure 4.17 (d), electrons with an energy of 5, 10, and 15 MeV exhibit an increase in mean  $y$ -range with magnetic fields up to 20 T, where the largest increase of as much as 200% occurs between 2 and 3 T. Beyond 20 T, the mean  $y$ -range is approximately constant. For electrons with an energy below 5 MeV, their mean  $y$ -range appears unaltered by the presence of a magnetic field. This is demonstrated by ratios of unity for the mean  $y$ -range of electrons (below 1 MeV) with and without magnetic field in figure 4.17 (e). However, the ratio for 1 MeV electrons does dip below unity (by as much as 20%) between a magnetic field of 5 and 75 T.

A ratio of the number of electrons with a negative  $y$ -endpoint ( $y < 0$  cm) to those with a positive  $y$ -endpoint ( $y > 0$  cm) is shown in figure 4.17 (f). For electrons with an energy below 0.5 MeV, ratios of unity are observed for all magnetic fields investigated. At greater electron energies of 1 MeV or higher, the ratio exceeds unity, reaching a maximum at 10 T for 1 MeV electrons, 3 T for 5 MeV electrons, and 2 T for 10 and 15 MeV electrons. The magnetic field at which the maximum mean  $y$ -range occurs is immediately

before that at which the minimum  $z$ -range occurs, which gives rise to sub-unity ratios of downstream to upstream electrons. The maximum lateral range of electrons corresponds to their mean  $y$ -range prior to exiting the magnetic field region (via the 7 cm boundary). Beyond the maximum, the ratio continues to decrease with increasing magnetic field, where it remains above unity as electrons become trapped and thus confined within the field region.

Figure 4.18 shows the mean range and spatial distribution of monoenergetic electrons starting at 7.5 cm depth inside the magnetic field. As shown in figure 4.18 (a) and (b), an increase in magnetic field produces a decrease of as much as 95% in the mean depth of interaction (i.e.  $z$ -range) of electrons. Generally, the decrease in mean  $z$ -range is greater for higher energy electrons except at field strengths below 10 T where the ratios for 10 and 15 MeV electrons are larger than those exhibited by less energetic electrons. Electrons with energies of 0.1, 0.05, and 0.01 MeV exhibit ratios of approximately unity at magnetic fields up to 10, 20, and 75 T respectively.

Figure 4.18 (c) plots a ratio of the electron population with a final position downstream of the start ( $z > z_{start}$ ) to that with a final position upstream of the start ( $z < z_{start}$ ). The plot reveals ratios greater than unity for all combinations of electron energy and magnetic field. Electrons with energies of 0.5 MeV or higher exhibit a decrease in ratio with increasing magnetic field, while 0.1, 0.05, and 0.01 MeV electrons exhibit a constant ratio at magnetic fields up to 5, 10, and 50 T respectively. Beyond these fields, the ratio can be seen to decrease towards a minimum at 100 T.

At a starting depth of 7.5 cm, electrons with an energy of 5 MeV or lower have insufficient  $z$ -range to escape the region of magnetic field via the 9 cm boundary. For more energetic electrons of 10 and 15 MeV, their larger ranges enables them to escape, although at stronger magnetic fields they too become trapped inside the field region. Ratios above unity for electrons with downstream to upstream final positions (relative to their start position,  $z_{start}$ ) suggest fewer electrons escape the magnetic field via the magnetic field boundary at 7 cm depth.

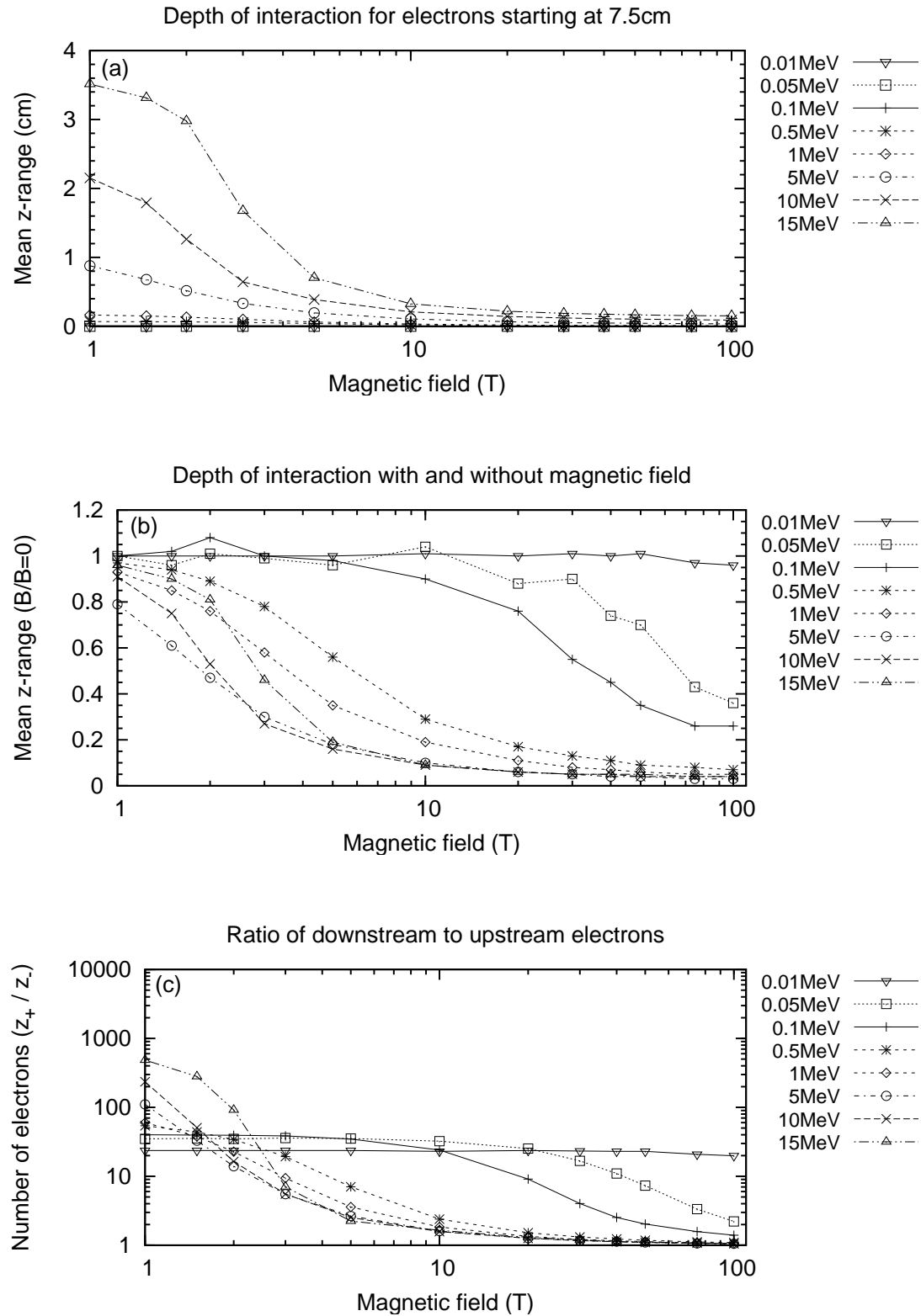


Figure 4.18: Magnetic field's influence on the interaction depths of electrons starting at 7.5 cm depth. Figure (a) plots the electrons' mean  $z$ -ranges as a function of magnetic field. A ratio of the mean  $z$ -ranges with and without magnetic field is shown in figure (b), and a ratio of electrons with final positions downstream of their initial position ( $z > z_{start}$ ) to those with final positions upstream ( $z < z_{start}$ ) is plotted in figure (c).

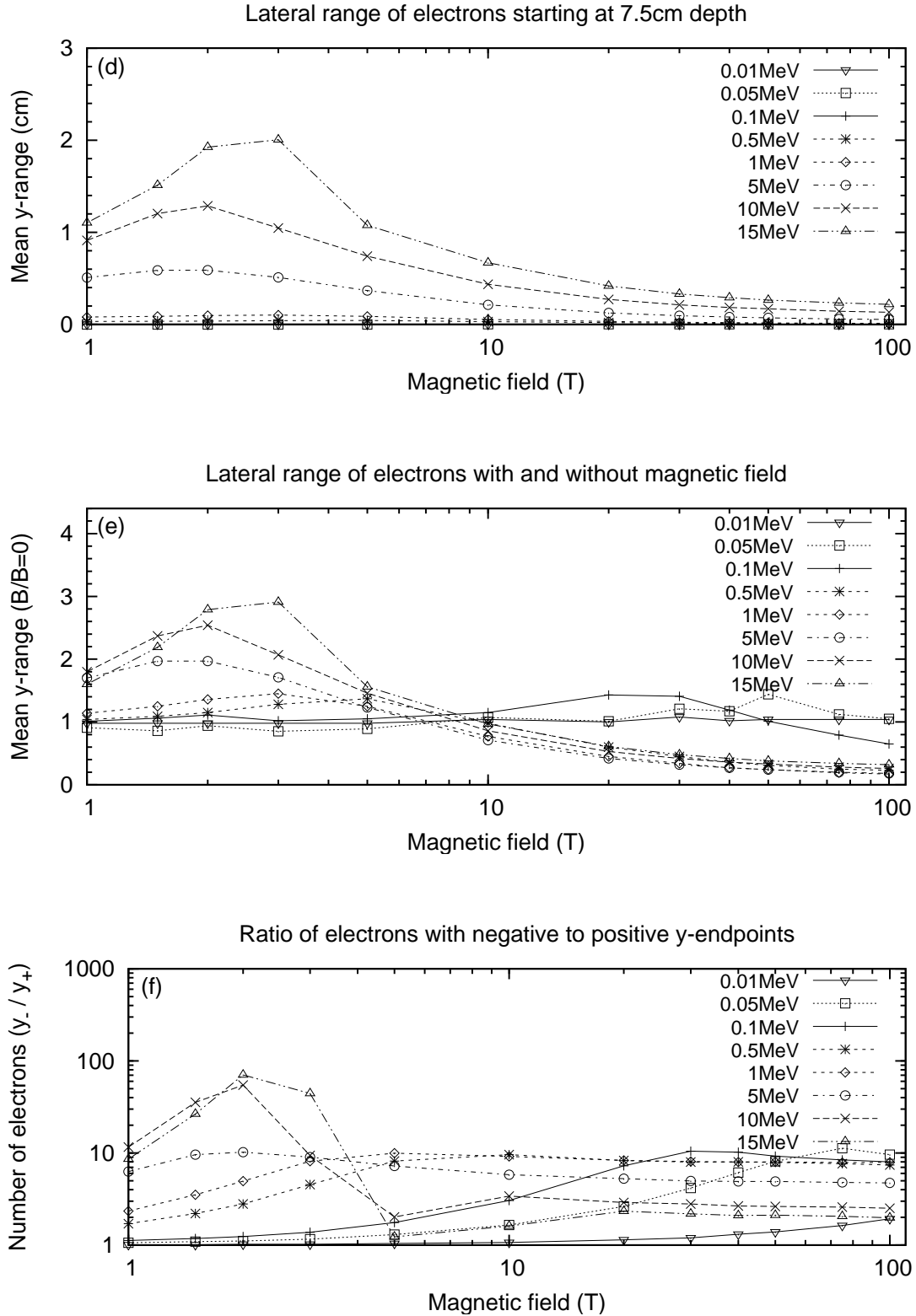


Figure 4.18: Magnetic field's influence on the lateral ranges of electrons starting at 7.5 cm depth. Figure (d) plots the mean y-ranges of electrons as a function of magnetic field. A ratio of the mean y-ranges with and without magnetic field is shown in figure (e), and a ratio of electrons with negative final y-positions ( $y < 0$ ) to those with positive final y-positions ( $y > 0$ ) is plotted in figure (f).

The magnitude of the electron's lateral range as a function of magnetic field is plotted in figure 4.18 (d). Electrons with an energy of 1 MeV or higher exhibit a maximum mean  $y$ -range between about 2 and 3 T. When subjected to stronger magnetic fields, the mean  $y$ -range steadily decreases to a minimum value at 100 T, where it is a factor of 10 lower than the maximum. A ratio of the mean  $y$ -range obtained with and without magnetic field is plotted in figure 4.18 (e). Electrons with an energy greater than 0.1 MeV, subjected to magnetic fields of up to 5 T, exhibit mean  $y$ -ranges larger than unity by as much as a factor of 2 (for 15 MeV electrons). Between 5 and 10 T, this ratio drops below unity where it steadily decreases towards 100 T. For 0.1 and 0.05 MeV electrons, the ratio rises above unity from 20 to 75 T and 5 to 50 T, respectively. The mean  $y$ -range of the 0.01 MeV electrons is unaffected by the presence of a magnetic field.

A ratio of electron population with a negative final  $y$ -position ( $y < 0$ ) to that with a positive final  $y$ -position ( $y > 0$ ) is plotted in figure 4.18 (f), where ratios greater than unity are observed at all electron energies. Generally, the magnetic field at which the maximum ratio occurs is stronger for lower energy electrons. For example, 15 MeV electrons reach a maximum ratio of about 70 at 3 T, while 0.01 MeV electrons exhibit a maximum ratio of around 2 at 100 T. Electrons with an energy of 5 and 10 MeV also exhibit a maximum ratio at 3 T, which is also the field at which their mean  $z$ -range becomes less than the 1.5 cm distance to the downstream field boundary (i.e. electrons become trapped within the magnetic field). Beyond the maximum, the electrons' mean  $y$ -ranges decrease with increasing magnetic field owing to their smaller cyclotron radii, and hence, confinement within the field.

Figure 4.19 shows the mean range and spatial distribution of monoenergetic electrons starting from 8.5 cm depth inside the region of magnetic field. A plot of the depth of interaction, or mean  $z$ -range, of electrons as a function of magnetic field is shown in figure 4.19 (a). A ratio of the electrons' mean  $z$ -ranges with and without the presence of a magnetic field are plotted in figure 4.19 (b). Electrons with an energy of 1 MeV or higher, subjected to magnetic fields less than 2 T, exhibit minor reductions in their mean

$z$ -range. At stronger magnetic fields, on the other hand, severe reductions in the mean  $z$ -ranges of as much as a factor of 3 are observed. This occurs at magnetic fields of about 2, 3, and 5 T for 5, 10 and 15 MeV electrons, respectively, and around 1 T for 0.5 and 1 MeV electrons. For lower energy electrons of 0.1, 0.05, and 0.01 MeV, a reduction in the ratio can be seen at 5, 10, and 50 T respectively.

Figure 4.19 (c) plots a ratio of the population of electrons with a final position downstream of the start ( $z > z_{start}$ ) to those with a final position upstream of the start ( $z < z_{start}$ ). With the exception of 5, 10, and 15 MeV electrons, these ratios are almost identical to those previously obtained with a start depth of 7.5 cm. The ratios of 5, 10, and 15 MeV electrons subjected to magnetic fields up to 20 T are substantially larger than those observed at 7.5 cm depth, while beyond 20 T they are comparable.

For electrons starting at 8.5 cm depth, the distance to the downstream magnetic field boundary is 0.5 cm. This enables electrons with a sufficient range (i.e. 5 MeV energy or higher) to escape the field region and deposit their energy further downstream. Lower energy electrons, on the other hand, remain trapped as they have insufficient  $z$ -range to escape. When higher energy electrons are subjected to strong magnetic fields, they too can become trapped within the field owing to their smaller cyclotron radii, particularly when their mean  $z$ -range becomes less than 0.5 cm. For 5, 10, and 15 MeV electrons, this occurs at about 3, 10, and 20 T respectively, as indicated by the steep drop-off in their mean  $z$ -ranges. For lower energy electrons, the drop-off occurs at stronger magnetic fields, where their ranges become comparable to their radii.

Figure 4.19 (d) shows the influence of a magnetic field on the mean lateral range, or  $y$ -range, of electrons. For 1 and 5 MeV electrons, a maximum mean  $y$ -range occurs at about 3 T, while 10 and 15 MeV electrons exhibit a maximum at 5 and 10 T respectively. At stronger magnetic fields, the mean  $y$ -range of these electrons is reduced by as much as a factor of 12. Figure 4.19 (e) plots a ratio of the mean  $y$ -range obtained with and without magnetic field. For 5, 10, and 15 MeV electrons, a maximum ratio is observed at about 3, 5, and 10 T respectively, which is immediately before the mean  $z$ -range becomes



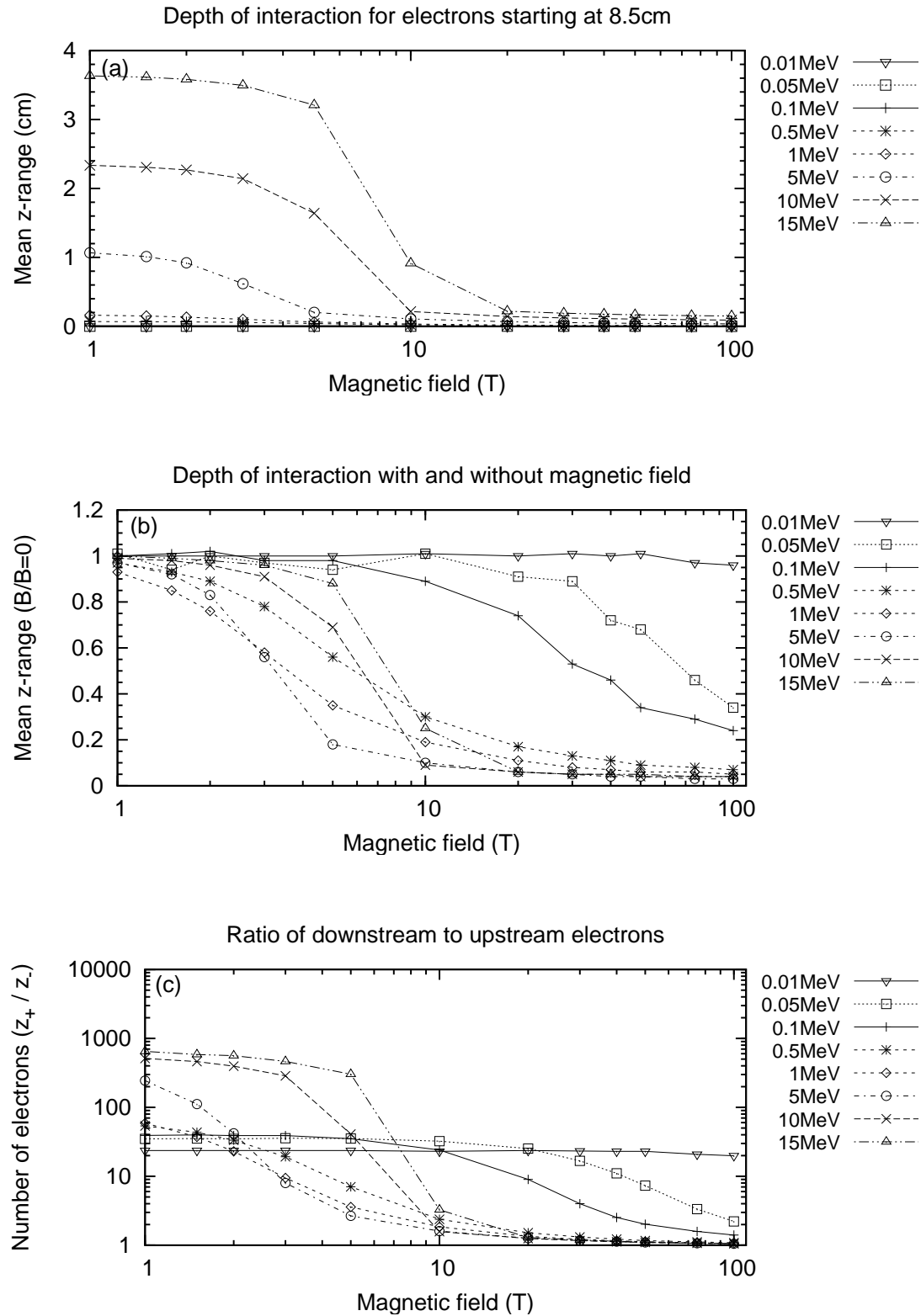


Figure 4.19: Magnetic field's influence on the interaction depths of electrons starting at 8.5 cm depth. Figure (a) plots the electrons' mean  $z$ -ranges as a function of magnetic field. A ratio of the mean  $z$ -ranges with and without magnetic field is shown in figure (b), and a ratio of electrons with final positions downstream of their initial position ( $z > z_{start}$ ) to those with final positions upstream ( $z < z_{start}$ ) is plotted in figure (c).

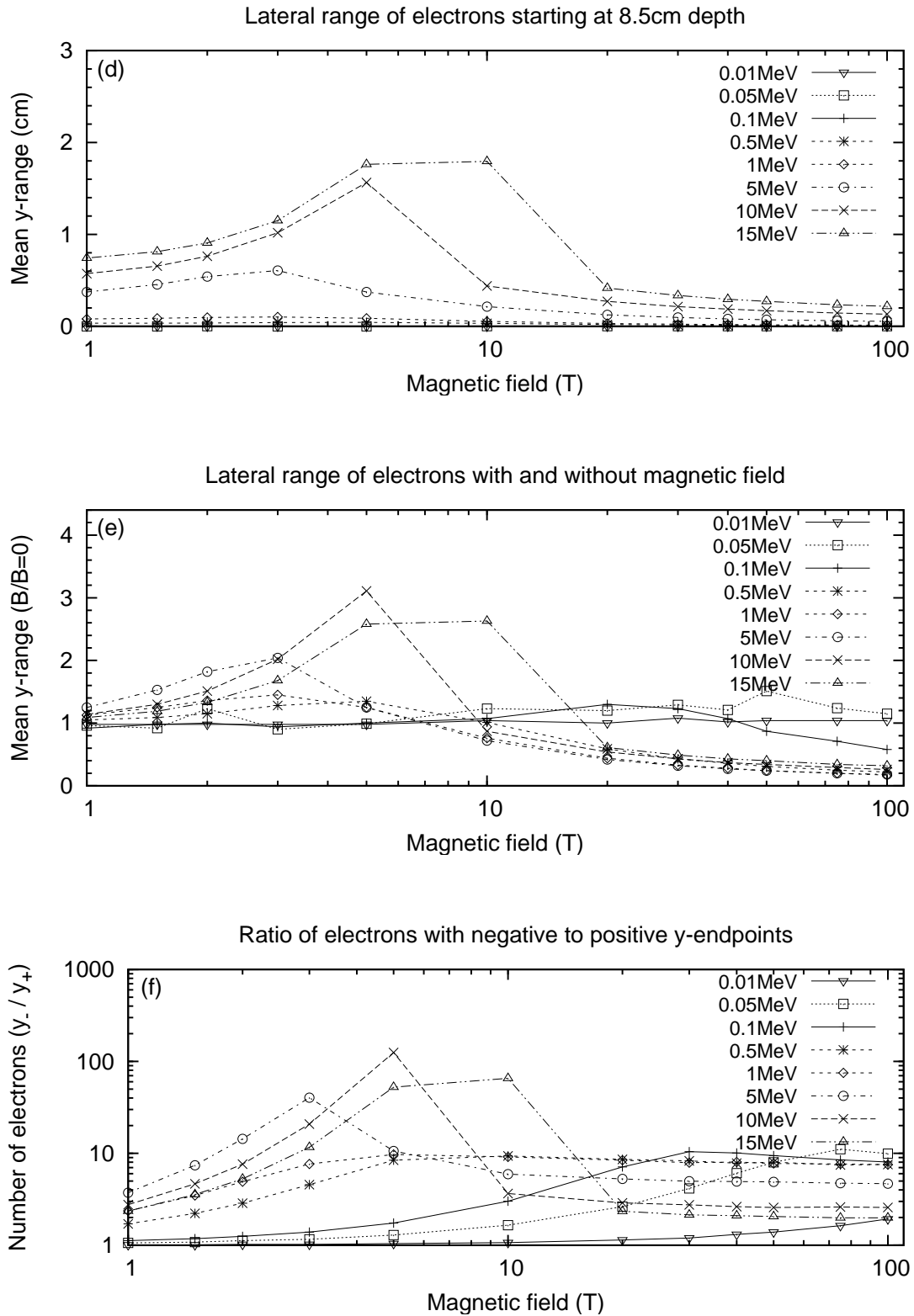


Figure 4.19: Magnetic field's influence on the lateral ranges of electrons starting at 8.5 cm depth. Figure (d) plots the mean y-ranges of electrons as a function of magnetic field. A ratio of the mean y-ranges with and without magnetic field is shown in figure (e), and a ratio of electrons with negative final y-positions ( $y < 0$ ) to those with positive final y-positions ( $y > 0$ ) is plotted in figure (f).

less than 0.5 cm (i.e. distance to the downstream field boundary). At stronger magnetic fields, the electrons' cyclotron radii become less than their range, which gives rise to the reduction in their mean  $y$ -ranges as the electrons become more confined.

Figure 4.19 (f) plots a ratio of the number of electrons with a negative final  $y$ -position ( $y < 0$ ) to those with a positive final  $y$ -position ( $y > 0$ ), where ratios above unity are observed for all electron energies. For 5, 10, and 15 MeV electrons, the ratios peak at about 3, 5, and 10 T respectively, before dropping by factors as large as 40, 50, and 30. For electrons with an energy less than 5 MeV, however, the lower the energy the stronger the magnetic field at which maximum ratio occurs, where a gradual decrease in ratio can be seen beyond the maximum (approaching 100 T). Electrons with an energy less than 0.1 MeV, on the other hand, exhibit ratios of unity as their mean  $z$ -ranges are smaller than their cyclotron radii.

Figure 4.20 shows the mean range and spatial distribution of monoenergetic electrons starting at a depth of 8.9 cm (in water) immediately before the downstream magnetic field boundary at 9 cm. The mean  $z$ -range of monoenergetic electrons subjected to different magnetic fields is shown in figure 4.20 (a). A ratio of the mean  $z$ -range with and without magnetic field is plotted in figure 4.20 (b). A reduction in the mean  $z$ -range of electrons occurs at different magnetic fields. For example, electrons with an energy of 5, 10, and 15 MeV exhibit a substantial reduction in mean  $z$ -range beyond magnetic fields of about 10, 20, and 30 T respectively. For less energetic electrons, a steady reduction in the mean  $z$ -range can be seen beyond 1 T for 0.5 and 1 MeV electrons, and 5, 10, and 50 T for 0.1, 0.05, and 0.01 MeV electrons, respectively.

Figure 4.20 (c) plots a ratio of the electrons with a final  $z$ -position downstream of their starting position ( $z > z_{start}$ ) to those with a final  $z$ -position upstream of the start ( $z < z_{start}$ ). Electrons with energies less than 1 MeV exhibit initial ratios of as much as 40, before they steadily decrease toward unity with increasing magnetic field. Similarly, higher energy electrons between 1 and 15 MeV exhibit large ratios of as much as 600 for magnetic fields up to around 10 T, at which their ratio drops rapidly toward unity.

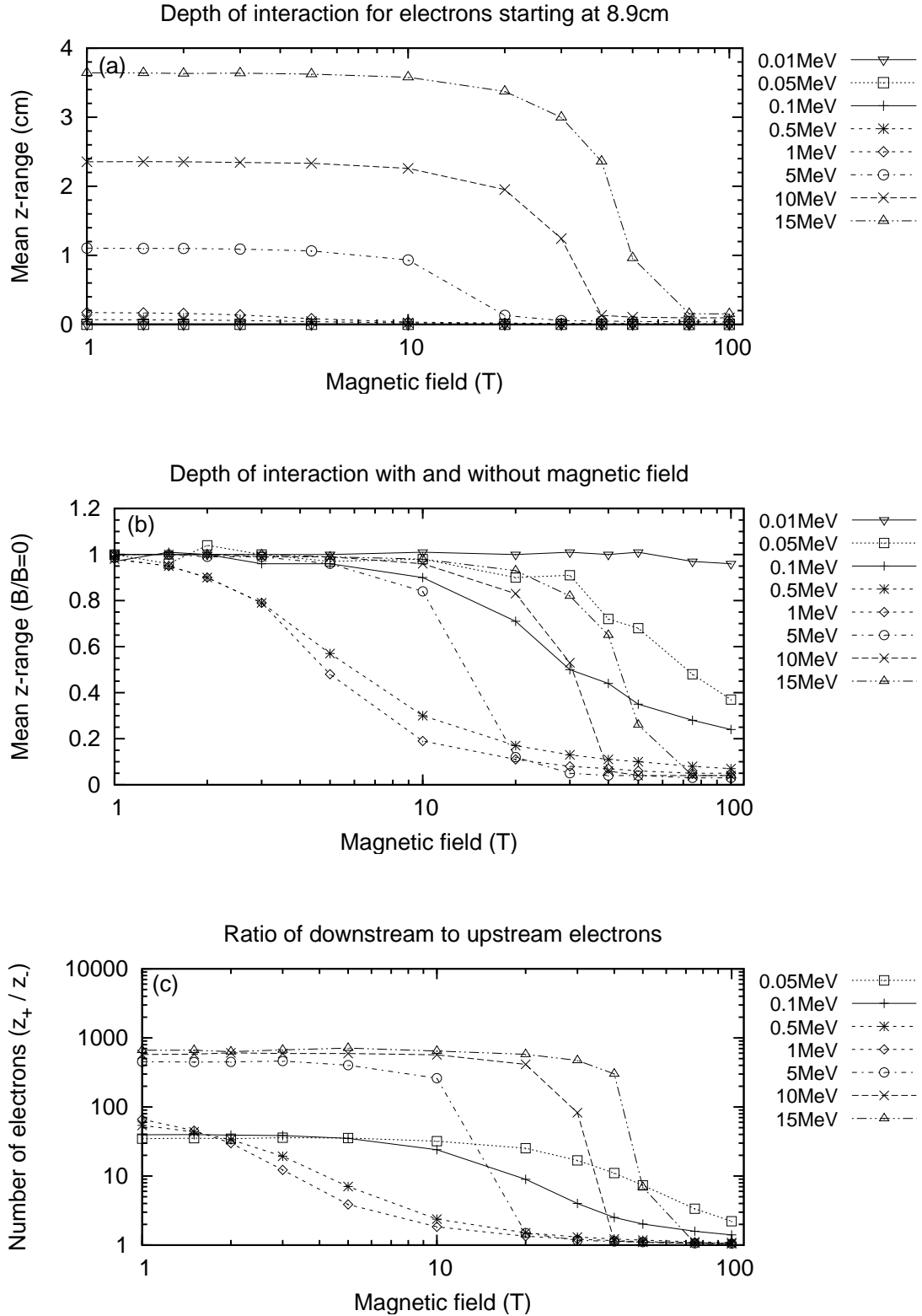


Figure 4.20: Magnetic field's influence on the interaction depths of electrons starting at 8.9 cm depth. Figure (a) plots the electrons' mean  $z$ -ranges as a function of magnetic field. A ratio of the mean  $z$ -ranges with and without magnetic field is shown in figure (b), and a ratio of electrons with final positions downstream of their initial position ( $z > z_{start}$ ) to those with final positions upstream ( $z < z_{start}$ ) is plotted in figure (c).

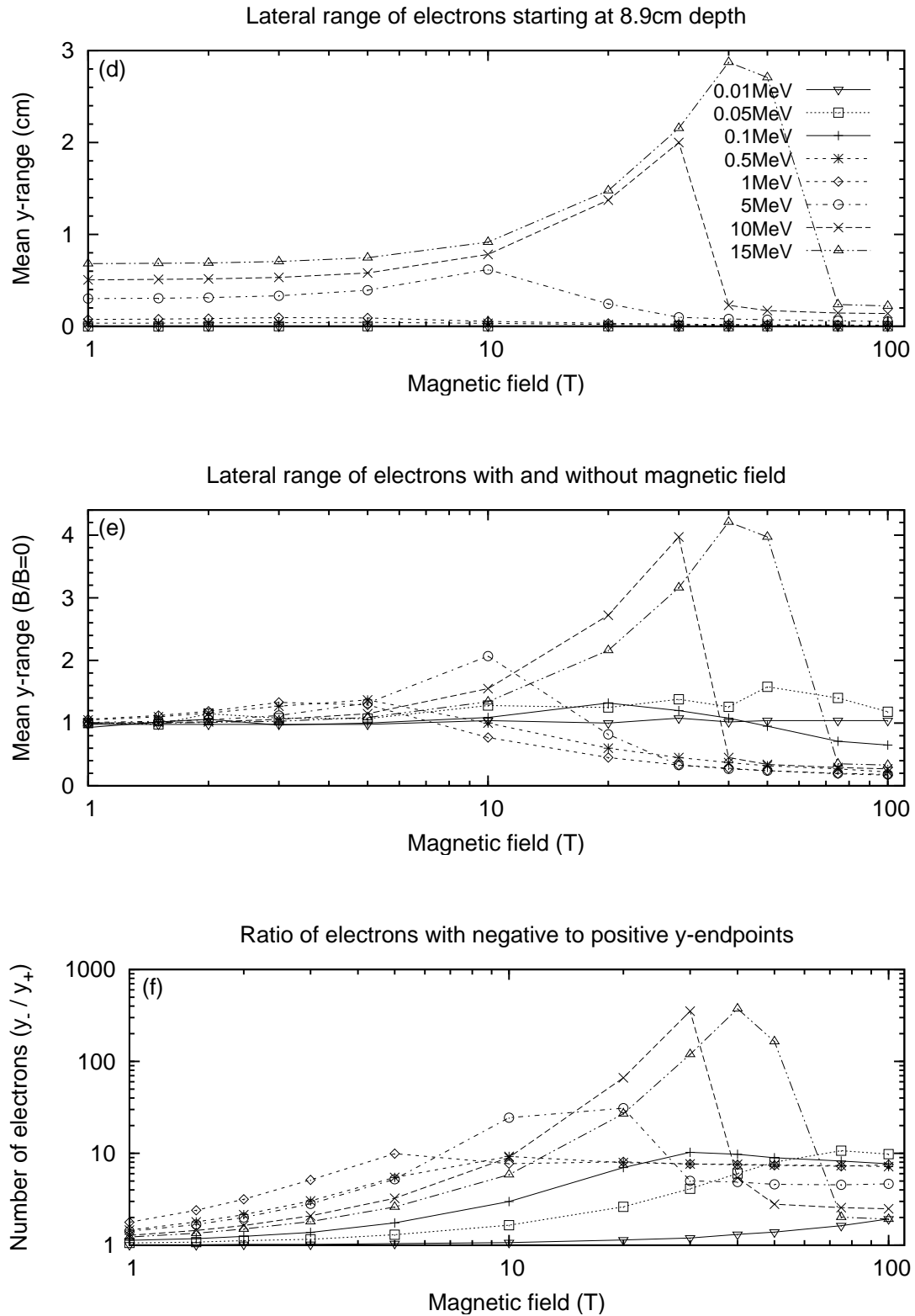


Figure 4.20: Magnetic field's influence on the lateral ranges of electrons starting at 8.9 cm depth. Figure (d) plots the mean y-ranges of electrons as a function of magnetic field. A ratio of the mean y-ranges with and without magnetic field is shown in figure (e), and a ratio of electrons with negative final y-positions ( $y < 0$ ) to those with positive final y-positions ( $y > 0$ ) is plotted in figure (f).

For electrons starting at 8.9 cm depth, those with an energy of 1 MeV and higher have sufficient range to exit the magnetic field region via the boundary at 9 cm depth. As these electrons need only traverse a depth of 0.1 cm to escape, almost no change will be observed in their mean  $z$ -range until it becomes comparable with their radii. For 1, 5, 10, and 15 MeV electrons, this occurs at magnetic fields of about 2, 10, 20, and 30 T respectively. When subjected to stronger magnetic fields, these electrons have radii less than 0.1 cm, thereby preventing their escape from the field region and producing a severe reduction in mean  $z$ -range. The consistent mean  $z$ -ranges of electrons with an energy of 1 MeV or lower at all starting depths inside the magnetic field region (i.e. 7.5, 8.5, and 8.9 cm) is due to their confinement within the magnetic field.

A maximum mean  $y$ -range of electrons is observed around the same magnetic field at which their mean  $z$ -range becomes less than the 0.1 cm distance to the downstream field boundary. The rapid drop-off in mean  $y$ -range beyond the maximum is due to the confinement of electrons within the magnetic field as their ranges become comparable with their cyclotron radii. This is confirmed by ratios of unity for electrons with downstream to upstream endpoints with respect to their initial  $z$ -position,  $z_{start}$ .

The effect of a transverse magnetic field on the lateral range of electrons is shown in figure 4.20 (d). The plot reveals an increase in the mean  $y$ -range of 1, 5, 10, and 15 MeV electrons with increasing magnetic field up to 5, 10, 30, and 40 T respectively. According to the ratio of mean  $y$ -range with and without magnetic field in figure 4.20 (e), 0.5, 0.1, 0.05, and 0.01 MeV electrons exhibit a maximum  $y$ -range at 5, 20, 50, and 30 T respectively. At field strengths beyond the maximum, the ratio drops below unity for 0.1 MeV and higher electrons as their smaller cyclotron radii increase their probability of confinement within the magnetic field.

In figure 4.20 (f), the ratio of electrons with a negative final  $y$ -position ( $y < 0$ ) to those with a positive  $y$ -position ( $y > 0$ ) is greater than unity for all electron energies. For 5, 10, and 15 MeV electrons, a maximum ratio occurs at magnetic fields of 10, 30, and 40 T respectively. The shift in the maximum ratio to stronger magnetic fields (compared

with those observed with starting depths of 7.5 and 8.5 cm) is attributed to the smaller cyclotron radii of electrons, and hence, greater confinement of trajectories within the field region. The consistent ratios exhibited by electrons with an energy of 1 MeV and lower at starting depths of 7.5, 8.5, and 8.9 cm, is indicative of their confinement within the magnetic field.

#### **4.4 Conclusion**

Normalisation of the electron distribution obtained with and without a slice of transverse magnetic field (between 7 and 9 cm depth) accentuated changes in the electron spectrum similar to those observed in the depth-dose profiles of chapter 3. An increase in secondary electron population was observed in the regions approaching and entering the magnetic field (5.5 to 6.5 cm and 6.5 to 7.5 cm depth, respectively), while a decrease in population was exhibited by the regions exiting and beyond the field (8.5 to 9.5 cm and 9.5 to 10.5 cm, respectively). This alteration in population is brought about by a change in the trajectories of electrons whose ranges are comparable to or larger than their radii of curvature. When these electrons are subjected to a transverse magnetic field, their depth of interaction is reduced as well as the depth at which any secondary particles are produced. This upstream migration of electrons gives rise to the augmentation of secondary electron population, and hence, dose enhancement in the regions before and entering the magnetic field. It is also responsible for the depletion of secondary electrons and the corresponding dose reduction beyond the magnetic field, with the exception of first generation electrons (as photon trajectories are unaffected by magnetic fields). The larger maximum and minimum electron populations obtained with field strengths of 5 T or higher, compared with 2 T, are attributed to the electrons' smaller radii of curvature, which increase their probability of confinement within the magnetic field.

Since the LET of an electron increases with decreasing energy, the redistribution of secondary electrons, particularly low-energy electrons may correspond with a change in the relative biological effectiveness (RBE). This being the case, the augmentation of

the low-energy electron population in the regions approaching and entering the magnetic field would correspond to an increase in RBE, and conversely, the reduction in low-energy electron population in the regions exiting and beyond the field would correspond to a decrease in RBE. Such an alteration of RBE would benefit the treatment of tumours near radiation-sensitive structures, where the regions of increased and decreased RBE would be aligned with the tumour volume and critical structure respectively. Quantification of the RBE associated with alterations in the secondary electron spectrum is needed to confirm this hypothesis.

Replacing the slice of uniform magnetic field with a realistic non-uniform field, such as the field produced by an MRI magnet, is also needed to determine whether the alterations in the electron spectrum associated with the regions of dose enhancement still exist.





## CHAPTER 5

### MOSFET DOSIMETRY IN MICROBEAM RADIATION THERAPY (MRT)

#### 5.1 Introduction

This chapter explores the performance of edge-on MOSFET dosimeters in Microbeam Radiation Therapy (MRT) with an investigation of their radiation response and ability to measure the dose profiles of monoenergetic and polyenergetic microbeams. The use of MOSFETs to estimate the peak-to-valley dose ratios (PVDRs) of microbeams is also studied. The MOSFET measurements are supplemented with theoretical results obtained by means of Monte Carlo PENELOPE simulations.

##### 5.1.1 Microbeam Radiation Therapy (MRT)

Microbeam Radiation Therapy (MRT) is an innovative experimental technique for the treatment of inoperable pediatric brain tumours which offers an alternative to other types of therapy deemed inadequate or unsafe [16, 18, 19, 21–23, 30, 80–82]. Studies have shown that the millimeter-wide X-ray beams used in conventional radiotherapy can be irretrievably damaging to a developing brain, especially for children less than three years of age, posing unacceptable risks of long-term neurological disability [15–19].

The advantage of MRT over broad-beam radiotherapy stems from the high tolerance of normal tissue to large amounts of radiation in small volumes, resulting in the preservation of tissue architecture. This was first observed in 1967 by Curtis at the Brookhaven National Laboratory (BNL) in a study of the cosmic radiation damage to brain tissue of astronauts [31]. Surrogate mice brains were irradiated with 22 MeV cyclotron-generated deuterons collimated to 1 mm and 25  $\mu\text{m}$  wide beams. Irradiation with a 1 mm wide beam and absorbed doses of  $\geq 140$  Gy obliterated the brain cortex,

while a 25  $\mu\text{m}$  wide beam and an absorbed dose of up to 4000 Gy left the cortex intact. Curtis proposed that this high tissue tolerance of microbeams was related to the regeneration of damaged blood vessels by surviving vasculature endothelial cells in the spaces between microbeams.

In the early 1990s, with the availability of high intensity synchrotron generated X-ray beams, investigations began into the potential applications of using X-ray microbeams in radiotherapy and radiobiology [32]. The extreme intensity of this electromagnetic radiation (generated from the acceleration of ultra-relativistic charged particles through magnetic fields) led Slatkin *et al.* to perform a study analogous to that by Curtis almost three decades earlier. Slatkin *et al.* irradiated normal rat brain tissue with a single microbeam 20 or 37  $\mu\text{m}$  wide and skin-entrance absorbed doses between 312 and 10000 Gy. Like Curtis, they found brain tissue to be highly resistant to radiation. No signs of necrosis were observed with irradiation entrance doses of  $\leq 5000$  Gy, and no signs of brain damage with doses of 312 or 625 Gy [83].

Current research in MRT, performed at the National Synchrotron Light Source (NSLS) at Upton, New York, USA and the European Synchrotron Radiation Facility (ESRF) in Grenoble, France uses a synchrotron and a multislit collimator to produce an array of parallel, rectangular, micron-sized X-ray beams (microbeams) analogous to the parallel panels of open vertical blinds [19–28]. Aimed at the tumour volume, the microbeams interact in tissue delivering a lethal radiation dose to endothelial cells lying directly in their path (i.e. *peak* regions). Cells lying in the fraction of a millimeter spacing between adjacent microbeams, known as *valley* regions, receive a superposition of dose contributions from laterally scattered photons and any secondary radiation produced from interactions in tissue. The dose in the valley is substantially smaller than that in the peak.

While the underlying radiobiological principle of MRT is not well understood, its effectiveness is believed to be related to the difference in regeneration of the radiation-damaged vasculature in the path of microbeams from the contiguous, minimally irradiated vasculature in the valleys [20, 84]. In normal tissue, the well-preserved vasculature

in the valley regions ensures the rapid regeneration of directly irradiated blood vessels. In tumour tissue, however, the irreparable damage to blood vessels starves the surviving tumour cells of oxygenated blood, resulting in their death [19, 24, 29, 82].

Over the past decade, numerous pre-clinical MRT studies on small animals have shown the extraordinary radiation tolerance of normal tissue to microscopically thin ionising radiation beams. In the late 1990s, Laissue *et al.* irradiated the cerebella of suckling rats bearing relatively advanced ( $\sim 4$  mm diameter) malignant tumours to explore the extent and severity of radiation damage with different MRT setups [29]. Irradiation of brain tissue with an array of 101 microbeams (each  $25\ \mu\text{m}$  wide and separated by  $100\ \mu\text{m}$ ) and a skin-entrance dose of up to 312.5 Gy was shown to slow tumour growth and, in more than half of the rats, eliminate it. In a later study, Laissue *et al.* irradiated the hind brain of young rats with 50 or 150 Gy using two different microbeam spacings ( $210\ \mu\text{m}$  and  $105\ \mu\text{m}$ ) to investigate any long-term effects of MRT on their brain development [20]. They found that brain tissue irradiated with  $210\ \mu\text{m}$  spacing maintained its normal architecture and showed little or no sign of neurological damage, while tissue irradiated with half the microbeam spacing ( $105\ \mu\text{m}$ ) exhibited greater susceptibility to neurological disability. The greater severity of radiotoxic effects prevalent with the smaller microbeam spacing is attributed to the larger valley dose, where fewer healthy cells survive the irradiation to carry out normal tissue repair.

In 2001, Laissue *et al.* used the cerebella of piglets as a surrogate for the human infantile brain to assess MRT's potential for inhibiting the growth of tumours while sparing radiotoxicity to the central nervous system (CNS) [21]. Piglet cerebella were irradiated with an array of microbeams (each  $28\ \mu\text{m}$  wide and separated by  $210\ \mu\text{m}$ ) and doses of up to 625 Gy. Post-irradiation, these piglets were found to mature normally alongside their unirradiated littermates despite the appearance of parallel stripes in their cerebella from the paths of microbeams in the CNS tissue. Within the same year, Dilmanian *et al.* irradiated embryonic duck brains to model the effects of MRT and broad-beam radiotherapy on the developmental process of a human infantile brain [30]. The embryos were

irradiated with either an array of MRT microbeams (each  $27\ \mu\text{m}$  wide and separated by  $100\ \mu\text{m}$ ) or a broad-beam ( $11\ \text{mm}$  wide) 3 to 4 days prior to hatching. Doses of up to  $450\ \text{Gy}$  and  $18\ \text{Gy}$  were used for the MRT and broad-beam regimes respectively. The brain tissue of duck embryos subjected to microbeam irradiation tolerated at least three times more dose than those irradiated with the broad-beam.

Small-animal MRT studies have shown that substantial therapeutic or palliative doses of up to several hundred Gy can be administered to cerebella without adverse radiotoxic side-effects. The radiobiological basis for this stems from the rapid repair of normal tissue by minimally irradiated endothelial and glial cells in the valley regions, and the irreparable radiation damage in multiple microscopic segments of the tumour vasculature. It is therefore essential that the valley dose is kept to a minimum to ensure the preservation of normal tissue architecture and sufficient survival of the endothelial cells needed for normal tissue repair. Based on these assumptions, the effectiveness of MRT is determined by the peak-to-valley dose ratio (PVDR), or the ratio of dose in the centre of the peak to that measured at the center of the adjacent valley.

The PVDR depends on factors such as the lateral scattering of synchrotron photons and related low-energy secondary electrons; the corresponding spectra of these electrons; the material composition of the interaction medium; and the microbeam collimator design (i.e. width, height, peak separation, and number of microbeams). Generally, a higher PVDR is obtained using narrow microbeams separated by a wide spacing, where the PVDR is higher at the surface than at depth. The PVDR is not uniform across an array of microbeams. It is smaller in the centre of the array than at the edges due to higher accumulative valley dose at the centre of the array from the overlapping dose tails of individual microbeams. A Monte Carlo study by Bräuer-Krisch *et al.* estimated the PVDR at the centre of an array of 48 microbeams ( $25\ \mu\text{m}$  wide,  $500\ \mu\text{m}$  high, and separated by  $210\ \mu\text{m}$ ) to be 30% less than at the edge [22].

The PVDR deteriorates with depth due to a greater number of particles experiencing lateral scattering into the valley regions as they undergo interactions within the

medium. A number of Monte Carlo studies have estimated the PVDR with depth for a variety of X-ray beam energies and MRT configurations [16, 22, 25, 32, 85]. Slatkin *et al.* used the EGS4 Monte Carlo code to study the PVDR with depth in the centre of an array of 150 microbeams (25  $\mu\text{m}$  wide, 0.3 cm high, and separated by 200  $\mu\text{m}$ ) [32]. For beam energies of 100 and 150 keV, the PVDR at 7.5 cm depth (in a human head phantom) was found to be about 60% less than at the surface (0.5 cm depth). Stepanek *et al.* repeated these PVDR calculations using the PSI version of the Monte Carlo GEANT code, where he found the PVDRs to be 10 to 20 % less [85]. The discrepancy between the PVDRs was attributed to the different electron transport methods used by the two codes (i.e. PSI-GEANT uses single collision transport whereas EGS4 uses condensed history transport). In a later Monte Carlo (PENELOPE) study, Siegbahn *et al.* showed the deterioration in PVDR with depth is due to a falloff in valley dose which is more gradual than the falloff in peak dose [86].

The deterioration in PVDR with depth has also been shown experimentally. Bräuer-Krisch *et al.* used an edge-on MOSFET to measure the peak and valley doses, and PVDR, with depth for an array of 48 microbeams (25  $\mu\text{m}$  wide, 500  $\mu\text{m}$  high, and separated by 210  $\mu\text{m}$ ) with the polyenergetic ESRF white beam. The measurements were accompanied with Monte Carlo PSI-GEANT simulations. While the absolute dose measurements in the peak and valley were found to be 20% lower than the theoretical values, the PVDRs were within 5% [22]. A study by Orion *et al.* showed reasonable agreement between a normalised dose profile of a single microbeam measured with a MOSFET dosimeter and simulated with Monte Carlo EGS4 [87].

While the PVDRs of monoenergetic microbeams have been investigated with Monte Carlo [25, 32, 85], absent from the literature are physical measurements of their dose profiles and PVDRs. This chapter compares the dose profiles and PVDRs of monoenergetic microbeams measured with a MOSFET dosimeter and simulated with Monte Carlo PENELOPE.

### 5.1.2 MOSFET dosimetry in MRT

An ongoing challenge in MRT is to find a suitable dosimeter that can measure the absolute dose deposition of microbeams with high spatial resolution on a micron scale [25]. Dosimetric systems commonly used in broad-beam radiotherapy, such as ion chambers, thermoluminescence dosimeters (TLDs) and radiochromic films, are unsuitable for microdosimetry. MRT dosimetry has therefore relied on a combination of experimental and theoretical Monte Carlo methods.

For MRT dosimetry at the ESRF, radiochromic film is used to provide information about the microbeam profiles, while ion chambers and TLDs are used to perform absolute dose measurements in homogeneous fields greater than  $1 \times 1 \text{ cm}^2$  [25]. Radiochromic film is advantageous in that it has a high spatial resolution of around 600 line pairs per  $\text{mm}^{-1}$  [88], which makes it suitable for use in applications involving high dose gradients and relatively high absorbed dose rates such as MRT [89]. The disadvantage of film, however, is that it is unable to provide accurate absolute dose measurement due to the non-linear energy response of the film in the low-energy region of the X-ray spectrum, which is between about 30 and 50 keV [25, 88].

An alternative dosimeter for use in MRT is the Metal-Oxide-Semiconductor Field-Effect Transistor (MOSFET). Its micron, or submicron, sensitive volume allows dosimetric measurements to be performed with high spatial resolution. Currently, it is the only real-time readout dosimeter capable of micron-sized spatial resolution. MOSFET dosimetry was introduced in 1974 by A. Holmes-Siedle, who proposed its use as a space-charge dosimeter [90]. Since then, MOSFET dosimetry has primarily been applied in space dosimetry for monitoring the effects of space radiation on Earth orbiting satellites [91]. In the last decade, however, MOSFET dosimetry has found its way into a number of medical applications ranging from in vivo dosimetry to surface dose measurements, where its use in synchrotron radiation was first investigated in 1998 by Kron *et al.* [92].

A MOSFET is based on the modulation of charge concentration by a MOS capacitance between a gate and body which are insulated by a gate dielectric layer such as silicon dioxide,  $\text{SiO}_2$ . Separated by the body region are two individual highly doped regions, called the source and drain, which are both either  $p$  or  $n$  type and of opposite type to the body region. The inversion layer, or conducting channel, between the source and drain is therefore either of  $n$  or  $p$  type semiconductor material, and hence, the device is accordingly named a  $n$ -MOSFET or  $p$ -MOSFET.

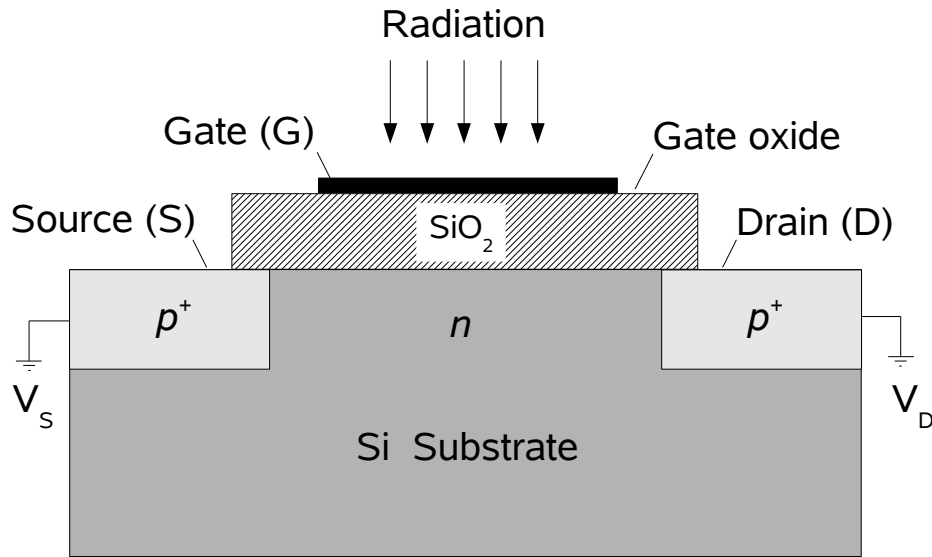


Figure 5.1: Schematic diagram of a  $p$ -MOSFET (Metal-Oxide-Semiconductor Field Effect Transistor) dosimeter.

In this thesis, MOSFET dosimetry was performed with  $p$ -type dosimeters. Figure 5.1 shows the construction of a  $p$ -MOSFET, where the source and drain are  $p^+$  regions and the body is an  $n$  region. The operation of a MOSFET is based on the generation of electron-hole pairs by ionising radiation in the gate oxide, where generally the amount of trapped charge is proportional to the energy imparted by the radiation ( $\sim 18$  eV of energy is required to create an electron-hole pair in  $\text{SiO}_2$ ). Applying a negative gate-substrate voltage forces positively charged holes to move towards the  $\text{Si/SiO}_2$  interface where they



become captured by traps in the gate oxide. This build-up of positive charge alters the conductivity in the p-channel, which leads to a change in the gate voltage (i.e. shift in threshold voltage  $\Delta V_{th}$ ) to ensure a constant current flow through the channel. If the gate voltage is less negative than the (negative) threshold voltage, the channel disappears and only a weak subthreshold current flows between the source and drain. The shift in threshold voltage before and after irradiation is proportional to the absorbed dose in  $\text{SiO}_2$  and can be measured by means of a MOSFET reader. A simplified readout circuit of a MOSFET reader is shown in figure 5.2.

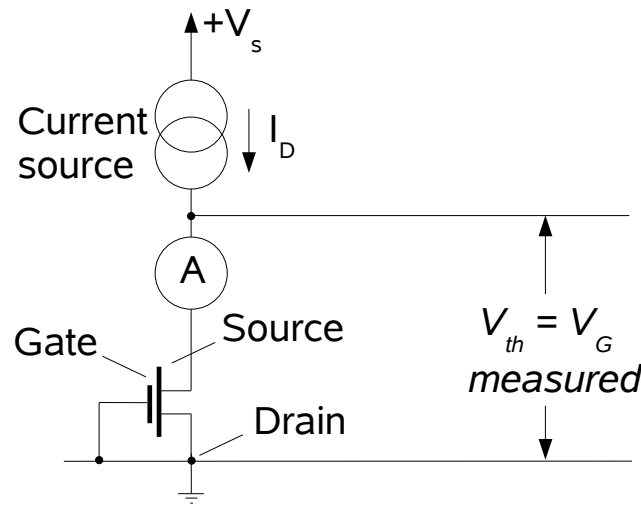


Figure 5.2: Schematic diagram of the MOSFET reader. The MOSFET dosimeter is read out under a constant current  $I_D$  with the gate and source grounded. The threshold voltage,  $V_{th}$ , measured across the MOSFET is proportional to the dose deposited in the  $\text{SiO}_2$  gate oxide.

Irradiation of MOSFET dosimeters can be either passive (without a voltage on the gate) or active (positive gate bias voltage). The application of a positive gate voltage reduces the recombination of electron-hole pairs in the  $\text{SiO}_2$  gate oxide, which increases the linearity and sensitivity of the MOSFET response. From basic electrostatic principles, the response of a p-MOSFET operated in passive and active mode can be approximated by equations 5.1 and 5.2

$$V_{th}^2 (passive) \sim 0.0022D^{0.4}t_{ox}^2 \quad (5.1)$$

$$V_{th}^2 (active) \sim 0.04Dt_{ox}^2f \quad (5.2)$$

where  $D$  is the amount of dose (in Rad) deposited in the gate oxide of thickness  $t_{ox}$  ( $\mu\text{m}$ ), and  $f$  is the fraction of holes which escape recombination (this approaches one with increasing positive bias voltage) [93, 94]. When a MOSFET is operated in passive mode, the dose response is sub-linear due to the repulsion by the Coulomb field produced by the trapped holes. In active mode, the dose response is essentially linear over a wide range. The linearity of response depends on the thickness of the oxide layer, electrical field in the oxide, and technology of the oxide growth [95]. The lifetime of a MOSFET is determined by dose limits at which the charge build-up effect saturates in the gate oxide, or the non-linear response becomes intolerable.

The small micron-sized sensitive volume and non-destructive readout of MOSFET dosimeters has led to their use in a wide range of radiotherapy applications during the last decade [96]. For most applications involving photon dosimetry, the MOSFET response in tissue-equivalent phantoms is driven by scattered electrons where it follows the Bragg-Gray cavity theory (i.e. number of electrons inside a cavity placed within a medium would also exist in the absence of the cavity). When a MOSFET is used in free-air geometries it, like any silicon device, has an energy dependence. For low-energy photon irradiation, such as the X-ray beam produced by a synchrotron, the MOSFET has been found to exhibit an over-response of dose when compared with tissue/water equivalent detectors [92]. This over-response is shown in figure 5.3 for the ‘Wollongong’ and ‘T & N’ MOSFETs, whose response differs because of their packaging materials [97].

The high spatial resolution of the MOSFET dosimeter was fully realised by Rosenfeld *et al.* who proposed operating the device in what is now called ‘edge-on’ mode (i.e. orientation of MOSFET chip is such that the interface between its sensitive volume and

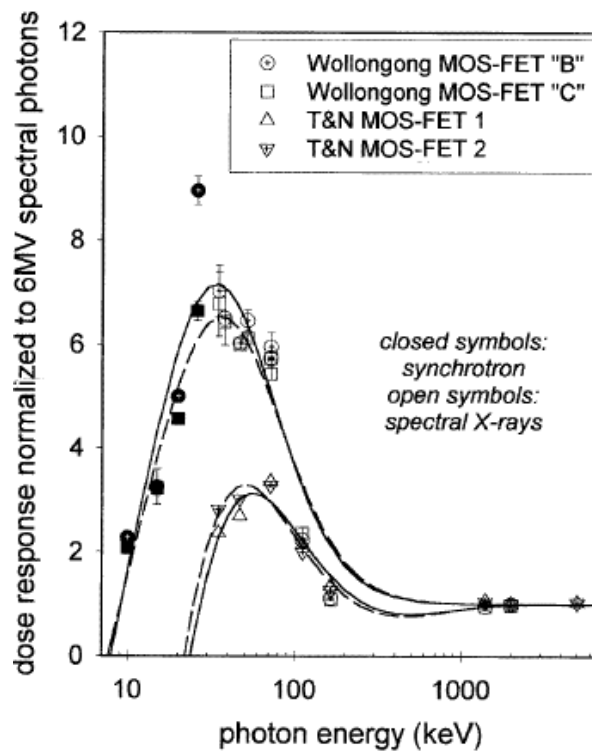


Figure 5.3: The dose response of MOSFET detectors to effective radiation energy. The dose response (in free-air geometry) was normalised to that obtained with 6 MV X-rays from a medical linear accelerator [92].

substrate is parallel with the beam direction) to provide a resolution of  $\sim 1 \mu\text{m}$  [98]. Since its inception, edge-on MOSFET dosimetry has received a lot of attention in microdosimetric applications. This chapter explores the MOSFET's suitability for dosimetry in MRT.

### 5.1.3 MRT at the ESRF ID-17 biomedical beamline

MRT experiments in the present work were conducted at the ID-17 biomedical beamline of the European Synchrotron Radiation Facility (ESRF) in Grenoble, France. The ESRF is a third generation electron synchrotron comprising a 6 GeV evacuated electron storage ring of 844 m circumference. Bunches of electrons orbit in  $2.8 \mu\text{s}$  to produce a maximum ring current of 200 mA, which has a decay time of 50 hours [22]. The ultra-relativistic electrons emerge from storage ring and pass through an alternating magnetic

field (generated by a wiggler insertion device) to produce synchrotron radiation with a characteristic small source size, high intensity, and a broad continuous spectrum spanning from infrared to X-rays [30]. Tangential to the storage ring is the ID-17 biomedical beamline which services the MRT facility. As illustrated in figure 5.4, it uses a polyenergetic X-ray spectrum (white beam) ranging from about 50 to 350 keV with a maximum intensity of 83 keV and a mean energy of 107 keV [16, 25, 86]. The lower energy photons have been filtered from the beam using 1.6 cm of aluminium.

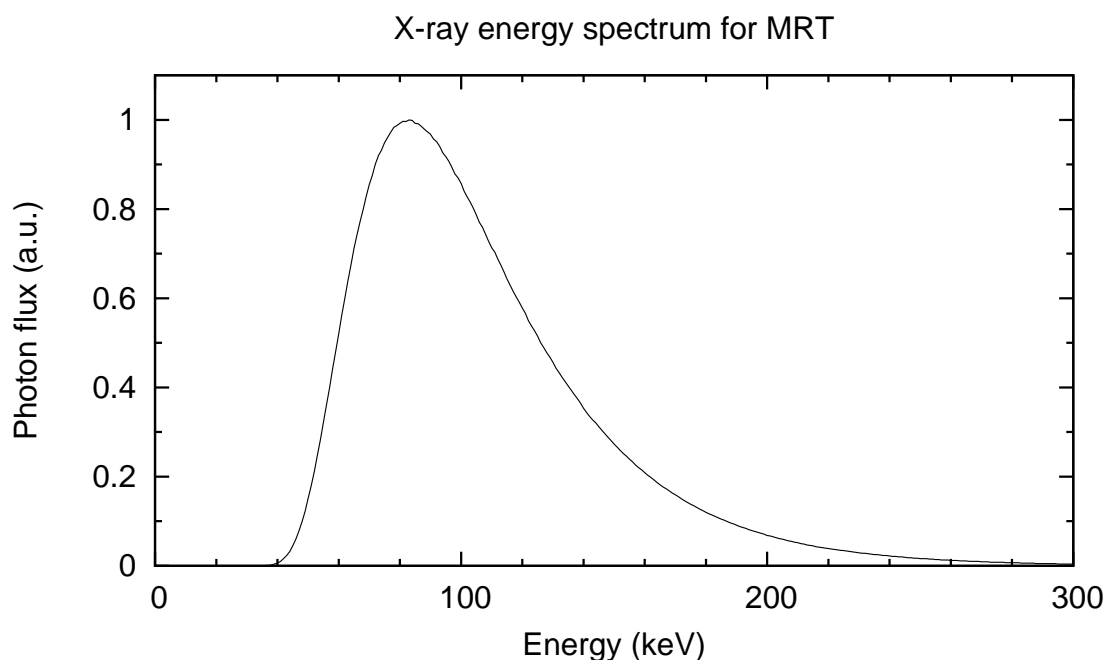


Figure 5.4: X-ray energy spectrum for MRT measured at the ESRF ID-17 biomedical beamline.

The filtered white beam emerges from a beryllium window into air and travels through an ionisation chamber before striking a multislit collimator 33 m downstream of the source [22, 23], as shown in figure 5.5. The multislit collimator, which is discussed in more detail in chapter 7, shapes the wide beam into an array of parallel, rectangular, micron-sized X-ray beams (microbeams) for MRT. Exiting the collimator, the microbeams travel through 1 m of air before striking a target which is fixed to the stage of a

three-axis goniometer device [23]. The Kappa-type goniometer<sup>1</sup> is a computer-controlled device which allows high-resolution rotation and translation of the target in 3-D with respect to the beam.

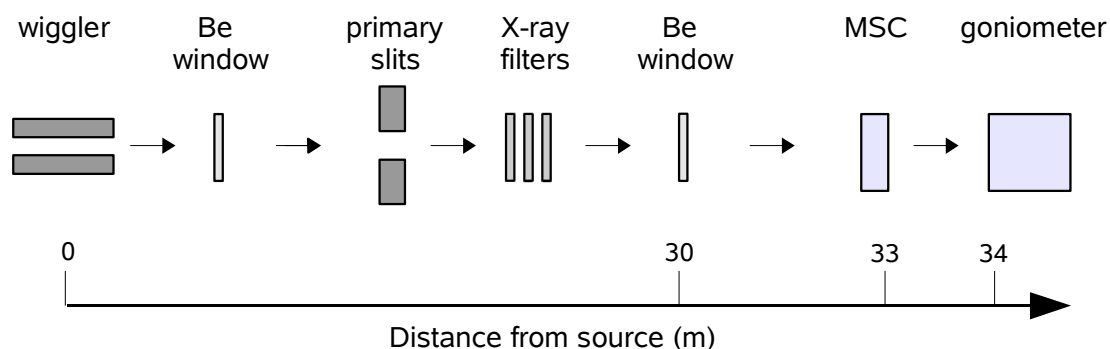


Figure 5.5: Schematic diagram of the MRT setup at the ESRF ID-17 beamline.

Monoenergetic beams are produced from the insertion of a crystal monochromator device into the path of the polyenergetic synchrotron beam. The crystal diffracts the incident X-ray beam to produce beams at specific angles depending on their wavelength, or energy. The desired beam energy is therefore selected by adjusting the angle of the crystal with respect to the incident beam.

Irradiation of the target is performed with either the expose or irradiate method, depending on the nature of the target. The expose method uses a stationary goniometer which is moved into position prior to irradiation of approximately 30 ms duration, which corresponds with the minimum reliable time that the fast shutter is open. Alternatively, the irradiation method is performed by moving the target upwards through the beam at a constant speed. For this method, the goniometer is programmed to move with vertical speed, acceleration, and deceleration to paint a prescribed dose (which takes into account the storage ring current) over a selected volume with millimeter and millisecond precision [22]. The time that each element of the target is exposed to the beam is determined by a fast shutter system [99], which is located upstream from the multislit collimator and

<sup>1</sup>Kappa-type goniometer manufactured by Huber, Germany.

synchronised with the goniometer's vertical translation. Acceleration and deceleration of the goniometer is timed in such a way to provide a constant speed of dose painting during beam delivery.

## 5.2 Experimental and simulation methods

MRT dosimetry was performed with a quadruple MOSFET, also known as a RADFET<sup>2</sup>. Figure 5.6 shows an image of the REM TOT500 RADFET chip which comprises two low-sensitivity MOSFETs, Q2 and Q3, and two high-sensitivity MOSFETs, Q1 and Q4, encapsulated in opaque epoxy of less than 2 mm [100]. The difference in sensitivity is attributed to the thickness of the gate oxide, which is 0.15 and 0.9  $\mu\text{m}$  for the low and high-sensitivity MOSFETs, respectively. These high and low-sensitivity MOSFETs will here on be referred to as MOSFET(H) and MOSFET(L) respectively.

The RADFET chip was connected to a computerised reader<sup>3</sup>, which measured the change in the source to drain voltage required to maintain a source to drain current,  $I_D$ , of about 160  $\mu\text{A}$ . The RADFET lifetime was limited to a threshold voltage of 27 V, which is the limit of operation of the reader and also the voltage at which the sensitivity of the RADFET significantly changes owing to the accumulation of absorbed dose. The accuracy of the reader was 1 mV and any variation due to background noise was less than 0.5 mV.

The experiments were conducted with the synchrotron operating in the 'four-bunch' storage-ring electron-filling mode, which generates a maximum ring current of about 40 mA, which is lower than usual at the ESRF (i.e.  $\sim 200$  mA). The lower current and X-ray flux of this mode reduces the severity of charge-collection saturation and ion recombination effects in MOSFET dosimetry. All irradiations were performed with the expose method. The measured change in MOSFET threshold voltage, or dose response, was normalised to the storage ring current and exposure time.

<sup>2</sup>RADFET manufactured by Radiation Experiments and Monitoring (REM), Oxford, UK.

<sup>3</sup>Reader developed by the Centre for Medical Radiation Physics, University of Wollongong, Australia.

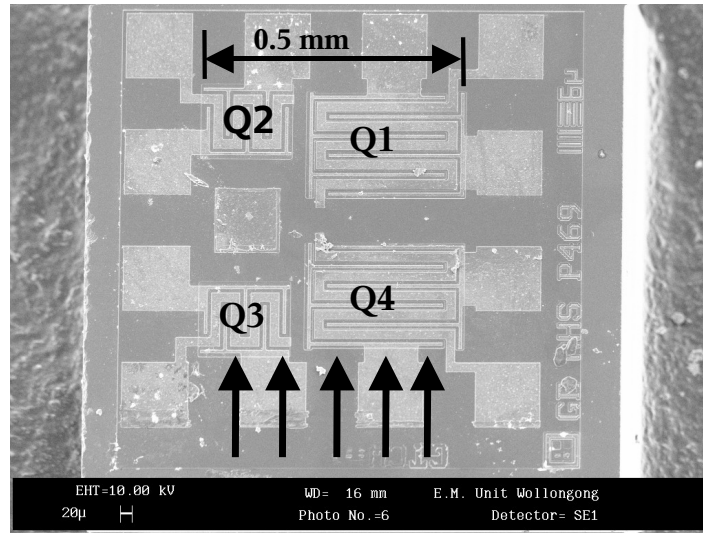


Figure 5.6: Scanning electron microscope image of the REM TOT500 RADFET chip ( $1 \times 1 \times 0.5 \text{ mm}^3$ ), which shows the two low-sensitive MOSFETs, Q2 and Q3, and two high-sensitive MOSFETs, Q1 and Q4. The direction of the X-ray microbeam is indicated by the arrows [22, 100].

The MOSFET's linearity of radiation response was studied at different threshold voltages for both monoenergetic and polyenergetic beams. The MOSFET(L) and MOSFET(H) dosimeters were operated in active mode and irradiated under a gate bias voltage of +15 and +5 V respectively, as they provided optimal linearity of threshold voltage versus dose for each RADFET. All measurements were performed with the edge-on MOSFET at 1.1 cm depth in a cylindrical perspex phantom of 2.5 cm diameter and 5 cm depth.

The linearity of response to polyenergetic radiation was studied with a MOSFET(H), which had an initial threshold voltage of 18.0 V. In order to reduce the intensity of the white beam, a multislit collimator and aluminium filter were inserted into the beam and the MOSFET was positioned at the centre of a valley region where the beam intensity is lowest. The MOSFET was exposed to 43 pulses of radiation, each with a duration of 0.15 s. After each pulse, the cumulative reader's threshold voltage was recorded and the change in voltage calculated.

The linearity of response to monoenergetic radiation was investigated for both the MOSFET(L) and MOSFET(H) dosimeters. The energy of the monoenergetic beam was

preselected via the control computer, which changes the beam energy by altering the angle of the crystal monochromator. Measurements were performed using a wide beam configuration (i.e. no multislit collimator and aluminium filter) since monoenergetic beams have a substantially lower intensity than that of the white beam. The radiation response of the MOSFET(L) was investigated with a 50 keV beam. This dosimeter had an initial threshold voltage of 4.6 V and was subjected to 19 pulses of radiation each of 0.03 s duration. The radiation response to 50 and 100 keV beams was investigated with a MOSFET(H). For the 50 keV beam irradiations, the dosimeter had an initial threshold voltage of 24.2 V and was exposed to 19 pulses of radiation each of 0.15 s duration. The same MOSFET(H) was used in an earlier investigation of the radiation response for the 100 keV beam. These measurements were performed with an initial threshold voltage of 22.4 V, and 25 pulses of radiation each of 10 s duration (longer exposures were needed due to the low intensity of the 100 keV beam).

MOSFET dosimetry was also used to measure the lateral dose profile of an array of 24 microbeams (each 25  $\mu\text{m}$  wide, 492.5  $\mu\text{m}$  high, and separated by 412  $\mu\text{m}$ ). Dose profiles of individual microbeams were scanned in 2  $\mu\text{m}$  steps with an edge-on MOSFET(L) at 1.1 cm depth (in perspex) using the orientation shown in figure 5.7. A dose profile of the central microbeam in the array (peak 12) was obtained for monoenergetic photon beams of 30, 50, 70, and 100 keV. Dose profiles of microbeams 17 and 22 (i.e. 5th and 10th microbeams right of centre when viewing the array from the source position) were also measured for the 50 keV beam. The peak 12 dose profile with the polyenergetic white beam was measured using a MOSFET(H) in the opposite vertical orientation (i.e. mirror image) to that shown in figure 5.7.

PVDR estimates were also obtained for all of the aforementioned beams except the 100 keV beam since its low intensity produces large uncertainties in the valley dose. The peak dose of the central microbeam (peak 12) was extracted from the measured dose profiles. The valley dose was measured with the MOSFET at the centre of the valley regions on either side of peak 12 (i.e.  $\pm 206 \mu\text{m}$ ), where three to five measurements were



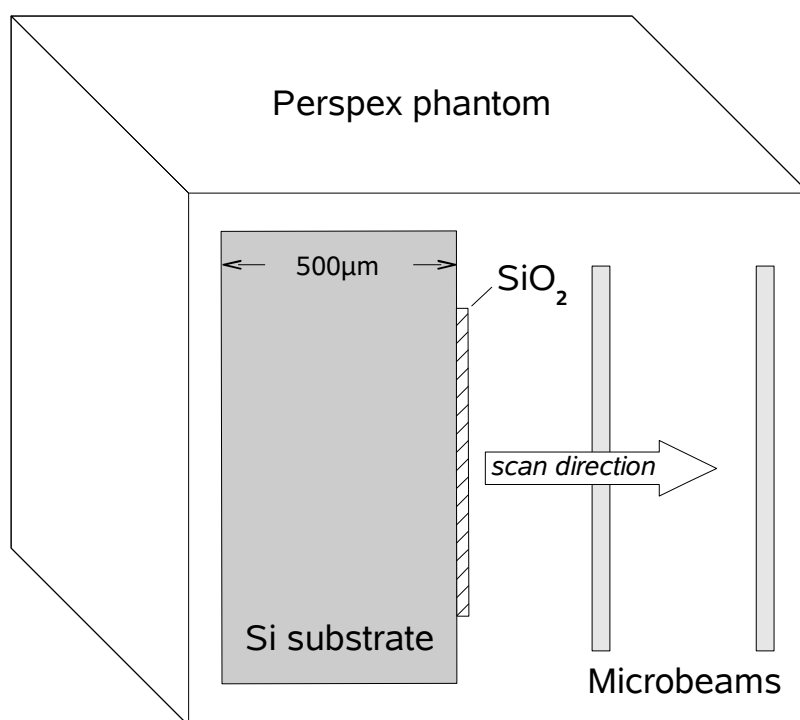


Figure 5.7: Illustration of the MOSFET configuration used to scan the dose profiles of monoenergetic microbeams, where the beam direction is into the page.

obtained. The PVDR was calculated using the dose at the centre of the peak and an average of the two valley doses on either side. Peak and valley dose measurements, and PVDRs, were also obtained for the 5th and 10th microbeams right of centre (peaks 17 and 22, respectively).

MOSFET dosimetry was also used to investigate the variation in PVDR with depth for an array of three microbeams (each 25  $\mu\text{m}$  wide, 492.5  $\mu\text{m}$  high, and separated by 412  $\mu\text{m}$ ) and the white beam. Peak and valley dose measurements were obtained with the edge-on MOSFET positioned at 0.9, 1.9, and 2.8 cm depth in perspex, and PVDRs were calculated for the central microbeam (peak 2).

Monte Carlo PENELOPE simulations were performed to supplement the measured microbeam dose profiles and PVDRs. These simulations incorporated a model of the multislit collimator, synchrotron source, and 34 m source-target distance used for MRT at the ESRF ID-17 beamline (refer to chapter 7 for details). The MOSFET dosimeter was

not modelled due to its complex geometry and material composition, and also the infeasibility of integrating dose contributions from the different MOSFET positions needed to construct a single dose profile.

A lateral dose profile of the full microbeam array was simulated with monoenergetic beams of 30, 50, 70, and 100 keV, as well as the ESRF polyenergetic white beam. Dose was scored between 1.0 and 1.2 cm depth (in perspex) for comparison with the profiles measured with a MOSFET at 1.1 cm depth. The scoring bins were 2  $\mu\text{m}$  wide (to match the step size used in the MOSFET measurements), 0.2 cm high, and 0.2 cm deep. The electron and photon transport cutoffs were set to 1 keV, and a total of  $10^{10}$  primary photon histories were simulated. The PVDRs of individual microbeams were calculated for the different beams using the dose in the central bin of the peak region and an average dose in four bins about the valley midpoint (i.e.  $\pm 206 \mu\text{m}$  from the peak centre).

Additional simulations were performed for each beam energy to determine the dose distribution of a single microbeam according to the type of initial photon interaction (i.e. Rayleigh scattering, photoelectric effect, or Compton scattering). These simulations used the PENELOPE variable ICOL, which describes the type of event that has been simulated (i.e. ICOL = 1, 2, or 3 corresponds to a Rayleigh scattering, Compton scattering, and photoelectric interaction, respectively). Following the initial interaction of a primary photon, the PENELOPE ILB(5) label, which is transferred to all descendants of a primary particle, was set to the value of ICOL. Hence, dose contributions from any descendant particles were tallied according to the type of initial interaction experienced by the primary photon. The dose was scored at 1.1 cm depth (in perspex) in bin volumes of  $0.0001 \times 0.6 \times 0.1 \text{ cm}^3$  (width  $\times$  height  $\times$  depth). A total of  $10^9$  primary photon histories were simulated using photon and electron transport cutoffs of 0.5 and 1 keV respectively.

Also simulated was the dose profile of an array of three microbeams at depths of 0.9, 1.9, and 2.8 cm to compare with the measured profiles. The bin volumes, energy cutoffs and total number of histories were identical to those used in the above simulations

for an array of 24 microbeams. The PVDR for the central microbeam (peak 2) was calculated using the dose scored in the central bin of the peak and an average of the dose in four bins about the valley midpoint (i.e.  $\pm 206 \mu\text{m}$  from peak centre). Additional simulations were performed to obtain the lateral dose profile, and hence PVDR, at 0.1, 0.2, 0.3, 0.5, 0.7, 1.1, and 1.2 cm depth in perspex.

### 5.3 Results and discussion

#### 5.3.1 Radiation response of MOSFET dosimeters

Figure 5.8 (a) shows the response of a MOSFET(H) dosimeter to polyenergetic white beam irradiation, normalised to the synchrotron storage ring current and exposure time. The normalised response of a MOSFET(L) dosimeter to 50 keV monoenergetic beam irradiation is shown in figure 5.8 (b). Figures 5.8 (c) and (d) plot the normalised radiation response of a MOSFET(H) to 50 and 100 keV beams, respectively.

The MOSFET(H) dosimeter exhibited a 12% falloff in response when subjected to polyenergetic white beam irradiation and operated between threshold voltages of 18 and 19.8 V (i.e.  $\sim 7\%$  per Volt). When exposed to monoenergetic radiation of 50 and 100 keV, it exhibited a 5% falloff in response over a 1.2 V range (i.e.  $\sim 4\%$  per Volt). The MOSFET(L) dosimeter, on the other hand, experienced a falloff of less than 2% when it was exposed to 50 keV radiation and operated at threshold voltages between 4.6 and 5.2 V (i.e.  $\sim 3\%$  per Volt).

The smaller falloff in radiation response exhibited by the MOSFET(L) dosimeter is attributed to its thinner gate oxide and higher gate bias voltage (i.e. stronger external electric field), which reduces the effect of accumulated positive charge. MOSFET(H) dosimeters, on the other hand, have a thicker gate oxide and therefore reach saturation sooner (at lower doses). The larger falloff in response exhibited by the MOSFET(H) subjected to polyenergetic radiation (than with 50 or 100 keV monoenergetic radiation) is due to the higher intensity of the white beam, causing saturation to occur sooner.

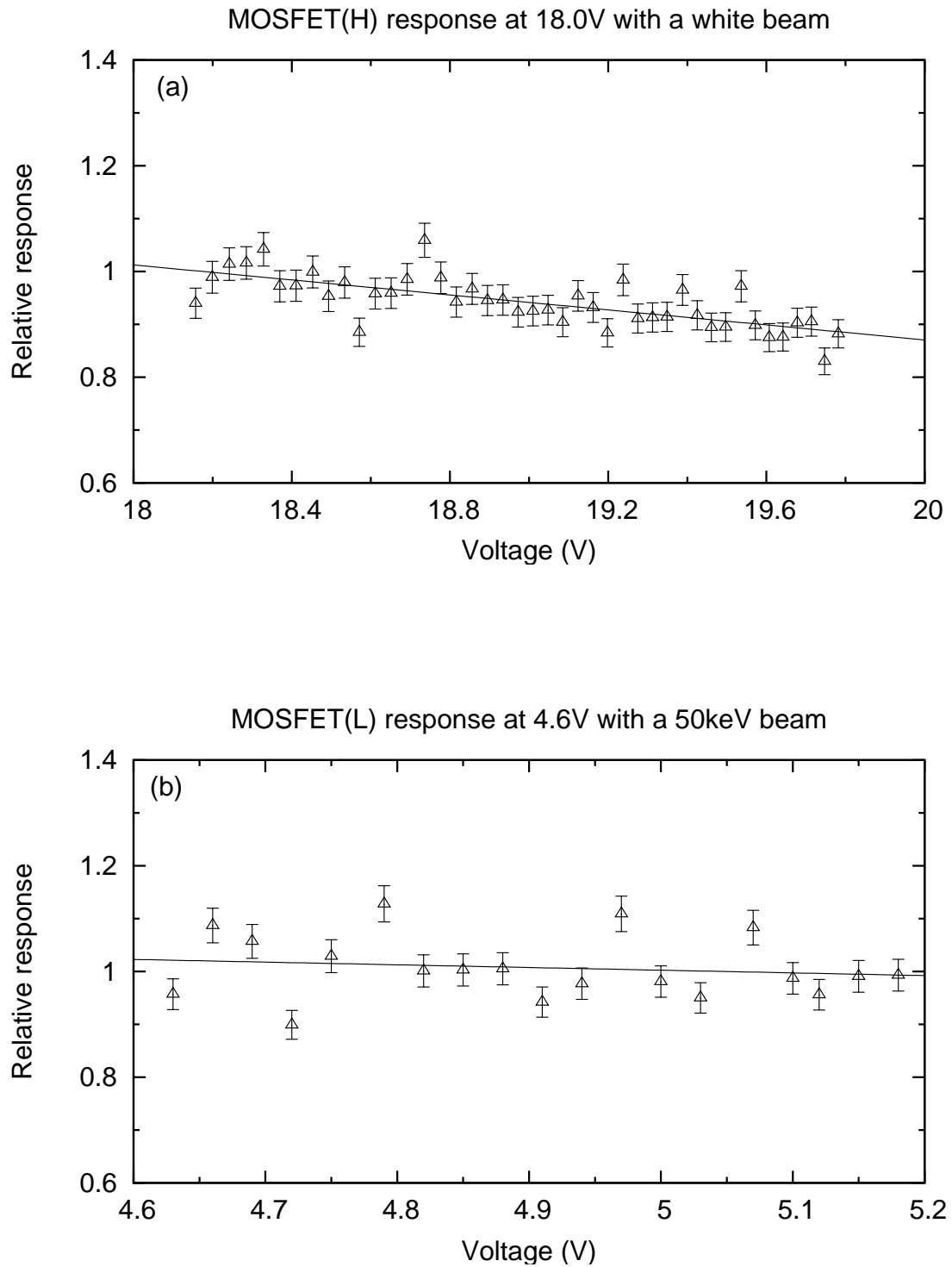


Figure 5.8: Radiation response of MOSFET dosimeters. Figure (a) plots the normalised response of a MOSFET(H) dosimeter subjected to  $43 \times 0.15$  s pulses of white beam radiation. The response of a MOSFET(L) dosimeter to  $19 \times 0.03$  s irradiations with a 50 keV beam is shown in figure (b).

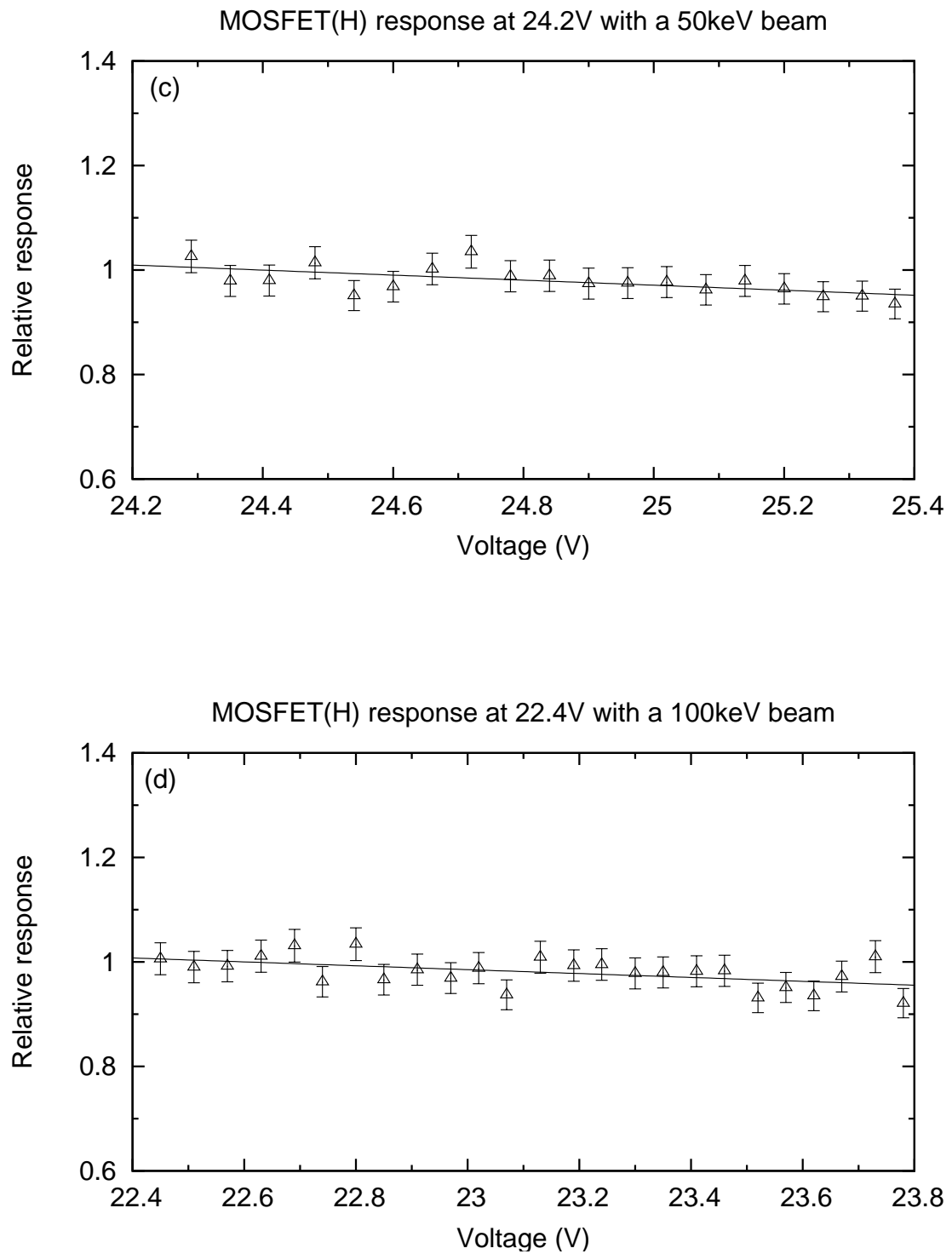


Figure 5.8: Radiation response of MOSFET dosimeters. Figure (c) plots the normalised response of a MOSFET(H) dosimeter subjected to  $20 \times 0.15$  s pulses of irradiation with a 50 keV beam. The response of a MOSFET(H) dosimeter to  $25 \times 10$  s irradiations with a 100 keV beam is shown in figure (d).

### 5.3.2 Measured and simulated dose profiles of microbeams

A MOSFET dosimeter was used to measure the lateral dose profile of the central peak in an array of 24 microbeams (peak 12) for monoenergetic beams of 30, 50, 70, and 100 keV, and the polyenergetic ESRF white beam. Figures 5.9 (a), (b), (c), and (d) plot the peak 12 dose profile measured with a MOSFET(L) dosimeter for monoenergetic beams of 30, 50, 70, and 100 keV respectively. The peak 12 dose profile for the polyenergetic white beam which was measured with a MOSFET(H) dosimeter is shown in figure 5.10.

Figure 5.11 compares the measured dose profiles of peak 12 obtained for the different beam energies, where only one scan (scan 1) is shown for each energy. The full-width at half-maximum (FWHM) of the 70 and 100 keV monoenergetic profiles was approximately the same. The FWHM of the 30 and 50 keV profiles, on the other hand, were about 3  $\mu\text{m}$  and 2  $\mu\text{m}$  smaller than those obtained with the 70 and 100 keV beams. Common to all monoenergetic profiles was an asymmetry about the peak centre, where the right penumbral dose was smaller than the left penumbral dose. This asymmetry was also observed in the dose profiles of peaks 17 and 22 (i.e. 5th and 10th microbeams right of centre when viewing the array from the source position) obtained with a 50 keV beam. The peak 12 profiles obtained with the white beam also exhibited asymmetry, however, it was an inverse of those observed in the monoenergetic profiles (i.e. the right penumbral dose was higher than the dose in the left penumbra).

The asymmetric profiles of measured microbeams prompted Monte Carlo simulation of the lateral dose profile of an array of 24 microbeams (each 25  $\mu\text{m}$  wide, 492.5  $\mu\text{m}$  high, and separated by 412  $\mu\text{m}$ ). Figure 5.12 shows the simulated dose profile of the central microbeam in the array (peak 12) obtained with the white beam and monoenergetic beams of 30, 50, 70, and 100 keV. The dose profile of a single microbeam (25  $\mu\text{m}$  wide and 492.5  $\mu\text{m}$  high) was also simulated for each beam energy for comparison with the peak 12 profile. A comparison of the penumbral and valley doses of the two microbeam profiles is shown in figure 5.13.

Comparison of the measured dose profiles in figure 5.11 with the simulated dose

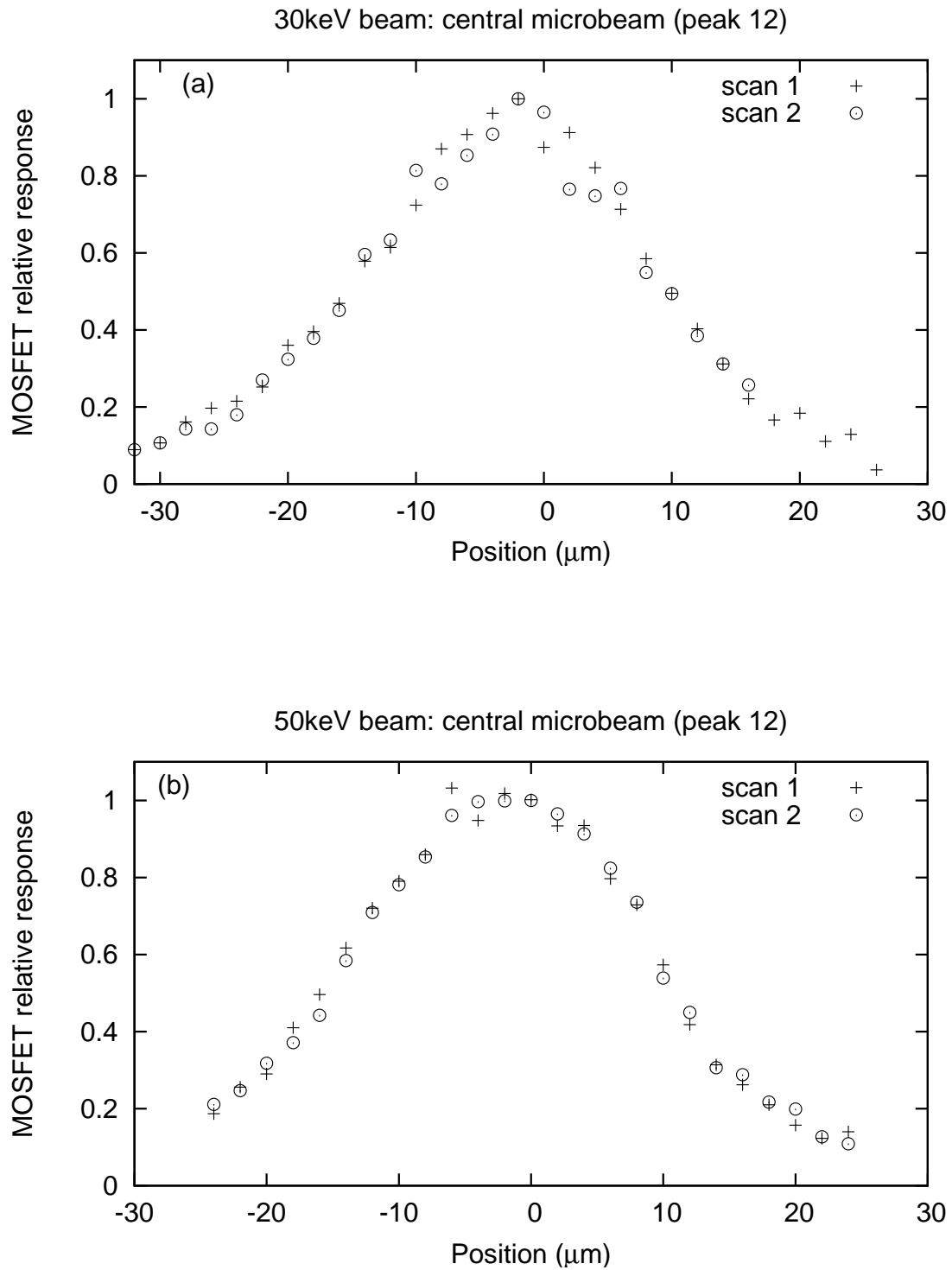


Figure 5.9: Dose profiles of monoenergetic microbeams measured at 1.1 cm depth (in perspex) with a MOSFET(L) dosimeter. Figures (a) and (b) show the dose profile of the central peak in an array of 24 microbeams (peak 12) for 30 and 50 keV beams, respectively.

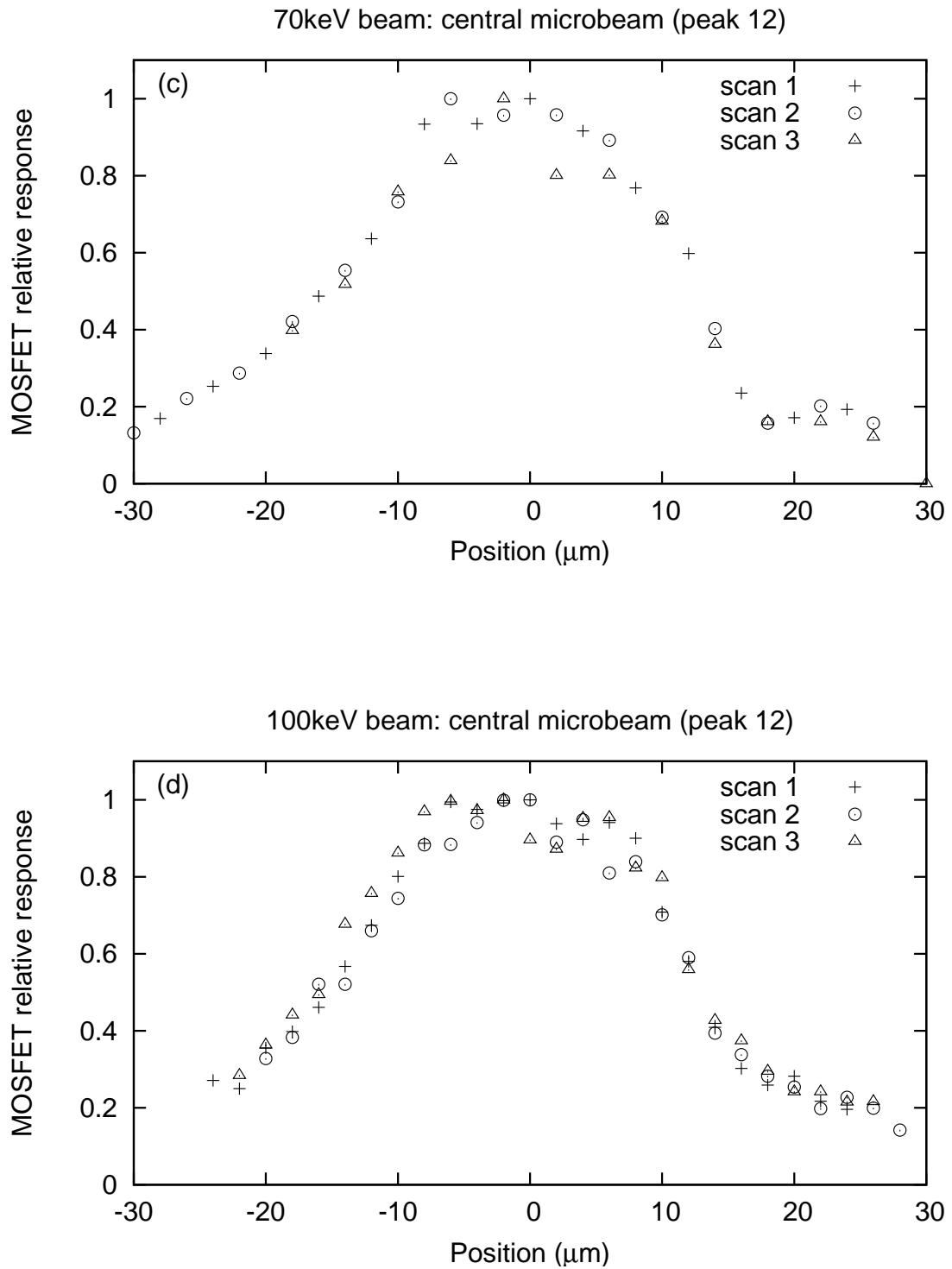


Figure 5.9: Dose profiles of monoenergetic microbeams measured at 1.1 cm depth (in perspex) with a MOSFET(L) dosimeter. Figures (c) and (d) show the dose profile of the central peak in an array of 24 microbeams (peak 12) for 70 and 100 keV beams, respectively.



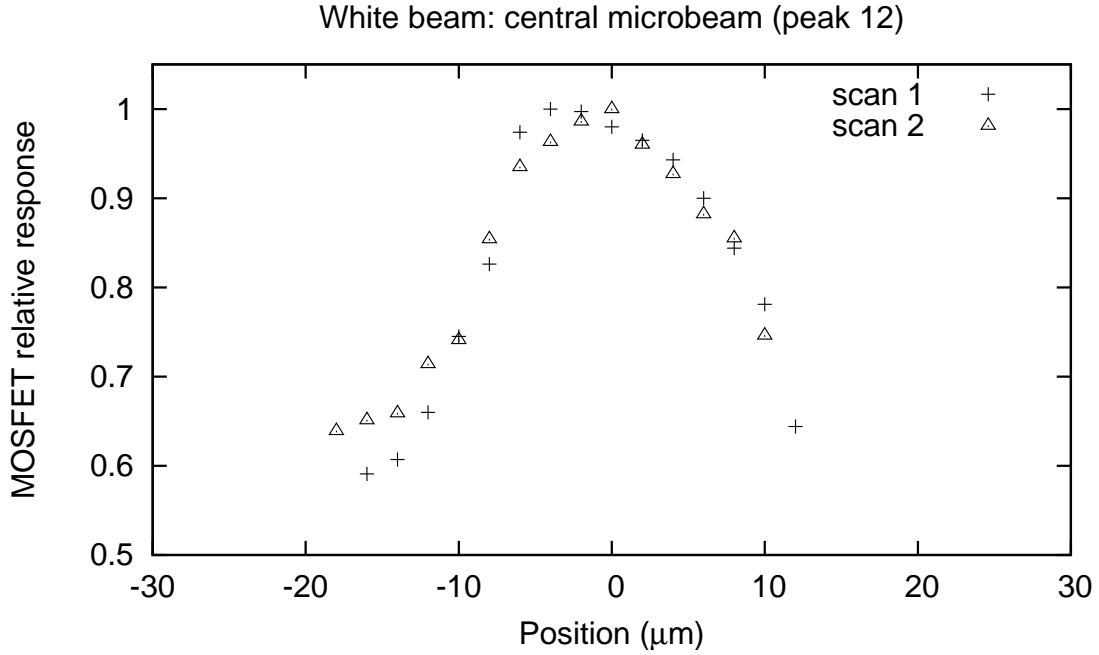


Figure 5.10: Dose profile of the central peak in an array of 24 microbeams (peak 12) obtained with the ESRF white beam and measured with a MOSFET(H) dosimeter at 1.1 cm depth (in perspex).

profiles in figure 5.12 reveals differences in their shape and FWHM. The measured profiles exhibit higher penumbral doses and an asymmetry about the peak centre which is not apparent in simulated profiles. In addition, the FWHM of the measured profiles varies by up to 3  $\mu\text{m}$ , while for simulated profiles it is approximately the same. Despite these differences, both the measured and simulated 30 keV microbeam profiles exhibit narrower peak doses than profiles obtained with higher energy beams. Beyond the edge of the microbeam (i.e. below the FWHM), the simulated profiles exhibit distinct differences in the penumbral dose, which suggests the FWHM is not a good measure of the changes in the beam profile with energy.

The variation in penumbral dose exhibited by simulated microbeam profiles of different energies can be explained by the range of scattered photons and electrons. For the case of a single microbeam in figure 5.13 (a), the distance from the peak at which the valley dose begins to level out corresponds to approximately the maximum range of photoelectrons in perspex. According to figure 5.15, this is about 15, 40, 70, and 120  $\mu\text{m}$

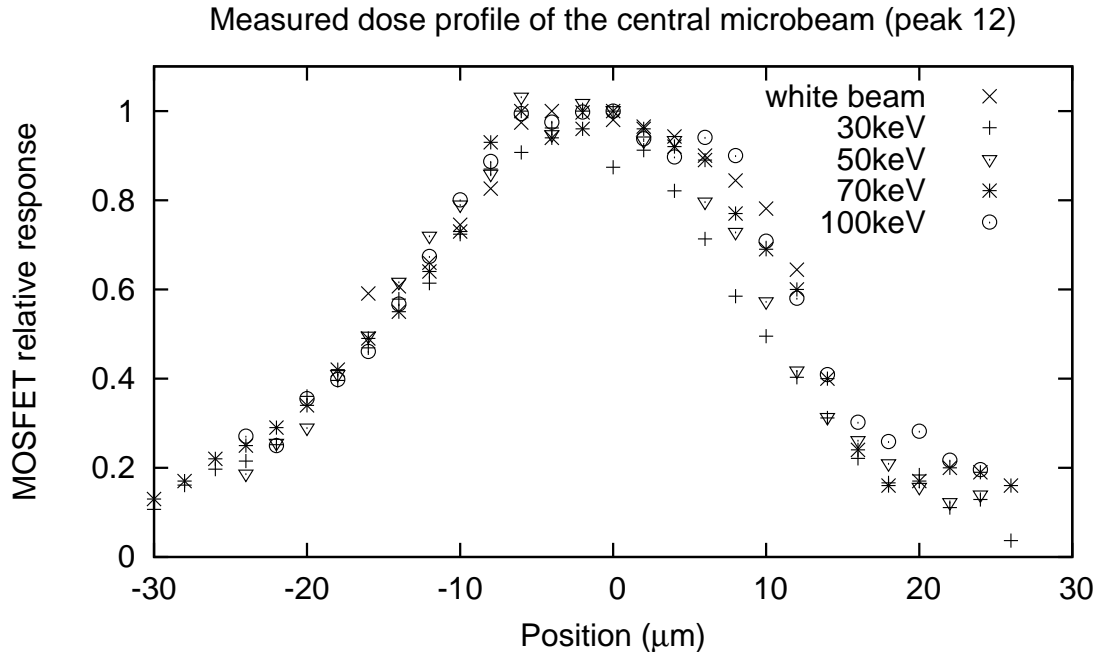


Figure 5.11: Comparison of the dose profile of the central peak in an array of 24 microbeams (peak 12) measured with a MOSFET at 1.1 cm depth (in perspex) for the white beam and monoenergetic beams of 30, 50, 70, and 100 keV.

for 30, 50, 70, and 100 keV electrons respectively. This is also indicated in the simulation results of figure 5.14, which shows the dose distribution of a single microbeam according to the type of initial photon interaction (i.e. Rayleigh scattering, photoelectric effect, or Compton scattering). For all beam energies, initial photoelectric interactions are primarily responsible for the penumbral dose extending over a distance approximately equal to the maximum range of photoelectrons (in perspex). Beyond this distance, most of the dose contribution is from primary photons undergoing Compton scattering, or to a smaller degree, Rayleigh scattering (whose cross section increases with decreasing energy).

The higher valley dose exhibited by peak 12 than by the single microbeam (refer to figure 5.13) is due to the superposition of overlapping valley dose tails of neighbouring microbeams within the array. Inside the peak region, most of the dose is from primary photons undergoing photoelectric or Compton scattering interactions. For the 30 keV beam, peak dose contributions are primarily from photoelectric interactions owing to its larger cross section at this energy. At higher beam energies of 50, 70 and 100 keV,

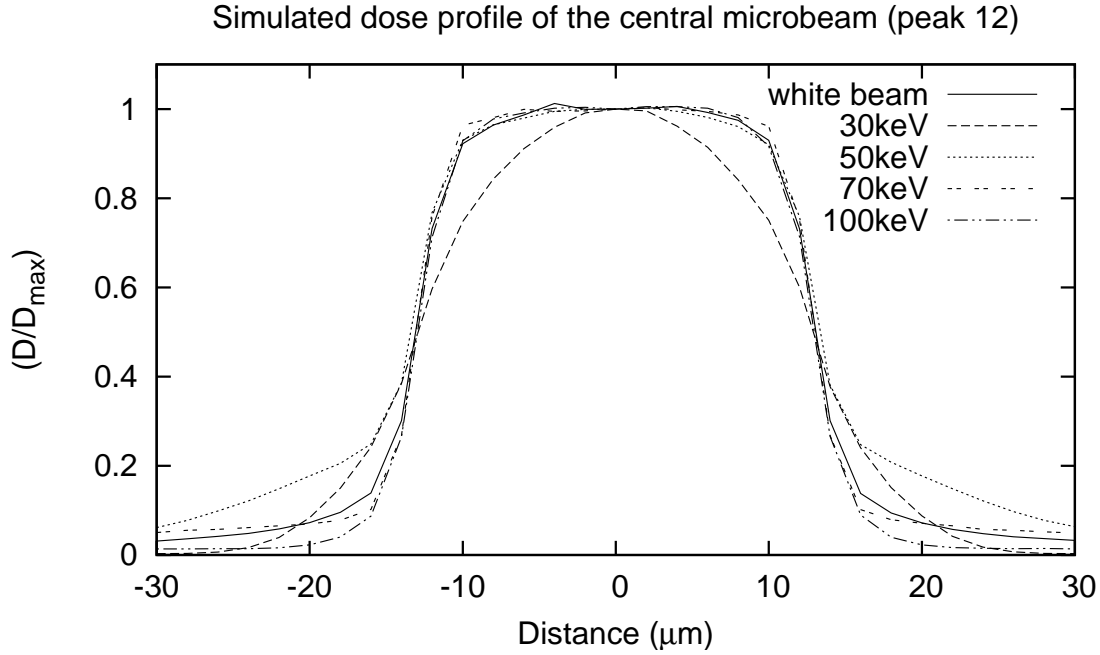


Figure 5.12: Simulated dose profile of the central microbeam in an array of 24 microbeams (peak 12) obtained at 1.1 cm depth (in perspex) for the white beam and monoenergetic beams of 30, 50, 70, and 100 keV.

however, most of the peak dose arises from Compton scattering as it is the dominant interaction mechanism at these energies. The lower valley dose exhibited by higher energy beams is due to the larger range of scattered photons, which enables some to contribute to neighbouring microbeams.

The simulated profiles do not exhibit the asymmetry observed in measured profiles. Considering the simulations were performed without a model of the MOSFET (i.e. its material composition was identical to that of the phantom), the asymmetry of the measured profiles is related to the construction and composition of the edge-on MOSFET. As shown in figure 5.7, the MOSFET comprises a micron-sized  $\text{SiO}_2$  sensitive volume ( $< 1 \mu\text{m}$  thick) positioned on top of a silicon substrate which is  $500 \mu\text{m}$  wide and  $1000 \mu\text{m}$  high. The MOSFET orientation used to scan the monoenergetic profiles from left to right was such that the sensitive volume led the silicon substrate. Since the height and peak-to-peak separation of microbeams were  $492.5 \mu\text{m}$  and  $412 \mu\text{m}$  respectively, the width of the MOSFET's substrate was able to span an entire peak and adjacent valley region. Hence,

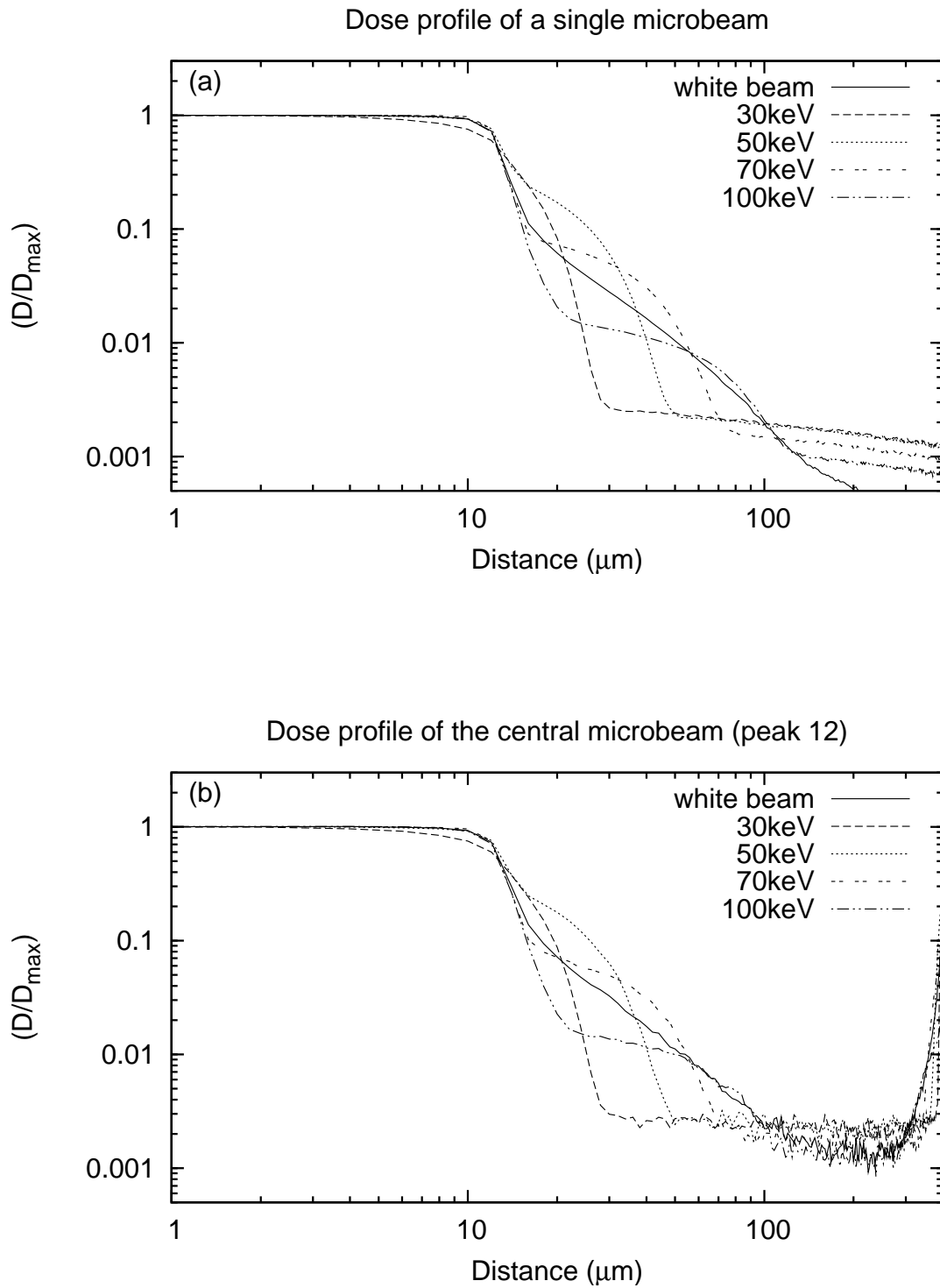


Figure 5.13: Simulated penumbral and valley dose of a single microbeam, and the central microbeam (peak 12) in an array of 24 microbeams. Figures (a) and (b) plot the dose profile of a single microbeam and peak 12, respectively, at 1.1 cm depth (in perspex) for the white beam and monoenergetic beams of 30, 50, 70, and 100 keV.

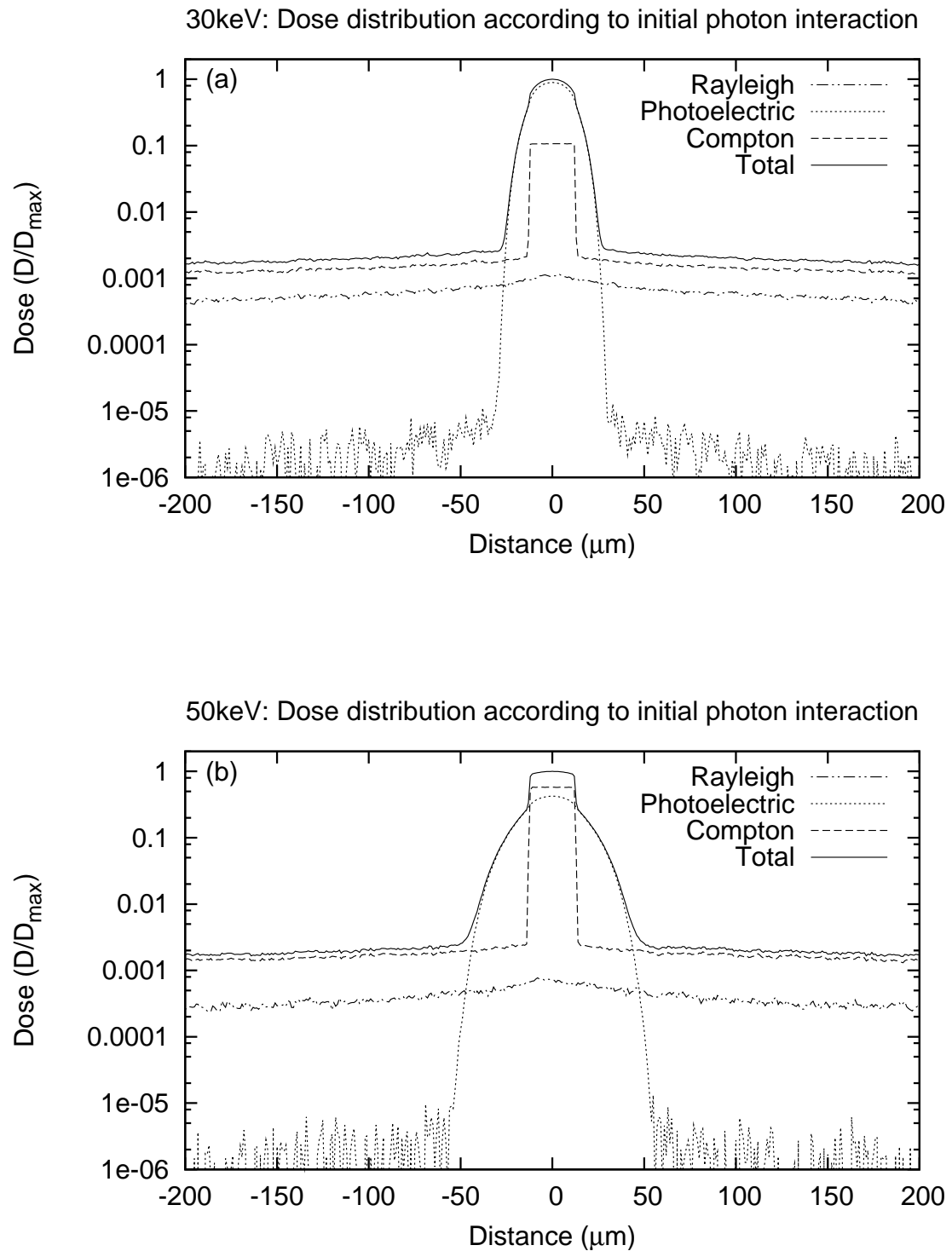


Figure 5.14: Simulated microbeam profile showing the dose distribution according to the type of initial photon interaction. Figures (a) and (b) plot the dose contributions of a single microbeam at 1.1 cm depth (in perspex) for monoenergetic beams of 30 and 50 keV, respectively.

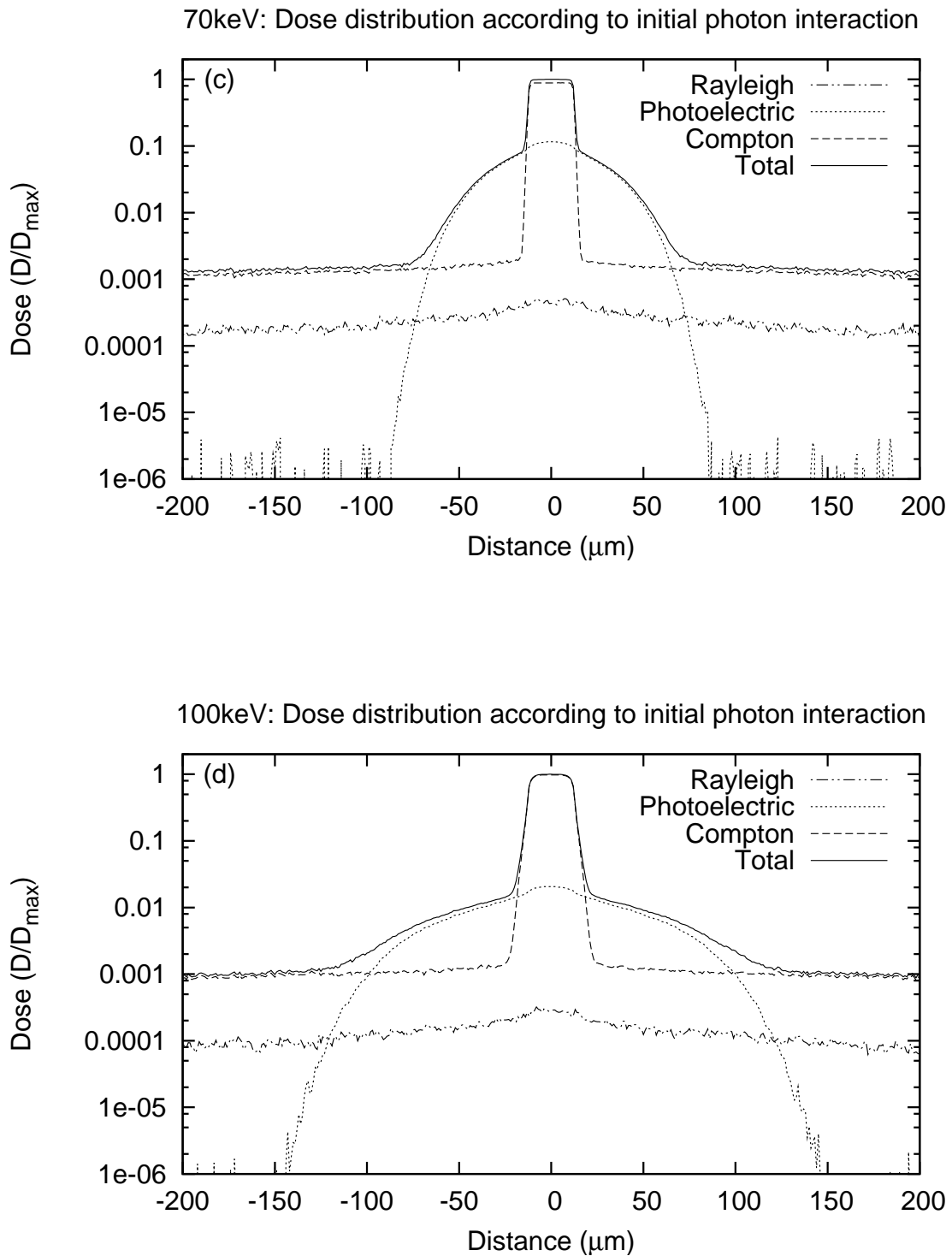


Figure 5.14: Simulated microbeam profile showing the dose distribution according to the type of initial photon interaction. Figures (c) and (d) plot the dose contributions of a single microbeam at 1.1 cm depth (in perspex) for monoenergetic beams of 70 and 100 keV, respectively.

when its sensitive volume was centred on a given peak, the substrate covered both the adjacent valley and peak regions to the left. Similarly, when the sensitive volume was positioned in the middle of the right valley region of a given peak, the substrate covered both the peak and valley regions to the left.

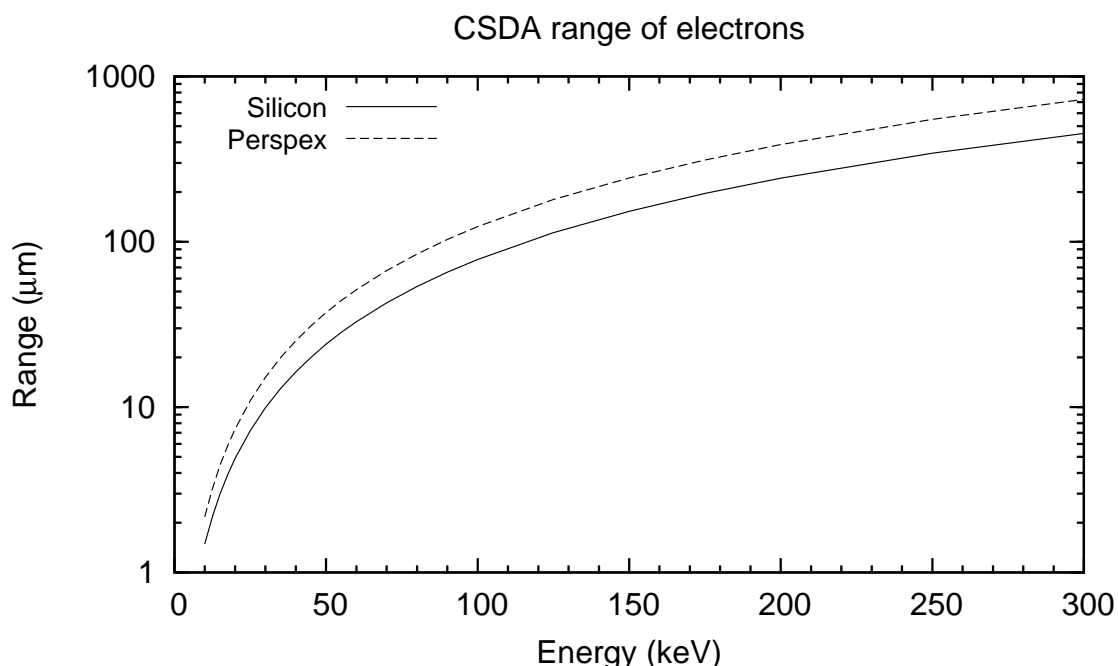


Figure 5.15: Comparison of the Continuous Slowing Down Approximation (CSDA) range of electrons in silicon and perspex [101].

The obscuration of microbeams by the silicon substrate would not present a problem if the photon and electron mass attenuation coefficients in silicon and perspex were equivalent. However, according to figure 5.15, the Continuous Slowing Down Approximation (CSDA) range of up to 300 keV electrons is about 40% lower in silicon than it is in perspex. For example, a 50 keV electron has a range of about 24  $\mu\text{m}$  in silicon compared with 37  $\mu\text{m}$  in perspex. Consequently, electrons traversing the silicon experience a higher mass energy attenuation coefficient than they would in perspex, resulting in fewer electrons reaching the sensitive volume. Photons of these energies, on the other hand, have longer ranges of the order of millimeters, and are hence less affected by the difference in mass attenuation coefficients. Considering the valley dose is primarily comprised

of scattered photons and electrons from the proximal peaks, fewer contributions from the left peak will reach the sensitive volume due to attenuation in the silicon substrate. This underestimation of dose is more apparent when the sensitive volume moves into the right penumbra of the peak (i.e. substrate covers the peak), since fewer photoelectrons reach the sensitive volume for detection. The same dose underestimation does not occur in the left penumbra as here the substrate obscures not the immediate peak, but the valley and peak regions to the left where dose contributions are substantially less.

The profiles obtained with the polyenergetic white beam exhibit an asymmetry that is the mirror of that observed in the monoenergetic profiles (i.e. lower dose in the left penumbral dose than in the right penumbra). This is because these profiles were scanned with the edge-on MOSFET rotated 180 degrees in the plane perpendicular to the beam, such that the silicon substrate led the sensitive volume.

Particle attenuation in the substrate was more severe with lower energy beams, where the FWHM of the 30 and 50 keV profiles were about 3  $\mu\text{m}$  and 2  $\mu\text{m}$  smaller than those obtained with 70 and 100 keV beams. According to the theoretical profiles in figure 5.12, these FWHM should be approximately equal apart from the 50 keV profile which is about 1  $\mu\text{m}$  larger. Since the photoelectric effect is the dominant photon interaction process in silicon below about 60 keV (refer to figure 5.16), the 3  $\mu\text{m}$  difference between the measured and theoretical 30 and 50 keV FWHM arises from the higher absorption of photoelectrons in the substrate prior to reaching the sensitive volume (where the range of a 60 keV electron is about 30  $\mu\text{m}$ ).

### 5.3.3 Measured and simulated peak-to-valley dose ratios (PVDRs)

Figure 5.17 shows the measured peak-to-valley dose ratio (PVDR) of the central microbeam (peak 12) obtained with monoenergetic beams of 30, 50, and 70 keV, and the polyenergetic white beam. The PVDRs of monoenergetic microbeams increased with increasing beam energy, where PVDRs of around 320, 400, and 460 were calculated for the 30, 50, and 70 keV beams respectively. The PVDR of the white beam, on the



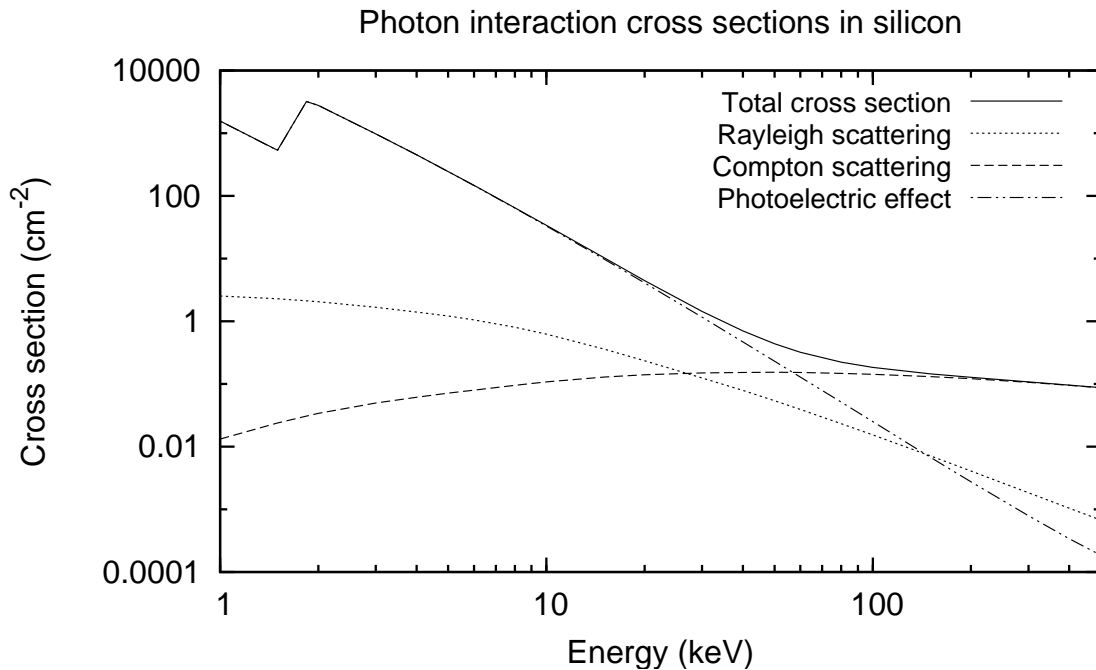


Figure 5.16: Photon interaction cross sections in silicon [36].

other hand, was substantially lower than that of the monoenergetic beams. According to the theoretical profiles in figure 5.13, the reduction in valley dose with increasing beam energy suggests the PVDR of the white beam (maximum intensity of 83 keV) should be higher than the PVDRs of the monoenergetic beams. This is shown in figure 5.18 with a comparison of the simulated PVDRs for different beam energies, where the PVDR increases with increasing beam energy.

For all beam energies, the measured PVDRs were lower than the theoretical values. For 30, 50, and 70 keV monoenergetic beams, the measured PVDRs were 46, 15, and 21% lower than the simulated values, while for the polyenergetic white beam the difference was more than a factor of two. The measured monoenergetic profiles also show an increase in PVDR between 30 and 50 keV which is not apparent in the corresponding simulated profiles. The PVDRs of the 30 and 50 keV theoretical profiles are almost identical, owing to their similar normalised valley doses.

The variation between the 30, 50, and 70 keV measured PVDRs is attributed not only to the different absorption cross sections of silicon and perspex as mentioned above,

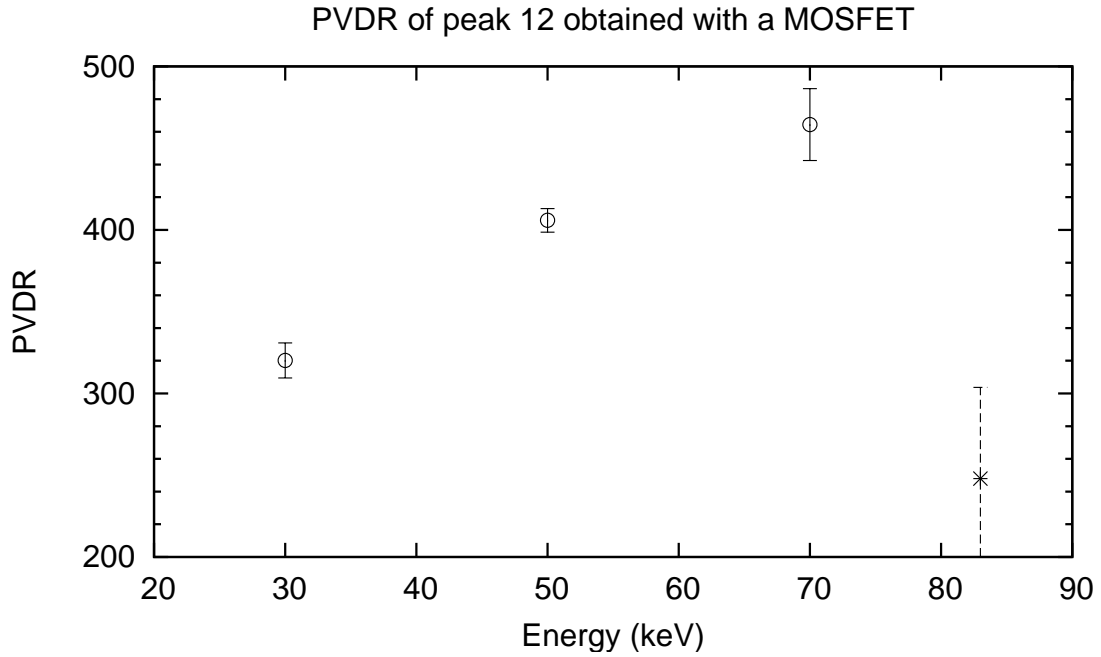


Figure 5.17: Measured PVDR of the central microbeam in an array of 24 (peak 12) calculated from peak and valley doses obtained at 1.1 cm depth (in perspex) for 30, 50, and 70 keV beams and the white beam (maximum intensity of 83 keV).

but also to a dose over-response of the MOSFET. As shown in figure 5.3, MOSFET dosimeters exhibit an overestimation of dose for photon energies up to a few hundred keV [92]. For the ‘T&N’ MOSFET, which is similar in design to the quadruple MOSFET used for MRT dosimetry in this thesis, the dose over-response occurs between about 30 and 200 keV, reaching a maximum of a factor of 3 at around 50 keV. Although the over-response occurs in both peak and valley regions, a larger effect can be seen in the peak owing to the higher photon fluence. As shown in figure 5.11, the effect of attenuation of electrons in the silicon substrate is greater for lower-energy beams due to the shorter range of electrons. Hence, the underestimation of peak dose and PVDR is greater for the 30 keV beam than for the higher energy beams.

It is a combination of the MOSFET’s over-response and attenuation of low-energy electrons in the silicon substrate that results in the larger PVDRs obtained with 50 and 70 keV beams. These factors, however, do not account for the underestimation of the PVDR measured for the white beam profiles. Considering the intensity of the white beam

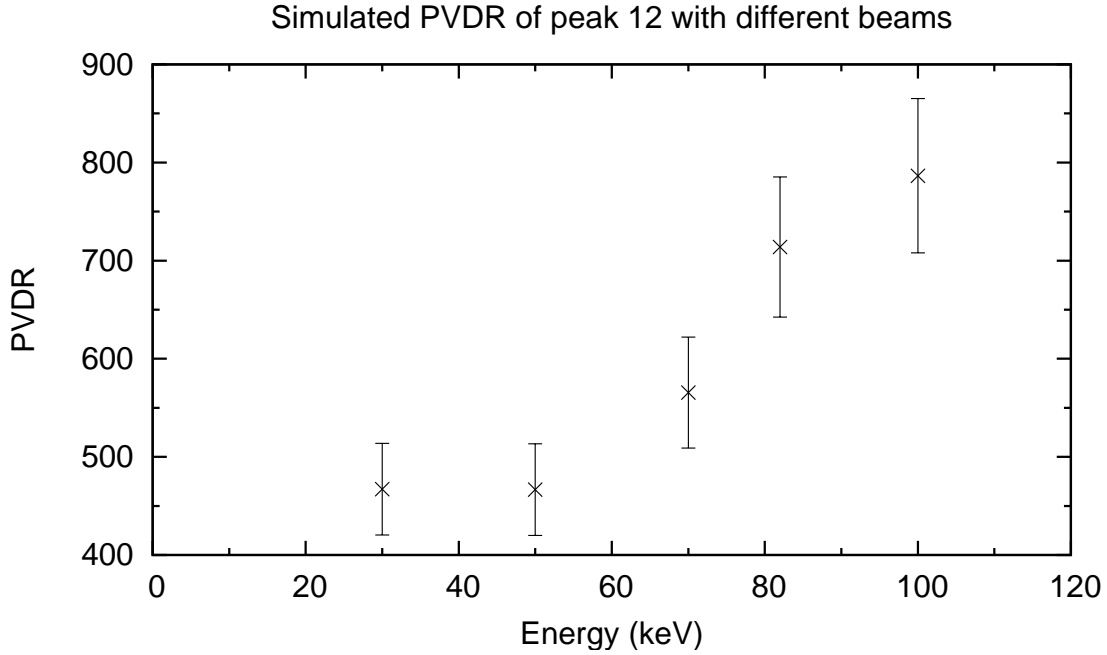


Figure 5.18: Simulated PVDR of the central microbeam in an array of 24 (peak 12) calculated from the theoretical dose profiles at 1.1 cm depth (in perspex) for 30, 50, 70, and 100 keV beams and the white beam (maximum intensity of 83 keV).

is substantially greater than those of monoenergetic beams, the underestimation of PVDR may be attributed to an under-response of peak dose caused by electric field screening (i.e. damping of electric fields by the presence of mobile charge carriers). This effect, which is known to occur in semiconductor materials exposed to intense electric fields, or high dose rates, increases the recombination of electron-hole pairs, thereby reducing the charge build-up in the gate oxide. One could further investigate this effect by measuring the dose response of the MOSFET in a peak region for different synchrotron storage-ring currents.

The fact that simulated PVDRs were higher than their measured counterparts may also be attributed to the simplified modelling of the MOSFET dosimeter whose composition was perspex (i.e. same material as the phantom) and sensitive volume was comparable to that of the scoring bins ( $0.0002 \times 0.2 \times 0.2 \text{ cm}^3$ ). Hence, the simulations did not account for the attenuation of electrons in the silicon substrate, nor the dose over-response which is characteristic of MOSFETs used at these photon energies. A Monte

Carlo study by De Felici *et al.* showed that modelling silicon detectors at depths of less than 2 cm in PMMA can yield up to 20% larger PVDRs than those obtained without a MOSFET model [16].

The higher simulated PVDRs may also relate to the use of scoring bins that were larger than the MOSFET's sensitive volume. This was done to ensure sufficient dose in valley regions, where little variation in the PVDR should arise as dose is integrated over the full height of the microbeam. It is also possible that the absence of beam polarisation models in the PENELOPE code may have introduced anomalies in the simulated valley dose since it neglects any alterations in dose distribution of scattered photoelectrons from polarised X-rays.

A comparison of measured and simulated PVDRs was also investigated for peaks 17 and 22 (i.e. 5th and 10th microbeams right of peak 12 when viewing the array from the source position). Figure 5.19 plots the measured PVDRs for peaks 12, 17, and 22 obtained with a 50 keV beam and polyenergetic white beam.

Both the 50 keV and white beam measured profiles exhibit an increase in PVDR with increasing microbeam number from the centre of the array (peak 12). For the 50 keV beam, the measured PVDRs of peaks 17 and 22 are about 15 and 25% larger than that of peak 12. A similar relationship is observed with the white beam, where the PVDRs of peaks 17 and 22 are around 25 and 30% larger than that of peak 12. This increase in PVDR for microbeams further from the centre of the array is commonly observed in MRT. It is brought about by the higher accumulative valley dose at the centre of the array from the superposition of overlapping dose tails of neighbouring microbeams. Since the valley dose has been shown to increase with decreasing beam energy (refer to figure 5.13), one would expect the PVDRs obtained with the white beam to be larger than those obtained with a 50 keV beam. This can be seen in figure 5.20, which plots the simulated PVDRs for an array of 24 microbeams for the 50 keV and white beams. Figure 5.21 plots the PVDRs of individual peaks within the array for different beam energies.

As observed with measured profiles, the PVDRs of simulated profiles also increase

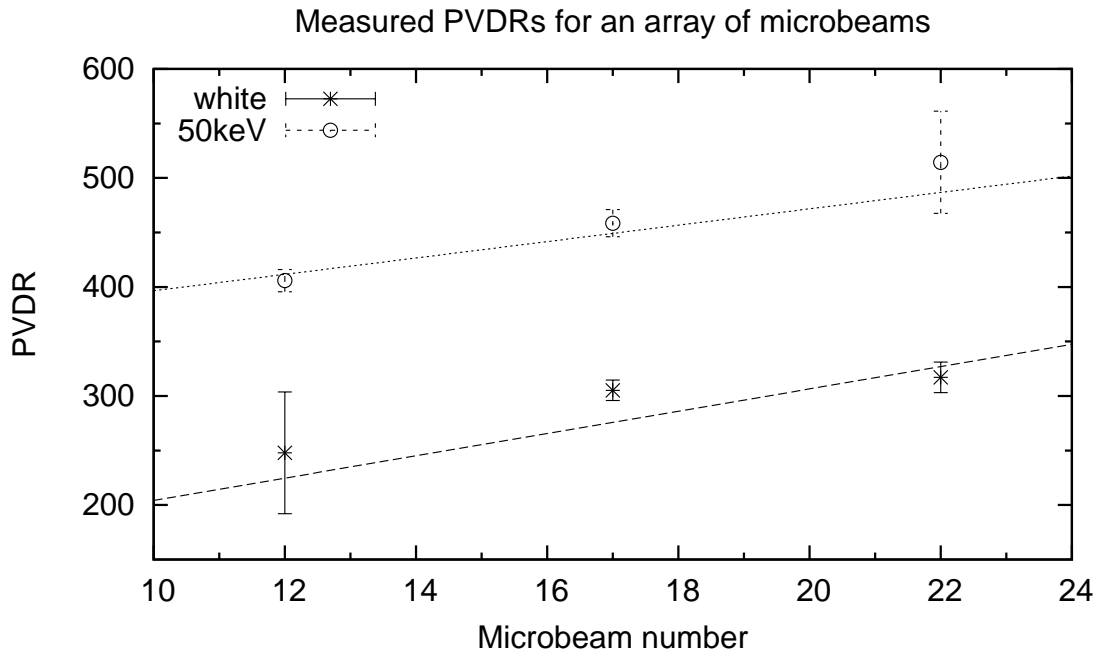


Figure 5.19: Measured PVDRs of microbeams 12, 17, and 22 (in an array of 24 microbeams) for the 50 keV and white beams, calculated from peak and valley dose measurements obtained with a MOSFET at 1.1 cm depth (in perspex).

for microbeams further from the centre of the array. This is due to the lower accumulative valley dose from overlapping dose tails of neighbouring microbeams at the edges of the array. The substantially larger PVDRs exhibited by the last two microbeams at either edge of the array suggest that valley dose contributions are significant only over two or three neighbouring microbeams. For the 50 keV beam, the measured and simulated PVDRs agree within uncertainties (i.e. within the variance of measured PVDRs, and  $\pm 3\%$  and  $\pm 10\%$  uncertainties in the peak and valley doses of simulated profiles, respectively). For the white beam, on the other hand, a substantial difference exists between the measured and simulated PVDRs, which is well outside the uncertainties. The difference may be attributed to electric field screening effects (mentioned above), which are characteristic of intense radiation. To a lesser extent, it may also stem from simplifications made in the model of the MOSFET dosimeter.

Measurements were also performed to investigate the PVDR at different depths in a

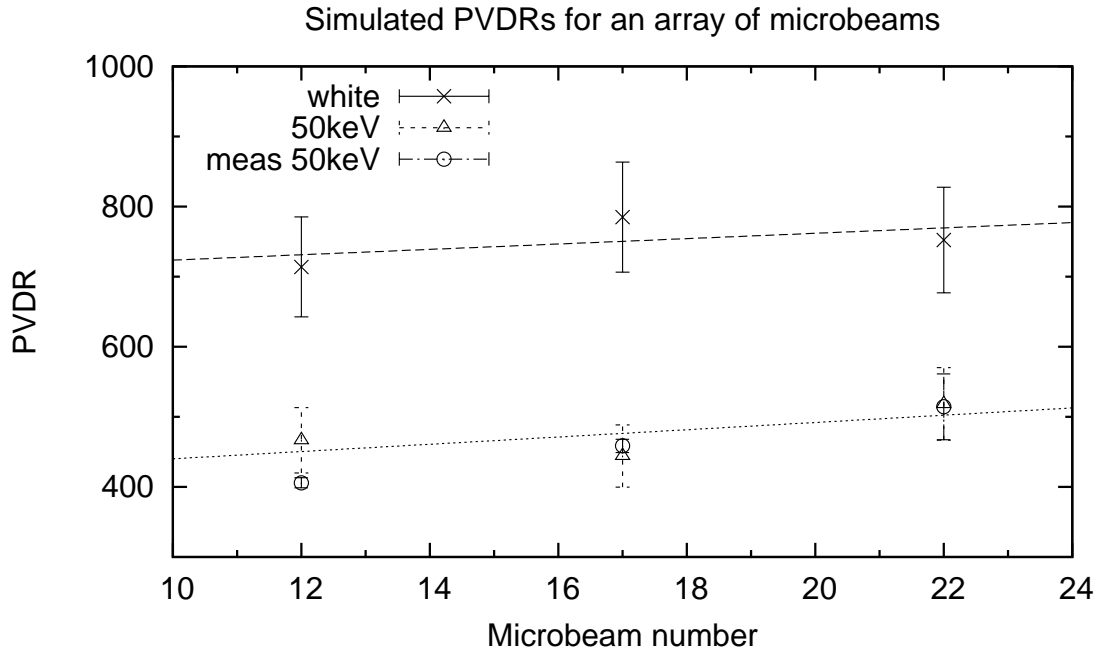


Figure 5.20: Simulated PVDRs of microbeams 12, 17, and 22 (in an array of 24 microbeams) for the 50 keV and white beams, calculated from the theoretical dose profiles obtained at 1.1 cm depth (in perspex). The 50 keV measured PVDRs (meas 50 keV) are also shown for comparison.

perspex phantom. This study used a MOSFET dosimeter to measure the peak and valley dose of an array of three microbeams (each  $25\ \mu\text{m}$  wide,  $492.5\ \mu\text{m}$  high, and separated by  $412\ \mu\text{m}$ ) at 0.9, 1.9, and 2.8 cm depths in perspex. Several peak and valley dose measurements were performed about the midpoint of the central peak (peak 2) and the valley regions on either side. All measurements were normalised to both the storage ring current and exposure time.

Figure 5.22 compares the measured and simulated PVDRs with depth in perspex for the array of three microbeams. The PVDR of the central microbeam (peak 2) was calculated using the peak dose and an average of the two valley doses on either side. While both measured and simulated profiles exhibited a decrease in the PVDR with increasing depth, the measured PVDRs were about 30% lower than those obtained from simulation. The difference between the measured and simulated results stems from the absence of modelling the silicon substrate and over-response of the MOSFET dosimeter.

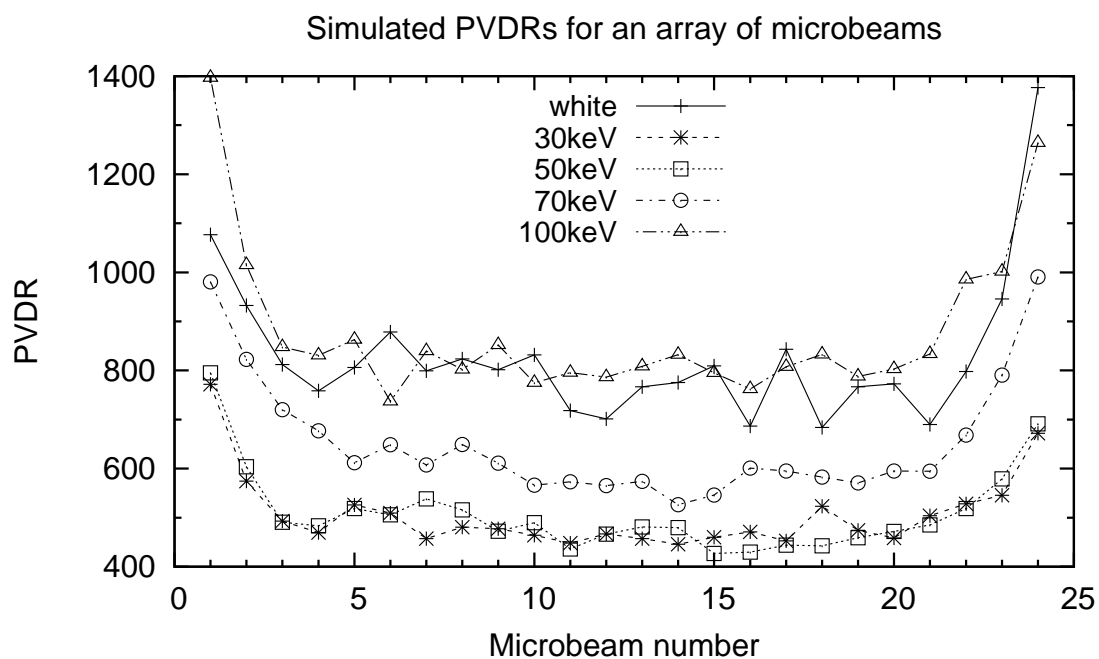


Figure 5.21: Simulated PVDRs for an array of 24 microbeams, calculated from the theoretical dose profiles obtained at 1.1 cm depth (in perspex) with the white beam and 30, 50, 70, and 100 keV monoenergetic beams.

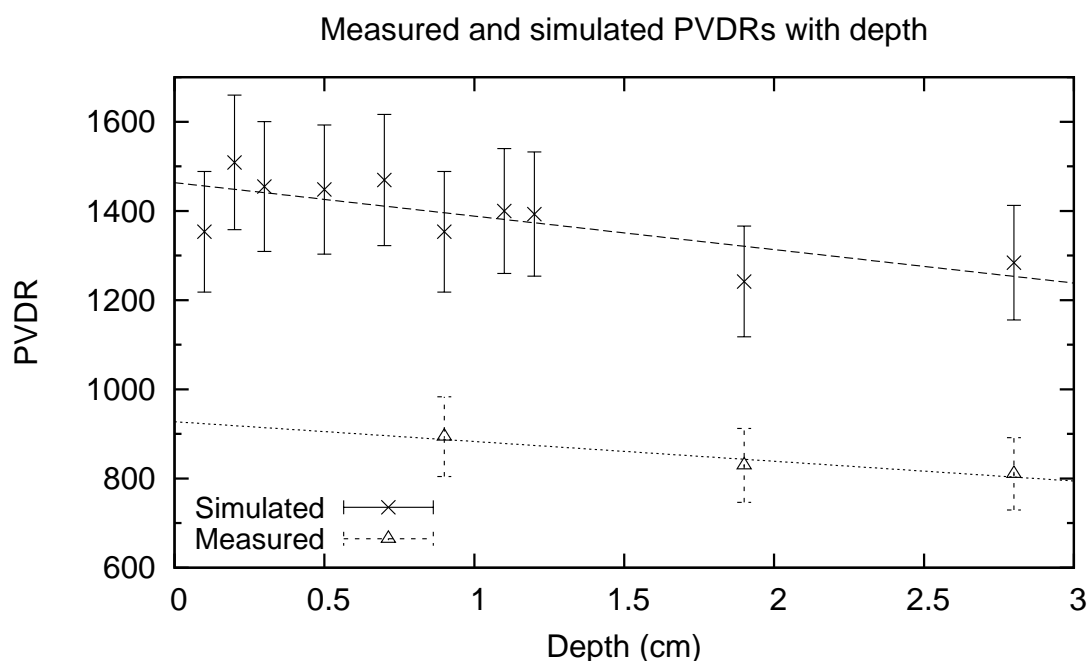


Figure 5.22: Measured and simulated PVDRs with depth (in perspex) for the central peak in an array of three microbeams (peak 2) produced with a white beam. The measured PVDRs were obtained at 0.9, 1.9, and 2.8 cm depth, and the theoretical PVDRs at various depths up to 1.2 cm.

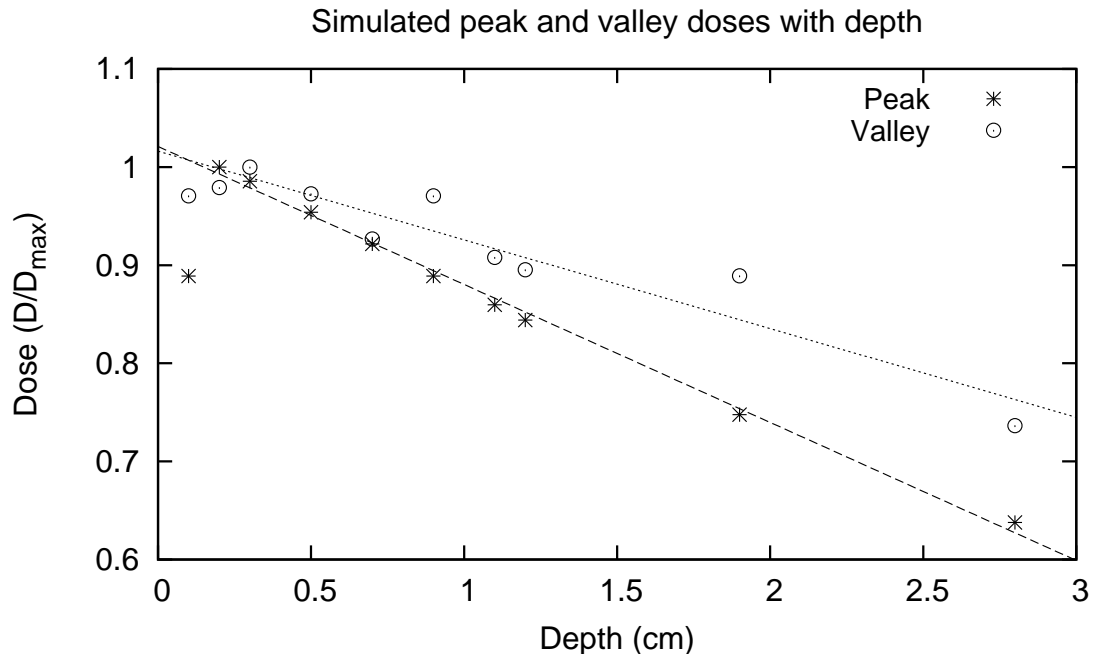


Figure 5.23: Simulated peak and valley doses for the central peak in an array of three microbeams (peak 2) up to 2.8 cm depth (in perspex). Peak and valley doses have been normalised to their maximum values.

The variation in PVDR with depth can be understood by examining the behaviour of peak and valley dose of the central microbeam (peak 2), which is plotted as a function of depth in figure 5.23. Both peak and valley doses have been normalised to their respective maximum values. The steady decrease in peak dose with increasing depth arises from the attenuation of photons. The initial increase in valley dose is from scattered photons and electron contributions, where beyond a depth of about 0.3 cm the valley can be seen to decrease with increasing depth. As the peak dose decreases with depth at a faster rate than the valley dose, so too does the PVDR. The higher PVDRs near the surface of the phantom are attributed to less photon attenuation in the peak and fewer scattered particles in the valley. These observations are consistent with the Monte Carlo simulation results obtained by Siegbahn *et al.* [25].



## 5.4 Conclusion

The falloff in linearity of radiation response of the MOSFET(L) dosimeter was less than that for the MOSFET(H) dosimeter. This is due to its thinner gate oxide and higher gate bias voltage (i.e. stronger external electric field), which reduces the effect of accumulated positive charge. The MOSFET(H) dosimeter, on the other hand, has a thicker gate oxide and therefore reaches saturation sooner (i.e. at lower doses). The larger falloff in response observed with the polyenergetic radiation when compared with monoenergetic beams is due to the higher intensity of the white beam.

The measured and simulated dose profiles exhibited differences in their shape and FWHM. Common to all measured profiles was an asymmetry about the peak centre which was not observed in the simulated microbeams. The difference in the left and right penumbral dose arises from the asymmetrical construction of the edge-on MOSFET, where the  $1\ \mu\text{m}$  wide sensitive volume is positioned on top of a  $500\ \mu\text{m}$  wide silicon substrate. As silicon has a higher mass attenuation coefficient than perspex, particles travelling through the substrate towards the sensitive volume are attenuated more than particles not obscured by the substrate. This leads to an underestimation of dose from short-range particles, such as low-energy electrons, which are absorbed in the substrate prior to reaching the sensitive volume for detection. This is particularly apparent when the substrate covers the peak region of a given microbeam (i.e. the sensitive volume is in the right penumbra), as here there exists a large population of short-range photoelectrons.

The measured dose profiles also exhibited a variation in FWHM with energy which was not observed in the corresponding simulated profiles. The FWHM of the 30 and 50 keV measured profiles were  $3\ \mu\text{m}$  smaller than the FWHM obtained with higher energy beams. This difference stems from the asymmetrical penumbral doses caused by particle attenuation in the silicon substrate, which was more apparent for the 30 and 50 keV profiles owing to the shorter ranges of particles).

The lower PVDRs for measured profiles relative to theoretical PVDRs were attributed to a combination of physical effects in MOSFET dosimetry and simplifications

in MOSFET modelling. While the simulated PVDRs for the 30 and 50 keV beams were approximately the same, the measured PVDRs exhibited a 25% increase between the two energies. For the measured 30 keV profile, the underestimation of peak dose and PVDR was due to particle attenuation in the silicon substrate. This was more apparent in the profiles of lower energy beams owing to the shorter ranges of particles, especially photoelectrons. The larger PVDRs of the 50 and 70 keV measured profiles can be attributed to the MOSFET's over-response to photons of these energies. Substantially smaller PVDRs were obtained for the white beam measured profiles than their simulated PVDRs due to an underestimation of peak dose caused by electric field screening and a simplified MOSFET model (comprised of perspex rather than silicon and SiO<sub>2</sub> materials). Hence, the simulations did not account for any particle attenuation in the silicon substrate or over-response of the MOSFET, both of which are characteristic at these photon energies. The absence of beam polarisation models in PENELOPE may have also had an effect on the simulated valley dose by not accounting for the altered dose distribution of scattered photoelectrons from polarised X-rays.

Both the measured and simulated PVDRs were found to increase toward the edges of the array. This is due to a higher accumulative valley dose at the centre of the array caused by overlapping dose tails of neighbouring microbeams. For the 50 keV profiles, the measured and simulated PVDRs for peaks 12, 17, and 22 in the array agreed within uncertainty. The corresponding PVDRs obtained with the white beam, however, exhibited a substantial difference between measured and simulated values. The smaller PVDRs obtained for the measured profiles were due to an underestimation of peak dose caused by electric field screening and simplifications of MOSFET modelling.

A reduction in PVDR with increasing depth was also observed for the measured and theoretical profiles. Simulations of the peak and valley dose with depth, revealed a reduction in the peak dose owing to photon attenuation. The reduction in peak dose was faster than that in the valley, resulting in smaller PVDRs with increasing depth. The higher PVDRs at shallower depths was therefore due to less photon attenuation in the

peak and fewer scattered particles in the valley.

Despite the drawbacks of particle attenuation and dose over-response, the edge-on MOSFET remains the only real-time dosimeter capable of micron, or sub-micron, resolution. With advances in technology, the feasibility of reducing the 500  $\mu\text{m}$  width of the silicon substrate to minimise particle attenuation will soon be realised. The use of a thinner substrate and an appropriate calibration curve (to correct for MOSFET response as a function of photon beam energy and dose rate) may improve the viability of MOSFET dosimetry in MRT.

An alternative real-time dosimeter for use in MRT is the silicon strip detector<sup>4</sup>. This device will be used to measure the peak and valley doses for individual microbeams in an array, as well as the instantaneous PVDR for an entire microbeam array. It comprises 128 strips of  $\text{p}^+$  p-n junctions (each 20  $\mu\text{m}$  wide, 500  $\mu\text{m}$  high, and spaced 200  $\mu\text{m}$  apart) bound to a 375  $\mu\text{m}$  thick n-type silicon substrate. The detector will also be used to instantaneously trigger beam stoppage in the event that an undesirable dose is administered to a patient undergoing MRT, where treatment times are in the order of milliseconds.

---

<sup>4</sup>The silicon strip detector is currently under development at the Centre for Medical Radiation Physics at the University of Wollongong, Australia.

## CHAPTER 6

### MAGNETO-MRT: INFLUENCE OF A MAGNETIC FIELD ON MICROBEAM PROFILES

#### 6.1 Introduction

This chapter investigates the potential for the application of magnetic fields in Microbeam Radiation Therapy (MRT), or magneto-MRT, to alter the dose profiles of microbeams and hence the effectiveness of the treatment.

Minimising valley dose in order to increase the survival of normal cells needed for tissue repair is an ongoing challenge in MRT. The valley dose comprises a superposition of energy depositions from electrons and photons that laterally scatter from peak regions. As shown in figure 6.1, a large component of the valley dose is produced by scattered secondary electrons [25].

In chapter 4, the application of transverse magnetic fields to high-energy photon beams was shown to alter the distribution of low-energy electrons (less than 1 MeV for a 15 MV beam). This alteration was brought about by a change in the trajectories of electrons whose ranges were comparable to or greater than their cyclotron radii. In MRT at the European Synchrotron Radiation Facility (ESRF), the polyenergetic X-ray (white) beam has a mean energy of 107 keV and a maximum intensity at 83 keV (refer to figure 5.4). According to the simulation results of first generation electrons<sup>1</sup> in figure 6.2, most secondary electrons have an energy less than 30 keV and a range (in perspex) of less than 15  $\mu\text{m}$ . As an electron loses energy the radius of curvature of its path decreases. This begs the question of whether the application of a magnetic field during MRT could

---

<sup>1</sup>First generation electron spectrum of the ESRF white beam simulated with Monte Carlo PENELOPE using  $10^8$  primary photon histories.

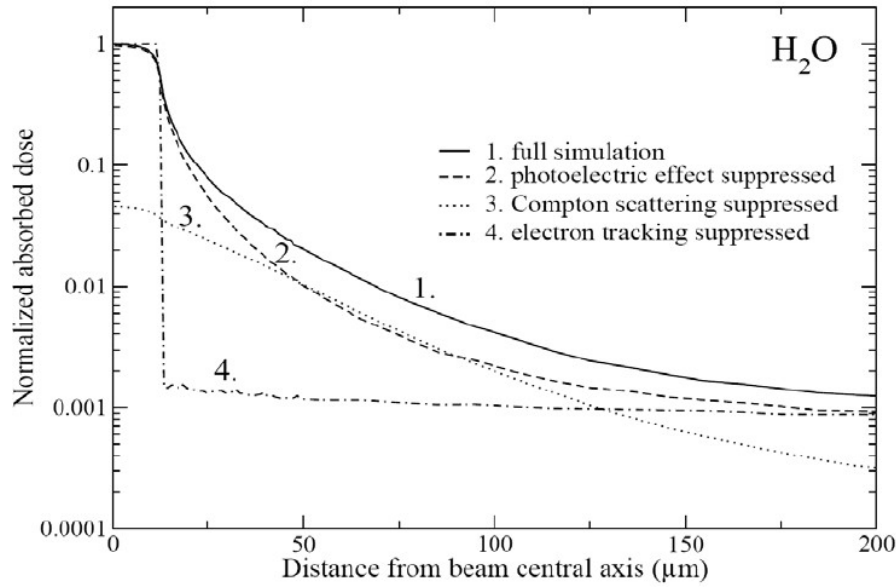


Figure 6.1: Impact of different types of interaction on the lateral dose profile of a single microbeam ( $25\ \mu\text{m}$  wide) obtained with the ESRF white beam. Curve 1 plots the microbeam profile comprising all interaction contributions. Curves 2, 3, and 4 plot the profile with suppression of the photoelectric effect, Compton scattering, and electron tracking, respectively [25].

alter the low-energy electron distribution to produce a change in the dose profile of microbeams, and in particular, the peak-to-valley dose ratio (PVDR).

According to figure 3.1, the range of a 100 keV electron becomes smaller than its cyclotron radius (in water) at magnetic fields less than about 7 T. For electrons below 100 keV, the range decreases at a faster rate than the reduction in cyclotron radius at a given magnetic field. Therefore, we would only expect to see an effect on the electron distribution and PVDR at magnetic fields of about 10 T or stronger. However, an EGS4 Monte Carlo study by Orion *et al.* [102] has shown that a 6 T longitudinal magnetic field applied to a single 20 keV microbeam ( $30\ \mu\text{m}$  wide) can reduce the penumbral width by a few microns. This result contradicts our hypothesis as the range of a 20 keV electron is about one order of magnitude smaller than its cyclotron radius at 6 T. Absent from the literature are other studies confirming this effect.

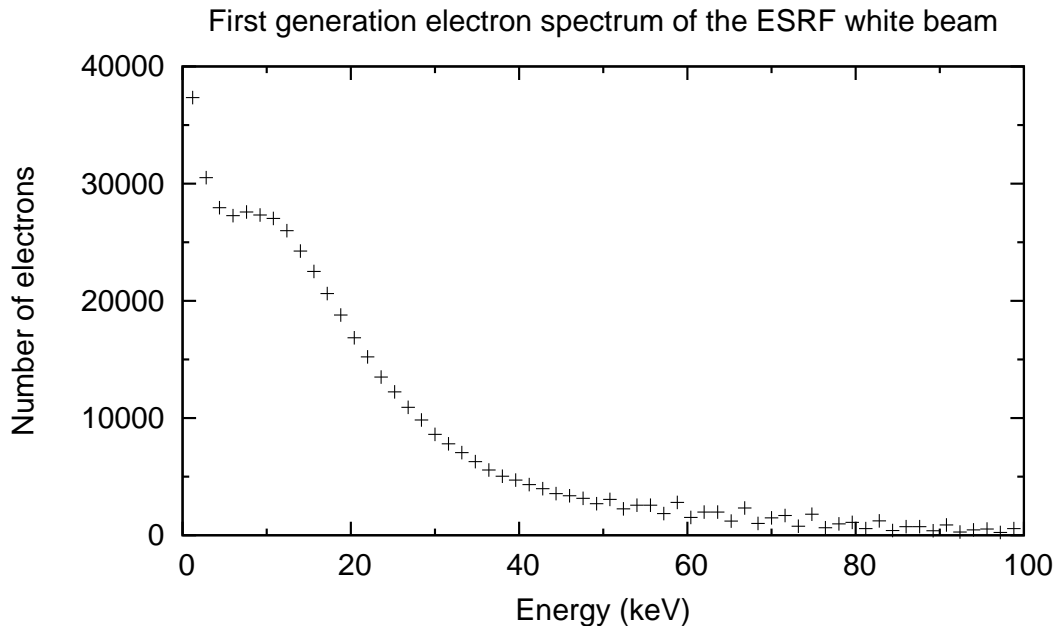


Figure 6.2: Simulated first generation electron spectrum of the white beam (in perspex).

This chapter uses a combination of experiments and Monte Carlo PENELOPE simulations to investigate the effect of transverse and longitudinal magnetic fields on the lateral dose profiles and PVDRs of microbeams. Measurements of peak and valley dose were performed separately with both MOSFET and radiochromic film dosimetry. MOSFET dosimetry was discussed in chapter 5 (refer to section 5.1.2). Radiochromic film comprises monomer crystals in a gel fixed to a Mylar substrate [103]. When irradiated, the energy deposition of particles initiates polymerisation of the monomers causing the film to change colour from light to dark blue. The dosimetry in the present work used HD-810 Gafchromic film<sup>2</sup>, which has a high spatial resolution of around 600 line pairs per mm<sup>-1</sup> [88]) and a dose range between 10 and 400 Gy. The dose response is linear below about 250 Gy [104], although it is possible to use the film at higher doses provided one uses appropriate dose calibration curves to interpret the results [103]. Since radiochromic film continues to polymerise for several hours post-irradiation, the film analysis<sup>3</sup> was performed the day after exposure.

<sup>2</sup>HD-810 Gafchromic film manufactured by ISP Technologies, NJ, USA.

<sup>3</sup>Film analysis used an Epson scanner and a set of calibration films to convert optical density to dose.

## 6.2 Materials and methods

The magneto-MRT experiments were conducted on the ID-17 biomedical beamline at the ESRF using three different magnet devices.<sup>4</sup> Each device was capable of producing either a transverse or longitudinal magnetic field up to a few Tesla. Measurements of the peak and valley doses, and hence, the PVDR were obtained with either Gafchromic film or a MOSFET embedded in a perspex phantom (perspex has a similar density to that of a human brain).

### 6.2.1 Magneto-MRT with a transverse magnetic field

The transverse magnetic field device used in the magneto-MRT experiments is shown in figure 6.3. The device comprises a pair of square NdFeB permanent magnets<sup>5</sup>, each  $5 \times 5 \times 2.5 \text{ cm}^3$  (width  $\times$  height  $\times$  depth) with a surface field of 1 T at the centre. A magnet pole separation of 0.5 cm generated a 1 T static transverse magnetic field<sup>6</sup>, where the direction of the field was orientated towards the handle of the device.

For magneto-MRT measurements, the magnet device was mounted on the goniometer stage (inside the MRT experiment hutch) as shown in figure 6.3. A MOSFET was positioned at 0.9 cm depth in a  $0.5 \times 2 \times 5 \text{ cm}^3$  (width  $\times$  height  $\times$  depth) perspex phantom, which was wedged between the magnet poles (0.5 cm separation). The lateral dose profile of an array of three microbeams (each  $25 \mu\text{m}$  wide,  $492.5 \mu\text{m}$  high, and separated by  $412 \mu\text{m}$ ) was measured with the 1 T transverse magnetic field using a wiggler gap of 75 mm (instead of the minimum gap of 24.8 mm often used for MRT). The larger gap reduced the intensity of the beam so that the entire dose profile could be measured with a single MOSFET. At the completion of the scan, the wiggler gap was reduced to 24.8 mm and peak and valley dose measurements of the microbeam array were obtained in the presence and absence of the 1 T transverse magnetic field.

---

<sup>4</sup>Magnet devices constructed at the Centre for Medical Radiation Physics, University of Wollongong, Australia.

<sup>5</sup>Square NdFeB magnets supplied by JWB Engineering, Bulli, NSW Australia.

<sup>6</sup>Magnetic field measured using a Daley electronics Pty Ltd Teslameter T-22A.

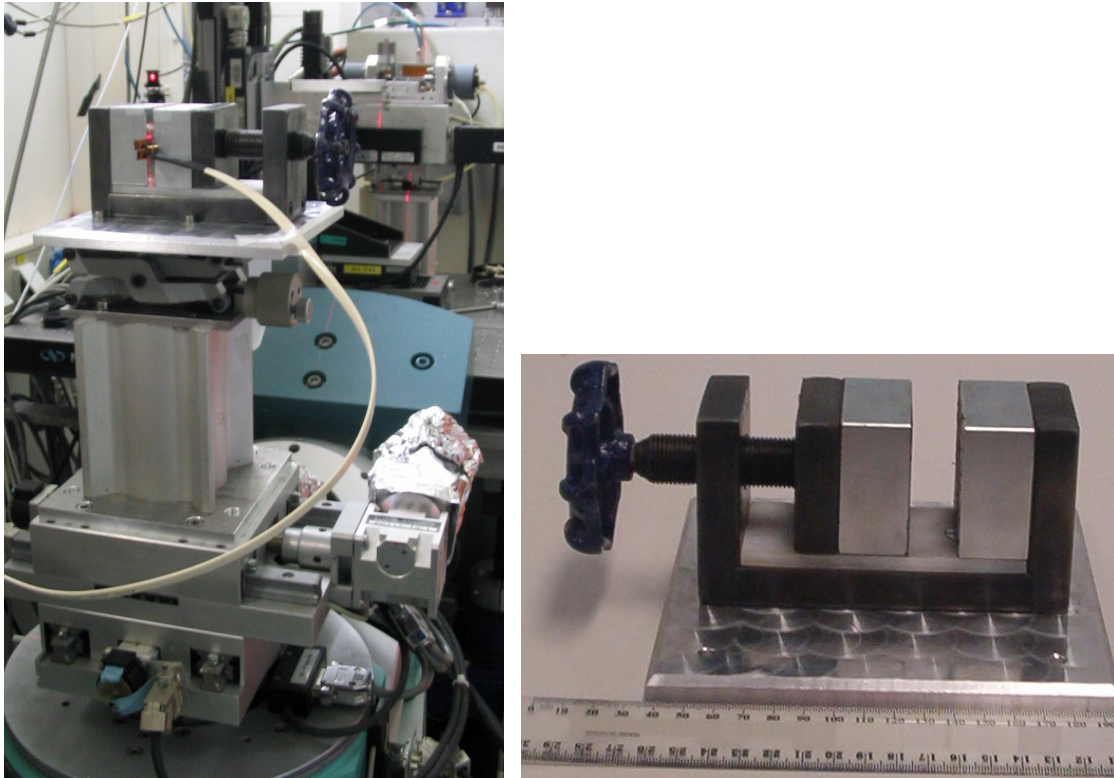


Figure 6.3: Photos of the 1 T transverse magnetic field device used for magneto-MRT experiments (direction of magnetic field is towards the handle). The magnet device (right) was mounted on the goniometer stage, where a perspex phantom containing a MOSFET was wedged between the magnet poles (left).

For the peak dose measurements, the MOSFET was moved into the centre of the middle peak in the array (peak 2), where it was subjected to a 0.03 s pulse of radiation. Valley dose measurements were performed in the centre of the valley regions to the left and right of peak 2,  $V_{12}$  and  $V_{23}$  respectively, using radiation pulses of 3 s duration. For peak and valley dose measurements obtained in the absence of magnetic field, the magnet apparatus was replaced by a pair of steel dummy magnets of the same dimensions and separation to maintain scatter conditions. All peak and valley dose measurements were normalised to the synchrotron storage ring current and radiation exposure time. PVDRs were calculated from the peak and valley dose measurements obtained with and without magnetic field.



## 6.2.2 Magneto-MRT with a longitudinal magnetic field

### 6.2.2.1 Permanent magnet devices

The influence of a longitudinal magnetic field on the dose profiles of microbeams was investigated with a modified version of the above transverse magnetic field device. As illustrated in figure 6.4, a 0.3 cm diameter hole was drilled through the centre of each NdFeB magnet to allow passage of the microbeam array parallel to the magnetic field. A pair of focus cones were fixed to the inside surface of each magnet to concentrate the magnetic field lines, where a separation of 0.5 cm produced a field strength of about 1 T.

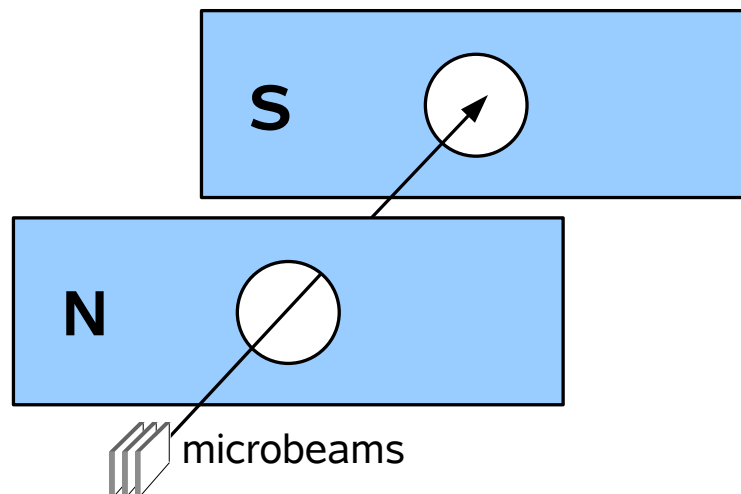


Figure 6.4: Illustration of the 1 T longitudinal magnetic field device used for magneto-MRT experiments. A 0.3 cm diameter hole was drilled through the centre of the permanent magnets to allow the passage of microbeams parallel to the direction of magnetic field.

Film dosimetry was used to obtain the lateral dose profile of an array of three microbeams (each  $25\ \mu\text{m}$  wide,  $492.5\ \mu\text{m}$  high, and separated by  $412\ \mu\text{m}$ ) in the presence and absence of a longitudinal magnetic field at different depths in perspex. For the profiles obtained with magnetic field, strips of Gafchromic film<sup>7</sup> were placed between 0.1 cm-thick perspex sheets. These sheets were wedged between the magnet focus cones

<sup>7</sup>Strips of Gafchromic film ( $110\ \mu\text{m}$  thick) were cut from one sheet and orientated in the same direction to minimise variation in dose response.

where dose profiles of the array were obtained at 0.1, 0.2, 0.3, and 0.4 cm depths. The effect of magnetic field on the peak profile of microbeams was investigated with an MRT peak dose of 500 Gy. The effect on the valley dose, on the other hand, was investigated with an MRT peak dose of 60 000 Gy in order to raise the level of valley dose to sit within the sensitive range of the Gafchromic film.

For measurements in the absence of magnetic field, the magnet device was replaced with a pair of dummy magnets to maintain similar scattering conditions. These were fashioned from steel (similar density to NdFeB) with the same dimensions as the permanent magnets. A stack of 0.1 and 0.2 cm-thick perspex sheets were wedged between the dummy magnets, where strips of Gafchromic film were placed at depths of 0.1, 0.2, 0.7, 1.1, and 1.2 cm (separation between dummy magnets was adjusted to allow dose profiles to be measured at depths beyond 0.5 cm).

Prior to constructing the above longitudinal magnet device, a series of Monte Carlo simulations were performed to investigate whether the passage of microbeams through the magnet device would generate any additional scattering. The simulations used a model of the 1 T longitudinal magnet device described above, using three different magnet materials: NdFeB, perspex, and air. This was done to compare the scattering contributions of the NdFeB magnets to no magnets (i.e. air replacing the magnets), and also the effect of more back scattering material (i.e. perspex replacing the magnets). A cylindrical scoring volume of 0.3 cm diameter  $\times$  5.6 cm depth occupied the cavities inside the magnets and part of the region between the magnets. The section inside magnet 1 and magnet 2 (magnet 1 was upstream of magnet 2) was modelled as air, and the section between the magnets was modelled as perspex. The remaining volume between the magnets, not already occupied by the cylindrical perspex volume, was modelled as air. The array of three microbeams was approximated as a pencil beam of 850  $\mu\text{m}$  (i.e. diameter equal to width of microbeam array). The initial direction of the beam was along the central axis, and the photon energy was sampled from the ESRF white beam spectrum. The

simulations were performed with electron and photon energy cutoffs of 0.1 and 1 keV respectively, and  $10^8$  primary photon histories. The dose was scored on axis in cylindrical bins of 0.15 cm diameter and 0.05 cm depth.

Figure 6.5 (a) plots the depth-dose profile of the pencil beam for different magnet materials (NdFeB, perspex, and air) in three regions along central axis: air cavity 1 (inside magnet 1), perspex phantom (between the magnets), and air cavity 2 (inside magnet 2). The simulations were repeated with the air cavity inside magnet 2 replaced with perspex to investigate the effect of additional backscattering material. The corresponding dose profile obtained for this setup is shown in figure 6.5 (b). The depth-dose profile obtained with NdFeB magnets exhibited up to 20% larger dose in both air cavities than the profiles obtained with perspex or air magnets. When perspex was inserted into air cavity 2, the depth-dose profiles in this region were the same as those obtained in the absence of magnets (i.e. air). Replacing the NdFeB magnet material with perspex resulted in the same depth-dose profile (within uncertainties) as that obtained without magnets.

Simulations were also performed to determine the effect of magnet scatter contributions on the radial dose inside the air cavities and perspex phantom. For these simulations, the dose was scored in concentric cylindrical volumes whose annuli were separated by 0.005 cm using identical simulation parameters as used previously. Figure 6.6 (a) plots a ratio of the radial dose obtained with and without NdFeB magnets at: the exit of air cavity 1 (i.e. 2.48 cm depth), 1 and 4 mm depth in perspex (i.e. 2.60 and 2.90 cm depth), and at the entrance to air cavity 2 (i.e. 3.02 cm depth). The simulations were repeated replacing the air in cavity 2 with perspex, to provide additional scattering material. A plot of the radial dose at the same depths is shown in figure 6.6 (b). Simulations were also performed to obtain the radial dose with and without perspex magnets (instead of NdFeB). A ratio of the radial dose in the presence and absence of NdFeB magnets is shown in figure 6.6 (c).

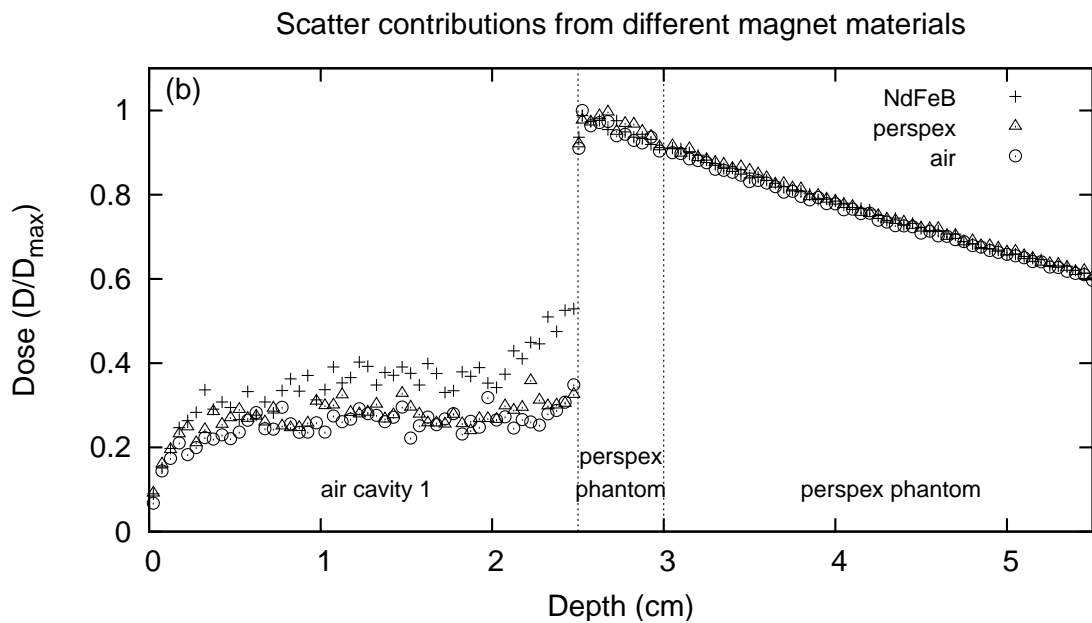
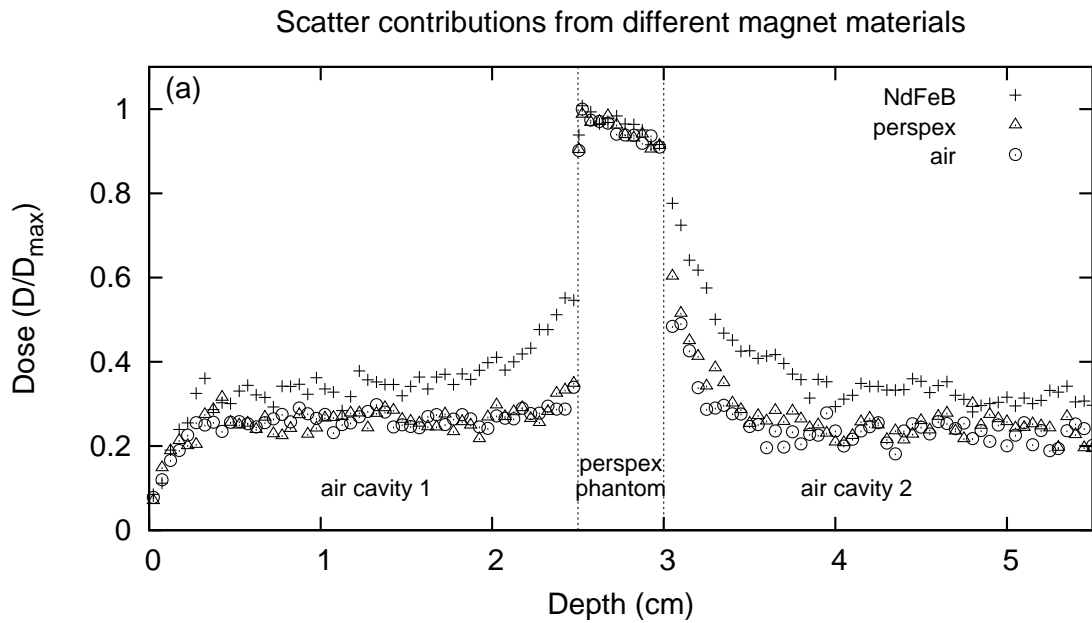


Figure 6.5: Scatter contributions from different magnet materials. Figure (a) plots the depth-dose profile of a pencil beam simulated with different magnet materials (NdFeB, perspex, and air) in three regions along central axis: air cavity 1, perspex phantom, and air cavity 2. Figure (b) plots the depth-dose profile with perspex replacing the air in cavity 2.

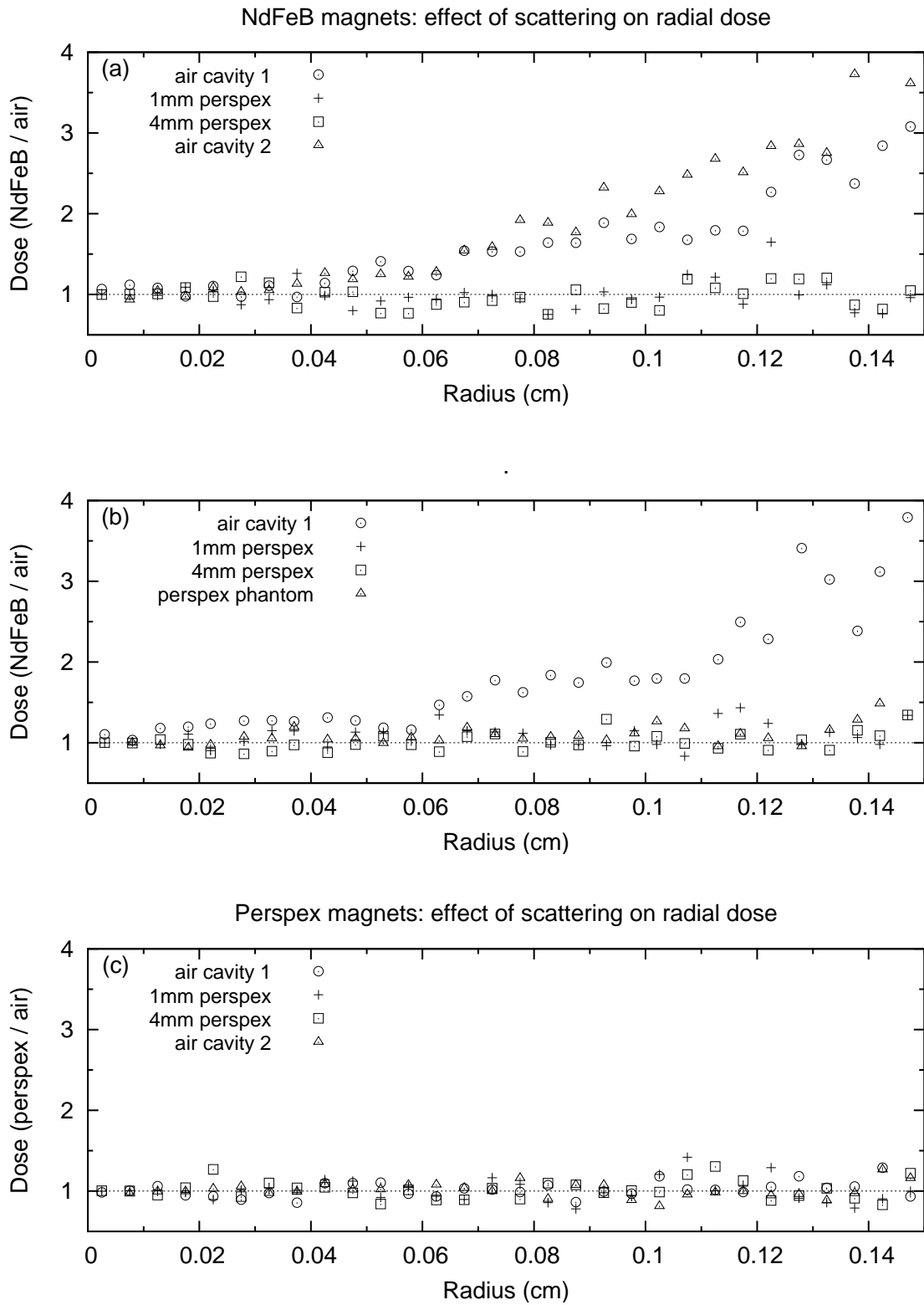


Figure 6.6: Effect of magnet scatter contributions on the radial dose. Figure (a) plots a ratio of the radial dose with and without NdFeB magnets, at the following depths: 2.48 cm (exit of air cavity 1), 2.60 and 2.90 cm (1 and 4 mm depth in perspex), and 3.02 cm (entrance to air cavity 2). Figures (b) and (c) plots the corresponding radial dose with perspex magnets instead of NdFeB, and perspex replacing the air in cavity 2.

Inside the perspex phantom at 1 and 4 mm depth, the ratio of radial dose with and without NdFeB magnets is unity. A ratio of unity is also observed inside the air cavities up to a radial distance of about 0.05 cm from the central axis. Beyond this distance, the ratio increases with increasing radial distance, whereas at the interface between the air cavity and magnet (0.15 cm) the radial dose with magnets is a factor of two larger than that obtained without. Replacing the air in cavity 2 with perspex reduced the ratio to unity. Replacing the NdFeB magnets with perspex (with air in cavity 2) resulted in ratios of unity at all depths.

Additional dose contributions near the interface between the air cavities and NdFeB magnets is due to scattered photons and electrons from interactions in the magnets. The larger radial dose in air cavity 2 than in air cavity 1 was due to the range of scattering angles at which the particles emerged from the perspex phantom between the magnets. When the air in cavity 2 was replaced with perspex, most of these scattered particles were attenuated prior to reaching the magnet material (range of a 100 keV electron in perspex is 0.015 cm), thereby reducing the ratio to unity. Inside the perspex phantom, the scatter contributions from magnet material were shown to have no effect on either the depth-dose or radial dose. One can therefore be confident that the passage of microbeams through the longitudinal magnet device has no effect on the dosimetry performed in the perspex phantom between the magnets.

The availability of stronger permanent magnets led to the construction of a second longitudinal magnetic field device for magneto-MRT experiments. The interest in stronger magnetic fields is due to electrons having smaller cyclotron radii, and hence, the potential for greater effect. As shown in figure 6.7, the device comprises a pair of cylindrical NdFeB magnets<sup>8</sup>, each 10 cm diameter  $\times$  5 cm depth with a surface field of 2 T. A 1.0 cm diameter hole through the centre of each magnet allowed the passage of microbeams parallel to the magnetic field. The magnets were fixed to a U-shaped iron circuit to maximise magnetic flux. A steel focus cone was fixed to the surface of each

---

<sup>8</sup>Neo Ring N42-type cylindrical NdFeB magnets supplied by AMF Magnetics, Mascot, NSW Australia.

magnet to concentrate the field lines along the axis. These focus cones were separated by 1 cm of air to produce a maximum flux<sup>6</sup> of about 2 T. MATLAB simulations<sup>9</sup> estimated a maximum field of 2.2 T between the focus cones, as shown in figure 6.8.

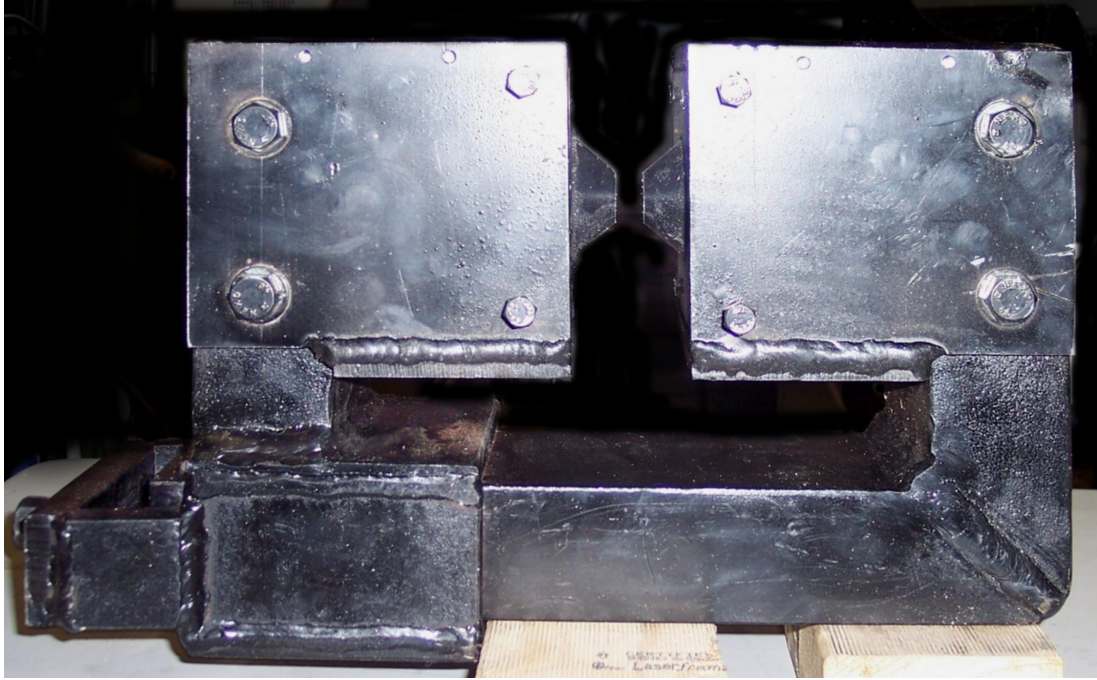


Figure 6.7: Photo of the 2 T longitudinal magnetic field device used for magneto-MRT experiments. The device comprises a pair of cylindrical NdFeB permanent magnets with steel focus cones and a U-shaped iron circuit to maximise magnetic flux.

The lateral dose profile of an array of 24 microbeams (each  $25\ \mu\text{m}$  wide,  $492.5\ \mu\text{m}$  high, and separated by  $412\ \mu\text{m}$ ) was obtained with and without a 2 T longitudinal magnetic field. For the measurements with magnetic field, four strips of Gafchromic film were positioned at 0.2, 0.4, 0.6, and 0.8 cm between a stack of 0.2 cm-thick perspex sheets wedged in the 1 cm gap between the focus cones. For measurements conducted in the absence of field, the magnet device was replaced with a set of steel dummy magnets of identical dimensions to maintain the similar scattering conditions.

---

<sup>9</sup>MATLAB simulations performed by Brad Oborn, a fellow PhD student at the Centre for Medical Radiation Physics, University of Wollongong, Australia.

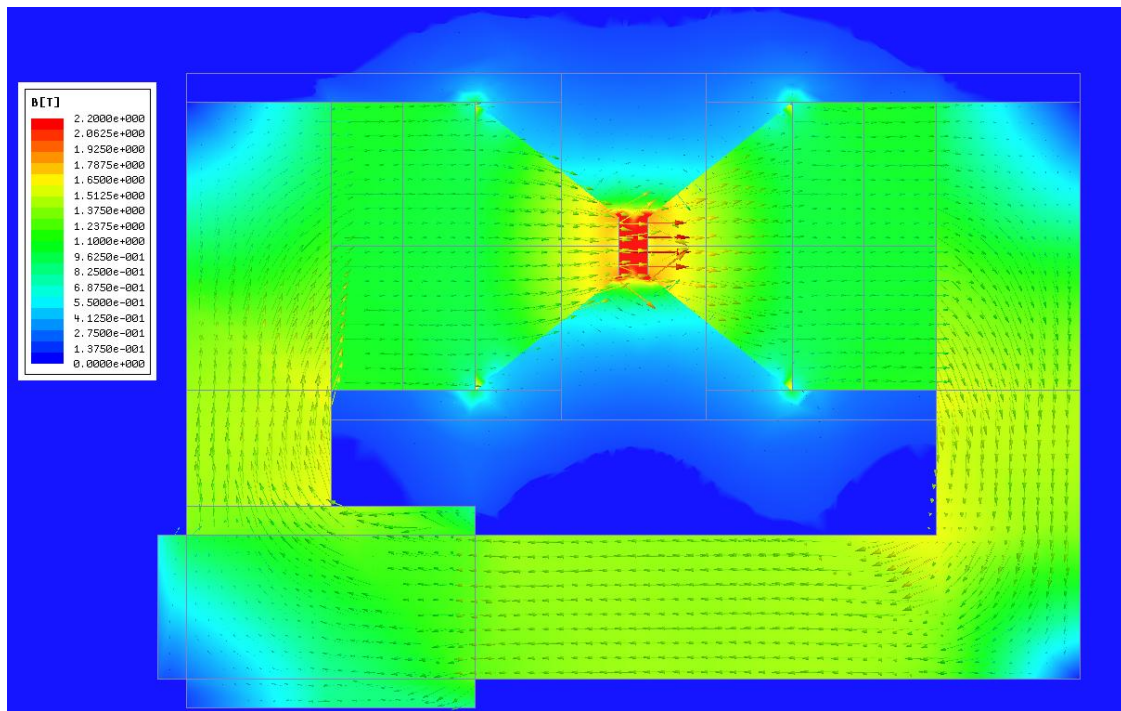


Figure 6.8: MATLAB simulation of the magnetic flux produced by the longitudinal magnetic field device. A maximum field of 2.2 T was calculated between the focus cones, which were separated by 1 cm.

#### 6.2.2.2 Magnet coil device

The influence of a longitudinal magnetic field on the PVDR of microbeams was also investigated with MOSFET dosimetry. The insufficient space between the focus cones in the above permanent magnet devices led to the construction of a magnet coil which could accommodate the MOSFET aligned in the direction of magnetic field. The advantage of using a magnet coil over permanent magnets is the unobscured and variable strength of longitudinal magnetic field, which is proportional to current, and the ability to perform dose measurements over a wider range of depths (i.e. not limited by the distance between magnets). Furthermore, because the magnetic field is pulsed, the coil can also be used for dose measurements in the absence of a magnetic field. This eliminates any anomalies in scattered dose contributions that may arise with the use of dummy magnets.



The magnet coil<sup>10</sup> comprises 828 turns of 0.236 cm diameter copper wire, with a 2.5 cm diameter air core at the coil centre. It measures 16.5 cm diameter  $\times$  7.0 cm depth and has a resistance and inductance of 0.986  $\Omega$  and 29 mH respectively. When a current of 200 A was pulsed through the coil, 1.3 and 2.5 T magnetic fields were estimated at the centre of the coil's surface and middle of the air core, respectively. These estimates were obtained by measuring the magnetic flux density at the surface of the coil with a low DC current. Knowing the magnetic flux,  $\phi_m$ , number of turns,  $N$ , and area of the coils,  $A$ , the magnetic field,  $B$ , was calculated from the expression  $B = \phi_m / NA$ . For a 1.0 A current, the magnetic field was 0.0065 T. Since magnetic field is proportional to current, 200 A of current through the coil will produce a magnetic field of about 1.3 T at the coil surface.

Magneto-MRT measurements were performed with the coil mounted on an aluminium stage, which was fixed to the goniometer as shown in figure 6.9. Electrical wires connected the coil to a current pulser box on the floor of the experimental hutch, which contained a bank of 16  $\times$  4700  $\mu$ F capacitors (refer to appendix A for circuit diagrams and descriptions of the current pulser and time delay circuits). To ensure synchronisation of the pulsed magnetic field with the 30 ms beam delivery, a logic pulse was used to trigger the discharge of capacitors (i.e. pulsed magnetic field) at the instant the fast shutter opened (a diode pulse is used to activate the shutter opening). The relationship between the diode pulse and current pulse was monitored on an oscilloscope, as shown in figure 6.10, where the optimal time delay between pulses was an 80 ms lead of the current over the diode. The coincidence of the pulsed current and the induced magnetic field (measured with a Hall probe Teslameter) was monitored on an oscilloscope. The output is shown in figure 6.11.

The influence of the pulsed magnetic field on the dose profile of an array of 24 microbeams (each 50  $\mu$ m wide, 492.5  $\mu$ m high, and separated by 412  $\mu$ m) was investigated with MOSFET dosimetry. Peak and valley dose measurements were obtained with an

---

<sup>10</sup>Magnet coil and current pulser circuit was constructed under the direction of Terry Braddock, an electrical engineer in the Centre for Medical Radiation Physics, University of Wollongong, Australia.

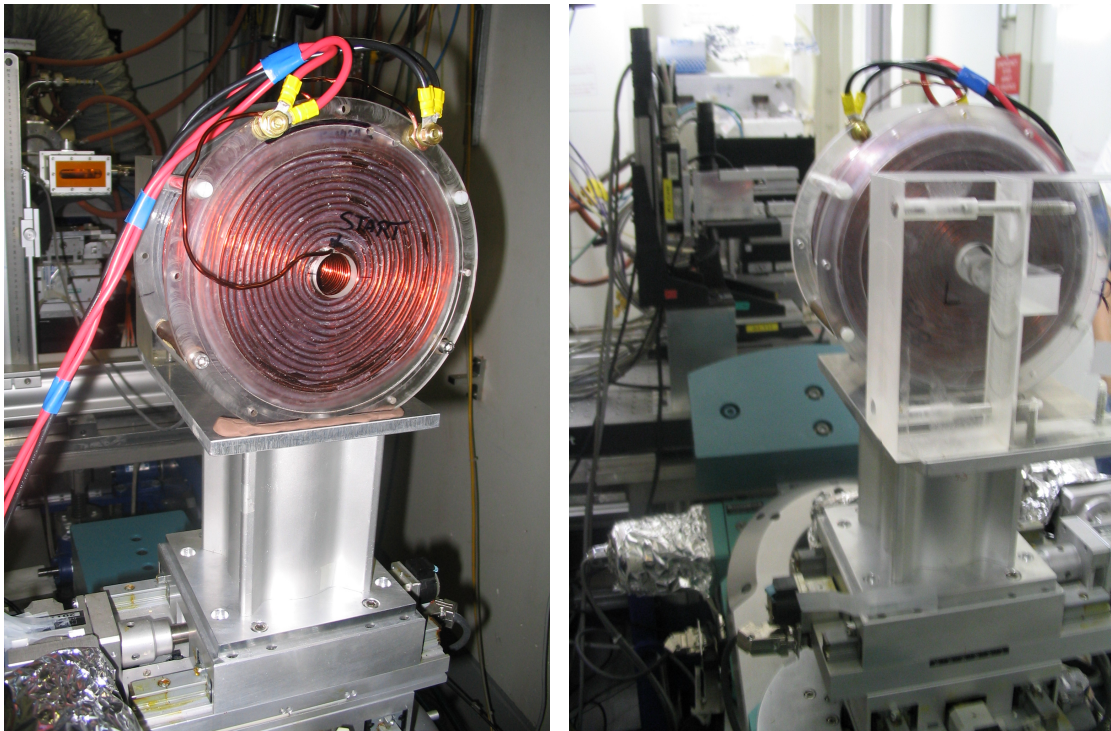


Figure 6.9: Photos of the magnet coil used for magneto-MRT experiments. The 828-turn copper coil was mounted on the goniometer (left), where the cylindrical perspex phantom (housing the MOSFET) was inserted into the air core and secured to a perspex block behind the coil (right).

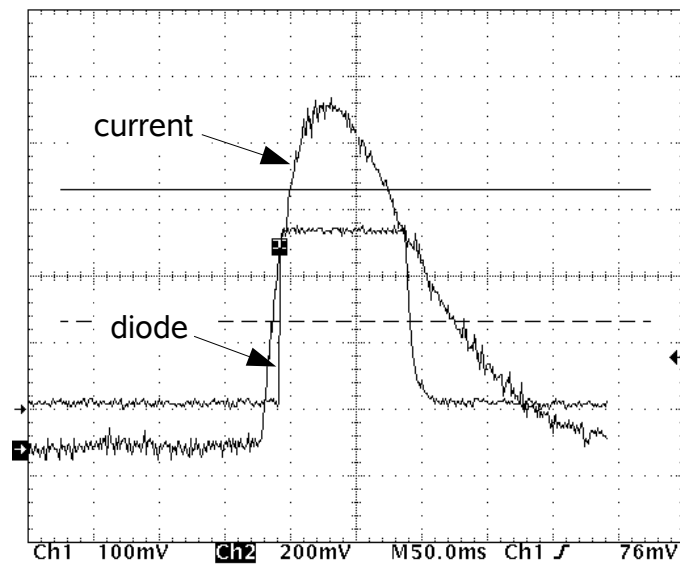


Figure 6.10: Oscilloscope output verifying the synchronisation of the current pulse (i.e. pulsed magnetic field) and the rectangular diode pulse (i.e. beam delivery).

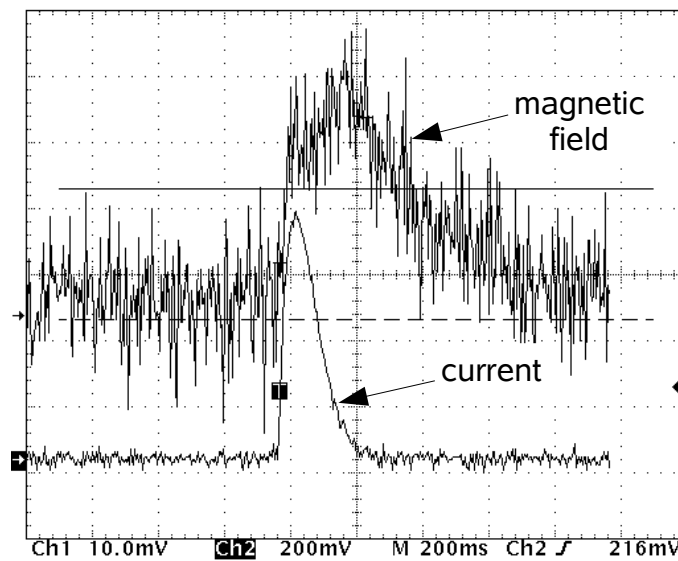


Figure 6.11: Oscilloscope output verifying the coincidence of the pulsed current (i.e. discharge of capacitors) and magnetic field. Delay between the current and diode pulses was adjusted to provide a maximum magnetic field during irradiation of the target.

edge-on MOSFET positioned at 1.1 cm depth in a perspex cylindrical phantom of 2.5 cm diameter and 5 cm depth. The phantom was inserted into the core and secured to a perspex block, which was flush against the exit surface of the coil as shown in figure 6.9. The MOSFET (and coil) was moved to the centre of peak 12 (central microbeam) where it was subjected to pulses of radiation with and without the 2.5 T pulsed magnetic field. The change in threshold voltage (i.e. absorbed dose) measured by the MOSFET reader was normalised to the synchrotron storage-ring current and exposure time. Measurements were also performed with the MOSFET at the microbeam edge (i.e.  $\pm 25 \mu\text{m}$  from peak centre) and in the valley region at  $\pm 50$ ,  $\pm 100$ , and  $\pm 206 \mu\text{m}$  from peak centre. The duration of radiation pulses were 10 ms at the centre and edges of the peak, 30 ms at  $\pm 50 \mu\text{m}$ , and 100 s in the middle of the valley ( $\pm 206 \mu\text{m}$ ).

### 6.2.3 Magneto-MRT Monte Carlo simulations

Monte Carlo PENELOPE simulations were performed to supplement the MOSFET and Gafchromic film results. The dose profile of a single microbeam and an array of three

microbeams were simulated with and without a 2 T magnetic field (i.e. same approximate field strength as used in the above magneto-MRT experiments). Additional simulations were performed with stronger magnetic fields of 10, 20, 50, and 100 T to investigate the dependence of PVDR on field strength. The simulations were performed with the ESRF white beam spectrum (refer to figure 5.4), and included a model of the Tecomet<sup>®</sup> multislit collimator, distributed synchrotron source, 33 m source to multislit collimator distance, and 1 m air region between the collimator and phantom (details of the modelled beamline components appear in chapter 7).

Profiles obtained in the presence of transverse and longitudinal magnetic fields were scored at 0.9 and 1.1 cm depth (in perspex), respectively, to facilitate comparison with measured profiles. Dose was scored in bin volumes of  $0.0002 \times 0.2 \times 0.2 \text{ cm}^3$  (width  $\times$  height  $\times$  depth). The simulations were performed with electron and photon transport cutoffs of 1 keV and a total of  $10^{10}$  primary photon histories. The average PVDR of the central peak in an array of three microbeams (peak 2) was calculated using the dose in the central bin of the peak region and an average of dose in four bins about the valley midpoint (i.e.  $\pm 206 \mu\text{m}$  from peak centre).

## 6.3 Results and Discussion

### 6.3.1 Effect of a transverse magnetic field on microbeam profiles

Figure 6.12 shows the dose profile of an array of three microbeams subjected to a 1 T transverse magnetic field measured with a MOSFET at 0.9 cm depth (in perspex). The variations in the peak intensity and FWHM of microbeams are related to the construction of the multislit collimator and its alignment. The collimator comprises a number of layers of thin tungsten foils glued together, where the rough inside edges of the apertures are known to produce up to  $4 \mu\text{m}$  differences in the full-width at half-maximum (FWHM) of microbeams [23]. While these variations have little influence on the intensity of microbeams, the alignment of the multislit collimator (with respect to the beam) does, as demonstrated with Monte Carlo simulation in the following chapter.

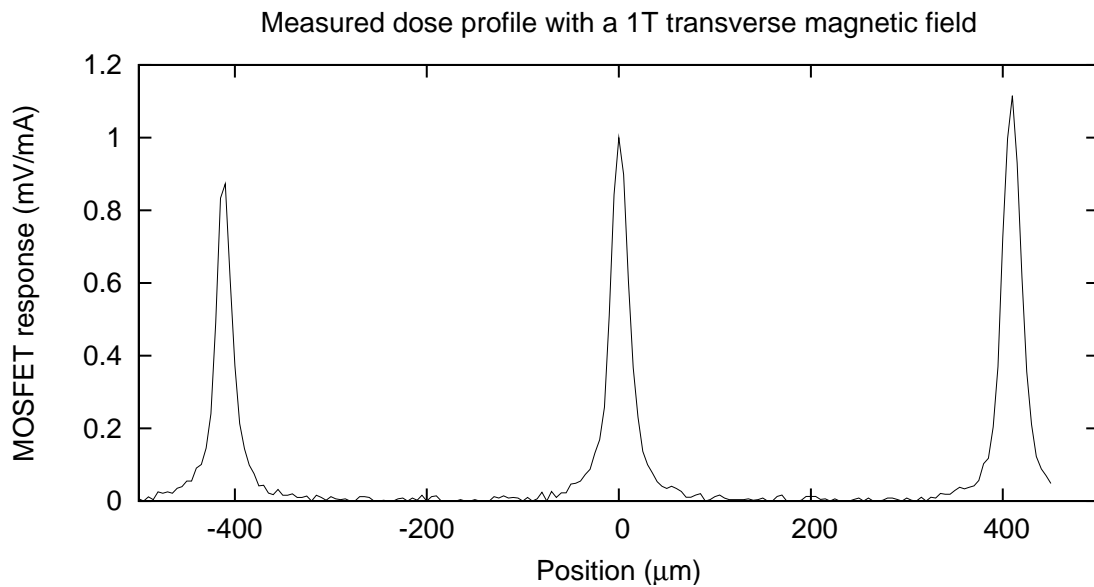


Figure 6.12: Lateral dose profile of an array of three microbeams measured with a MOSFET at 0.9 cm depth (in perspex) in the presence of a 1 T transverse magnetic field.

Figures 6.13 (a) and (b) plot the dose profiles of valleys  $V_{12}$  and  $V_{23}$  (to the left and right of the central microbeam, respectively) with and without a 1 T transverse magnetic field. These profiles were measured with a MOSFET at 0.9 cm depth in perspex using a wiggler gap of 24.8 mm (standard MRT conditions). The  $V_{12}$  and  $V_{23}$  valley dose profiles measured in the absence of field exhibit differences in dose at the centre and left edges of their profiles. The valley profiles obtained in the presence of a 1 T transverse magnetic field, on the other hand, are almost identical. These profiles exhibit a reduction in dose and widening of the valley, when compared with the valley profiles obtained in the absence of field, suggesting a narrowing of the peak.

Considering the valley profiles obtained with and without magnetic field were acquired on different days, one cannot make a direct comparison between the two without examining the effect on peak dose. The impracticality of measuring the peak profile (i.e. peak dose intensity severely reduces a MOSFET's lifetime) led to dose measurements at the peak centre in the presence and absence of magnetic field. Figures 6.14 (a) and (b) plot  $V_{12}$  and  $V_{23}$  valley dose at 0.9, 1.9, and 2.8 cm depth (in perspex) with and without a 1 T transverse magnetic field. Figures 6.14 (c) and (d) plot the peak dose and PVDR of the central microbeam (peak 2) with and without magnetic field at the same depths.

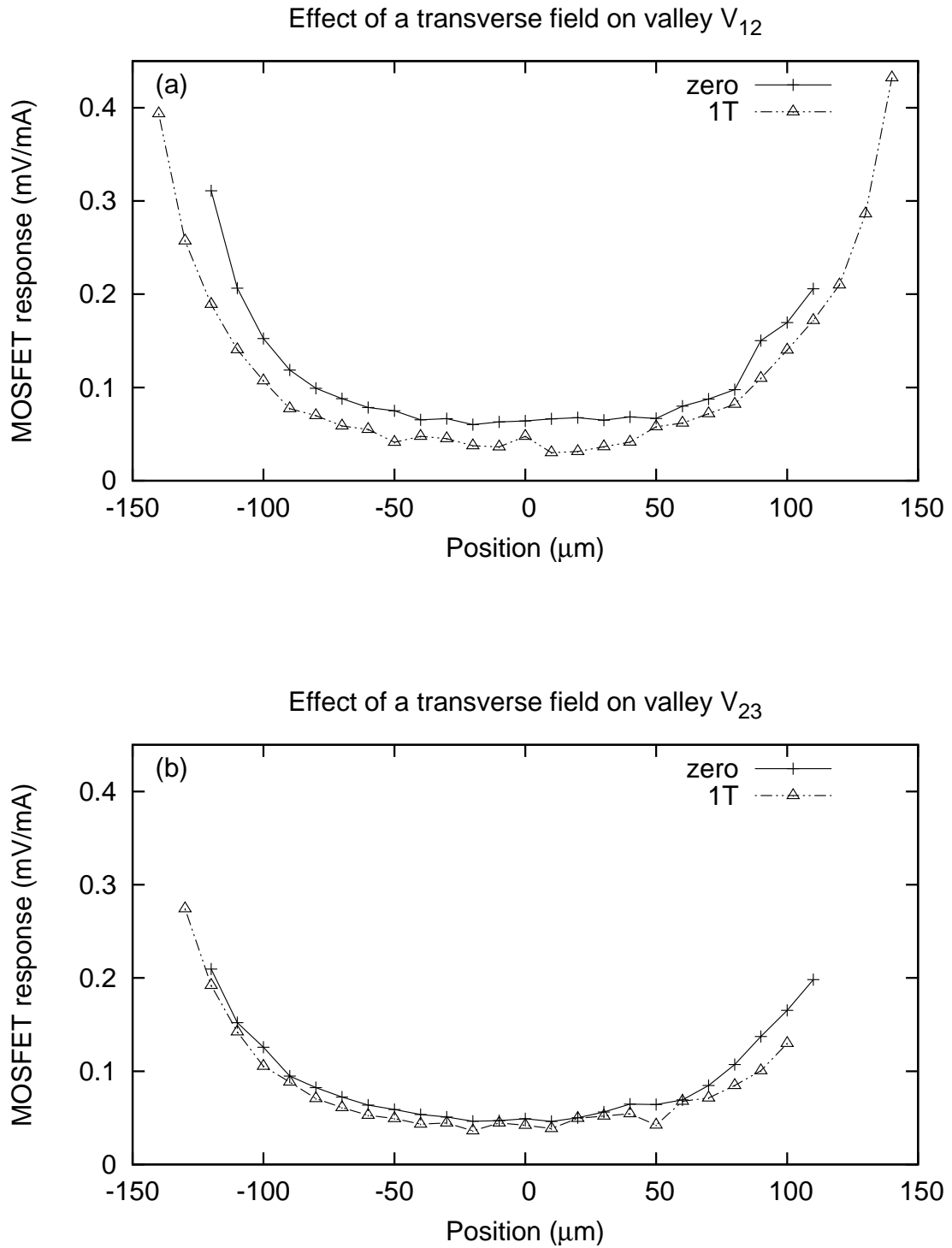


Figure 6.13: Effect of a 1 T transverse magnetic field on the valley dose of an array of three microbeams. Figures (a) and (b) plot the dose profiles of valley regions  $V_{12}$  and  $V_{23}$  (i.e. left and right of the central microbeam, peak 2) respectively, measured with a MOSFET at 0.9 cm depth (in perspex) in the presence and absence of magnetic field.

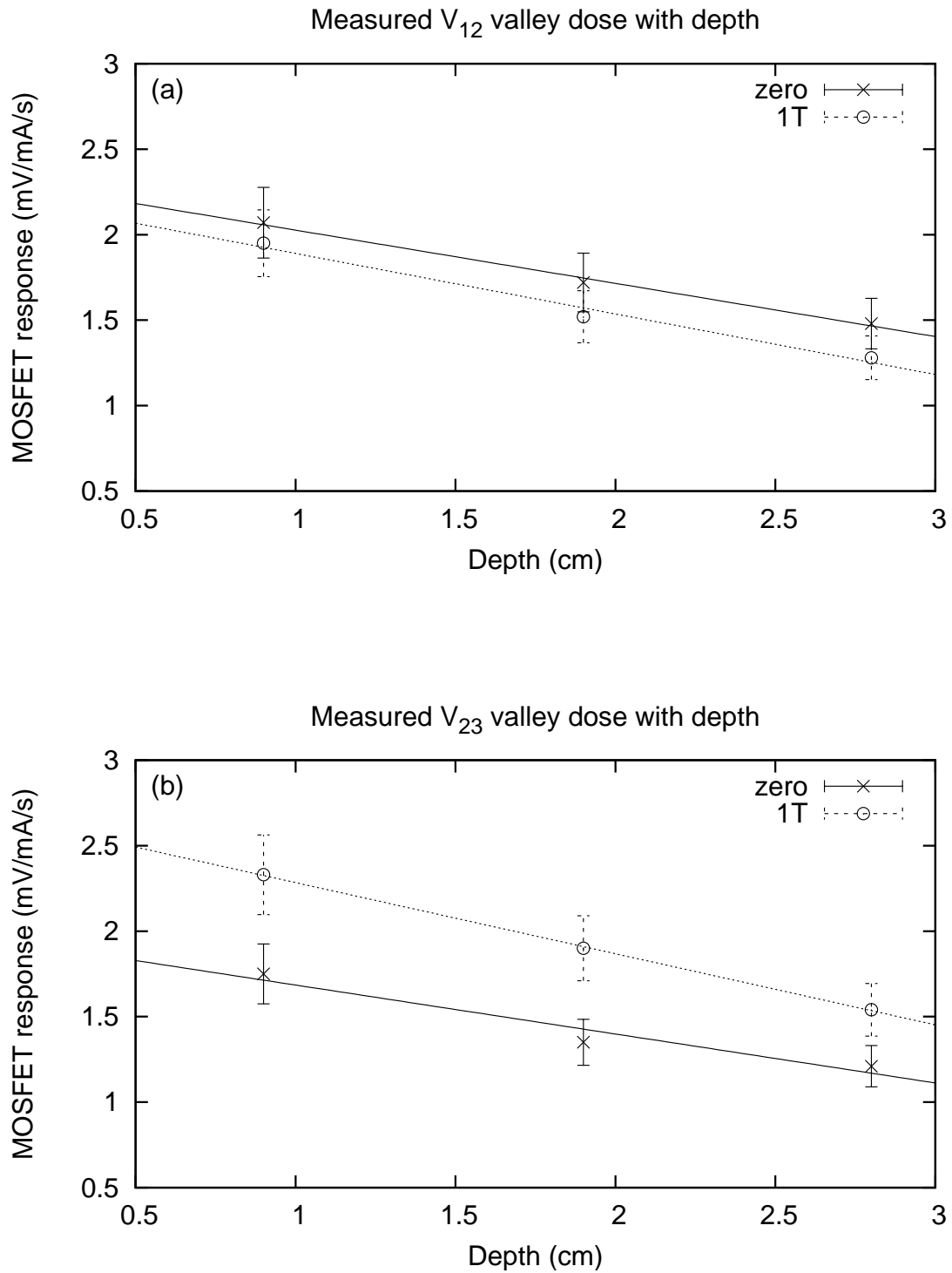


Figure 6.14: Valley dose for an array of three microbeams measured with a MOSFET at 0.9, 1.9, and 2.8 cm depth (in perspex). Figures (a) and (b) plot the dose at the centre of valleys  $V_{12}$  and  $V_{23}$  (i.e. left and right of the central microbeam, peak 2) respectively, in the presence and absence of a 1 T transverse magnetic field.

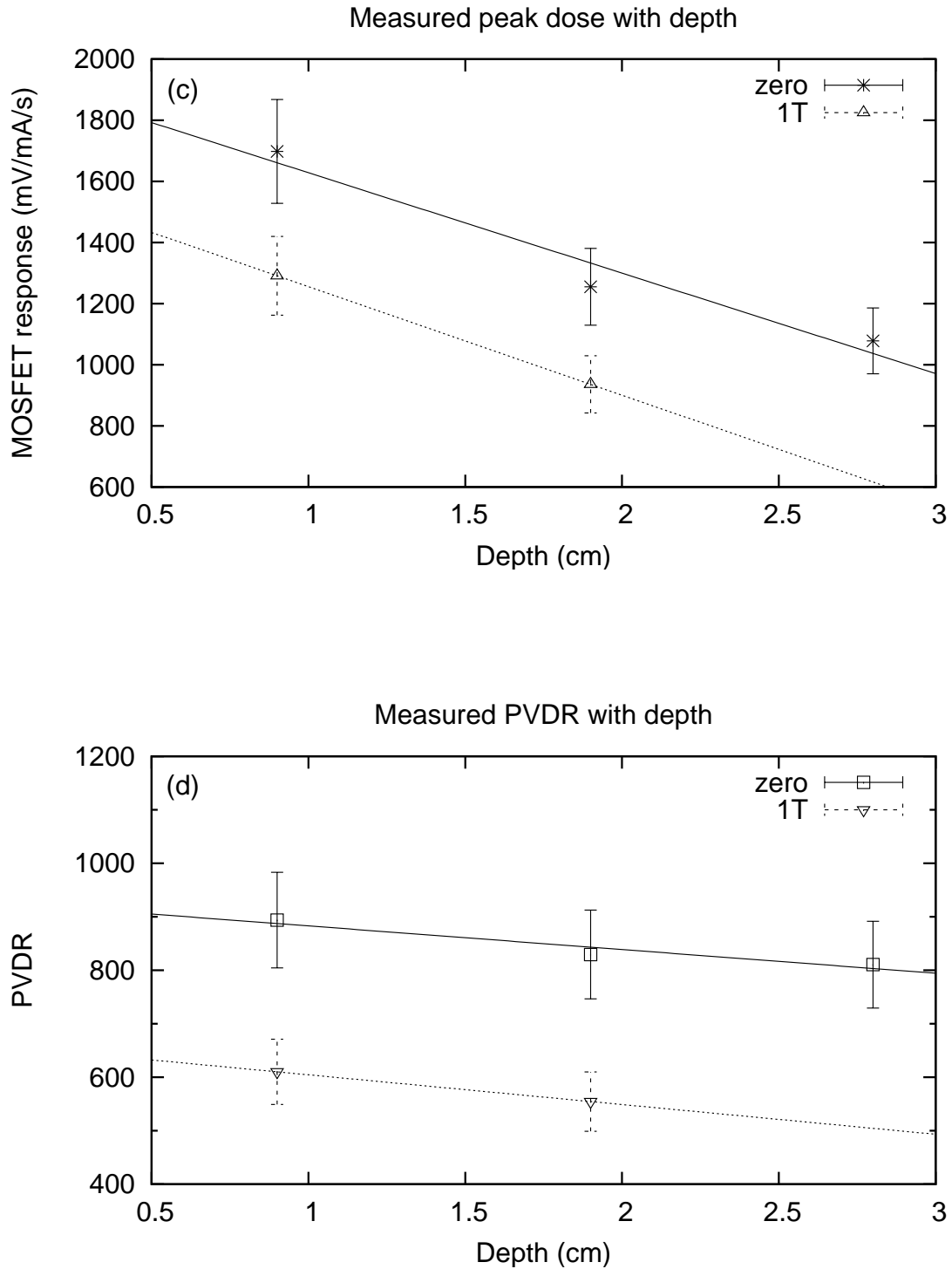


Figure 6.14: Peak dose and PVDR for the central microbeam in an array of three microbeams (peak 2) measured with a MOSFET at 0.9, 1.9, and 2.8 cm depth (in perspex), in the presence and absence of a 1 T transverse magnetic field, is shown in figures (c) and (d) respectively. The PVDR was calculated using the dose at the centre of peak 2 and valleys  $V_{12}$  and  $V_{23}$  on either side.



The peak and  $V_{12}$  and  $V_{23}$  valley regions exhibit a reduction in dose with depth. Unfortunately, only three depths were investigated owing to beamtime constraints. Ideally, more measurements at different depths would have been performed to improve the overall quality of the data. Nevertheless, these data exhibit trends consistent with those seen in both the previous chapter and literature [25]. The reduction in peak dose with increasing depth is due to photon attenuation. Valley dose can also be seen to decrease with depth owing to the presence of fewer scattered photons, and hence, secondary electrons. The faster rate of dose reduction in the peak than in the valley gives rise to the reduction in PVDR with depth. This is consistent with the Monte Carlo results in the previous chapter and literature [25, 32, 85].

It is difficult to make a direct comparison between the results obtained with and without magnetic field as they were performed on different days. The reason for this is that daily adjustments are made to the alignment of the MOSFET and multislit collimator (i.e. microbeam array) to correct for any shift in the synchrotron beam. The valley profiles in figure 6.13 are testimony to this, where the  $V_{12}$  and  $V_{23}$  profiles obtained with magnetic field are almost identical, while those produced without magnetic field differ at the centre and left edges of their profiles. In retrospect, these measurements should have been performed consecutively on the same day to minimise any variations in alignment.

Monte Carlo simulations were performed to determine the effect of a transverse magnetic field on the PVDR of a microbeam array. Figure 6.15 plots the simulated dose profile of an array of three microbeams scored between 0.8 and 1.0 cm depth in perspex (to match the 0.9 cm depth of the MOSFET) in the presence and absence of a 2 and 100 T transverse magnetic field. PVDRs of  $600 \pm 50$ ,  $590 \pm 50$ , and  $580 \pm 50$  were calculated for the profiles obtained with zero, 2, and 100 T respectively, using the dose at the centre of peak 2 and an average of four bins in the middle of the two adjacent valleys (uncertainties in the peak and valley dose were 3% and 8% respectively). The PVDR and peak and valley doses were within their uncertainties, which suggests the dose profiles of microbeams are unaffected by the presence of a transverse magnetic field.

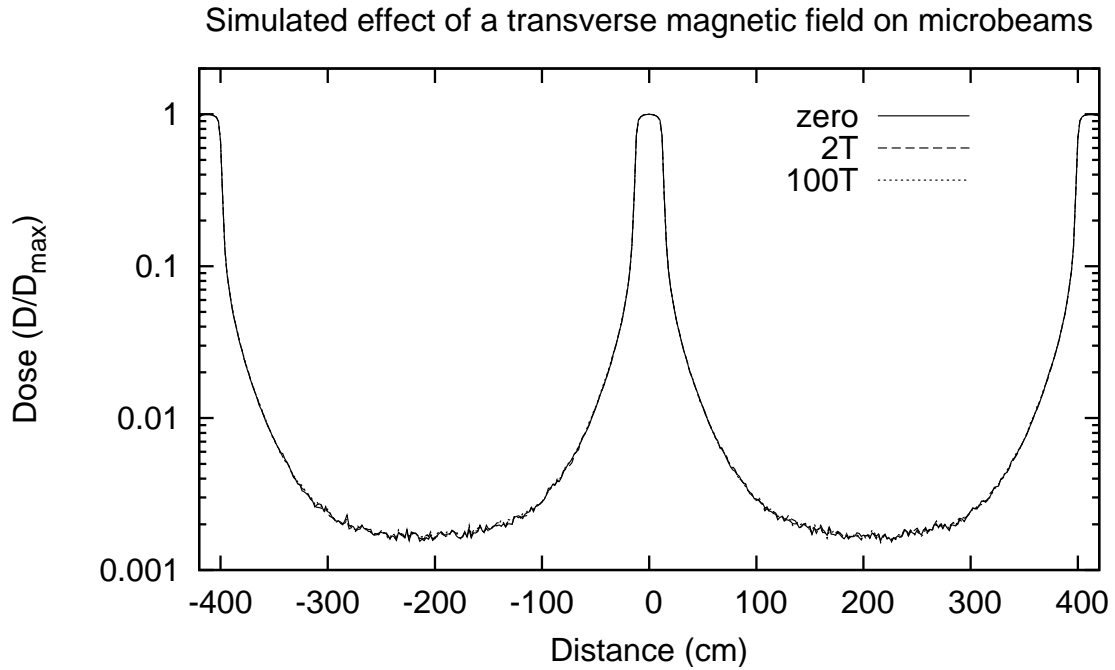


Figure 6.15: Simulated effect of a transverse magnetic field on the dose profile of an array of three microbeams. A plot of the microbeam array scored between 0.8 and 1.0 cm depth (in perspex) in the presence and absence of a 2 and 100 T transverse magnetic field.

### 6.3.2 Effect of a longitudinal magnetic field on microbeam profiles

Figure 6.16 plots the lateral dose profile of an array of three microbeams (each  $25\ \mu\text{m}$  wide,  $492.5\ \mu\text{m}$  high, and separated by  $412\ \mu\text{m}$ ) measured in the absence of magnetic field with Gafchromic film at 0.1, 0.2, 0.7, 1.1, and 1.2 cm depths (in perspex). These profiles exhibit a reduction in peak dose with increasing depth due to the attenuation of photons. Dose profiles of the microbeam array in the presence of a 1 T longitudinal magnetic field were also measured with Gafchromic film. Owing to the 0.5 cm separation between the magnet focus cones, these profiles were limited to depths of 0.1, 0.2, 0.3, and 0.4 cm. Figure 6.17 plots the peak dose of the central microbeam with depth in the presence and absence of magnetic field. Despite larger peak doses with magnetic field, the values were within the uncertainties of those obtained in the absence of field.

Further measurements comparing the peak and valley doses of an array of three

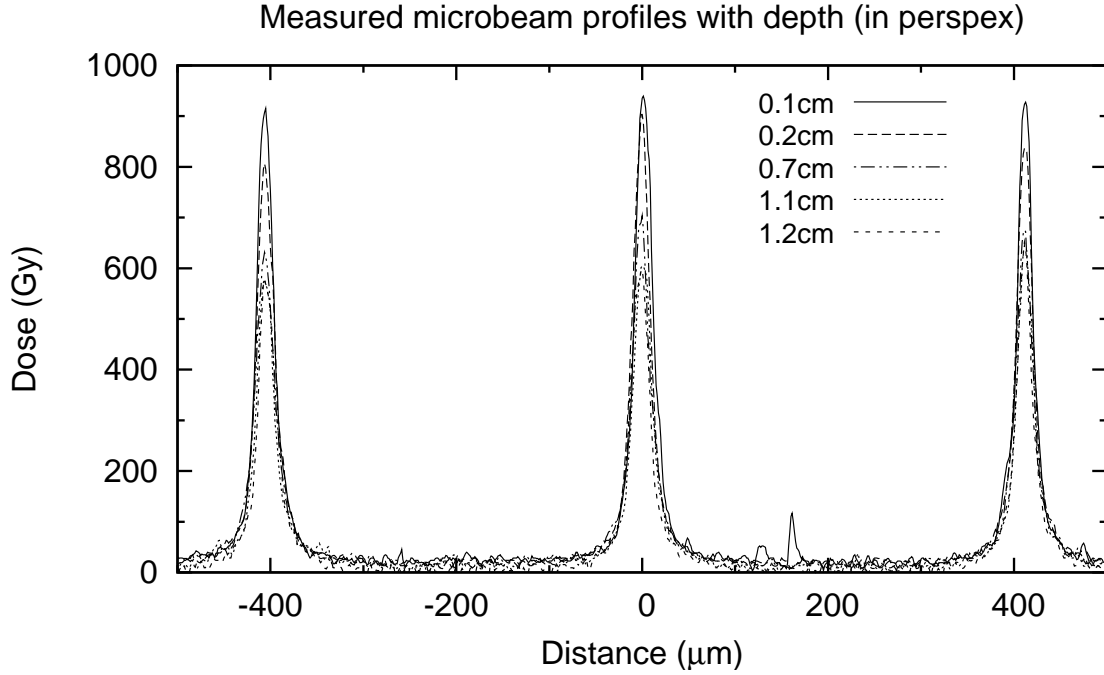


Figure 6.16: Dose profile of an array of three microbeams measured with Gafchromic film at 0.1, 0.2, 0.7, 1.1, and 1.2 cm depths (in perspex) in the absence of magnetic field.

microbeams in the presence and absence of a 1 T longitudinal magnetic field is shown in figures 6.18 (a) and (b) respectively. The profiles were measured with Gafchromic film at 0.2 cm depth (in perspex) using an MRT peak dose of 500 Gy for the peak profiles, and 60 000 Gy for the valley profiles (in order to raise the level of valley dose to sit within the sensitive range of the film).

The presence of a 1 T longitudinal magnetic field yielded larger peak doses (up to 30%) and smaller valley doses (up to 25%), which suggests a reduction in the lateral spread of electrons into the valleys (i.e. reduction in the orthogonal component of electron trajectories with respect to the direction of magnetic field). This gives rise to larger PVDRs, as shown in table 6.1, which compares the PVDRs of the central microbeam (peak 2) at 0.1 and 0.2 cm depth (in perspex) in the presence and absence of magnetic field. A comparison of the peak dose and valley dose (averaged over 10  $\mu\text{m}$  at the centres of valleys  $V_{12}$  and  $V_{23}$ ) is also shown. The PVDR uncertainty was calculated as the square of the relative uncertainties in the peak and valley dose, both of which were 10%.

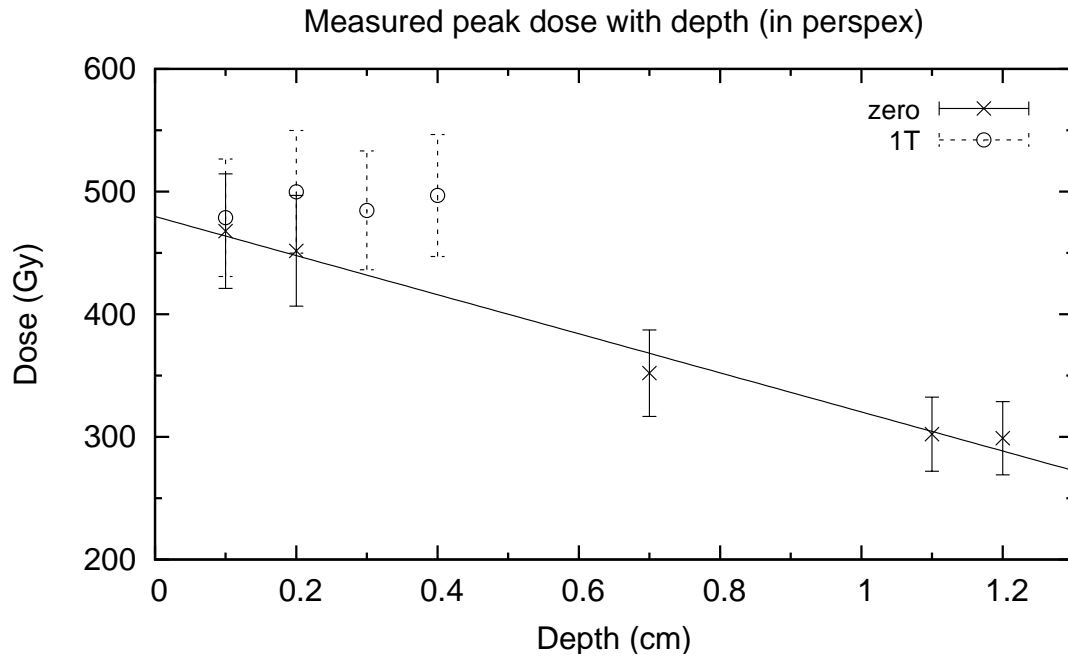


Figure 6.17: Peak dose of the central microbeam in an array of three microbeams (peak 2) with depth. A plot of the peak dose measured with Gafchromic film at depths (in perspex) of 0.1, 0.2, 0.3, and 0.4 cm in the presence of a 1 T longitudinal magnetic field, and 0.1, 0.2, 0.7, 1.1, and 1.2 cm in the absence of magnetic field.

Table 6.1: Peak and valley doses and PVDR of the central peak (peak 2) in an array of three microbeams. Peak and valley doses were measured with Gafchromic film at 0.1 and 0.2 cm depth (in perspex) in the presence and absence of a 1 T longitudinal magnetic field, B.

	0.1 cm depth		0.2 cm depth	
	B = zero	B = 1 T	B = zero	B = 1 T
$Dose_{Peak}$ (Gy)	$470 \pm 50$	$480 \pm 50$	$450 \pm 50$	$500 \pm 50$
$Dose_{Valley}$ (Gy)	$0.74 \pm 0.07$	$0.57 \pm 0.06$	$0.76 \pm 0.08$	$0.57 \pm 0.06$
PVDR	$630 \pm 90$	$840 \pm 120$	$590 \pm 80$	$880 \pm 120$

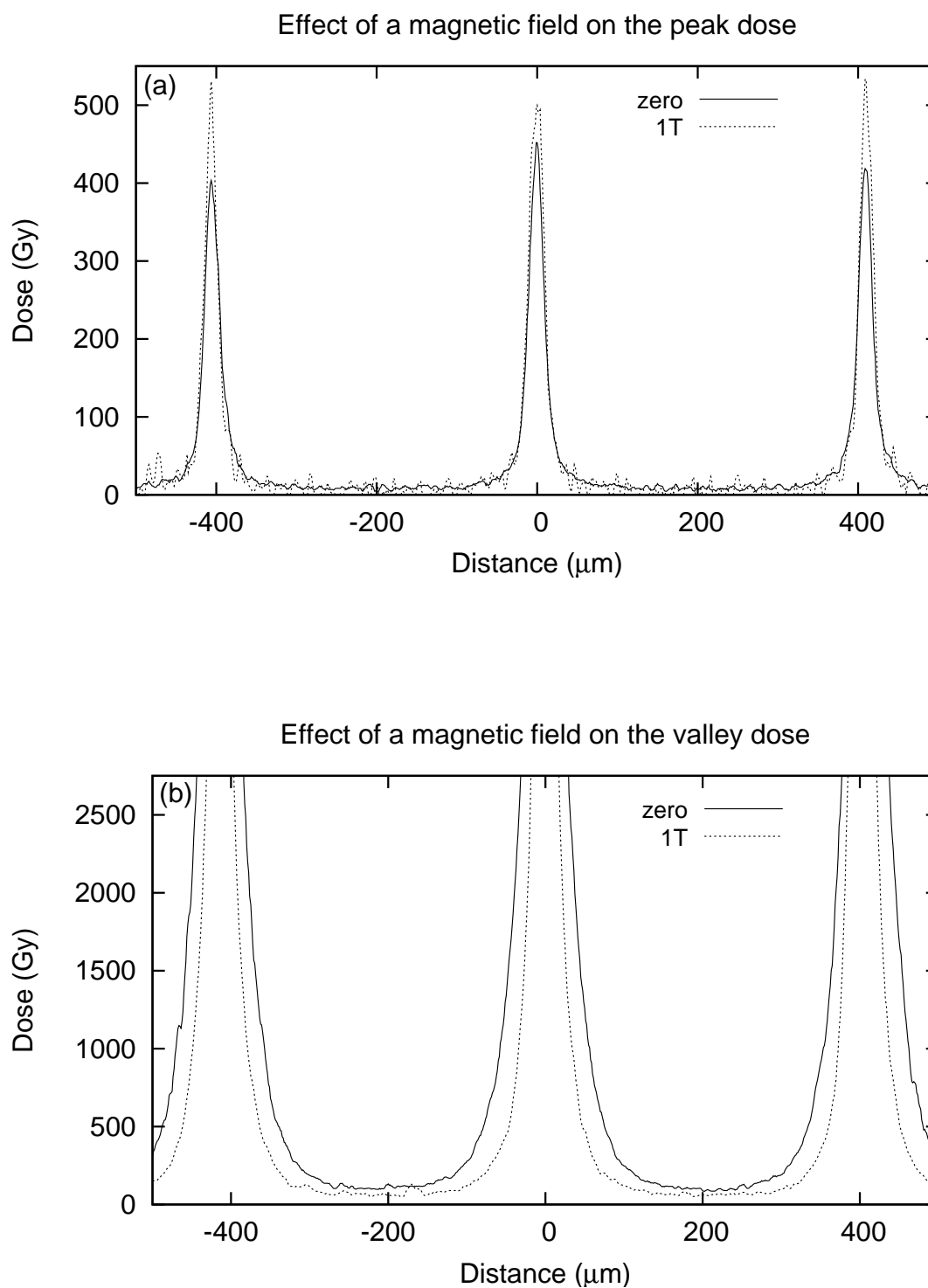


Figure 6.18: Effect of a 1 T longitudinal magnetic field on the peak and valley doses of an array of three microbeams. Figures (a) and (b) show the peak and valley dose profiles, respectively, measured with Gafchromic film at 0.2 cm depth (in perspex) in the presence and absence of magnetic field.

The availability of stronger magnets led to the construction of a 2 T permanent magnet device (refer to section 6.2.2.1) to investigate the potential for further gains in PVDR. For these experiments, the dose profile of an array of 24 microbeams was measured with Gafchromic film at 0.2, 0.4, 0.6, and 0.8 cm depth in perspex. Profiles were also measured at these depths in the absence of magnetic field using a pair of steel dummy magnets. A comparison of the profiles obtained with and without magnetic field revealed no consistent differences in the peak or valley dose, and hence, no change in the PVDR. This contradicted earlier film results with a 1 T longitudinal magnetic field, which showed an increase in the PVDR in the presence of magnetic field. The discrepancy between Gafchromic film results may stem from the non-uniform energy response across individual sheets of film which can be as much as  $\pm 8\%$  [104].

The discrepancy in film results motivated the use of an alternative dosimeter to perform a final investigation of the effect of a longitudinal magnetic field on the dose profiles of microbeams. The edge-on MOSFET dosimeter was chosen for these measurements as it has a high spatial resolution of about  $1\ \mu\text{m}$ . Magneto-MRT experiments were performed with a magnet coil (built to accommodate the MOSFET and perspex phantom within its air core) which produced a maximum longitudinal magnetic field of 2.5 T. Peak and valley dose measurements were obtained for an array of 24 microbeams (each  $50\ \mu\text{m}$  wide,  $492.5\ \mu\text{m}$  high, and separated by  $412\ \mu\text{m}$ ) with and without a magnetic field. These measurements were performed with the MOSFET in the centre of peak 12 and at the right edge of the peak (i.e.  $25\ \mu\text{m}$  from peak centre). Penumbra and valley dose measurements were also obtained at  $50$  and  $206\ \mu\text{m}$  from the peak centre, respectively. Exposure times of  $0.01$ ,  $0.03$ , and  $10\ \text{s}$  were used for dose measurements in the peak, penumbra, and valley regions respectively.

For each position in the peak 12 profile, dose measurements in the presence and absence of magnetic field were the same within uncertainties. Different time delays between the current and diode pulses (i.e. pulsed magnetic field and beam delivery) similarly, had

no affect. These results were consistent with those obtained with the 2 T permanent magnetic device and Gafchromic film. They also verify the hypothesis that the range of the electrons must be comparable to or greater than their cyclotron radii in order to see an effect. At magnetic fields of 1 or 2 T, the range of a 100 keV electron is an order of magnitude smaller than its cyclotron radius. For a 10 keV electron, this difference is two orders of magnitude, where a magnetic field of about 100 T is needed to reduce its cyclotron radius to a distance comparable with its range. The presence of a longitudinal magnetic field of a few Tesla has no effect on the dose profiles nor the PVDRs of microbeams. The strength of magnetic field needed to produce an effect can be seen in the following Monte Carlo results.

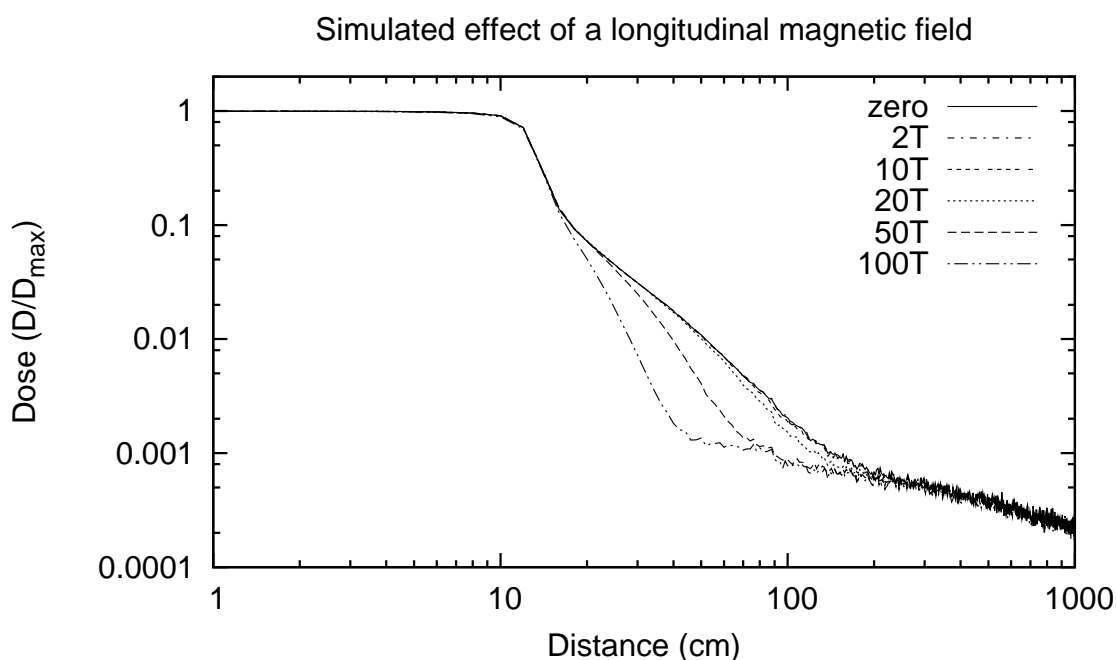


Figure 6.19: Simulated effect of a longitudinal magnetic field on the dose profile of a single microbeam. A plot of the profile scored between 1.0 and 1.2 cm depth (in perspex) in the presence and absence of a 2, 10, 20, 50, and 100 T magnetic field.

Figure 6.19 compares the dose profile of a single microbeam (25  $\mu\text{m}$  wide and 492.5  $\mu\text{m}$  high) scored between 1.0 and 1.2 cm depth (in perspex) with and without a 2, 10, 20, 50, and 100 T longitudinal magnetic field. The dose profiles obtained in the

presence of 2 and 10 T magnetic fields are almost identical to those produced in the absence of field. Microbeams subjected to magnetic fields of 20 T or greater, on the other hand, exhibit reductions in their penumbral and valley doses. Larger reductions were observed with stronger magnetic fields due to a reduction in the lateral scattering of electrons as their ranges become comparable to or greater than their cyclotron radii (refer to figure 3.1).

The reductions in valley dose correspond with increases in PVDR of as much as 15%. Noting that the valley dose of an array comprises a superposition of overlapping dose tails from individual microbeams, additional simulations were performed with an array of three microbeams (each 25  $\mu\text{m}$  wide, 492.5  $\mu\text{m}$  high, and separated by 412  $\mu\text{m}$ ) to determine whether a reduction in valley dose still existed.

Figure 6.20 (a) compares the dose profile of the array scored between 1.0 and 1.2 cm depth (in perspex) in the presence and absence of a 2, 10, 20, 50, and 100 T longitudinal magnetic field. The profiles have been normalised to the peak dose in the central microbeam of the array (i.e.  $D_{max}$ ). A ratio of the dose profiles obtained with and without magnetic field is shown in figure 6.20 (b).

The microbeam dose profiles obtained in the presence of 20, 50, and 100 T longitudinal magnetic fields exhibit penumbral dose reductions of as much as 20, 65, and 85% respectively. The 2 and 10 T profiles also exhibit minor reductions in penumbral dose, however, these are within the 8% uncertainties. In the centre of the valleys (i.e.  $\pm 206 \mu\text{m}$ ), the reduction in dose is substantially lower than that near the peak, where profiles obtained in the presence of 20, 50, and 100 T magnetic fields exhibit reductions of approximately 7, 10, and 15% respectively. As doses have been normalised to peak dose, valley dose reductions correspond to PVDR increases of 7, 10, and 15% respectively, as shown in figure 6.21. The higher PVDRs obtained with stronger magnetic fields is due to the smaller cyclotron radii of electrons, confining the lateral component of their trajectories and thereby reducing valley dose.



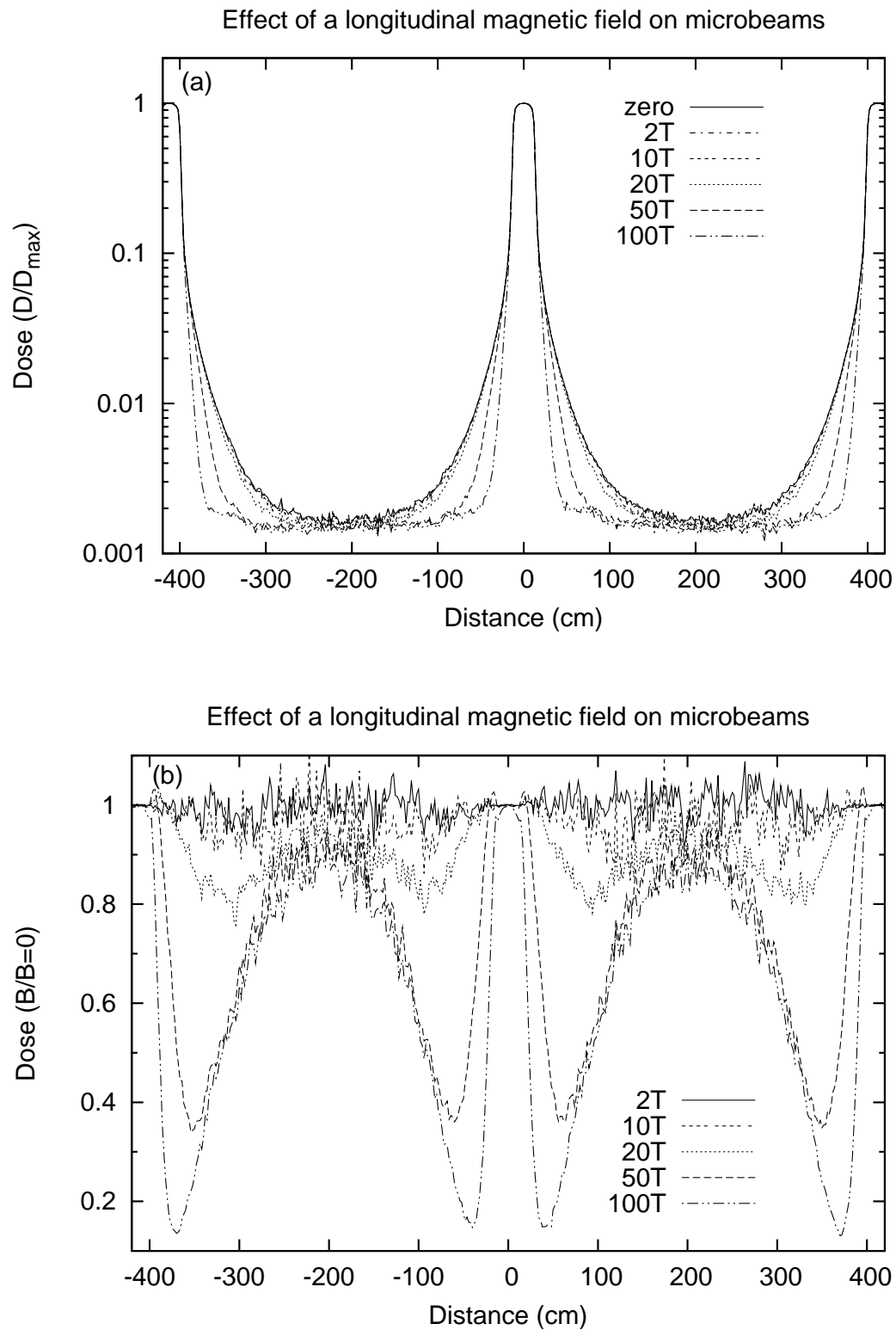


Figure 6.20: Simulated effect of a longitudinal magnetic field on the dose profile of an array of three microbeams. Figure (a) shows the dose profile of the array scored between 1.0 and 1.2 cm depth (in perspex) in the presence and absence of a 2, 10, 20, 50, and 100 T magnetic field. A ratio of the dose profile with and without magnetic field is plotted in figure (b).

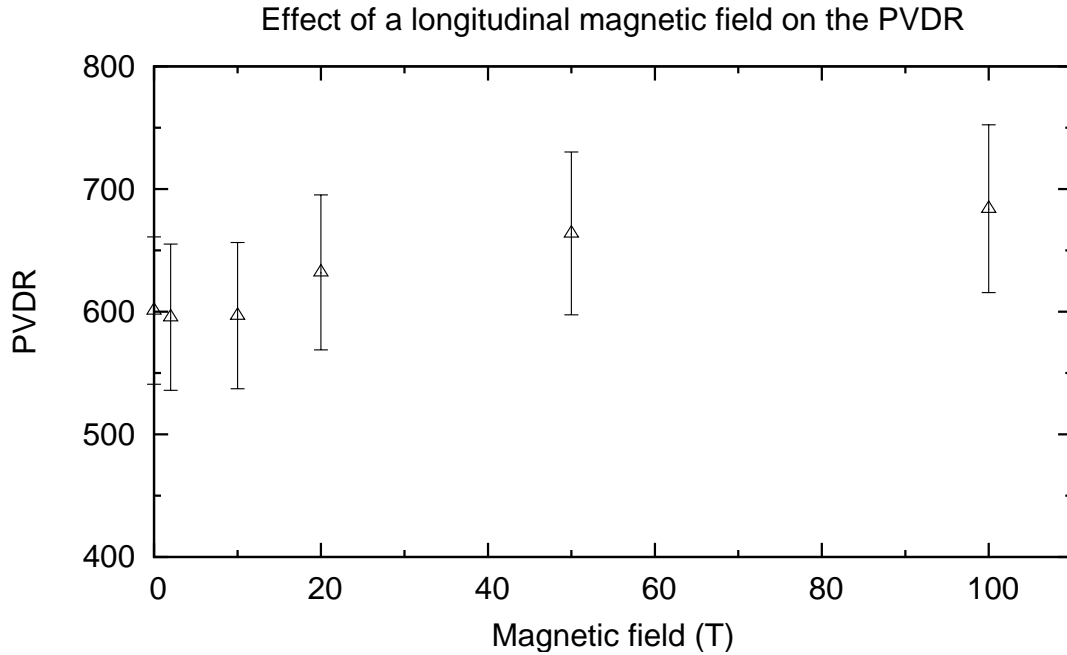


Figure 6.21: Simulated effect of a longitudinal magnetic field on the PVDR of an array of three microbeams. A plot of the PVDR of the central microbeam against magnetic field strength, using the dose profiles scored between 1.0 and 1.2 cm depth (in perspex).

#### 6.4 Conclusion

The presence of a transverse or longitudinal magnetic field of a few Tesla was shown both experimentally and theoretically to have no effect on the dose profiles of microbeams. According to Monte Carlo PENELOPE simulations, longitudinal magnetic fields greater than 10 T are needed to produce an effect. This contradicts Orion's ESG4 result which shows a reduction in the penumbral dose (of a few microns) for a single 20 keV microbeam subjected to a 6 T longitudinal magnetic field. Apart from the different photon beam energies, the difference between the two simulation results may stem from the modelling of polarisation effects. While modelling of photon polarisation for Compton scattering is included in the EGS4 distribution, it is not accounted for in the 2003 version of the PENELOPE code used for this work. However, considering the penumbral dose for a 20 keV microbeam is predominantly produced by photoelectric interactions (refer to figure 5.14), any polarisation effect at these energies are negligible. A

direct comparison of the codes, which is now possible with the recent inclusion of photon polarisation in the 2008 version of PENELOPE, is needed to verify this hypothesis.

The effect of 20, 50, and 100 T longitudinal magnetic fields on an array of three microbeams was to increase the PVDRs by 7, 10, and 15% respectively. The higher PVDRs are brought about by a reduction in the lateral spread of secondary electrons, whose ranges are comparable to or greater than their cyclotron radii. The application of a transverse magnetic field of up to 100 T, on the other hand, had no effect on the dose profile or PVDR of microbeams. This is because the direction of magnetic field is parallel with the lateral component of an electron's trajectory, and hence, only the orthogonal components of the electron's path are affected. It is therefore possible that sufficiently strong transverse magnetic fields may alter the depth-dose profile of microbeams.

While the presence of magnetic fields of a few Tesla during MRT has no effect on electron distribution, it is possible that they may influence the repair mechanisms of tissue. Studies have shown the application of magnetic fields can influence the orientation of molecular domains in cell membranes, thus changing their structure and curvature [105] and potentially altering the diffusion of molecules across the membrane surface (a process critical to normal membrane function and antibody binding) [106]. In liquid water, the presence of static magnetic fields (between 1 and 10 T) have also been shown to enhance the hydrogen bonds of water molecules, thereby improving their stability [107]. A study of breast cancer patients exposed to magnetic fields prior to irradiation reported substantial, and in some cases complete, tumour regression [108]. Could the application of a magnetic field before, during, or after MRT irradiation alter the repair mechanisms of brain tissue in such a way to improve the efficacy of the treatment?

## **CHAPTER 7**

### **A MONTE CARLO STUDY OF THE INFLUENCE OF MRT BEAMLINE COMPONENTS ON MICROBEAM PROFILES**

#### **7.1 Introduction**

Monte Carlo simulation is a popular theoretical tool used to estimate the dose distribution in radiotherapy. It is particularly useful in Microbeam Radiation Therapy (MRT) as it allows the study of dose deposition on a micron scale which may otherwise be difficult to measure. However, its potential use in future MRT dose planning is currently hindered by an ongoing discrepancy between measured and theoretical dose profiles of microbeams. The need to resolve this discrepancy is driven by the desire to make MRT available to humans in the next few years.

This chapter examines common simplifications in MRT modelling which may account for the differences between theoretical and measured dose. One simplification is the commencement of microbeam transport on the surface of the target, which neglects the effect of the synchrotron source, multislit collimator, and beam divergence between them. This work investigates the influence of these components on microbeam profiles, together with the effect of collimator alignment, interaction medium, and height of the scoring region. Many of the results appearing in this chapter have been published in a peer-reviewed journal article [109].

In MRT, a multislit collimator is placed in the path of the beam between the source and target, to shape the wide beam into a linear array of parallel, rectangular, micron-sized X-ray beams (microbeams) for treatment. For more than a decade, numerous collimator designs have been trialled to investigate optimal microbeam characteristics for treatment. Before the advent of a multislit collimator, MRT irradiations were performed

with a single-aperture collimator and multiple exposures [29, 30, 32, 82, 83]. This time-intensive process increased the risk of target (small animal) movement, blurring the otherwise steep dose gradients at the edge of the irradiated microslices. The invention of the multislit collimator made it possible to deliver a large array of microplanar beams in a single fast exposure, thereby reducing the treatment time and broadening of irradiated microslices due to target movement.

The first multislit collimator used for MRT at the European Synchrotron Radiation Facility (ESRF) was the Archer-type multislit collimator (AMSC) [110]. It comprised two stacks of alternating aluminium and gold foils, where microbeam width was determined by the lateral translation of one stack relative to the other [20, 23]. The AMSC's 10  $\mu\text{m}$  variation in the full-width at half-maximum (FWHM) of microbeams led to its replacement by the Tecomet<sup>®</sup> variable-width collimator. As shown in figure 7.1, this collimator comprises two identical stacks, each containing 125 parallel, 100  $\mu\text{m}$  wide, 8 mm deep air apertures separated by 300  $\mu\text{m}$  wide tungsten teeth to produce 400  $\mu\text{m}$  centre-to-centre spacing between adjacent microbeams [23]. Lateral translation of these motor-controlled stacks enables the width of microbeams to be adjusted. Originally constructed from a number of layers of thin tungsten foils glued together, the rough inside edges of the collimator apertures produced variations of up to 4  $\mu\text{m}$  in the FWHM of microbeams [23].

Improved technology for the manufacture of collimators has led to the recent replacement of the multilayered tungsten foil stacks with solid tungsten-carbide blocks comprising smooth, wire-cut apertures. In the future, once optimal microbeam parameters for MRT have been determined, it may be desirable to replace the variable-width multislit collimator with a single-stack design whose apertures are of fixed width.

Monte Carlo simulation has been used in MRT to estimate the peak-to-valley dose ratio (PVDR) across an array of microbeams with various X-ray beam energies, centre-to-centre microbeam spacings, and depths of interaction [16, 19, 22, 23, 25, 32, 85, 87]. These studies have used the superposition of the dose profile from a single microbeam to

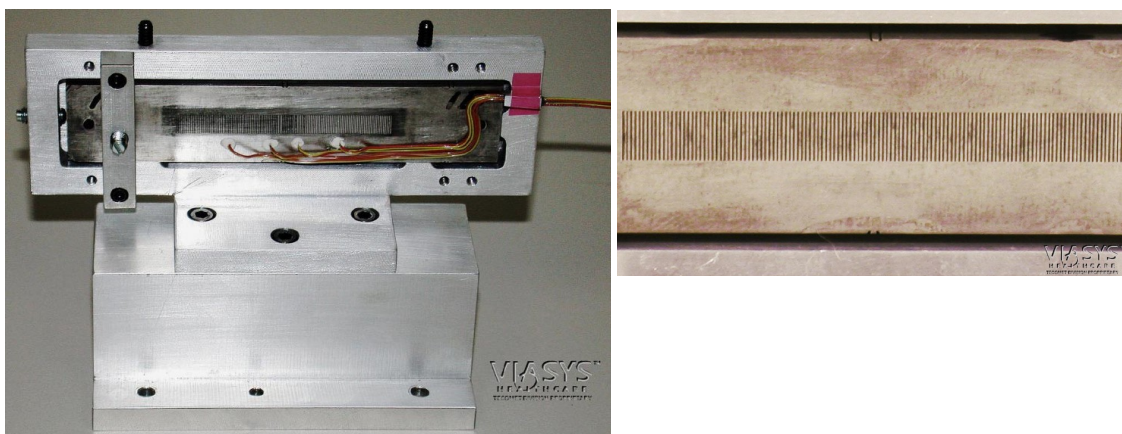


Figure 7.1: Photo of the Tecomet<sup>®</sup> multislit collimator (left) which comprises two identical tungsten air stacks mounted in an aluminum frame. Each stack (right) contains 125 parallel,  $100\ \mu\text{m}$  wide,  $8\ \text{mm}$  deep apertures with  $400\ \mu\text{m}$  centre-to-centre spacing [23].

estimate the PVDR of microbeams. Bräuer-Krisch *et al.* compared the PVDR of a microbeam array measured with a MOSFET to that simulated with a modified version of the Monte Carlo GEANT code used at the Paul Scherrer Institute (PSI) [85]. The measured PVDRs were found to be within 5% of the theoretical values, despite the absolute peak and valley dose measurements being 20% lower than those obtained theoretically [22]. The authors attribute the difference to a  $\pm 30\%$  fluctuation in the measured FWHM of microbeams emerging from the AMSC, and the modelling of identical planar rectangular microbeams.

A later study by Siegbahn *et al.* [86] compared the dose profile of a microbeam array measured with Gafchromic film to that simulated with Monte Carlo PENELOPE. Measured valley doses were approximately double those obtained theoretically, corresponding to PVDRs of about half of the simulated values. The authors attribute the discrepancy to crude simplifications in the modelling of the real irradiation geometry (i.e. absence of a multislit collimator model, beam divergence, and polarisation of the synchrotron beam). A Monte Carlo EGS4 study by De Felici *et al.* used a  $3 \times 3\ \text{cm}$  array of microbeams ( $25\ \mu\text{m}$  wide and separated by  $200\ \mu\text{m}$ ) to demonstrate the effect of the beam polarisation. While polarisation caused a 16% difference in the dose deposition at

the far edges of the array, its effect in the centre of the array was negligible [16].

Simplification of the real irradiation geometry, such as the assumption that identical rectangular microbeams emerge from the multislit collimator, is a common practice in theoretical MRT studies. Owing to the inefficiency of lengthy simulation times needed to simulate a small detector volume tens of metres from a synchrotron source, microbeam transport is often commenced on the surface of the target about to be penetrated [16, 25, 32, 85, 87]. This simplification fails to account for the beam divergence between the source and multislit collimator. It also neglects any geometrical and scattering effects that may arise from radiation transport through the multislit collimator.

The MRT facility at the ESRF has been recently renovated to prepare for clinical MRT trials on dogs, which if successful may lead to the clinical administration of MRT to humans. Such implementation will demand an accurate dose planning system for MRT, increasing the urgency of the need to resolve the ongoing discrepancies between the measured and theoretical dose profiles of microbeams. This chapter uses Monte Carlo PENELOPE simulation to investigate the source of these discrepancies. Three different simulation strategies are used to determine the influence on the microbeam dose profiles, and hence, importance of modelling the real MRT irradiation geometry (i.e. source, multislit collimator, beam divergence, and interaction medium). A comparison of the lateral dose profiles and PVDRs of a microbeam array produced from a single simulation of the entire array, with that obtained using the superposition of a single microbeam profile, is also investigated.

## 7.2 Materials and Methods

Modelling of the MRT irradiation geometry was based on the current setup used on the ID-17 biomedical beamline at the ESRF. Up until recently, this setup used a source to multislit collimator distance of 33 m, as shown in figure 5.5. Recent renovations have extended this distance to 41 m in preparation for upcoming clinical MRT trials. The elliptical source measures  $125 \times 25 \mu\text{m}$  (FWHM) along the horizontal and vertical axes,

respectively [111]. As shown in figure 5.4, it produces a spectrum of X-ray energies ranging from 30 to 600 keV with a maximum intensity of 83 keV and a mean energy of 107 keV [16, 25]. The Tecomet<sup>®</sup> multislit collimator, which is moved into the path of the beam to produce an array of microbeams, comprises two identical stacks, each consisting of 125 parallel, 100  $\mu\text{m}$  wide air apertures (see figure 7.2). These 8 mm deep air apertures are separated by 300  $\mu\text{m}$  wide tungsten teeth to produce 400  $\mu\text{m}$  centre-to-centre spacing between adjacent microbeams [23]. The lateral offset of these overlapping stacks allows adjustment of the microbeam width. The target, situated 1 m downstream of the multislit collimator, is fixed to a stereotactic frame and mounted on a three-axis goniometer device.

The PENELOPE code contains cross section data and uses transport algorithms well benchmarked for the energy ranges arising from synchrotron radiation [112]. The simulations in this chapter focus on the lateral dose profiles of an array of 25 microbeams scored between 1 and 2 cm depth in a  $10 \times 10 \times 10 \text{ cm}^3$  water phantom using bin volumes of  $0.0001 \times 0.20 \times 1.00 \text{ cm}^3$  (width  $\times$  height  $\times$  depth). For simulations of the entire microbeam array, the width of scoring bins was increased from 0.0001 to 0.0002 cm. Unless otherwise stated, the simulations were performed with the MRT setup described above. The elliptical synchrotron source was approximated as a circular source of 125  $\mu\text{m}$  diameter (to match the horizontal dimension of the ellipse). The additional height of the circular source should not affect the microbeam profiles as the dose is integrated over the full height of the microbeams. The collimator stacks were laterally translated to produce microbeams with a FWHM of 50  $\mu\text{m}$ . Primary photon energies were sampled between 30 and 600 keV according to their distribution in the measured ID-17 spectrum.

Primary photon transport was commenced on the surface of the multislit collimator, where each photon was given an initial direction as if it had originated from the source 41 m upstream (air region between the collimator and phantom was modelled). The initial direction cosines were calculated using a random point on the frontal surface of the multislit collimator ( $x_1, y_1$ ), and another random point on the distributed source ( $x_0, y_0$ ).



These points were selected following a Gaussian distribution with a standard deviation equal to the source radius, where any radial position exceeding the source diameter was rejected to maintain a finite source size.

For all simulations, the width and height of the planar microbeams at the exit surface of the multislit collimator were  $50\text{ }\mu\text{m}$  and  $1\text{ cm}$  respectively. Electron and photon transport cutoffs of  $1\text{ keV}$  were selected after finding that lower values led to variations smaller than the uncertainties. Most simulations were performed with  $2 \times 10^9$  primary photon histories to give a relative uncertainty in the dose (98% confidence level) of less than 1% in the peak and about 8% in the valley. For simulations of the entire microbeam array, the number of photon histories was increased to  $2 \times 10^{10}$  to counteract the effect of sharing the histories between a larger number of microbeams.

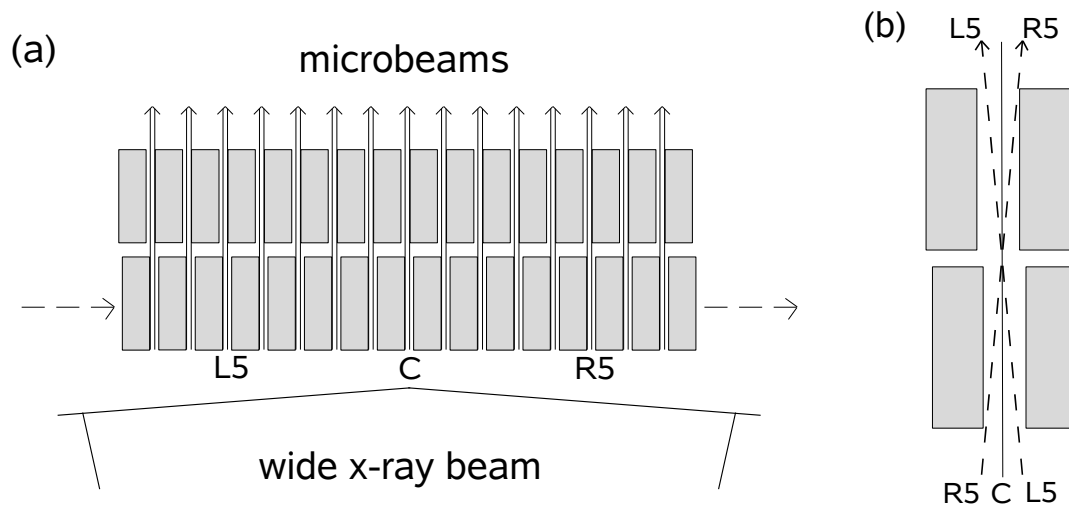


Figure 7.2: Illustration of the lateral offset of the multislit collimator stacks. Figure (a) illustrates the adjustment of microbeam width by laterally moving one stack relative to the other (as indicated by arrows). Figure (b) shows an enlargement of a single collimator element, comparing the photon transmission through the central collimator aperture (C) and the fifth apertures to the left and right of centre (L5 and R5 respectively).

Three simulation models were used to investigate the influence of different MRT beamline components on the lateral dose profiles of microbeams. The first of these models, the single-beam model, uses a single element of the multislit collimator to produce

individual microbeams within the array, where the microbeam position is selected by moving the source an integer number of microbeam spacings ( $410\ \mu\text{m}$ ) to the right or left of the element's central axis. This is illustrated in figure 7.2 (b), where the L5 profile, or the fifth microbeam left of centre (when viewing the collimator from the source) was simulated by moving the source position five microbeam spacings ( $2050\ \mu\text{m}$ ) to the right of the element's central axis (and vice versa for the R5 profile). The second, full array model, uses the entire multislit collimator to produce an array of 25 microbeams in a single simulation. The third and final model, the superposition model, generates a pseudo-array of 25 microbeams using the superposition of the lateral dose profile of a single microbeam (i.e. central microbeam). A comparison of the lateral dose profiles obtained with the different simulation models is used to ascertain their potential accuracy for use in a future MRT dose planning system.

The influence of multislit collimator alignment on the FWHM and PVDRs of microbeams was also investigated. This was performed by rotating the collimator through a small angle relative to the beam (as illustrated in figure 7.3), where the axis of collimator rotation (y-axis) is in the direction pointing into the page. Orthogonal to the axis of rotation is the beam direction (z-axis) and the lateral offset of the collimator stacks (x-axis). The dose profile of an array of 25 microbeams was simulated with the collimator rotated about the y-axis through angles of  $\pm 0.05$ ,  $\pm 0.1$ , and  $\pm 0.2$  degrees, where positive rotations correspond to clockwise rotations (and vice versa). The PVDR was calculated using the dose in the central bin of the peak and an average of four bins about the valley midpoint (i.e.  $\pm 205\ \mu\text{m}$  from peak center).

The similar density of water and polymethyl methacrylate (PMMA) to that of soft tissue makes them a popular choice of phantom material for studies in radiotherapy. This motivated a study of the influence of the interaction medium on the FWHM and PVDR of microbeams, using water and PMMA phantoms.

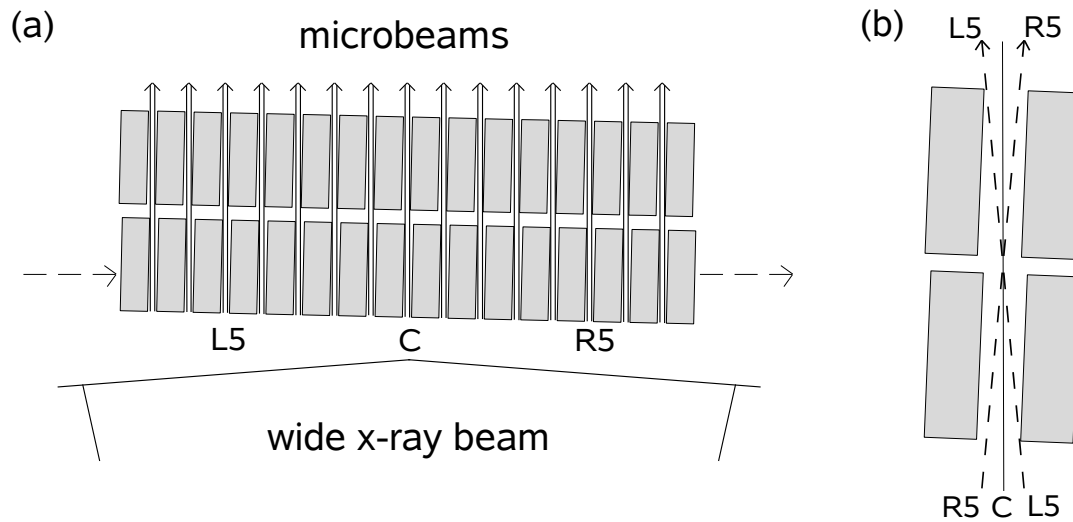


Figure 7.3: Illustration of the effect of multislit collimator alignment. Figure (a) shows the multislit collimator rotated through a small positive angle (with respect to the beam). Figure (b) shows an enlargement of a single collimator element, comparing the photon transmission through the central aperture (C) and the fifth apertures to the left and right of centre (L5 and R5 respectively).

### 7.3 Results and discussion

#### 7.3.1 Effect of the beam divergence

The influence of the beam divergence on microbeam profiles was investigated for a source to target distance of 42 m. Two simulations were performed to obtain a lateral dose profile of a single microbeam (scored between 1 and 2 cm depth in water) with and without beam divergence. The first simulation neglected beam divergence by commencing the microbeam transport on the surface of the target (water phantom), where each primary photon was given an initial direction parallel to the axis of the beam. The second simulation accounted for beam divergence by commencing the primary photons on the surface of the phantom with an initial direction as if they had originated from a point source 42 m upstream. The initial position of these primary photons was randomly selected within a microbeam width and height of  $51.22 \mu\text{m}$  and  $1.024 \text{ cm}$  respectively. This was conducted to allow comparison of these microbeam profiles with the profiles emerging from a multislit collimator (1 m upstream of the phantom), which have a FWHM

and height (at the collimator) of  $50\ \mu\text{m}$  and  $1\ \text{cm}$  respectively. A comparison of the microbeam dose profiles obtained with and without beam divergence (i.e. Diverge and On Phantom, respectively) is shown in figure 7.4 (a), and a ratio of these dose profiles is plotted in figure 7.4 (b).

The dose profile obtained with beam divergence (Diverge) reveals larger penumbral doses (up to 26% more) than the profile neglecting beam divergence (On Phantom). The steeper dose gradients between the peak and valley regions of the On Phantom profile (i.e. more rectangular profile) give rise to an 8% drop in the ratio of penumbral dose immediately before the increase to 26%. Beyond the penumbra, the Diverge profile exhibits up to 10% larger valley doses than the On Phantom profile, which decays almost to unity midvalley ( $\sim 200\ \mu\text{m}$ ). Similar dose increases in both the penumbral and valley regions were observed with a distributed source instead of a point source.

The broader Diverge profile arises from the wider range of incident angles at which primary photons strike the phantom as they diverge from a source position  $42\ \text{m}$  upstream. Such broadening is not exhibited by the On Phantom profile as the initial direction of primary photons is parallel to the beam and at normal incidence to the phantom's surface. Consequently, the On Phantom profile exhibits steeper dose gradients between the peak and valley regions (i.e. more rectangular profiles).

### 7.3.2 Effect of the multislit collimator

The larger penumbral and valley doses obtained with beam divergence prompted an investigation of the multislit collimator's influence on emerging microbeams. The dose profile of a single microbeam was simulated with the single-beam model, which uses a single element of the multislit collimator and a point source. Microbeam transport was commenced on the surface of the collimator, where primary photons were given an initial direction as if they had originated from a source position  $41\ \text{m}$  upstream. The source origin was centered on the axis of both the beam and collimator aperture to simulate the central peak, C, in an array of microbeams. Figure 7.5 (a) plots a ratio of the microbeam

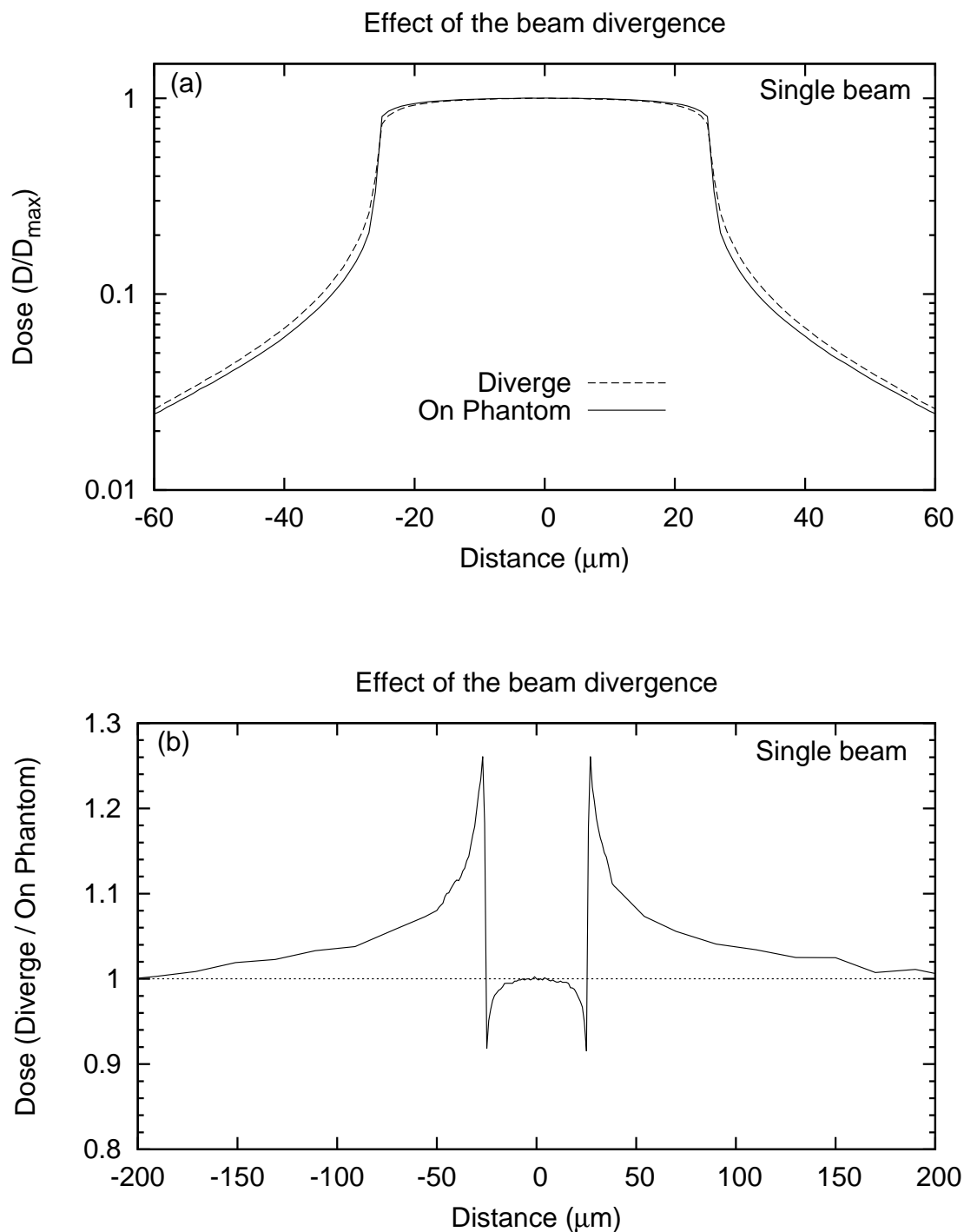


Figure 7.4: The influence of the beam divergence (i.e. source to target distance). Figure (a) compares the dose profile of a single microbeam scored between 1 and 2 cm depth (in water) with and without beam divergence (Diverge and On Phantom, respectively). A ratio of the Diverge and On Phantom profiles is shown in figure (b).

profiles obtained with and without the multislit collimator (MSC and NoMSC<sup>1</sup>, respectively) and a point source. The simulations were subsequently repeated with a distributed source instead of a point source. A ratio of the MSC and NoMSC profiles obtained with a distributed source is plotted in figure 7.5 (b).

For both the point source and distributed source, the inclusion of a multislit collimator produced less than 2% difference in the valley dose when compared with the profiles obtained without the collimator. While this difference appears to favour an increase in valley dose for the profiles obtained with the multislit collimator, it is within the uncertainties and therefore requires longer simulation times to improve the statistics in this region. In addition, as these profiles were scored between 1 and 2 cm depth they would not reveal any dose contributions from low-energy particles produced from photon interactions in the tungsten collimator walls. Investigation of these contributions would require dose measurements on the surface of the phantom with and without the collimator.

The ratio of profiles obtained with a distributed source exhibits a dose perturbation at the edges of the microbeam which is not observed in the corresponding point source profiles (i.e. ratio drops 14% below unity before rising to 26%). This perturbation arises from the steeper dose gradients between the peak and valley regions of the NoMSC profile (i.e. it is more rectangular than the MSC profile). The broader MSC profile is attributed to the wider range of incident photon angles from scattering within the collimator walls.

### 7.3.3 Effect of the source model

The difference in penumbral dose exhibited by the distributed source profiles obtained with and without a multislit collimator led to an investigation of the effect of the source model. Figure 7.6 (a) compares the dose profile of a single microbeam obtained with a point source (Pt src) to that produced by a distributed source (Dist src), using a model of the multislit collimator. The dose profiles were scored between 1 and 2 cm depth (in water), where a ratio of the profiles is shown in figure 7.6 (b).

---

<sup>1</sup>The NoMSC profile is the Diverge profile in section 7.3.1

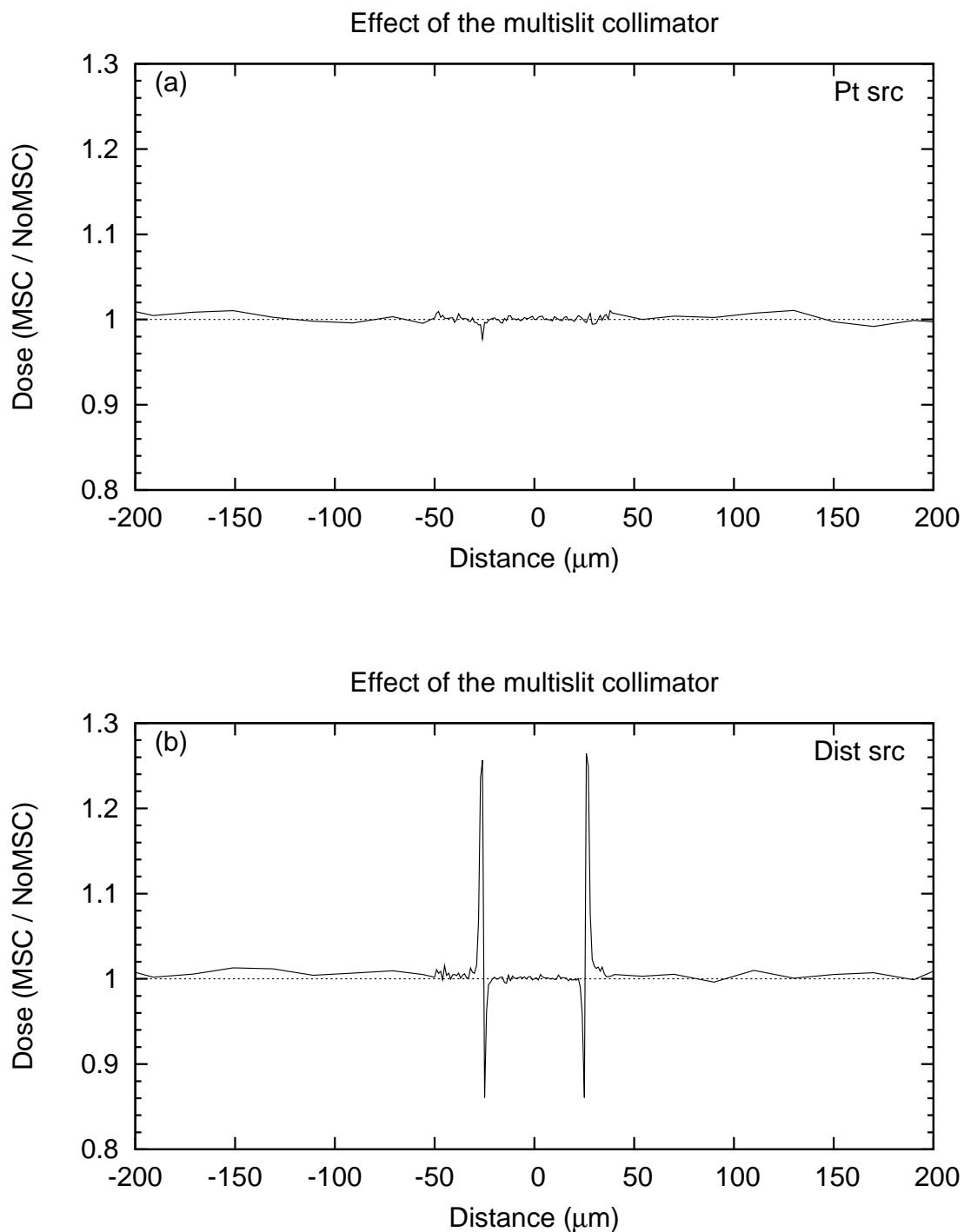


Figure 7.5: The effect of the multislit collimator. Figure (a) plots a ratio of the dose profile of a single microbeam obtained with and without the multislit collimator (MSC and NoMSC, respectively) and a point source (Pt src). A ratio of the corresponding MSC and NoMSC profiles obtained with a distributed source (Dist src) is plotted in figure (b). All dose profiles were scored between 1 and 2 cm depth in water.

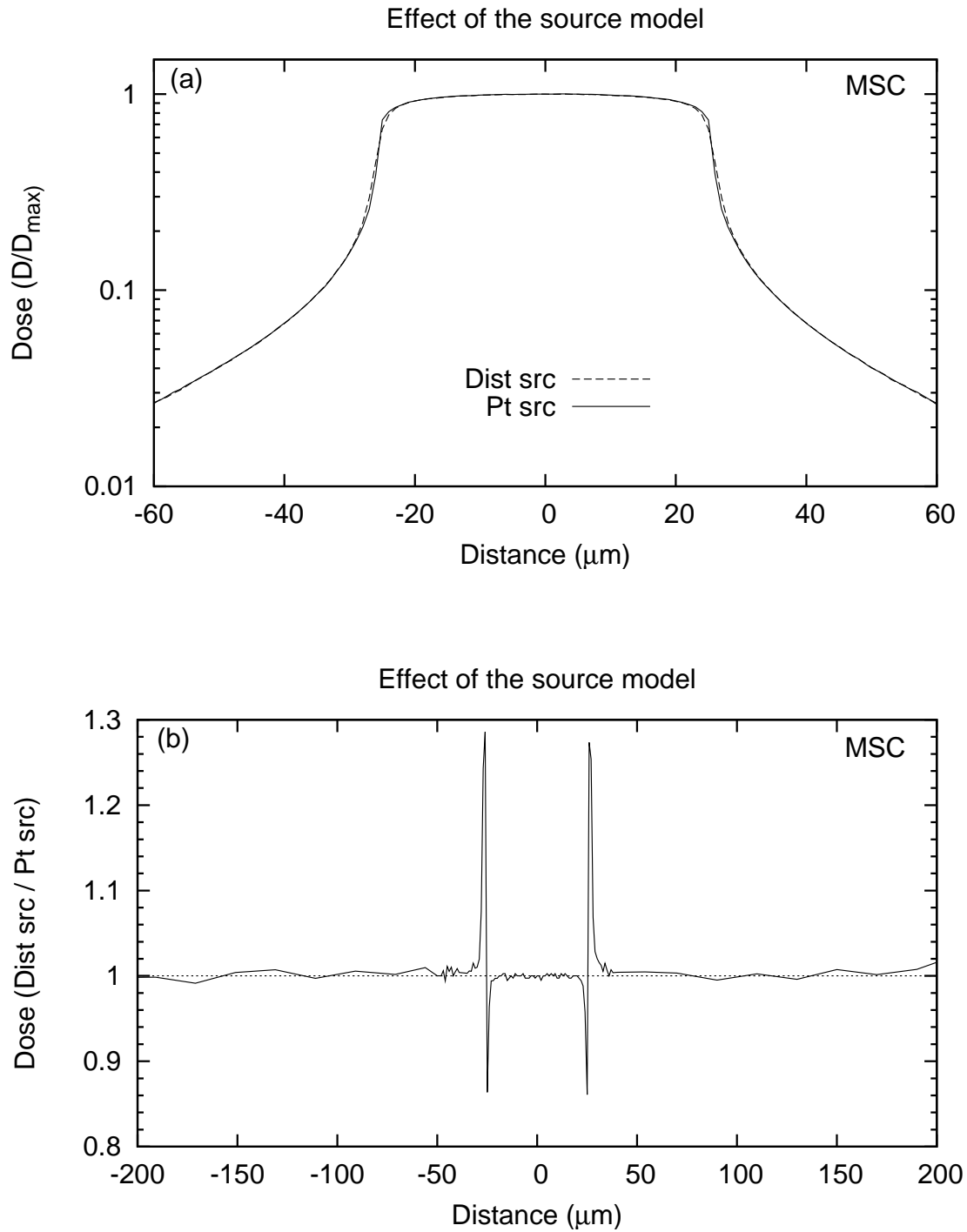


Figure 7.6: The effect of the source model. Figure (a) compares the dose profile of a single microbeam obtained with a point source (Pt src) to that produced by a distributed source (Dist src), using the multislit collimator (MSC). The dose profiles were scored between 1 and 2 cm depth (in water), where a ratio of the profiles is plotted in figure (b).



The ratio of dose obtained with the distributed source and point source is unity across most of the profile except at the edges of the microbeam, where the ratio drops 14% below unity before rising to almost 30% above it. This dose perturbation arises from steeper dose gradients between the peak and valley regions of the point source profile, and is brought about by the range of incident photon angles subtended being wider from a distributed source than from a point source. For example, photons originating near the edge of a distributed source can subtend larger angles to collimator apertures than photons originating at the source's centre (i.e. from a point source).

#### 7.3.4 Effect of the multislit collimator lateral offset

The dose profiles in section 7.3.3 were obtained with the source position centered on both the collimator aperture and beam axis, producing a dose profile equivalent to the central microbeam in an array. As the two overlapping stacks of the multislit collimator are laterally offset, each aperture will have a different vantage point in relation to the source. This motivated an investigation of the effect of the collimator's lateral offset on the dose profiles of emerging microbeams.

Simulations were performed with the single-beam model (which uses a single collimator element) to obtain individual dose profiles of the 5th and 12th microbeams to the left and right of the central microbeam. These profiles were scored between 1 and 2 cm depth in water. Figures 7.7 (a) and (b) compare the dose profile of the central microbeam, C single, with those obtained for the 5th and 12th microbeams to the left and right of centre, respectively (i.e. L5 single and L12 single in the LHS array, and R5 single and R12 single in the RHS array, when viewing the array from the source position). A comparison of the dose profiles of the 5th and 12th microbeams on either side of the central microbeam (i.e. L5 single with R5 single, and L12 single with R12 single) is shown in figures 7.7 (c) and (d) respectively.

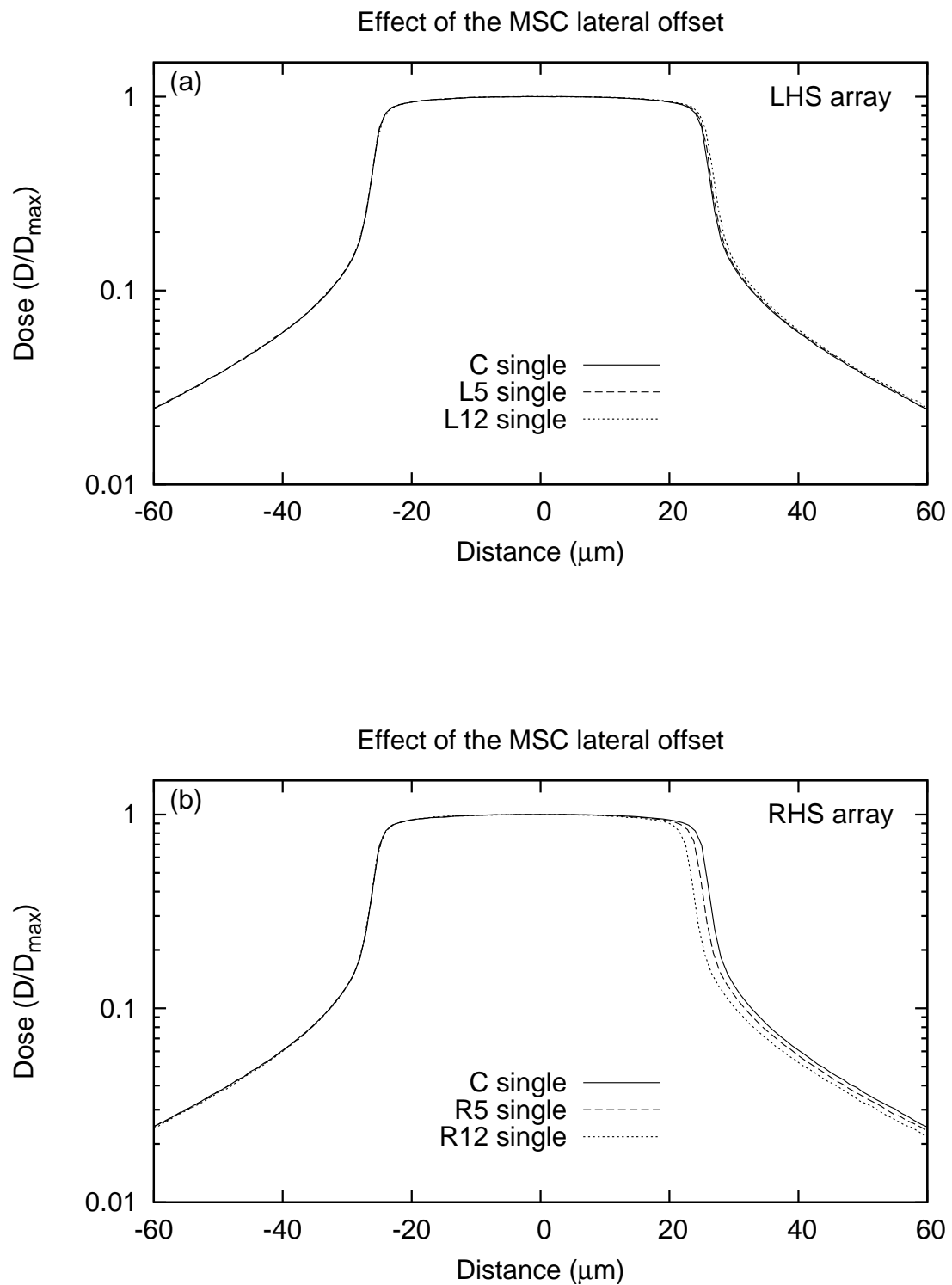


Figure 7.7: The effect of the multislit collimator (MSC) lateral offset. Figures (a) and (b) compare the dose profile of the central microbeam (C single) with those obtained for the 5th and 12th microbeams to the left and right of centre, respectively (i.e. in LHS array and RHS array).

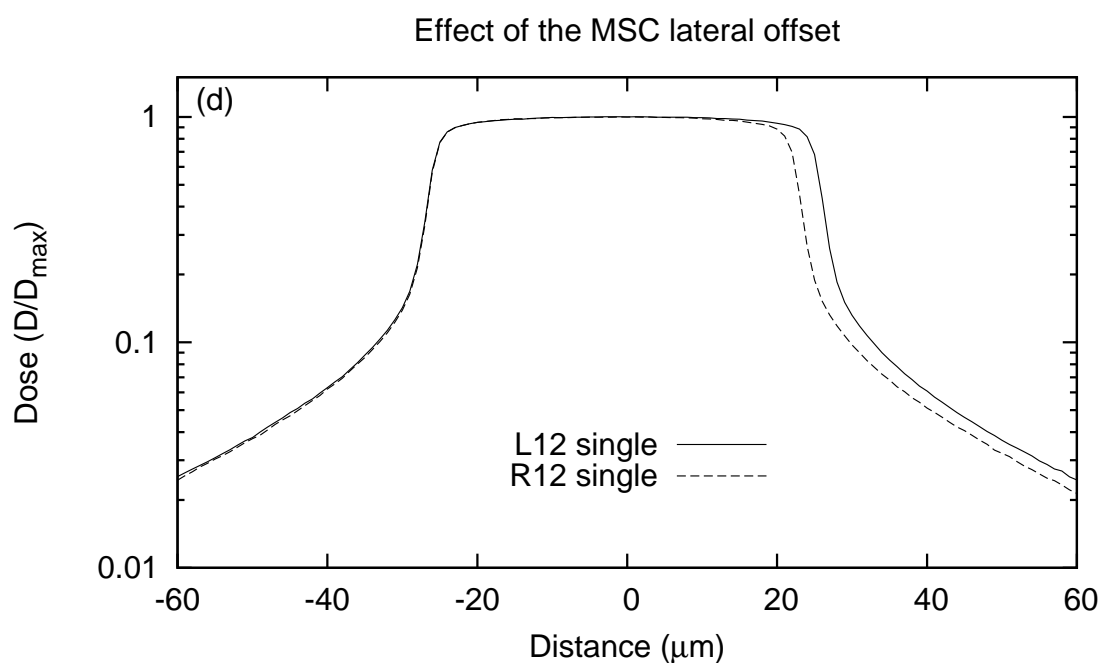
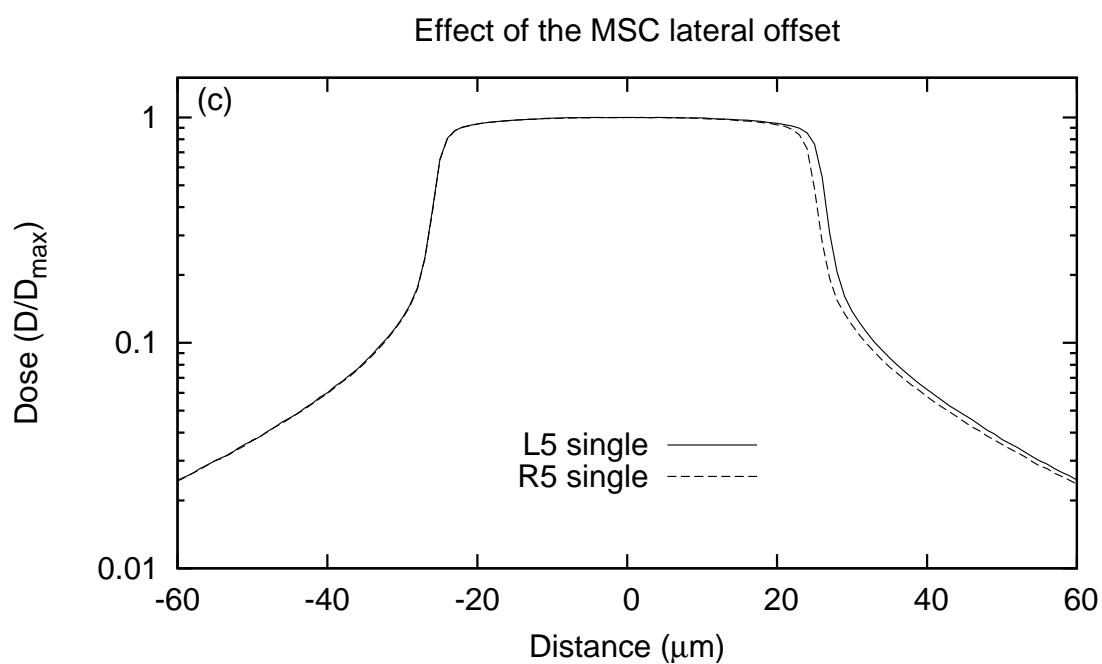


Figure 7.7: The effect of the multislit collimator (MSC) lateral offset. Figures (c) and (d) compare the dose profiles of the 5th and 12th microbeams on either side of centre, respectively (i.e. L5 single with R5 single and L12 single with R12 single).

When compared with the central microbeam, the dose profiles of the R5 single and R12 single microbeams in the RHS of the array exhibit smaller FWHM of almost 2 and 4  $\mu\text{m}$  respectively. Conversely, in the LHS of the array the FWHM of the L5 single and L12 single profiles are marginally larger than that of the central microbeam. Comparison of the FWHM of the 5th and 12th microbeams on either side of centre (i.e. L5 single with R5 single, and L12 single with R12 single) revealed differences of 2 and 4  $\mu\text{m}$  respectively, where the LHS profiles were broader than the corresponding RHS profiles.

The variation in microbeam FWHM, which is consistent with the  $\sim 4 \mu\text{m}$  difference measured by Bräuer-Krisch *et al.* [23], arises from the lateral offset of the multislit collimator stacks. As illustrated in figure 7.2 (b), photons traversing a collimator aperture right of centre, such as the R5 aperture (i.e. five microbeams right of center), experience a larger degree of obscuration from the laterally offset collimator stacks than photons traversing an aperture left of centre, such as the L5 aperture. As shown in figure 7.7, the further right of centre the aperture, the greater the degree of obscuration experienced by photons, and thus, the larger the reduction in the FWHM of the emerging microbeam. Conversely, microbeams left of centre do not experience a reduction in FWHM as the lateral offset favours the transmission of photons through the LHS apertures. In fact, microbeams left of centre experience a slight increase in FWHM (as much as 1  $\mu\text{m}$  for the L12 microbeam at the array's LHS edge) due to the wider range of incident angles that photons can subtend to these apertures.

### 7.3.5 Effect of the simulation model

Simulation of individual microbeams using only one element of the multislit collimator does not account for additional dose contributions from neighbouring microbeams in the array. The present study investigates the effect of the simulation model by comparing individual microbeam profiles obtained with the single-beam model, to those produced with the full array model (which uses the entire multislit collimator to simulate the dose profile of 25 microbeams in a single simulation). Figure 7.8 (a) compares the dose

profile of the central microbeam obtained with the full array simulation model, C full, to that obtained with the single-beam model, C single. A ratio of these profiles is shown in figure 7.8 (b). Also included in this figure is a ratio of the corresponding dose profiles of the 12th microbeams on either side of the central microbeam (i.e. L12 full to L12 single, and R12 full to R12 single).

According to the ratios, microbeam profiles obtained with the full array model exhibit substantially larger valley doses than those obtained with the single-beam model. For example, the valley doses in the C full dose profile are up to 8 times larger than those in the C single profile. Similarly, at the edges of the array, the valley doses in the L12 full and R12 full microbeam profiles are up to 6 times larger than those in the corresponding L12 single and R12 single profiles. The substantially larger valley doses obtained with the full array model arise from the overlapping dose tails of neighbouring microbeams in the array. Since the single-beam model uses only one element of the multislit collimator to simulate individual microbeams, it does not account for additional valley dose contributions from neighbouring microbeams.

Comparison of the 5th and the 12th full array profiles on either side of the central microbeam (i.e. L5 full with R5 full, and L12 full with R12 full) reveals a difference in their FWHM of 2 and 4  $\mu\text{m}$  respectively, where the LHS profiles are broader than the corresponding RHS profiles. These FWHM variations were also exhibited by the microbeam profiles obtained with the single-beam model (refer to section 7.3.4).

Consistent differences in the FWHM of microbeams simulated with the single-beam and full array models prompted a study of the effect of the simulation model on the PVDR of microbeams. Previous Monte Carlo studies in MRT have used the superposition of the dose profile from a single microbeam to generate an array of microbeams [16, 22, 23, 25, 32, 85, 87]. This present study compares the PVDRs of an array of microbeams generated with the superposition model with those obtained with the full array model, which uses the entire multislit collimator to produce an array of microbeams in a single simulation.

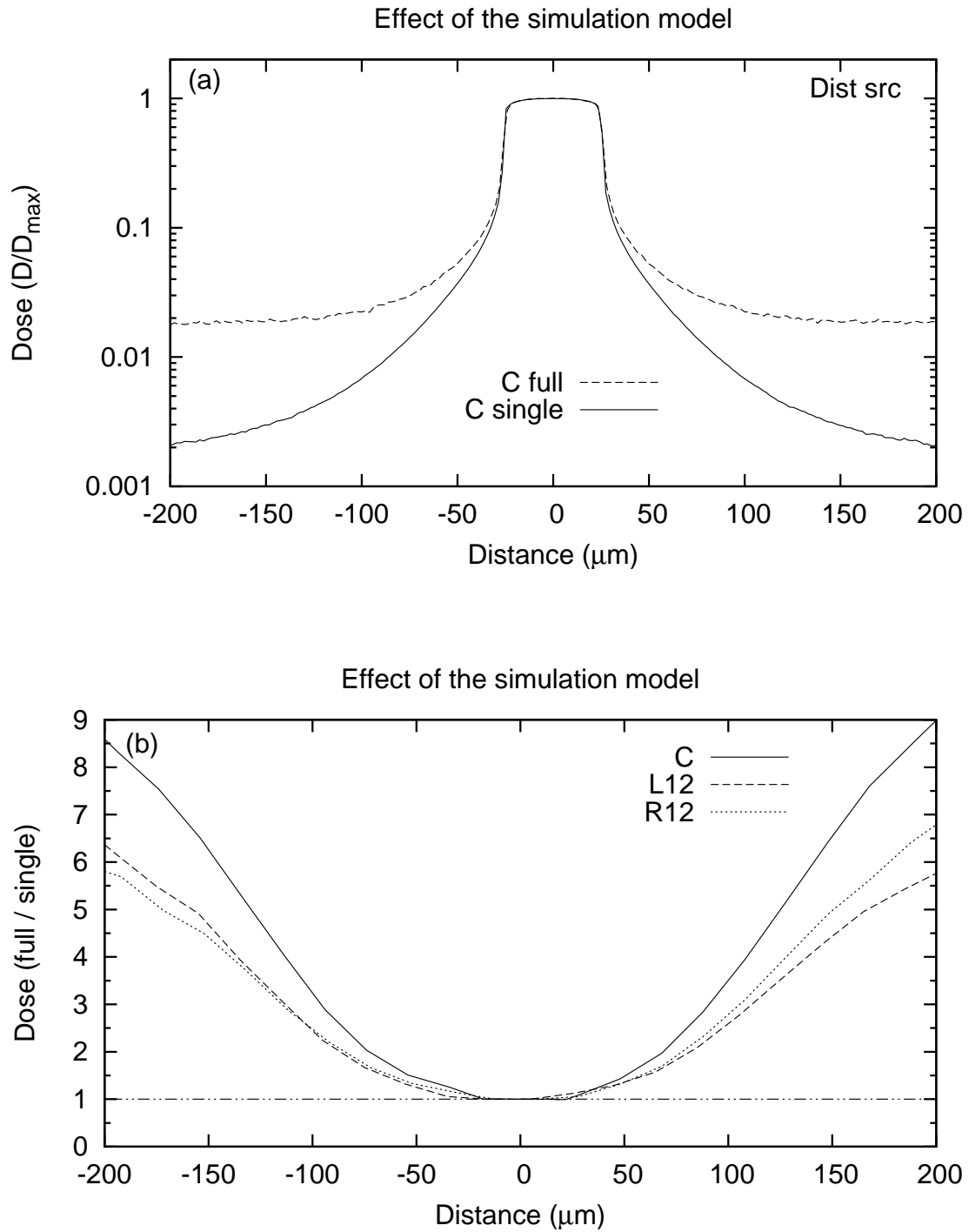


Figure 7.8: The effect of the simulation model. Figure (a) compares the dose profile of the central microbeam simulated with the single-beam and full array models (C single and C full, respectively) and scored between 1 and 2 cm depth in water. A ratio of these C profiles, and those obtained for the L12 and R12 microbeams at either edge of the array, are shown in figure (b).

The superposition simulation model used the dose profile of a single microbeam shown in figure 7.9 (a), which was obtained with photon transport commencing on the surface of the phantom with an initial direction parallel to the beam. The lateral range of scoring bins for this profile was twice the width of the array to ensure the inclusion of all valley dose contributions from neighbouring microbeams (i.e. the dose tail of a microbeam at the LHS edge of the array extended to the RHS edge, and vice versa).

Figure 7.9 (b) plots the dose profile of an array of 25 microbeams (each  $50\ \mu\text{m}$  wide, 1 cm high, and separated by  $410\ \mu\text{m}$ ) generated with the superposition and full array simulation models (i.e. sup array and full array, respectively). A ratio of the sup array and full array dose profiles is plotted in figure 7.9 (c). The superimposed sup and full array profiles appear to be identical. A ratio of the profiles, however, reveals substantial differences in the penumbral dose of microbeams on either side of the central microbeam, where the sup array overestimates the penumbral dose of microbeams right of centre (i.e. in RHS array) and underestimates the penumbral dose of microbeams left of centre (i.e. in LHS array).

An enlargement of the ratio of the L12 and R12 microbeam profiles at either edge of the array (where the difference in penumbral dose is largest) is shown in figure 7.10 (a). At the left edge of the microbeam array, the L12 sup profile exhibits left and right penumbral doses of up to 34% less and 12% more than the corresponding penumbral doses of the L12 full profile. At the opposite edge of the array, the left and right penumbral doses of the R12 sup profile are as much as 50% and 98% larger than the corresponding penumbral doses of the R12 full profile. According to the comparison of FWHM for the C full, L12 full and R12 full profiles in figure 7.10 (b), the FWHM of the central microbeam (C full) is  $4\ \mu\text{m}$  greater and almost  $1\ \mu\text{m}$  smaller than the respective R12 full and L12 full microbeams at the right and left edges of the array.

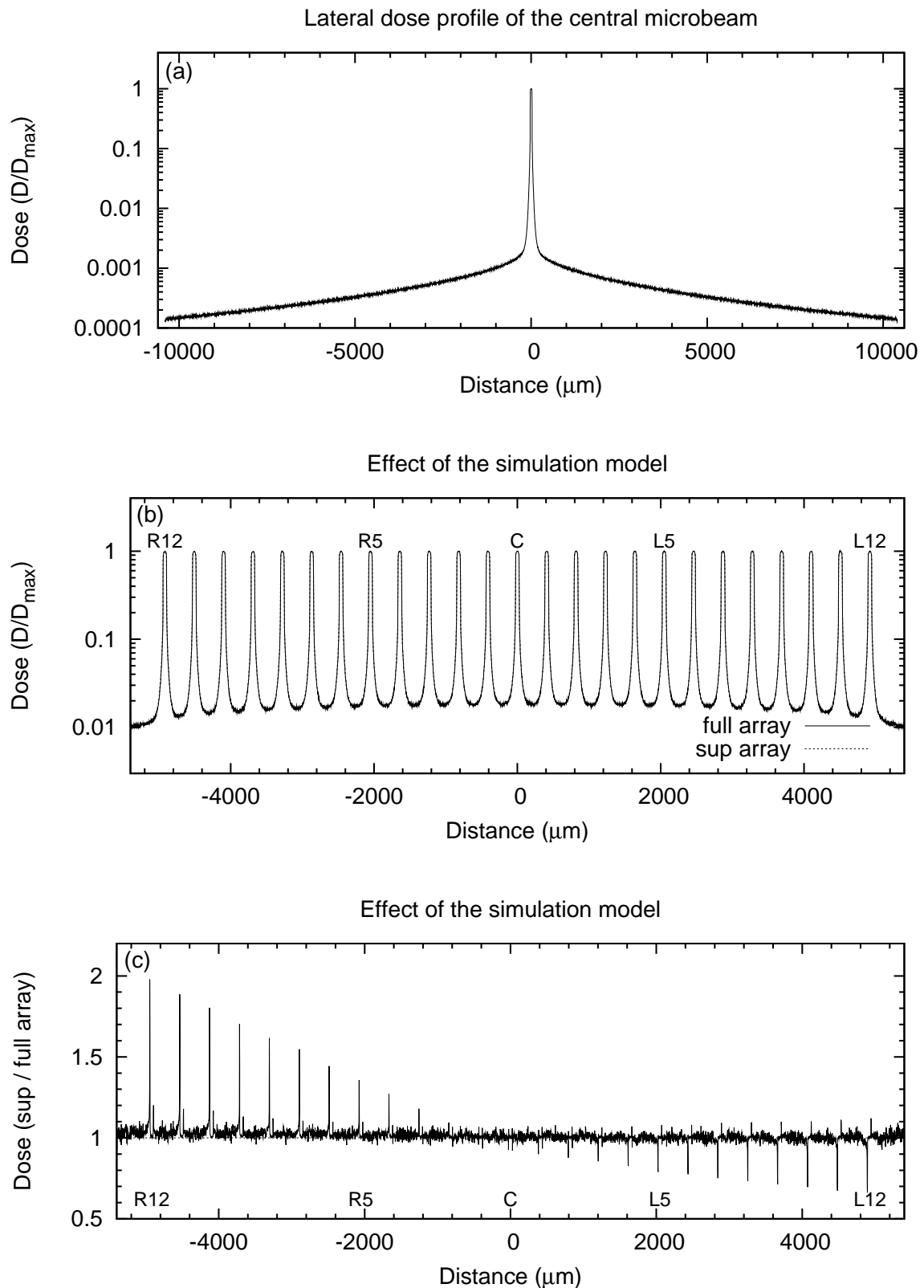


Figure 7.9: Effect of the simulation model. Figure (a) shows the dose profile of a single microbeam used by the superposition model. Figure (b) plots the dose profile of the sup and full arrays obtained with the superposition and full array models, respectively, where a ratio of these profiles is shown in figure (c). All profiles were scored between 1 and 2 cm depth (in water).



The differences in FWHM arise from the sup array failing to account for the lateral offset of the multislit collimator stacks. Since the sup array is generated from the superposition of a single dose profile, each microbeam within the array has the same FWHM. This assumption neglects the varying degrees of obscuration experienced by photons traversing different apertures in the multislit collimator, which give rise to the variations in microbeam FWHM in the full array.

Variations in the penumbral dose and FWHM of the full and sup array profiles led to a study of their corresponding peak-to-valley dose ratios (PVDRs). The PVDR of individual microbeams in the array was calculated using the dose in the central bin of the peak and an average of four bins about the valley midpoint on either side of the peak (i.e.  $\pm 205 \mu\text{m}$  from peak center). Figure 7.11 (a) plots the PVDR as a function of microbeam position for both the sup and full array. A ratio of their peak and valley doses and PVDRs is plotted in figure 7.11 (b).

While a ratio close to unity is observed for the peak dose of microbeams in the sup and full arrays, the ratio of valley dose, and hence PVDR, reveals up to 4% variation across the array. In the RHS array (i.e. microbeams 1 to 12), the valley dose of the sup array is up to 4% larger than that of the full array, while in the LHS array (i.e. microbeams 14 to 25) they are up to 2% smaller. Consequently, the PVDRs of microbeams in the LHS of the sup array are as much as 4% smaller than the corresponding PVDRs in the full array, while the PVDRs of microbeams in the RHS of the sup array are up to 2% larger than those in the full array. Considering both the sup array and full array exhibit peak doses of approximately unity, the sup array's underestimation of PVDRs in the RHS of the full array is due to an overestimation of valley dose. Similarly, the sup array's overestimation of PVDRs in LHS of the full array arises from an underestimation of valley dose.

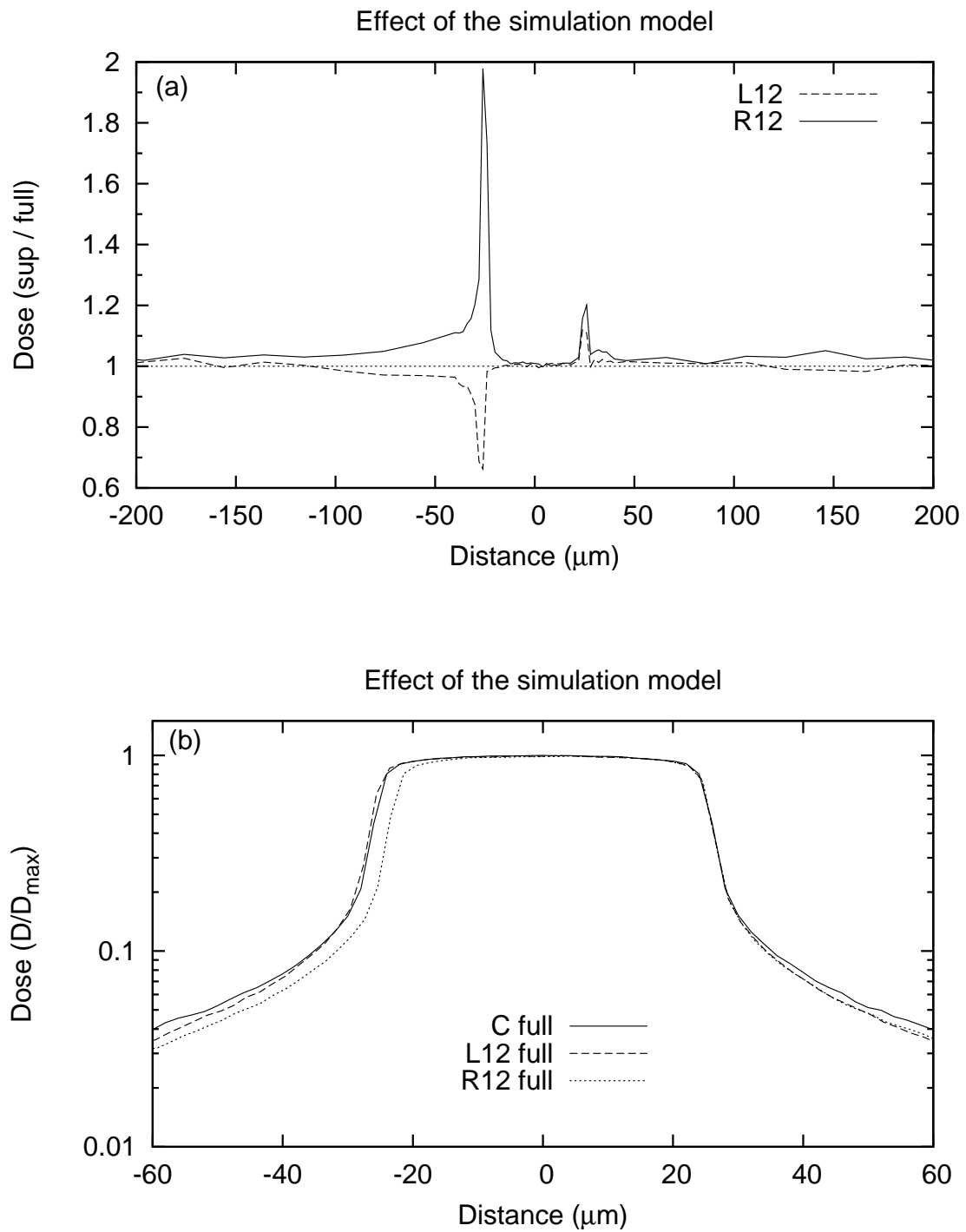


Figure 7.10: The effect of the simulation model. Figure (a) plots a ratio of the sup and full array dose profiles of the L12 and R12 microbeams at the left and right edges of the array, respectively. Figure (b) compares the central microbeam profile in the full array (C full) with those at the left and right edges of the array (L12 full and R12 full, respectively).

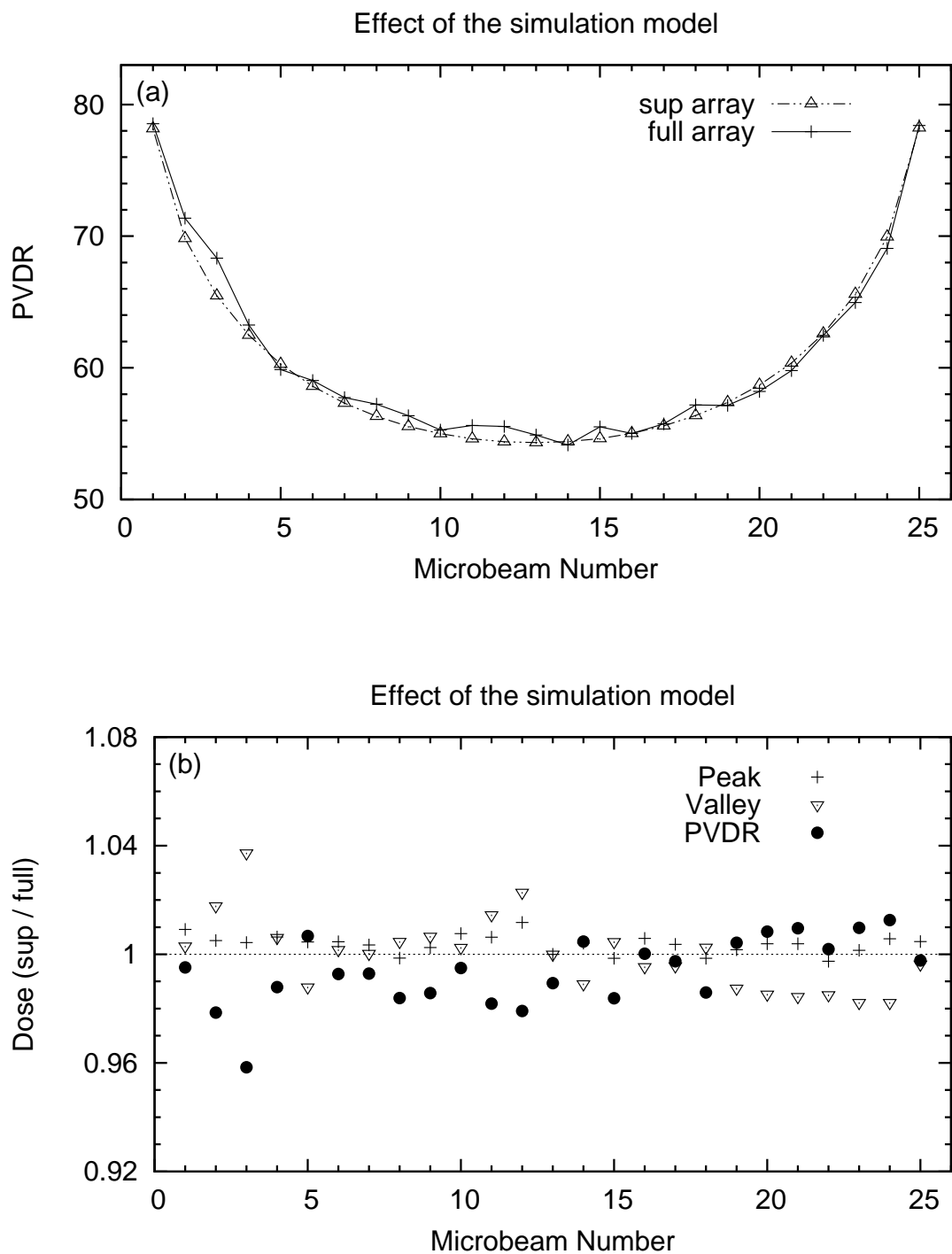


Figure 7.11: The effect of the simulation model. Figure (a) compares the PVDRs of microbeams in the sup array and full array. A ratio of the peak and valley doses and PVDRs of microbeams in the sup and full arrays is plotted in figure (b).

### 7.3.6 Effect of the multislit collimator alignment

In MRT, the multislit collimator alignment is adjusted until the FWHM of microbeams are approximately uniform. The substantial 10% variation between the FWHM of an array of 25 microbeams prompted a study of the influence of multislit collimator alignment on microbeam dose profiles. This was performed by rotating the collimator through small angles, as illustrated in figure 7.3. A comparison of the dose profiles of the full array obtained with and without a collimator rotation of  $\pm 0.05^\circ$ ,  $\pm 0.1^\circ$ , or  $\pm 0.2^\circ$  is shown in figures 7.12 (a), (b), and (c) respectively. An enlargement of the dose profile of the central microbeam (peak 13) for collimator rotations of  $\pm 0.05^\circ$ ,  $\pm 0.1^\circ$ , and  $\pm 0.2^\circ$ , is shown in figures 7.13 (a), (b), and (c), respectively.

The dose profiles of the array obtained with positive angles of collimator rotation reveal increases in the FWHM and valley dose of individual microbeams. The enlargement of the central microbeam dose profile reveals an increase in the original  $50\text{ }\mu\text{m}$  FWHM of 4, 8, and  $16\text{ }\mu\text{m}$  for collimator rotations of  $0.05^\circ$ ,  $0.1^\circ$ , and  $0.2^\circ$  respectively, as well as a slight increase in valley dose. Conversely, the microbeam profiles obtained with a negative collimator rotation of  $-0.05^\circ$  or  $-0.1^\circ$ , exhibit reductions in FWHM of 18 and  $36\text{ }\mu\text{m}$  respectively, and up to 3 times lower valley doses. Higher valley doses and larger FWHM obtained with a rotation of  $-0.2^\circ$  are attributed to severe photon obscuration and scattering through the collimator apertures, and hence, loss of microbeam definition.

Figures 7.14 (a), (b), and (c) compare the dose profile of the central microbeam, C full, with the L12 full and R12 full microbeams (at the left and right edges of the array) for positive collimator rotations of  $0.05^\circ$ ,  $0.1^\circ$ , and  $0.2^\circ$  respectively. The C full microbeam exhibits a FWHM  $1\text{ }\mu\text{m}$  larger than the L12 full profile and  $1\text{ }\mu\text{m}$  smaller than the R12 full profile, which is caused by the lateral offset of the collimator stacks. As shown in figure 7.3, rotating the collimator through small positive angles advantages the transmission of photons through RHS apertures and disadvantages those through LHS apertures. Thus, positive collimator rotations of up to  $0.2^\circ$ , reduced the difference between the L12 and R12 microbeam FWHM from  $5\text{ }\mu\text{m}$  (in the absence of rotation) to  $2\text{ }\mu\text{m}$ .

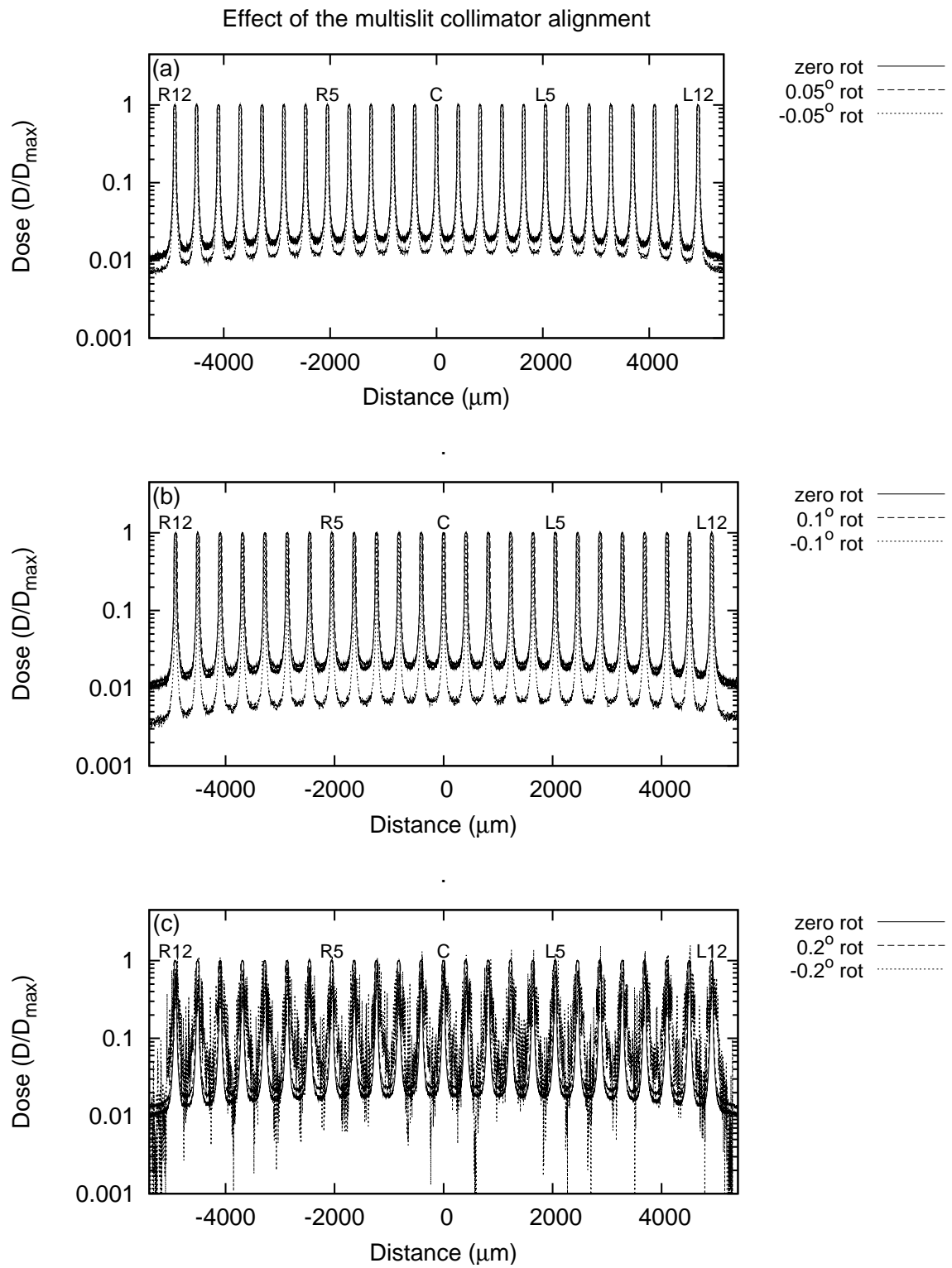


Figure 7.12: The effect of the multislit collimator alignment on the dose profile of an array of 25 microbeams. Figures (a), (b), and (c) compare the dose profile of the full array with and without collimator rotations of  $\pm 0.05^\circ$ ,  $\pm 0.1^\circ$ , and  $\pm 0.2^\circ$  respectively.

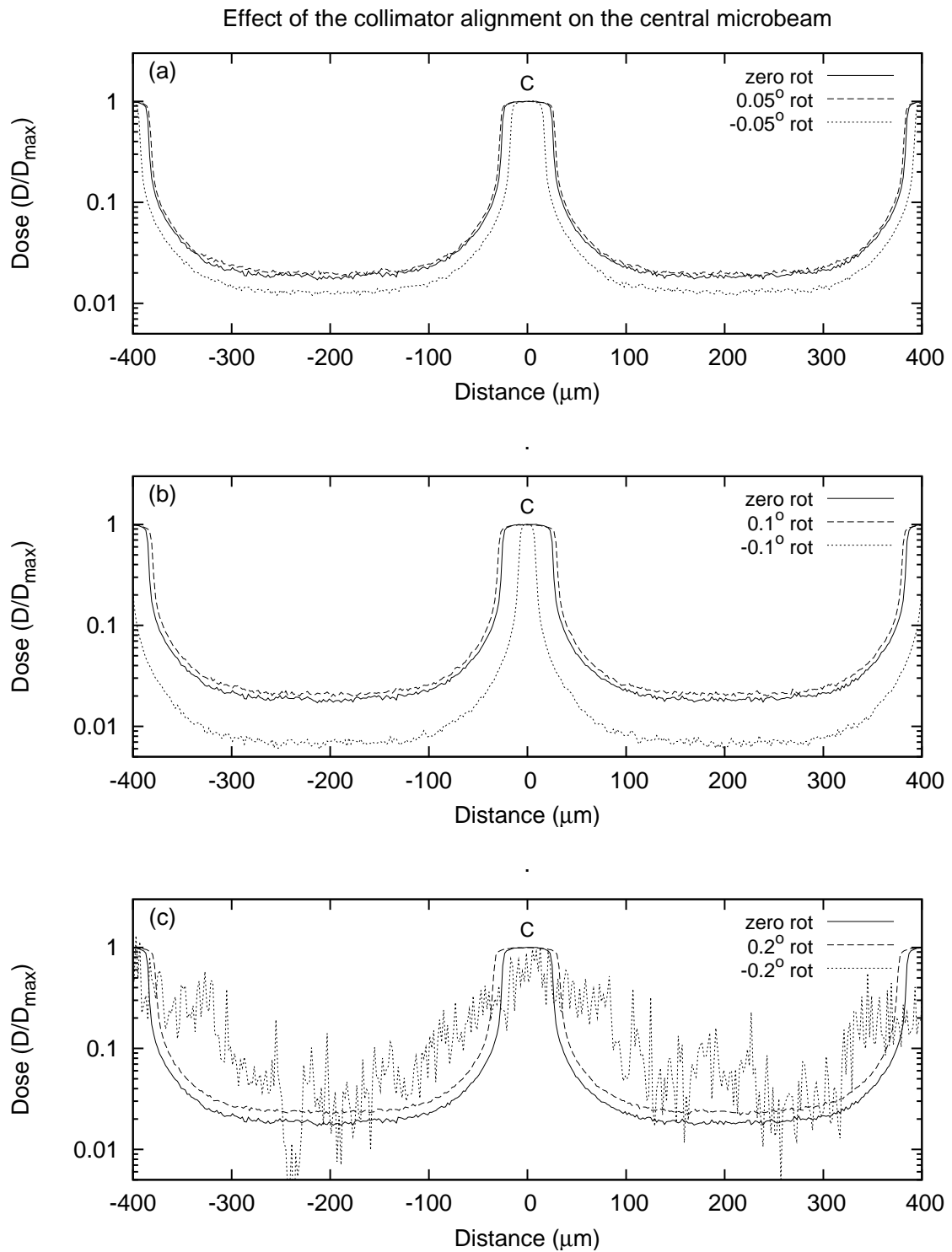


Figure 7.13: The effect of the multislit collimator alignment on the dose profile of the central microbeam. Figures (a), (b), and (c) compare the dose profile of the central microbeam (C) produced with and without collimator rotations of  $\pm 0.05^\circ$ ,  $\pm 0.1^\circ$ , and  $\pm 0.2^\circ$  respectively.

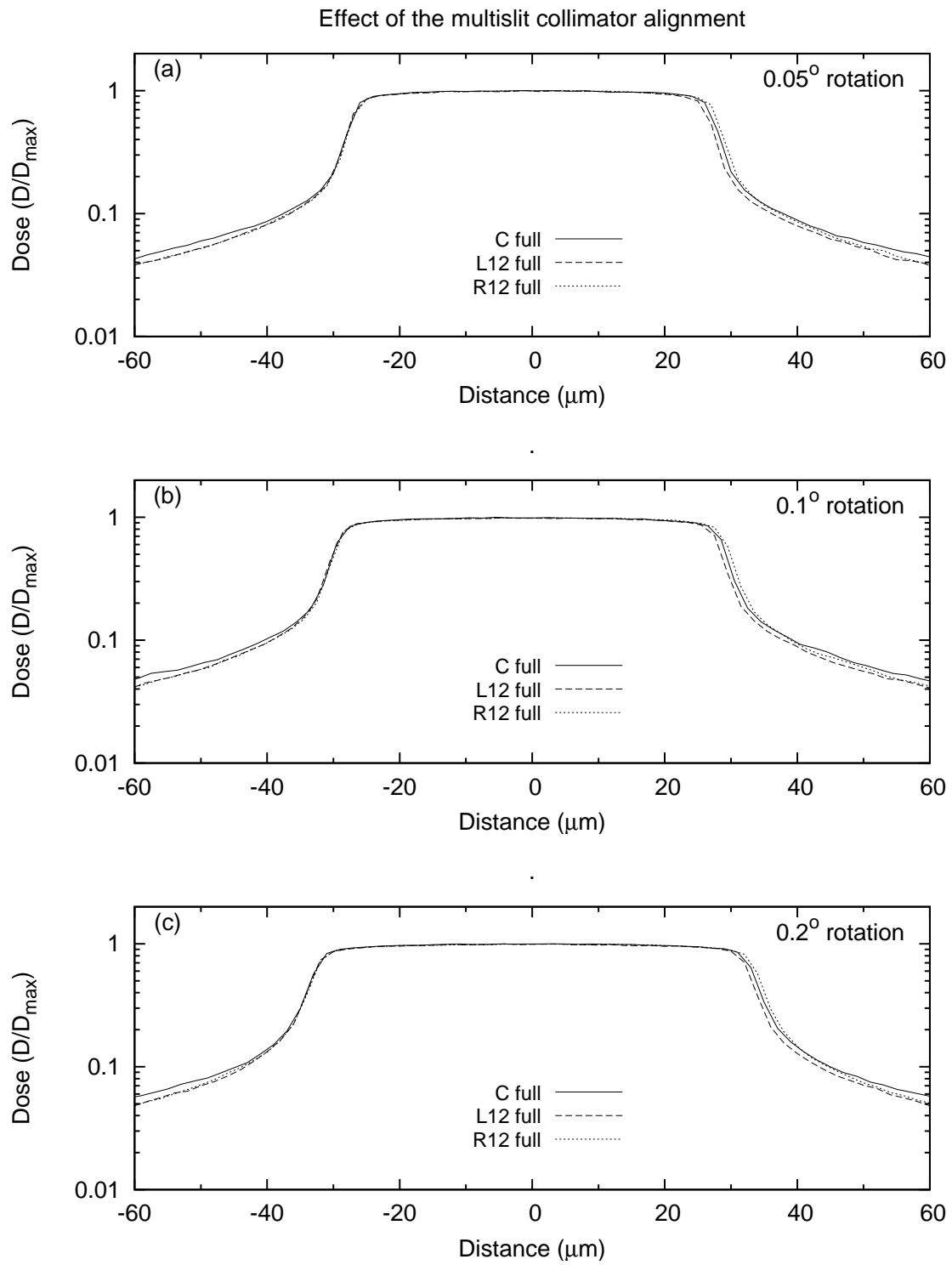


Figure 7.14: The effect of positive angles of collimator rotation on the dose profiles of microbeams. Figures (a), (b), and (c) compare the dose profile of the central microbeam (C full) with those at the left and right edges of the array (L12 full and R12 full) for collimator rotations of 0.05, 0.1, and 0.2° respectively.

Figures 7.15 (a), (b), and (c) compare the dose profile of the central microbeam, C full, with the L12 full and R12 full microbeams (at the left and right edges of the array) for negative collimator rotations of  $-0.05^\circ$ ,  $-0.1^\circ$ , and  $-0.2^\circ$  respectively. For both  $-0.05^\circ$  and  $-0.1^\circ$  rotations, the FWHM of the C full microbeam is about  $4\text{ }\mu\text{m}$  larger than the L12 full profile and  $4\text{ }\mu\text{m}$  smaller than the R12 full profile.

The larger FWHM and valley doses exhibited by microbeams in the RHS array compared with those in the LHS array are attributed to the greater obscuration and therefore scattering experienced by photons traversing the RHS apertures. At a larger collimator rotation of  $-0.2^\circ$ , the paths of photons through the apertures are almost completely obscured, leading to increased scattering and broader microbeams whose FWHM are difficult to ascertain owing to poor statistics.

An investigation of the effect of collimator alignment on the PVDR of microbeams was conducted in response to the variations in peak and valley dose with the positive and negative multislit collimator rotations. Figures 7.16 (a) and (b) respectively plot the peak dose and valley dose of an array of 25 microbeams for collimator rotations of  $\pm 0.05^\circ$ ,  $\pm 0.1^\circ$ , and  $\pm 0.2^\circ$ , where the dose has been normalised to the peak and valley dose in the central microbeam. A plot of the PVDR as a function of microbeam position is shown in figure 7.17 (a), and a ratio of the PVDR obtained with and without collimator rotation is plotted in figure 7.17 (b).

When the collimator was rotated through positive angles of  $0.05^\circ$ ,  $0.1^\circ$ , and  $0.2^\circ$ , the valley dose increased with increasing angle, while the intensity of peak dose remained constant. As a result, the PVDR of microbeams decreased with increasing angle. For example, the PVDR of the central microbeam decreased from 55.3 without collimator rotation to 50.0, 47.1, and 43.1 with collimator rotations of  $0.05^\circ$ ,  $0.1^\circ$ , and  $0.2^\circ$  respectively (i.e. reductions in the PVDR of around 10, 15, and 20% respectively).



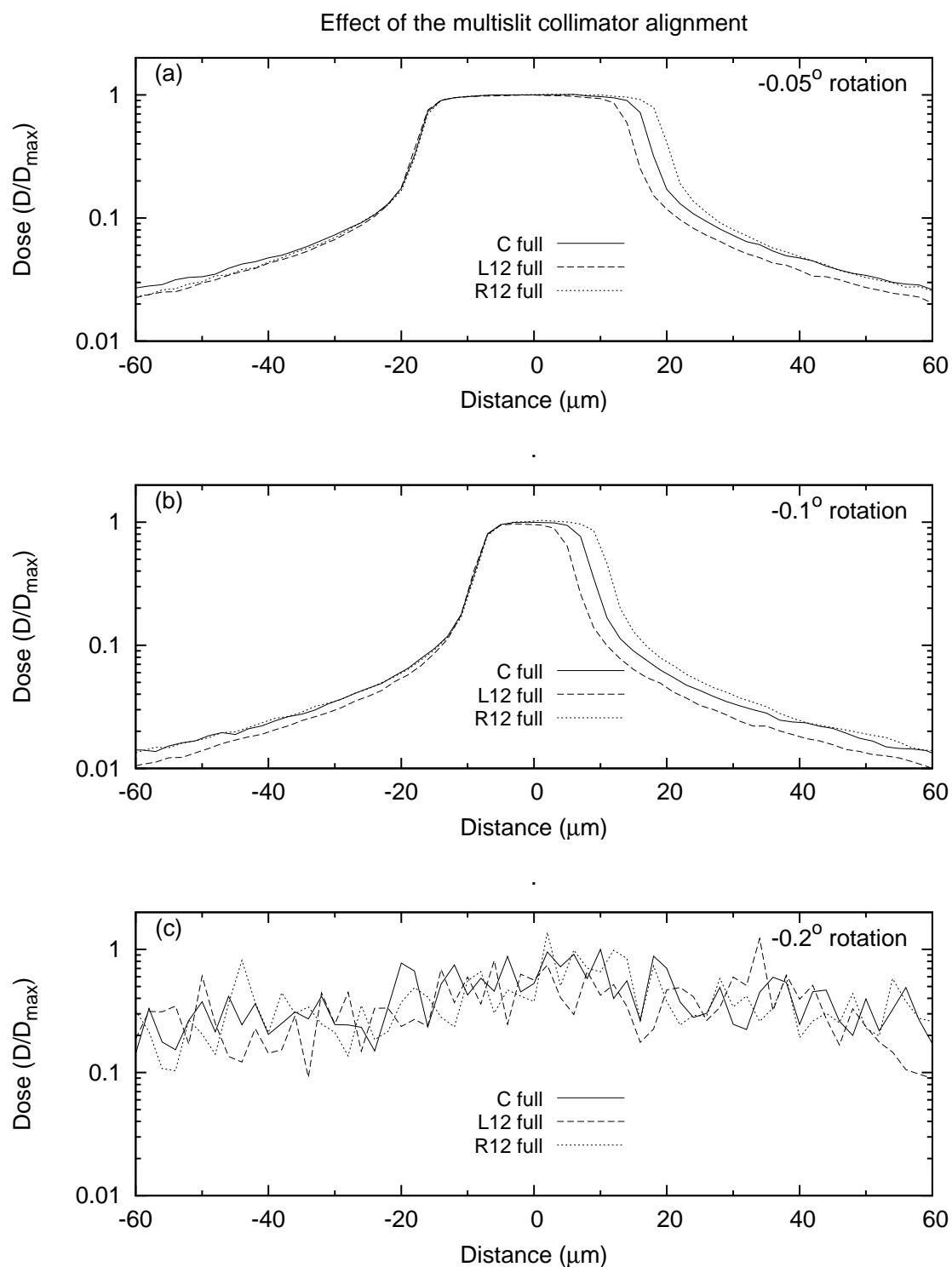


Figure 7.15: The effect of negative angles of collimator rotation on the dose profiles of microbeams. Figures (a), (b), and (c) compare the dose profile of the central microbeam (C full) with those at the left and right edges of the array (L12 full and R12 full) for collimator rotations of  $-0.05^\circ$ ,  $-0.1^\circ$ , and  $-0.2^\circ$  respectively.

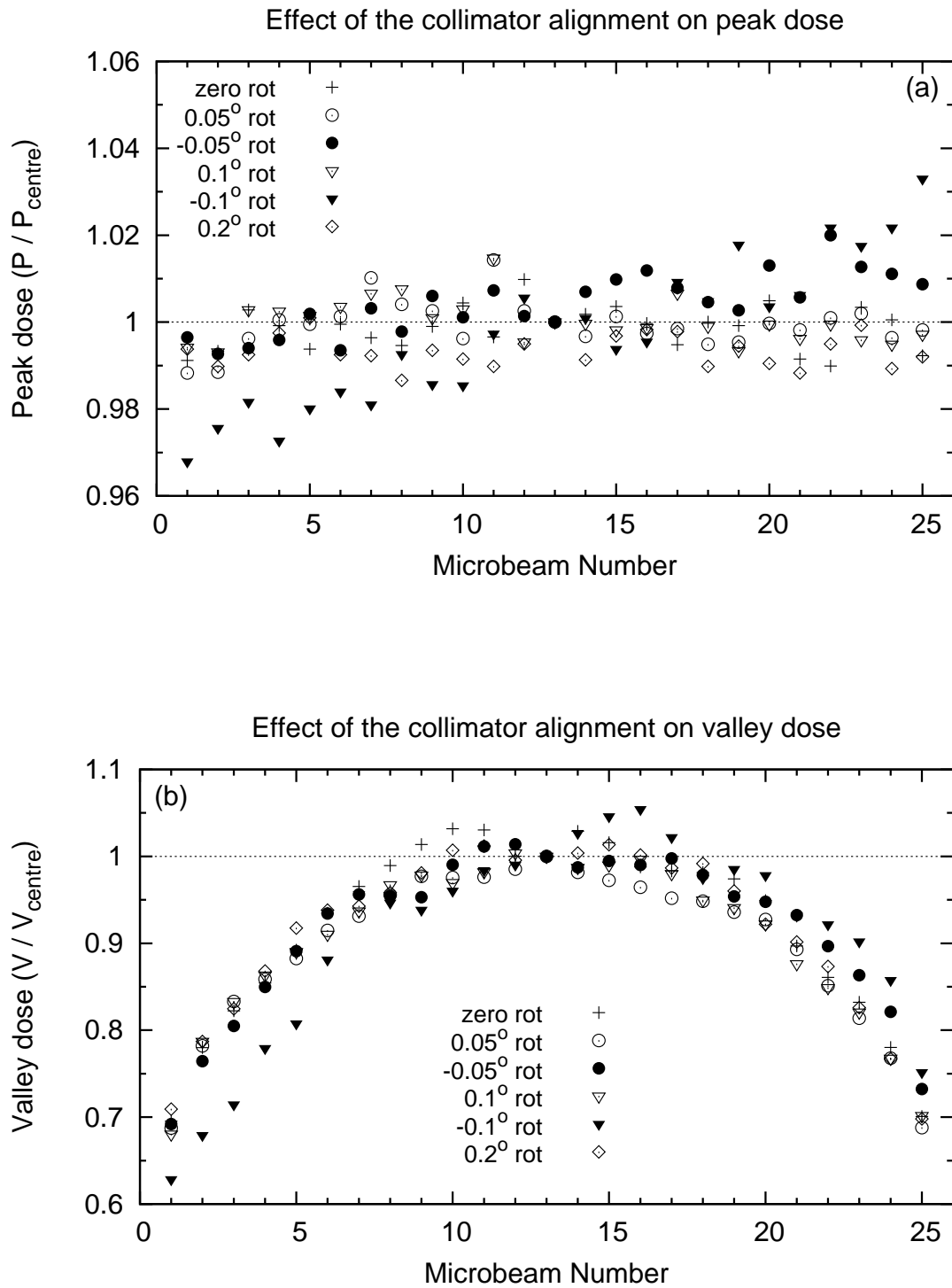


Figure 7.16: The effect of the multislit collimator alignment on the peak and valley doses of microbeams. Figures (a) and (b) respectively compare the peak and valley doses of a microbeam array (normalised to dose in the central microbeam) with and without collimator rotations of  $\pm 0.05^\circ$ ,  $\pm 0.1^\circ$ , and  $0.2^\circ$ . The dose profile obtained with a  $-0.2^\circ$  rotation is not shown owing to poor statistics.

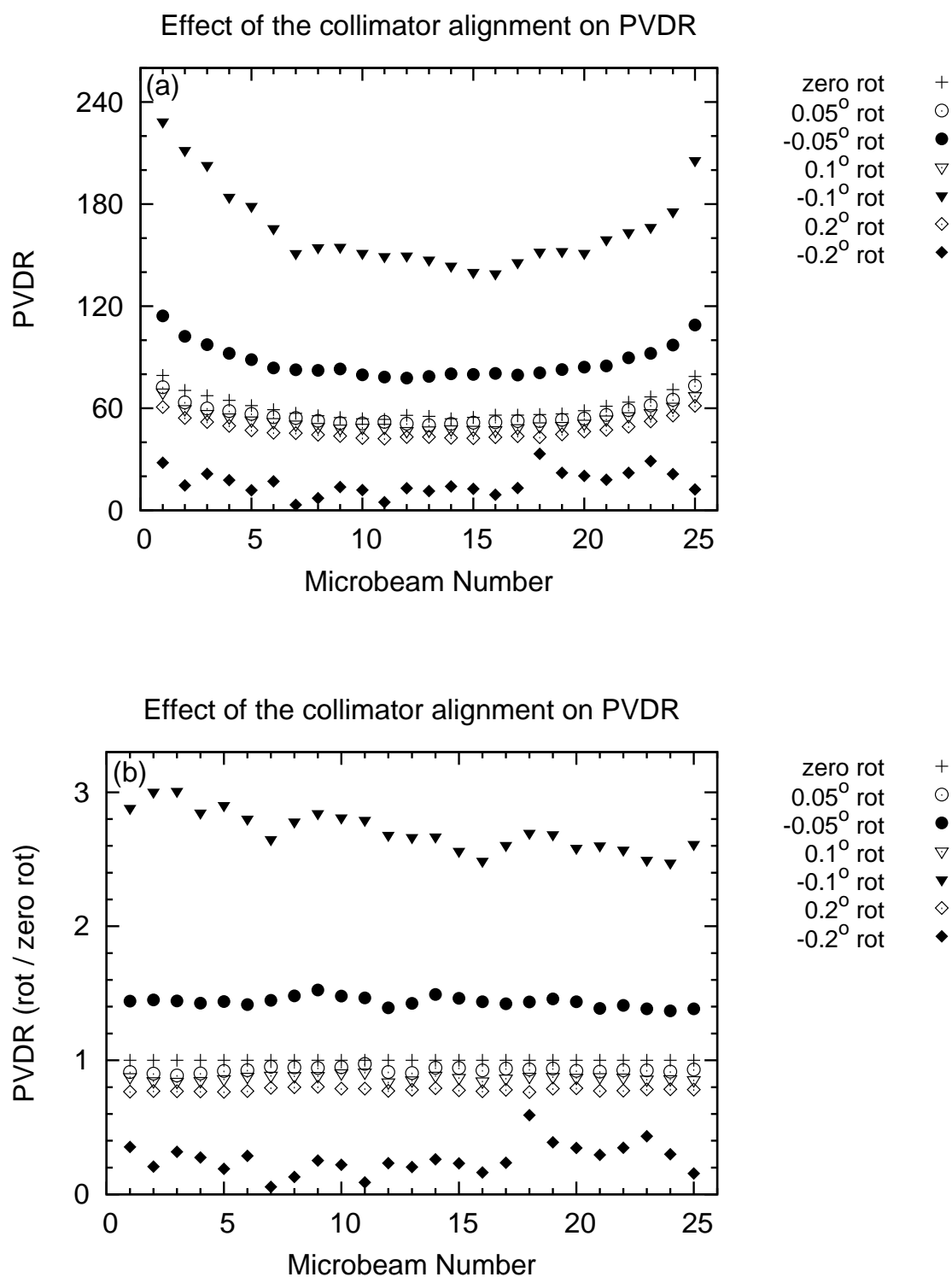


Figure 7.17: The effect of the multislit collimator alignment on the PVDRs of microbeams. Figure (a) compares the PVDRs of a microbeam array obtained with collimator rotations of  $\pm 0.05^\circ$ ,  $\pm 0.1^\circ$ , and  $\pm 0.2^\circ$ . A ratio of the PVDRs with and without collimator rotation is plotted in figure (b).

For negative collimator rotations, variations occurred in both the peak and valley doses of microbeams. Peak doses in the LHS array (i.e. microbeams 1 to 12) exhibited a reduction of up to 3%, while the peak doses in the RHS array (i.e. microbeams 14 to 25) revealed increases of as much as 3%. Similarly, the valley dose of LHS microbeams decreased by up to 10%, while the valley dose of RHS microbeams increased by up to 8%. These variations in peak and valley dose are the result of photon obscuration through the laterally offset collimator stacks, where a negative collimator rotation reduces photon transmission through RHS apertures.

Despite variations in the peak and valley dose lying within the uncertainties (i.e. less than 1% in the peak and 8% in the valley), there is a consistent shift in the PVDR with collimator rotation, as observed in figure 7.17 (b). While the PVDRs for positive rotation angles are within 20% of those obtained in the absence of collimator rotation, those obtained with  $-0.05^\circ$  and  $-0.1^\circ$  rotations are about 50 and 180% larger respectively. However, for a collimator rotation of  $-0.2^\circ$ , the PVDRs are about 80% lower than those obtained without rotation, owing to severe photon obscuration and scattering through the apertures.

### 7.3.7 Effect of the collimator design

As shown in section 7.3.4, the asymmetric construction of the dual stack multislit collimator gives rise to a 10% variation in the FWHM of an array of 25 microbeams. The advantage of using a dual stack collimator is that it allows adjustment of the microbeam width. In the future, once optimal microbeam widths for treatment have been determined, the dual stacks may be replaced with a single stack of fixed microbeam width. In anticipation of this advancement, the present study compared the influence of collimator design on the uniformity of microbeams.

Figures 7.18 (a) and (b) compare the dose profiles of the central microbeam, C full, and the L12 full and R12 full microbeams (at the left and right edges of the array) for the dual stack and single stack multislit collimators, respectively.

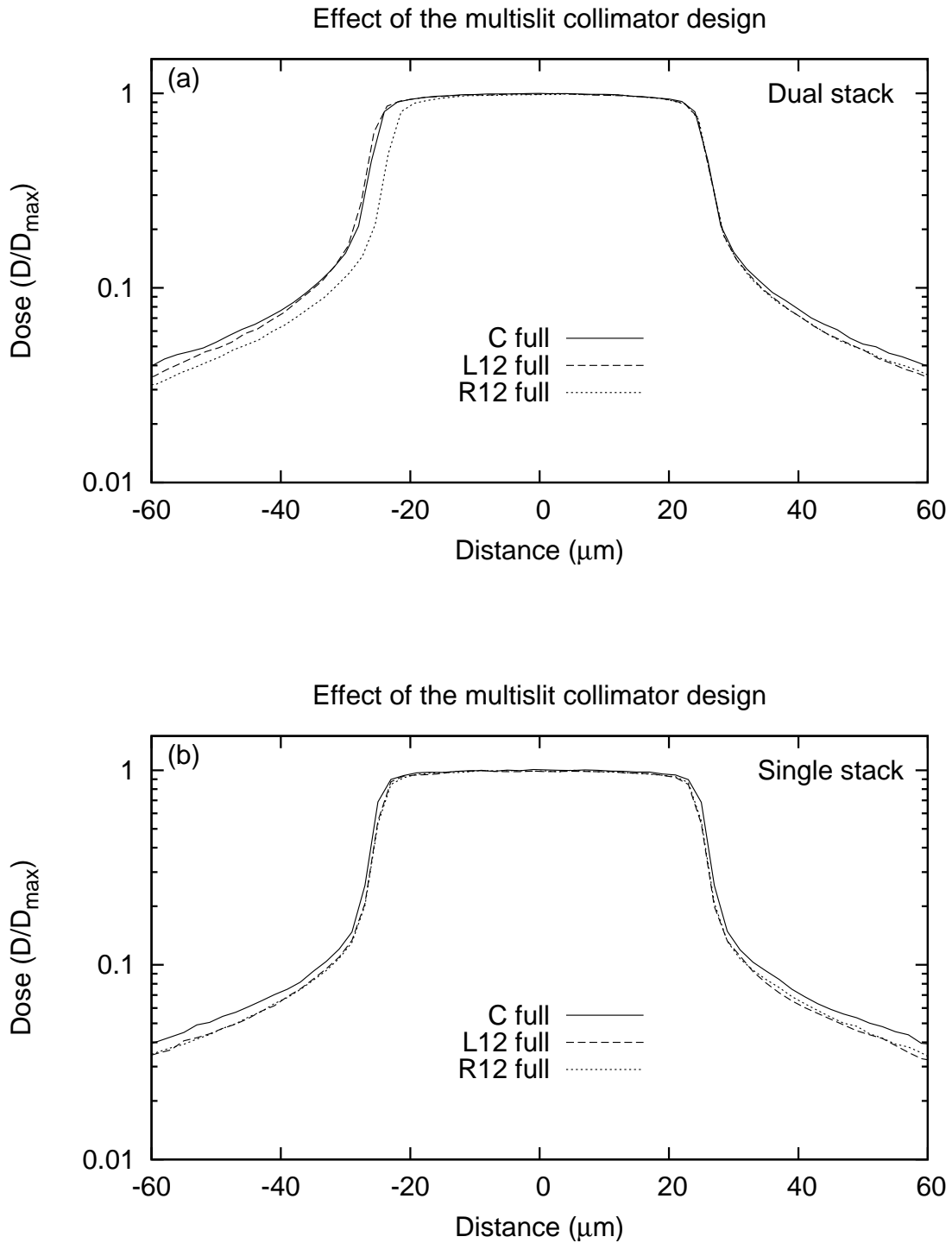


Figure 7.18: The effect of the multislit collimator design on microbeam profiles. Figure (a) compares the dose profile of the central microbeam produced with the dual stack collimator (C full) with those at the left and right edges of array (L12 full and R12 full). The corresponding microbeam profiles obtained with a single stack collimator are shown in figure (b).

Microbeams emerging from the dual stack collimator exhibit FWHM variations of up to 5  $\mu\text{m}$ , where RHS microbeams are narrower than those in the LHS array. Microbeams produced with a single stack collimator, on the other hand, exhibit less than 2  $\mu\text{m}$  variation in their FWHM, where complementary microbeams (on the left and right of the central microbeam) have identical FWHM since the photon obscuration through these apertures is the same. The narrowing of microbeams further from the centre arises from the wider angles subtended by primary photons (from the source to the collimator), and hence, greater obscuration occurs through these apertures.

The influence of multislit collimator alignment was also investigated for the fixed-width, single stack collimator. Figures 7.19 (a) and (b) compare the C full, L12 full, and R12 full microbeam profiles obtained with collimator rotations of 0.05 and -0.05° respectively. When the collimator was rotated 0.05°, the C full microbeam exhibited a FWHM that was 2  $\mu\text{m}$  smaller than the R12 full microbeam and 2  $\mu\text{m}$  larger than the L12 full microbeam. Conversely, when the collimator was rotated -0.05°, the FWHM of the C full microbeam was 2  $\mu\text{m}$  larger than the R12 full microbeam and 2  $\mu\text{m}$  smaller than the L12 full microbeam. For both rotations, the FWHM of the C full microbeam was 44  $\mu\text{m}$ .

The broader RHS profiles obtained with positive angles of collimator rotation is due to the favoured photon transmission through RHS apertures rather than LHS apertures, and vice versa for negative rotations. The uniformity of the C full FWHM for both positive and negative rotations of equal magnitude was not observed with the dual stack collimator owing to the lateral offset of its stacks (i.e. FWHM for the C Full microbeam of 34 and 56  $\mu\text{m}$  for -0.05 and 0.05° rotations, respectively).

### 7.3.8 Effect of the interaction medium

The tissue equivalence of water and polymethyl methacrylate (PMMA) make them a popular choice of phantom material for research in radiotherapy. The present study investigated the influence of these interaction media on the dose profile and PVDR of

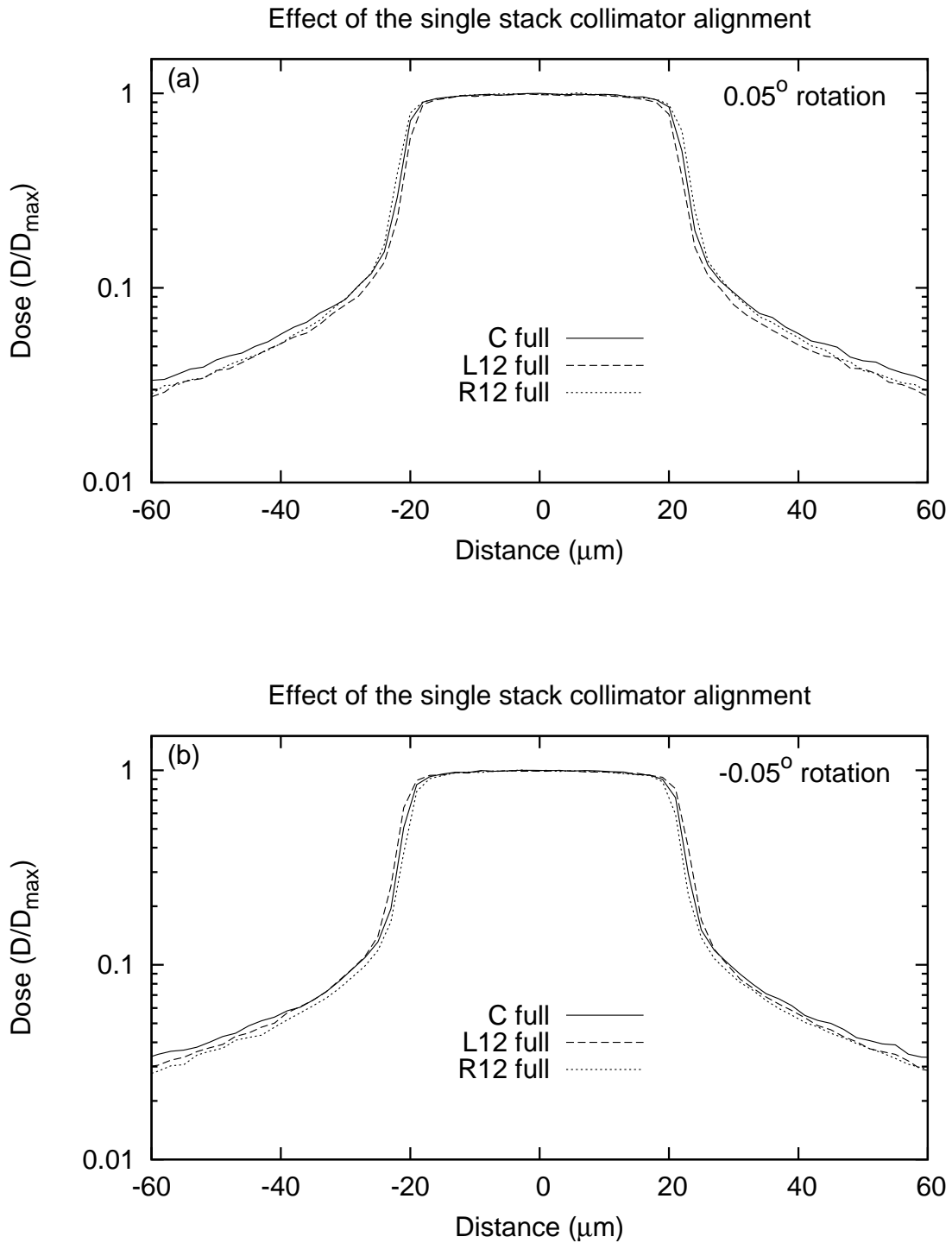


Figure 7.19: Effect of the alignment of the single stack collimator on the dose profiles of microbeams. Figures (a) and (b) plot the dose profiles of the central microbeam (C full) and the L12 full and R12 full microbeams (at the left and right edges of the array) produced with the single stack collimator rotated through 0.05 and -0.05°, respectively.

an array of 25 microbeams. Figure 7.20 (a) compares the dose profile of the central microbeam scored between 1 and 2 cm depth in water and PMMA, respectively. A ratio of the dose profiles is plotted in figure 7.20 (b).

The microbeam profiles obtained in H<sub>2</sub>O and PMMA exhibit the same FWHM, but different penumbral and valley doses. The profiles obtained in PMMA exhibit up to 20% lower penumbral dose and 10% higher valley dose than the profiles in water, corresponding to approximately 10% smaller PVDRs. The variations in dose stem from the different density and photon interaction cross sections of the two materials (PENELOPE uses a density of 1.0 and 1.19 gcm<sup>-3</sup> for H<sub>2</sub>O and PMMA respectively).

In chapter 5, simulations were performed with monoenergetic photon beams to determine the dose distribution of a single microbeam in perspex, or PMMA, according to the type of initial photon interaction (i.e. Rayleigh scattering, photoelectric effect, or Compton scattering). These simulations were repeated with a water phantom in order to ascertain the differences in the profiles obtained in PMMA. Figure 7.21 compares the dose distribution in PMMA and H<sub>2</sub>O for a single 100 keV microbeam (i.e. mean energy of the ESRF white beam) according to the type of initial photon interaction. Rayleigh scattering contributions are not shown as they are substantially lower than those from photoelectric or Compton scattering interactions, and hence, have a minimal influence on the overall dose profile.

Initial photon interactions via the photoelectric effect are responsible for the yield of secondary particles producing most dose contributions in the penumbra (i.e. over a distance approximately equal to the maximum range of photoelectrons). The higher penumbral dose exhibited by the microbeam in H<sub>2</sub>O compared with PMMA is attributed to the larger range of electrons in water. Beyond the penumbra, the majority of dose contributions are from primary photons undergoing Compton scattering interactions. The lower valley dose exhibited by microbeams in H<sub>2</sub>O than in PMMA is attributed to the smaller cross sections for Compton scattering in water at these energies.



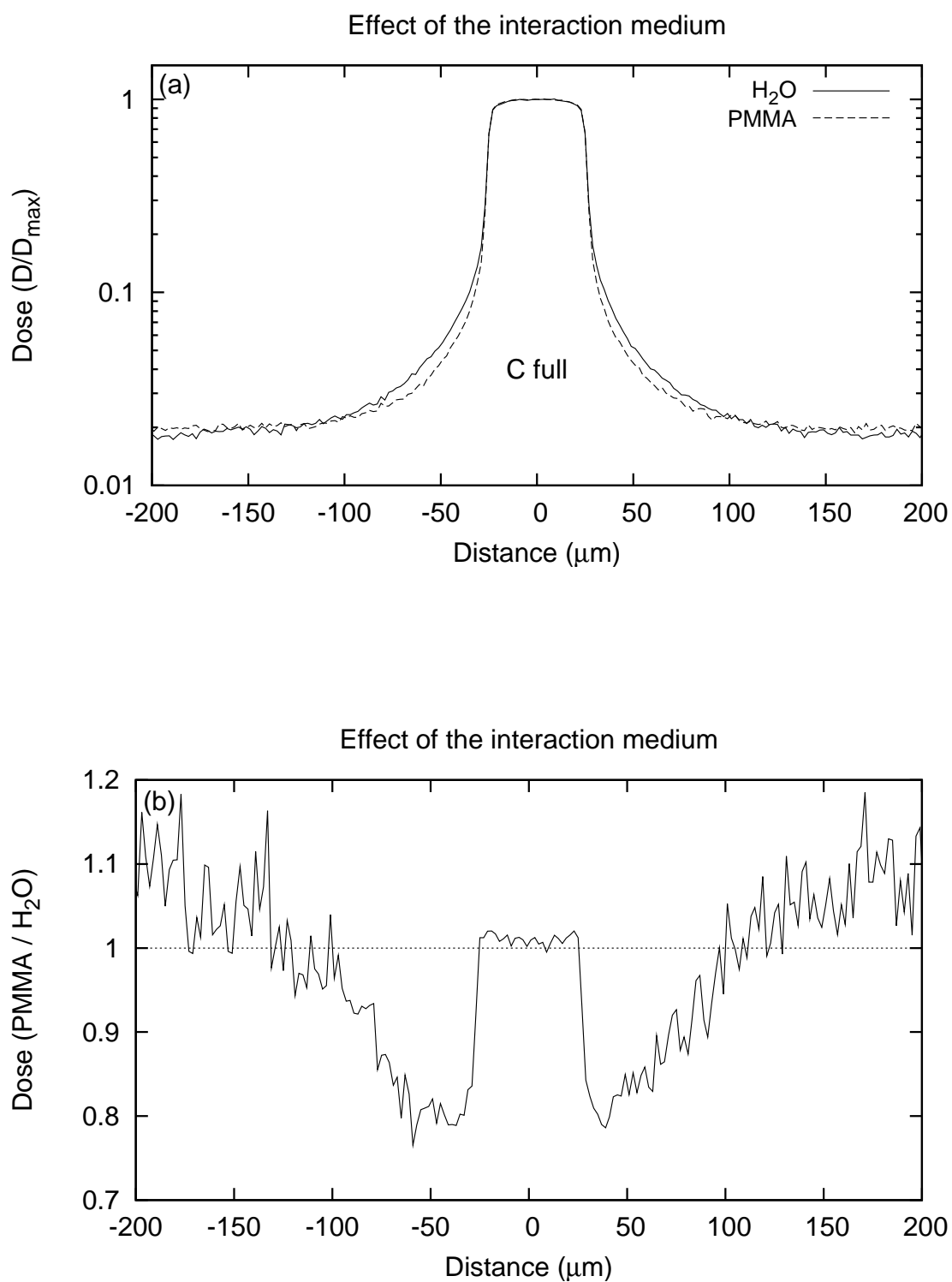


Figure 7.20: Effect of the interaction medium on microbeam profiles. Figure (a) compares the dose profile of the central peak in an array of 25 microbeams (C full) scored between 1 and 2 cm depth in water ( $H_2O$ ) and polymethyl methacrylate (PMMA). A ratio of the dose profiles is shown in figure (b).

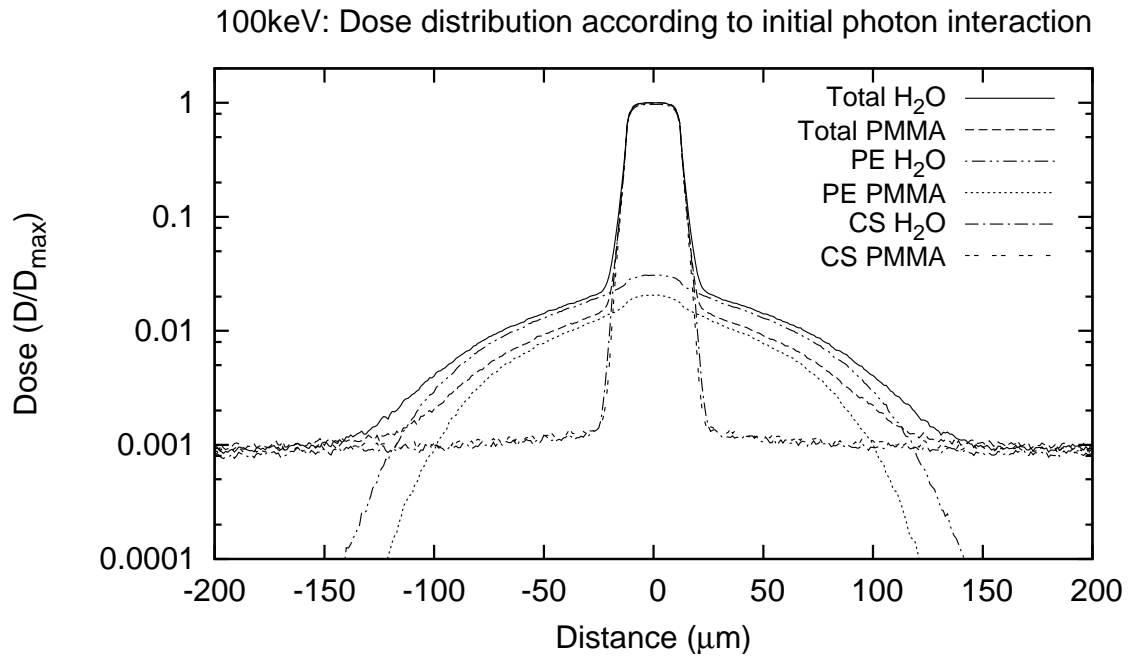


Figure 7.21: Single microbeam profile showing the dose distribution according to the type of initial photon interaction in water ( $\text{H}_2\text{O}$ ) and polymethyl methacrylate (PMMA) for a 100 keV beam, where CS = Compton scattering, PE = Photoelectric effect, and Total = contributions from CS, PE, and Rayleigh scattering.

### 7.3.9 Effect of the height of scoring regions

In any given valley region, the spectrum of primary and secondary particles is not uniform over the height of the microbeams from which it is derived. This motivated a study on the influence of the height of scoring regions on the valley dose and PVDR of an array of 25 microbeams (each  $50\ \mu\text{m}$  wide, 1 cm high, and separated by  $410\ \mu\text{m}$ ). The height of the array was divided into five lateral slices of scoring bins: 0 to 0.2 cm, 0.2 to 0.4 cm, 0.4 to 0.6 cm, 0.6 to 0.8 cm, and 0.8 to 1.0 cm. Dose was scored between 1 and 2 cm depth (in water) in bins of  $0.0002 \times 0.2 \times 1.0\ \text{cm}^3$  (width  $\times$  height  $\times$  depth).

Figure 7.22 compares the valley dose on either side of the central microbeam (C full) in each lateral slice, to the total valley dose in all slices (i.e. 0 to 1 cm). A ratio of the PVDR in each slice to that integrated over all slices (i.e. total height of array) is plotted as a function of microbeam number in figure 7.23.

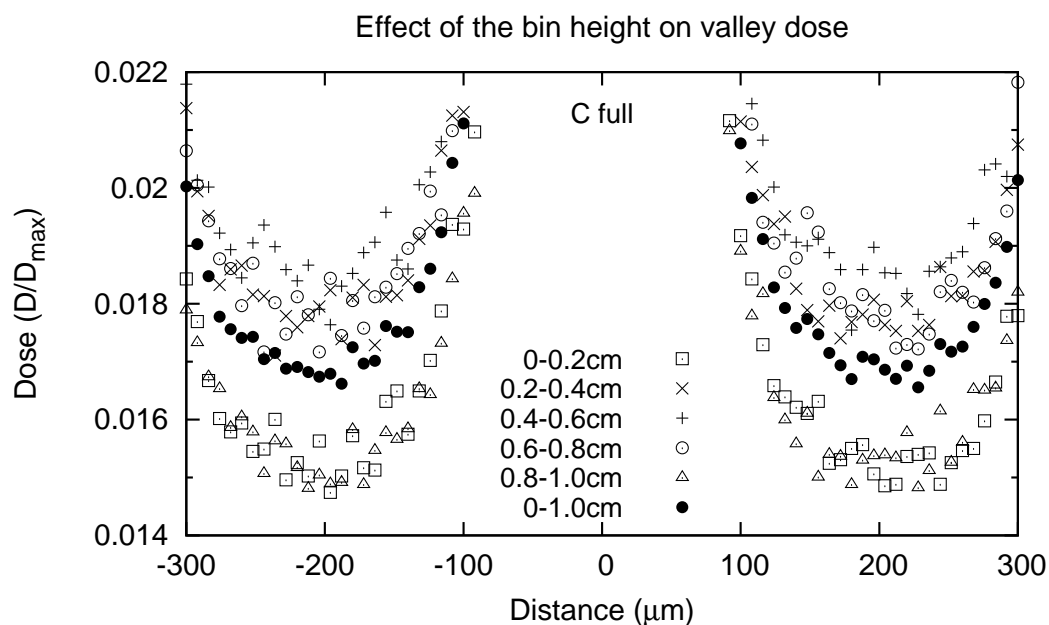


Figure 7.22: Effect of the height of scoring regions on the valley dose of microbeams. Comparison of the valley dose of the central microbeam (C full) in five lateral slices (each 0.2 cm high) to the total valley dose in all slices (i.e. 0 to 1 cm).

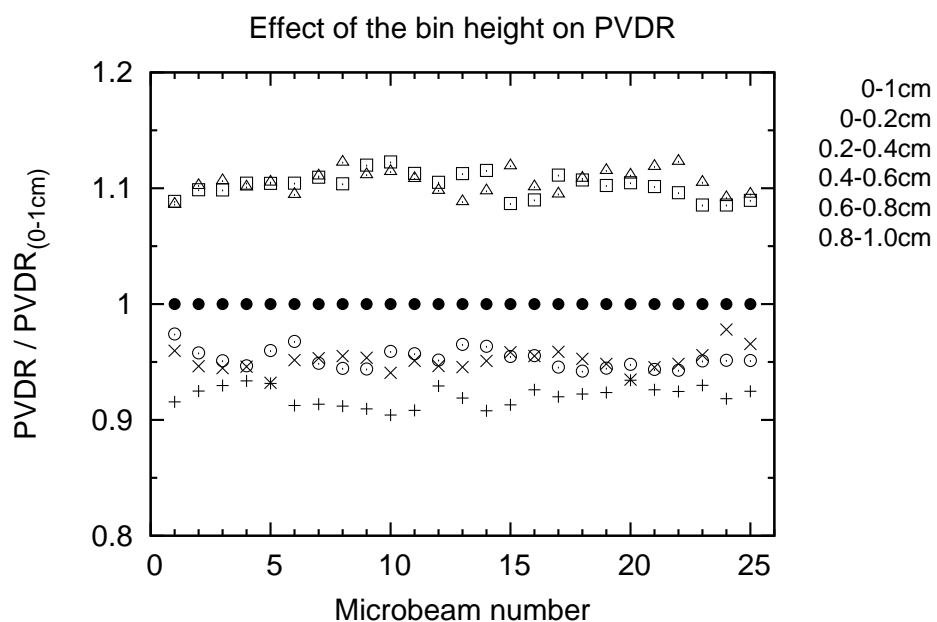


Figure 7.23: Effect of the height of scoring regions on the PVDR of microbeams. A ratio of the PVDR in five individual lateral slices (each 0.2 cm high) to the total PVDR integrated over all slices (i.e. 0 to 1 cm).

The largest valley dose was observed in the central slice (0.4 to 0.6 cm). The smallest valley dose occurred in the slices at the bottom and top of the array, 0 to 0.2 cm and 0.8 to 1.0 cm, respectively. The valley doses in the slices on either side of centre (i.e. 0.2 to 0.4 cm and 0.6 to 0.8 cm) were smaller than those observed in the central slice, but larger than the total valley dose (i.e. 0 to 1 cm).

As there was minimal variation in the peak dose obtained in each slice, the corresponding PVDRs in each slice followed a trend opposite to that of the valley dose. Compared with the integrated PVDRs (i.e. 0 to 1 cm), the PVDRs in the bottom and top slice (0 to 0.2 cm and 0.8 to 1.0 cm) were about 10% larger, while the PVDRs in the central slice (0.4 to 0.6 cm) were around 8% lower. For the slices on either side of centre (0.2 to 0.4 cm and 0.6 to 0.8 cm), the PVDR was approximately 5% lower than the integrated PVDR. The larger PVDRs in the slices at the top and bottom of the array stem from lower valley doses, which result from fewer scatter contributions from immediate and neighbouring peaks.

## 7.4 Conclusion

Simplifying microbeam transport by commencing perfect rectangular microbeams on the surface of the target, neglects the influence of the source, multislit collimator, and beam divergence between them. Common simplifications such as this have been shown to produce inaccuracies in the dose profiles and peak-to-valley dose ratios (PVDRs) of microbeams.

In this study, simulations accounting for the beam divergence, produced microbeam profiles with up to 26% larger penumbral and valley doses. Modelling the synchrotron source as a distributed source rather than a point source resulted in penumbral dose increases of almost 30%. While the inclusion of a multislit collimator produced little difference in the dose profile of a single microbeam (equivalent to the central microbeam in an array), it did alter the FWHM of microbeams at different positions within the array. The FWHM of the central microbeam, C single, was almost 1  $\mu\text{m}$  smaller and 4  $\mu\text{m}$  larger

than the respective microbeams at the left and right edges of the array (i.e. L12 single and R12 single). The difference in the FWHM arises from the lateral offset of the multislit collimator stacks, where primary photons traversing RHS apertures are subject to more obscuration than those traversing LHS apertures.

The microbeam profiles produced with the single-beam and superposition simulation models varied slightly from those produced in a single simulation with the full array model. While the profiles obtained with the single-beam model were useful for the study of individual microbeams, they failed to account for the valley dose contributions of neighbouring microbeams, and hence, exhibited substantially smaller valley doses than the corresponding full array profiles.

The superposition model, on the other hand, did account for neighbouring valley dose contributions, although as it used the superposition of a single microbeam to generate a pseudo-array (sup array), it neglected the influence of the multislit collimator's lateral offset on different microbeams. This resulted in the sup array overestimating the FWHM of RHS microbeams by as much as  $4\text{ }\mu\text{m}$ , and underestimating the FWHM of LHS microbeams by almost  $1\text{ }\mu\text{m}$ , which correspond to variations in penumbral dose of as much as 98% and 34% respectively. Despite these differences, the ratio of peak doses in the full and sup arrays were around unity, and the valley doses and PVDRs were within 4%.

While the microbeam array generated with the full array simulation model was more realistic than the single-beam and superposition models (as it accounted for the collimator's lateral offset), longer simulation times were needed to obtain equivalent statistics to that of the pseudo-sup array. The only differences between the full and sup arrays are due to the asymmetric construction of the multislit collimator. In the absence of such an asymmetric construction, the superposition model should be sufficient for MRT treatment planning.

The alignment of the multislit collimator affected the uniformity of microbeam FWHM and PVDRs. Rotating the collimator through angles of  $0.05^\circ$ ,  $0.1^\circ$ , and  $0.2^\circ$  (with

respect to the beam) led to FWHM increases of as much as  $16\text{ }\mu\text{m}$  (i.e. 32%), while negative rotations of  $-0.05^\circ$  and  $-0.1^\circ$  caused a reduction in the FWHM of as much as  $36\text{ }\mu\text{m}$  (i.e. 72%). Correspondingly, positive collimator rotations caused a reduction in PVDRs of as much as 20%, whilst negative rotations produced an increase in PVDR of up to 170%. These variations in FWHM and PVDR are due to the lateral offset of the collimator stacks, where positive angles of rotation reduce the effect and negative angles exacerbate it. The magnitude of these variations demonstrates the importance of accurate collimator alignment for dose planning and treatment. The severity of these effects could be reduced by substituting the dual stacks with a single stack design of fixed width. Simulation results in this work suggest the variations in FWHM for an array of 25 microbeams could be decreased from  $5\text{ }\mu\text{m}$  to less than  $2\text{ }\mu\text{m}$ .

The interaction medium and height of the scoring region also had an effect on the PVDR. Microbeams travelling through water exhibited PVDRs that were about 10% higher than in PMMA, owing to the different density and photon interaction cross sections of the two materials. The lower valley doses exhibited by microbeams in water than in PMMA is attributed to the smaller cross sections for Compton scattering (in water) at these energies. Scoring the dose profile of the array in five lateral regions revealed non-uniformities in the dose distribution over the height of the microbeams. The PVDRs in the top and bottom lateral slices were about 10% larger than the total PVDR (integrated over all five slices), while the PVDRs in the central slice and those on either side of it were lower than the total PVDR by about 8% and 5% respectively.

The results in this chapter have demonstrated that accurate modelling of the source, multislit collimator, beam divergence, interaction medium, and the height of scoring regions are all important considerations for the development of a future MRT dose planning system.



## **CHAPTER 8**

### **CONCLUSION**

This work is comprised of a theoretical and experimental study of dose distributions in conventional external beam radiotherapy and the emerging Microbeam Radiation Therapy (MRT). It is the first comprehensive investigation of potential changes in the radiobiological effectiveness of clinical photon beams caused by a redistribution of electrons in a magnetic field. It is also a fundamental study of both the influence of magnetic fields on the peak-to-valley dose ratio (PVDR) of microbeams and the accuracy of theoretical modelling for dose planning in MRT.

The interest in magneto-radiotherapy, or the use of magnetic fields to produce a favourable redistribution of dose, has intensified over the past decade with developments in magnet and radiotherapy technology. Its practical feasibility was recently realised with the development of an integrated 1.5 T MRI scanner and 6 MV linac for soft-tissue tumour imaging, position verification and treatment monitoring in image-guided radiotherapy [60, 62, 77]. Monte Carlo studies have shown the potential for magnetic fields to alter the dose distribution of radiotherapy beams. However, an investigation of the effect of a magnetic field on the electron distribution of these beams and any related change in their relative biological effectiveness (RBE), is absent from the literature. Considering the recent implementation of the hybrid MRI-linac system, there is a need to ascertain the importance of these effects in treatment planning. This has been the impetus for the work in chapters 3 and 4.

The influence of transverse magnetic fields on the dose distribution from clinical photon beams was investigated in chapter 3. A comparative study was also made between the dose redistribution obtained with the Monte Carlo PENELOPE and EGS4 codes for the purpose of benchmarking PENELOPE's algorithm for charged particle transport in



electromagnetic fields. High-energy photon beams subjected to a slice of uniform transverse magnetic field (between 7 and 9 cm depth) were shown to produce localised regions of dose enhancement at the magnetic field's entrance (up to 91%) and dose reduction (up to 77%) at its exit. Such a dose alteration may benefit the treatment of tumours close to radiation-sensitive structures in the body, where the regions of dose enhancement and dose reduction would be aligned with the tumour and sensitive organs, respectively.

The dose enhancement arises from a reduction in the depth of interaction of electrons as they move through the transverse magnetic field. This produces a deficiency of electrons further downstream, thereby reducing the dose beyond the magnetic field (where photons are the primary dose contributors as their trajectories are unaltered by magnetic fields). The breadth of the dose enhancement depends on the range and cyclotron radius of electrons. Higher energy photon beams exhibit larger dose enhancements as the photons interact at greater depths to produce more electrons in the vicinity of the magnetic field. For a given photon beam, broader dose enhancements are observed with stronger magnetic fields owing to the electrons depositing their energy further upstream. Most of the dose enhancements and reductions obtained with PENELOPE were within 4% of those obtained with the Monte Carlo EGS4 code.

Varying the width of the magnetic field had no effect on the magnitude of dose enhancement, nor did its application at shallower depths. However, an effect was observed when the magnetic field was applied to the surface. The substantial 185% dose enhancement observed with the slice of magnetic field at the surface is owing to the large population of short-range, low-energy electrons in the build-up region. In terms of therapeutic benefit, the width of magnetic field could be selected according to the distance between the tumour and critical structure in the body, where the treatment of superficial tumours may benefit from the application of magnetic field at the surface.

Chapter 4 investigated the influence of a magnetic field on the spatial distribution of electrons from high-energy photon beams. Electrons with an energy below 1 MeV were scored according to their point of origin. The resulting spectrum revealed an increase

in electron population entering the magnetic field and a reduction in population beyond it, which correlates with the regions of dose enhancement and dose reduction observed in chapter 3. The augmentation in electron population, which is more predominant at lower energies, is caused by a reduction in the depth of interaction of electrons (and any secondary particles they produce) whose ranges are comparable to or greater than their cyclotron radii. This results in a depletion of secondary electrons in the regions exiting and beyond the magnetic field. Larger variations in the electron population are observed with magnetic fields greater than 2 T owing to the smaller cyclotron radii, which increases the confinement of electrons within the field.

As the linear energy transfer (LET) of an electron increases with decreasing energy, the redistribution of electrons, particularly low-energy electrons, may lead to an alteration in RBE. This being the case, the augmentation of electron population in the regions approaching and entering the magnetic field would correspond to an increase in RBE. Conversely, the depletion of electrons exiting and beyond the magnetic field would correspond to a decrease in RBE, which would benefit the treatment of tumours close to radiation-sensitive structures in the body. Quantification of the RBE associated with these changes in the electron spectrum is needed to confirm this hypothesis. Further work could include replacing the slice of homogeneous magnetic field with a realistic non-uniform field, such as that produced by an MRI magnet, to establish whether alterations in the electron spectrum associated with the regions of dose enhancement still exist.

The redistribution of electrons from magnetic fields applied to high-energy photon beams stimulated an investigation of whether the effect may also exist in MRT. The only mention of an effect is a preliminary Monte Carlo EGS4 study by Orion *et al.* [102], which showed a reduction of a few micron in the penumbra of a 20 keV microbeam (30  $\mu\text{m}$  wide) subjected to a 6 T longitudinal magnetic field. This result was the impetus for the work in chapter 6, which theoretically and physically explores the potential for magneto-MRT, or the application of magnetic fields in MRT, to alter the dose profiles and PVDRs of microbeams.

The magneto-MRT experiments were performed with MOSFET and radiochromic film dosimetry. Characterisation of the radiation response of edge-on MOSFETs and their ability to measure the dose profiles of microbeams was investigated in chapter 5. High and low sensitivity MOSFETs exhibited a linear radiation response to within a few percent over the course of their lifetime, particularly the low-sensitivity MOSFET whose thinner gate oxide and higher gate bias voltage reduces the effect of positive charge saturation. Microbeam profiles measured with a MOSFET reveal an asymmetry about the peak centre which is caused by particle attenuation in the silicon substrate of the device. The overestimation of measured PVDRs for the 50 and 70 keV beams arises from the MOSFET's over-response to radiation of these energies. The difference between the measured and simulated PVDRs is attributed to the forementioned dose effects with the MOSFET and simplifications in the modelling of the device.

Despite its drawbacks, the edge-on MOSFET remains the only real-time dosimeter capable of micron, or sub-micron, resolution. The silicon strip detector is an alternative real-time dosimeter which is currently under development for use in MRT at the Centre for Medical Radiation Physics, University of Wollongong, Australia. This device consists of 128 strips of  $p^+ p-n$  junctions (separated by  $200\text{ }\mu\text{m}$ ), which will enable the instantaneous measurement of peak and valley dose of multiple microbeams, and hence, their corresponding PVDRs.

The influence of a magnetic field on the dose profile and PVDR of microbeams was discussed in chapter 6. The presence of transverse or longitudinal magnetic fields of a few Tesla were shown both experimentally and theoretically to have no effect on the lateral dose profiles of microbeams. According to Monte Carlo PENELOPE simulation, longitudinal magnetic fields greater than 10 T are required to produce an effect. The increase in PVDR is caused by a reduction in the lateral spread of secondary electrons whose ranges are comparable to or greater than their cyclotron radii. The application of a strong transverse magnetic field (up to 100 T), on the other hand, was shown to have no effect on the dose profile or PVDR of microbeams, as the direction of the magnetic

field is parallel to the lateral component of an electron's trajectory. Since a transverse magnetic field only influences the orthogonal components of an electron's path, it is possible that sufficiently strong transverse magnetic fields may alter the depth-dose profile of microbeams (as observed in chapter 3).

Despite the inability of magnetic fields of a few Tesla to alter the electron distribution in MRT, their presence may influence the repair mechanisms of tissue. This premise is based on studies which have shown the application of a magnetic field to influence the orientation of molecular domains in cell membranes, thereby changing their structure and curvature [105] and the diffusion of molecules across the membrane surface (a process critical to normal membrane function and antibody binding) [106]. A study of breast cancer patients exposed to magnetic fields prior to irradiation observed substantial, and in some cases complete, tumour regression [108]. This begs the question of whether the application of a magnetic field before, during, or after MRT irradiation could alter the repair mechanisms of brain tissue in such a way to improve the efficacy of the treatment.

Monte Carlo simulation can be used in radiotherapy to theoretically estimate the dose required for treatment. Its potential use in MRT dose planning, however, is currently hindered by significant discrepancies between the measured and theoretical dose profiles of microbeams. The need to resolve these discrepancies is driven by the desirability of making MRT available to humans in the next few years. In chapter 7, Monte Carlo PENELOPE simulation was used to demonstrate the importance of accurate beam-line modelling for dose calculation in MRT, in particular the influence of the source, multislit collimator, and beam divergence. The composition of the interaction medium and height of the scoring region were also shown to be important considerations for MRT dose planning.

A common simplification in MRT modelling is the assumption of perfect rectangular microbeams whose transport is commenced on the surface of the target. This simplification fails to account for the influence of the source, the multislit collimator, and the beam divergence between them. Simulation results in this work have shown that

modelling a distributed source and beam divergence can increase the penumbral dose of microbeams by almost 30%. While the inclusion of a multislit collimator was shown to have no effect on the dose profile of the central peak in an array of 25 microbeams, it did cause a 10% variation in the full-width at half-maximum (FWHM) of neighbouring microbeams. The difference in FWHM stems from the lateral offset of the multislit collimator stacks, where the paths of photons traversing RHS apertures suffer more obscuration than those traversing LHS apertures.

Another common practice in MRT modelling is the generation of an array of microbeams using the superposition of the dose profile of a single microbeam. This work compared the dose profiles and PVDRs of an array of microbeams produced from a single simulation (full array) to that obtained using the superposition of a single microbeam profile (sup array). The sup array was found to overestimate the FWHM of microbeams in the RHS of the array by as much as 4  $\mu\text{m}$ , and underestimate the FWHM of microbeams in the LHS of the array by almost 1  $\mu\text{m}$ . The variation in FWHM stems from the sup array omitting the influence of the multislit collimator's asymmetric construction (lateral offset) on different microbeam positions in the array. Despite these differences, the ratio of peak doses in the full and sup arrays was approximately unity, and a ratio of valley doses and PVDRs were all within 4%. Considering the only differences between the full and sup arrays are due to the multislit collimator's lateral offset, in the absence of such an asymmetric construction the Superposition model should be sufficient for MRT treatment planning.

In MRT, the alignment of the multislit collimator is adjusted until the FWHM of microbeams is approximately uniform across the array. The 10% variation in the FWHM of an array of 25 microbeams (caused by the asymmetric collimator construction) led to a study of the effect of collimator alignment on the dose profile of microbeams. This was investigated by rotating the collimator through small angles of  $\pm 0.05^\circ$ ,  $\pm 0.1^\circ$ , and  $\pm 0.2^\circ$  with respect to the beam direction. Positive angles of collimator rotation yielded increases in the FWHM and valley dose of microbeams, which corresponded to reductions in the

PVDR of up to 20%. Conversely, negative angles of rotation caused severe reductions in the FWHM and valley dose, resulting in PVDR enhancements of up to 170%. This is because collimator rotation through small positive angles reduces the effect of the collimator's lateral offset, whilst negative angles exacerbate it. The severity of these effects could be reduced by substituting the dual stacks with a single stack of fixed microbeam width, where simulation results estimate a reduction in FWHM variation from 5  $\mu\text{m}$  to less than 2  $\mu\text{m}$ . Further work could include the measurement of microbeam FWHM dependence on collimator alignment, which could be obtained with the aforementioned strip detector.

Other considerations for theoretical dose calculation are the interaction medium of the target and the height of scoring regions. Microbeams travelling through water exhibited PVDRs that were about 10% higher than in PMMA, owing to the different density and photon interaction cross sections of the two materials. Scoring the dose profile of the microbeam array in five lateral regions revealed non-uniformities in the dose distribution over the height of the microbeams. The PVDRs calculated in the top and bottom lateral slice were about 10% larger than the total PVDR integrated over all five slices, while the PVDRs in the central slice and those on either side of it were lower than the total PVDR by about 8% and 5% respectively. Accurate modelling of the interaction medium and the height of scoring regions, together with the source, multislit collimator, and beam divergence, are all important considerations for the development of a future MRT dose planning system.



## **APPENDIX A**

### **HIGH CURRENT PULSER FOR THE MAGNET COIL IN MAGNETO-MRT EXPERIMENTS**

The following pages contain a description and circuit diagrams of the high current pulser for the magnet coil used in the Microbeam Radiation Therapy experiments at the European Synchrotron Radiation Facility in Grenoble, France. The high current pulser and time delay circuits were constructed by Terry Braddock, an electrical engineer at the Centre for Medical Radiation Physics, University of Wollongong, Australia.

The high current pulser for the magnet coil was designed to charge a bank of capacitors ( $16 \times 4700 \mu\text{F}$ , 400 V) to a given voltage less than the peak supply voltage. Discharge of the capacitor bank was initiated with a trigger signal generated from either a manual trigger button on the control panel or by an external transistor-transistor logic (TTL) input pulse. This resulted in a surge of current through the coil, and hence, a pulse of magnetic field. A time delay of up to about 330 ms between the external trigger signal and the firing of the thyristor was set by the potentiometer on the operator panel. The range of the time delay could be changed, if necessary, by altering components on the timer board shown in figure A.24.

When the start button was pressed, relays C1 and C2 were energised. As shown in figure A.25, C1 connected the mains supply to the rectifier bridge via the current limiting choke, whilst C2 bypassed the start button latching in both C1 and C2. During the charging period, the closed side of the contact on C2 opened and de-energised the gate pulse relay (GPR). This was to ensure that the switching transients could not fire the thyristor when the charging current was switched off. The pickup of the GPR was delayed using a  $39 \Omega$  resistor and a  $33 \mu\text{F}$  capacitor across the coil to ensure that all transients had ceased prior to energising the GPR for enabling the thyristor gate circuit.



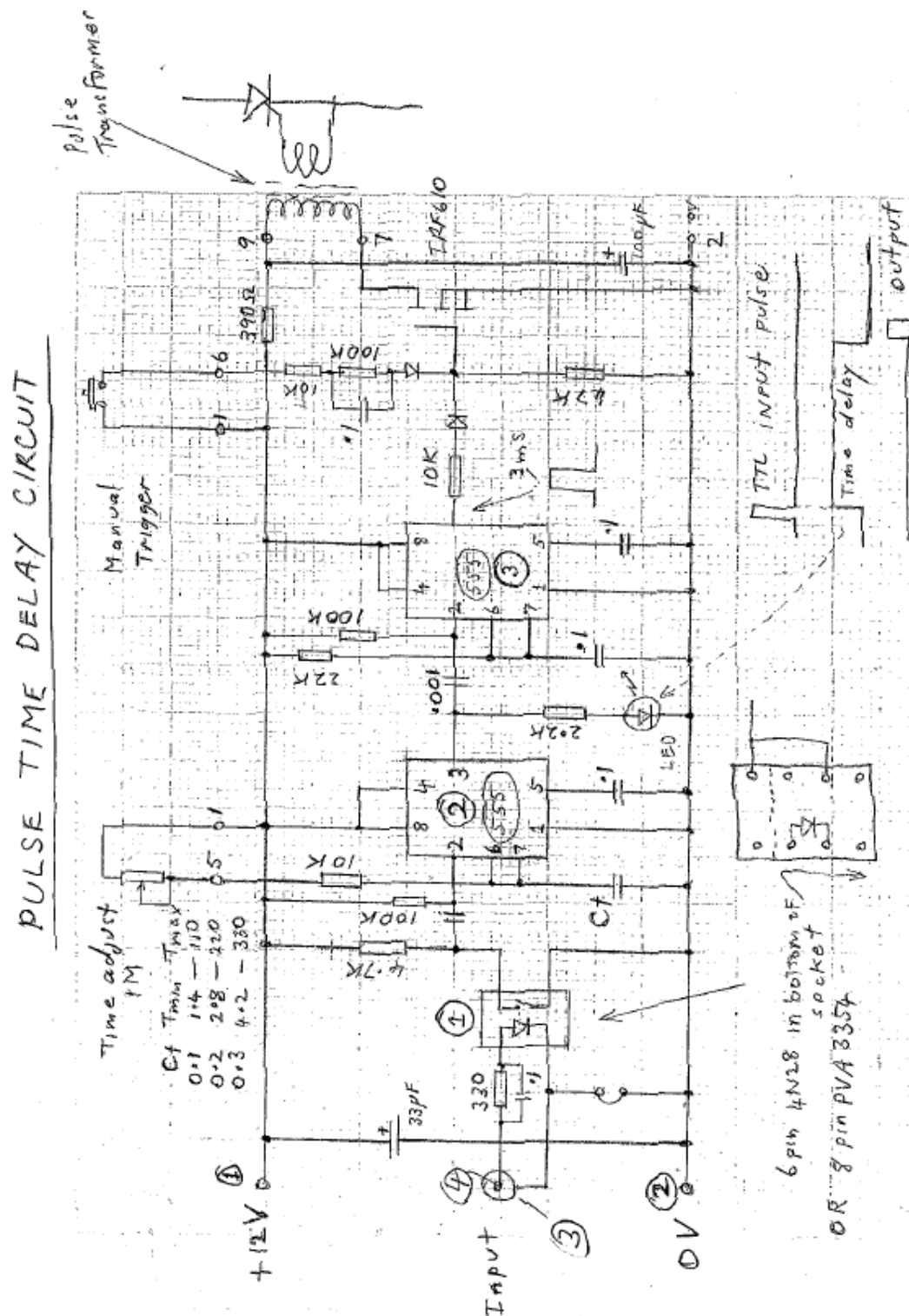
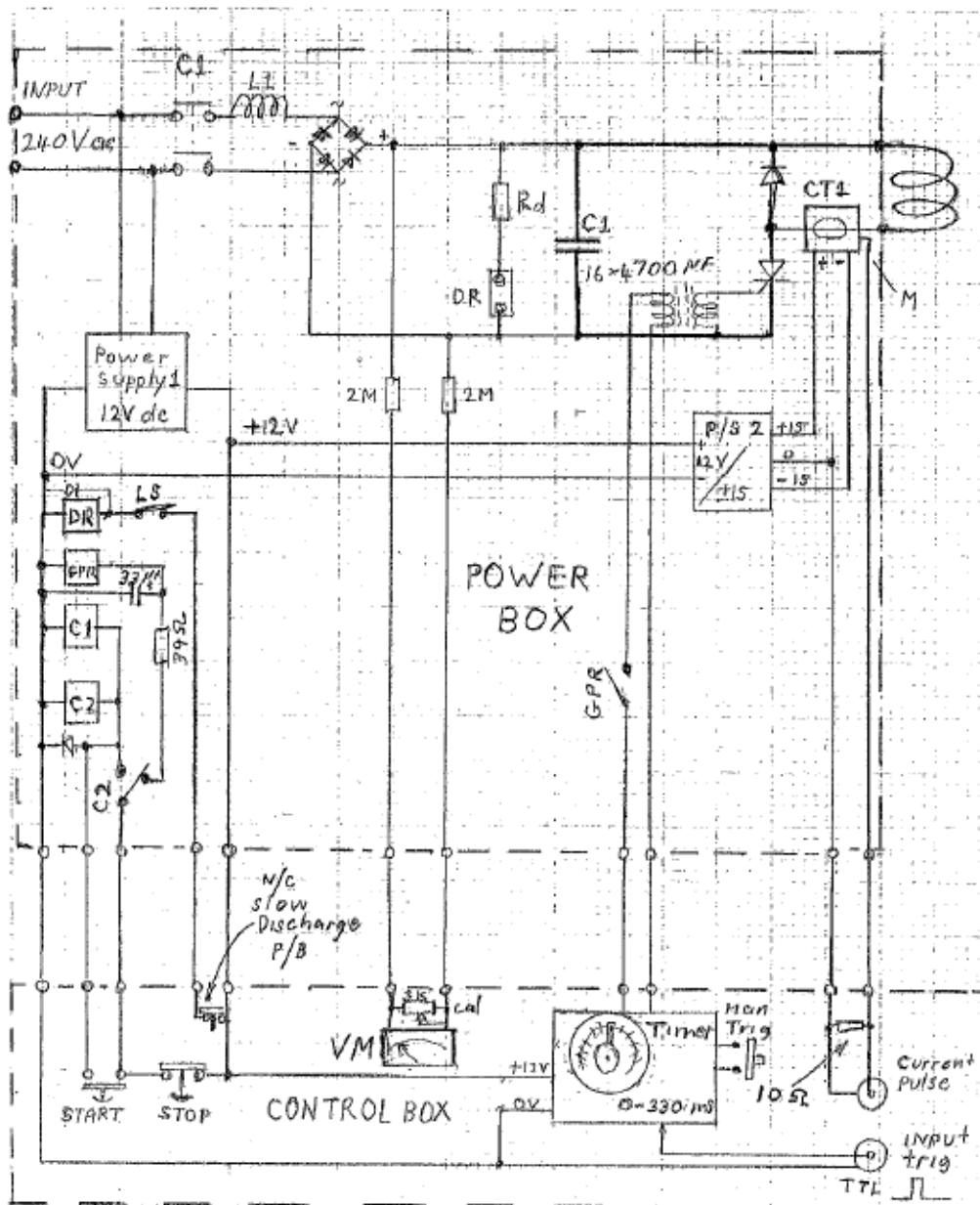


Figure A.24: Circuit diagram of the pulse time delay. Discharge of the capacitor bank was initiated with a trigger signal generated from either a manual trigger button on the control panel or by an external transistor-transistor logic (TTL) input pulse.



Start Button Closes relay  $C_1$  &  $C_2$  and starts capacitor charging

Stop Button Opens " " stops " "

$V_m$  Capacitor Volts 0-100V = 0-400 Volts

CT1 Hall effect current transformer 2000:1 ratio LEM LA100P

Timer 0 to 200 ms delay between input pulse & thyristor trig

DR Capacitor discharge relay, Discharge if lid opens  
and if control box unplugged

Figure A.25: Circuit diagram of current pulser. When a current of 200 A was pulsed through the coil, a magnetic field of about 2.5 T was estimated at the centre of the coil's air core.

The initial charging current for a 240 V supply was about 20 A. Charging the capacitor bank to 300 V took about 2.5 minutes. The discharge current at this voltage was about 200 A, as shown in figure A.26. Charging could be stopped at any chosen voltage by pressing the stop button. A meter on the control panel showed the capacitor voltage from 0 to 500 V.

For safety reasons, all control relays operated from 12 V. An isolating Hall-effect current transducer (CT) was used to monitor the current pulse in the coil. In the power circuit box, a 2.2 M $\Omega$  resistor was used for both sides of the capacitor voltage monitoring circuit. A discharge relay (DR) with a normally closed contact was used to connect a resistor across the capacitor bank when the following events occurred: the unit was switched off, the lid of the power box was opened, the control box was unplugged, or the slow discharge button on the control box was pressed.

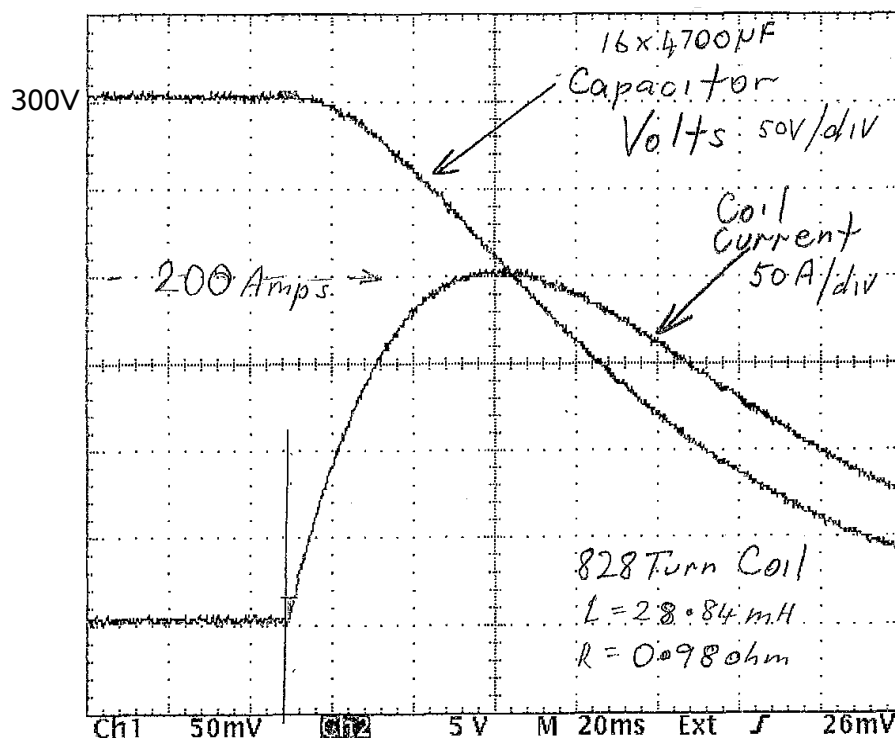


Figure A.26: Test results for the magnet coil. Charging the capacitor bank to 300 V enabled a discharge current of around 200 A to be pulsed through the coil. This corresponded to a peak flux of 1.3 T at the centre of the coil's surface.

## REFERENCES

- [1] World Health Organization. *Cancer: WHO fact sheet no. 297*. [Online: <http://www.who.int/mediacentre/factsheets/fs297/en/index.html>]. Accessed 21 September, 2008.
- [2] B W Stewart and P Kleihues. *World Cancer Report*. International Agency for Research on Cancer, Lyon, France, 2003.
- [3] Australian Institute of Health and Welfare & Australasian Association of Cancer Registries (AACR). *Cancer in Australia: An overview, 2006*. Australian Institute of Health and Welfare, Canberra, 2007.
- [4] J Van Dyk. *The Modern Technology of Radiation Oncology (Volume 1)*. Medical Physics Publishing, Madison, 1999.
- [5] E H Grubbé. Priority in the therapeutic use of x-rays. *Radiol.*, 21:156–162, 1933.
- [6] J Bernier, E J Hall, and A Giaccia. Radiation oncology: a century of achievements. *Nat. Rev. Cancer*, 4:737–747, 2004.
- [7] W D Coolidge. A powerful Röntgen ray tube with a pure electron discharge. *Phys. Rev.*, 2:409–430, 1913.
- [8] C W Miller. Travelling wave linear accelerator for x-ray therapy. *Nature*, 171: 297–299, 1953.
- [9] C A P Wood and G R Newberry. Medical Research Council linear accelerator and cyclotron. *Nature*, 173:233–235, 1954.

- [10] P Metcalfe, T Kron, and P Hoban. *The Physics of Radiotherapy X-Rays and Electrons*. Medical Physics Publishing, Madison, rev. edition, 2007.
- [11] T R Mackie, P Reckwerdt, T McNutt, M Gehring, and C Sanders. Photon beam dose computations. In *Proceedings of AAPM Summer School - Teletherapy: Present and Future*, pages 103–137. Advanced Medical Publishing, Madison, 1996.
- [12] R Mohan. Why Monte Carlo? In *Proceedings XII International conference on the Use of Computers in Radiation Therapy*, pages 16–18. Medical Physics Publishing, Madison, 1997.
- [13] J Van Dyk. *The Modern Technology of Radiation Oncology (Volume 2)*. Medical Physics Publishing, Madison, 2005.
- [14] T Yamamoto, T Mizowaki, Y Miyabe, H Takegawa, Y Narita, S Yano, Y Nagata, T Teshima, and M Hiraoka. An integrated Monte Carlo dosimetric verification system for radiotherapy treatment planning. *Phys. Med. Biol*, 52:1991–2008, 2007.
- [15] B Lannering, I Marky, A Lundberg, and E Olsson. Long-term sequelae after pediatric brain tumors: their effect on disability and quality of life. *Med. Pediatr. Oncol.*, 18:304–310, 1990.
- [16] M De Felici, R Felici, M Sanchez del Rio, C Ferrero, T Bacarian, and F A Dilmajian. Dose distribution from x-ray microbeam arrays applied to radiation therapy: An EGS4 Monte Carlo study. *Med. Phys.*, 32(8):2455–2463, Aug. 2005.
- [17] S Rutkowski. Current treatment approaches to early childhood medulloblastoma. *Exp. Rev. Neurother.*, 6:1211–1221, 2006.
- [18] J A Laissue, H Blattmann, H P Wagner, M A Grotzer, and D N Slatkin. Prospects for microbeam radiation therapy of brain tumours in children to reduce neurological sequelae. *Dev. Med. Child Neurol.*, 49(8):577–581, Aug. 2007.

- [19] J Spiga, E A Siegbahn, E Bräuer-Krisch, P Randaccio, and A Bravin. The GEANT4 toolkit for microdosimetry calculations: Application to microbeam radiation therapy MRT. *Med. Phys.*, 34(11):4322–4330, Nov. 2007.
- [20] J A Laissue, N Lyubimova, H P Wagner, D W Archer, D N Slatkin, M Di Michiel, C Nemoz, M Renier, E Bräuer, P O Spanne, J Gebbers, K Dixon, and H Blattmann. Microbeam radiation therapy. *Proc. SPIE*, 3770:38–45, 1999.
- [21] J A Laissue, H Blattmann, M Di Michiel, D N Slatkin, N Lyubimova, R Guzman, W W Zimmermann, A Jaggy, H M Smilowitz, R Stettler, P Kircher, T Bley, E Bräuer, J Stepanek, A Bravin, R Renier, G Le Duc, C Nemoz, W C Thomlinson, and H P Wagner. The weanling piglet cerebellum: a surrogate for tolerance to MRT (Microbeam Radiation Therapy) in pediatric neuro-oncology. *SPIE*, 4508: 65–73, 2001.
- [22] E Bräuer-Krisch, A Bravin, M Di Michiel, M L F Lerch, A B Rosenfeld, J Stepanek, and J A Laissue. MOSFET dosimetry for microbeam radiation therapy at the European Synchrotron Radiation Facility. *Med. Phys.*, 30(4):583–589, 2003.
- [23] E Bräuer-Krisch, A Bravin, , L Zhang, E Siegbahn, J Stepanek, H Blattmann, D N Slatkin, J O Gebbers, M Jasmin, and J A Laissue. Characterization of a tungsten/gas multislit collimator for microbeam radiation therapy at the European Synchrotron Radiation Facility. *Rev. Sci. Instrum.*, 76:064303, 2005.
- [24] F A Dilmanian, Y Qu, S Liu, C D Cool, J Gilbert, J F Hainfeld, C A Kruse, J Laterra, D Lenihan, M M Nawrocky, G Pappas, C I Sze, T Yuasa, N Zhong, Z Zhong, and J W McDonald. X-ray microbeams: Tumor therapy and central nervous system research. *Nucl. Instrum. Meth. Phys. Res. A*, 548:30–37, 2005.
- [25] E A Siegbahn, J Stepanek, E Bräuer-Krisch, and A Bravin. Determination of dosimetrical quantities used in microbeam radiation therapy (MRT) with Monte Carlo simulations. *Med. Phys.*, 33(9):3248–3259, 2006.

- [26] M Miura, H Blattmann, E Bräuer-Krisch, A Bravin, A L Hanson, M M Nawrocky, N Lyubimova, P L Micca, D N Slatkin, and J Laissue. Radiosurgical palliation of aggressive murine SCCVII squamous cell carcinomas using synchrotron-generated X-ray microbeams. *Br. J. Radiol.*, 79:71–75, 2006.
- [27] H M Smilowitz, H Blattmann, E Bräuer-Krisch, A Bravin, M Di Michiel, J O Gebbers, A L Hanson, N Lyubimova, D N Slatkin, J Stepanek, and J Laissue. Synergy of gene-mediated immunoprophylaxis and microbeam radiation therapy for advanced intracerebral rat 9L gliosarcomas. *J. Neurooncol.*, 78:135–143, 2006.
- [28] P Regnard, G Le Duc, E Bräuer-Krisch, I Tropès, E A Siegbahn, A Kusak, C Clair, H Bernard, D Dallery, J A Laissue, and A Bravin. Irradiation of intracerebral 9L gliosarcoma by a single array of microplanar x-ray beams from a synchrotron: balance between curing and sparing. *Phys. Med. Biol.*, 53:861–878, 2008.
- [29] J A Laissue, G Geiser, P O Spanne, F A Dilmanian, J O Gebbers, M Geiser, X Y Wu, M S Makar, P L Micca, M M Nawrocky, D D Joel, and D N Slatkin. Neuropathology of ablation of rat gliosarcomas and contiguous brain tissues using a microplanar beam of synchrotron-wiggler-generated x rays. *Int. J. Cancer.*, 78:654–660, 1998.
- [30] F A Dilmanian, G M Morris, G Le Duc, X Huang, B Ren, T Bacarian, J C Allen, J Kalef-Ezra, I Orion, E M Rosen, T Sandhu, P Sathe, X Y Wu, Z Zhong, and H L Shivaprasad. Response of avian embryonic brain to spatially segmented X-ray microbeams. *Cell. Mol. Biol.*, 47:485–494, 2001.
- [31] H J Curtis. The interpretation of microbeam experiments for manned space flight. *Radiat. Res. Suppl.*, 7:258–264, 1967.
- [32] D N Slatkin, P O Spanne, F A Dilmanian, and M Sandborg. Microbeam radiation therapy. *Med. Phys.*, 19(6):1395–1400, 1992.

- [33] J F Ward. Mechanisms of DNA repair and their potential modification for radiotherapy. *Int. J. Radiat. Oncol. Biol. Phys.*, 12(7):1027–1032, Jul. 1986.
- [34] B Boudaïffa, P Cloutier, D Hunting, M Huels, and L Sanche. Resonant formation of DNA strand breaks by low-energy (3 to 20 eV) electrons. *Science*, 287:1658–1660, 2000.
- [35] B Sutherland, P Bennett, O Sidorkina, and J Laval. Clustered DNA damages induced in isolated DNA and in human cells by low doses of ionizing radiation. *Proc. Natl. Acad. Sci.*, 97(1):103–108, 2000.
- [36] M J Berger, J H Hubbell, S M Seltzer, J Chang, J S Coursey, R Sukumar, and D S Zucker. *XCOM: Photon Cross Sections Database (version 1.3)*. [Online: <http://physics.nist.gov/xcom>], National Institute of Standards and Technology, Gaithersburg, MD, 2005, .
- [37] H E Johns and J R Cunningham. *The Physics of Radiology*. Charles C Thomas, Springfield, 4th edition, 1983.
- [38] F Salvat, J M Fernández-Varea, and J Sempau. *PENELOPE - A Code System for Monte Carlo Simulation of Electron and Photon Transport*. OECD Nuclear Energy Agency, Issy-les-Moulineaux, France, 2003.
- [39] S A Dupree and S K Fraley. *A Monte Carlo Primer: A Practical Approach to Radiation Transport*. Kluwer Academics / Plenum Publishers, New York, 2002.
- [40] M Ljungberg, S-E Strand, and M A King. *Monte Carlo Calculations in Nuclear Medicine: Applications in Diagnostic Imaging*. Institute of Physics Publishing, Bristol, 1998.
- [41] J M Fernández-Varea, R Mayol, J Baró, and F Salvat. On the theory and simulation of multiple elastic scattering of electrons. *Nucl. Instrum. Meth. B*, 73:447–473, 1993.



- [42] D E Cullen, J H Hubbell, and L Kissel. EPDL97 The evaluated data library '97 version. *Report UCRL-50400*, Vol.6, rev.5, Lawrence Livermore National Laboratory, Livermore, CA, 1997.
- [43] M J Berger and J H Hubbell. XCOM: Photon Cross Sections on a Personal Computer. *Report NBSIR 87-3597*. National Bureau of Standards, Gaithersburg, MD, 1987.
- [44] R Ribberfors. X-ray incoherent scattering total cross sections and energy absorption cross sections by means of simple calculation routines. *Phys. Rev. A*, 27: 3061–3070, 1983.
- [45] S T Perkins, D E Cullen, M H Chen, J H Hubbell, J Rathkopf, and J Scofield. Tables and graphs of atomic subshell and relaxation data derived from the LLNL evaluated atomic data library (EADL),  $Z = 1-100$ . *Report UCRL-50400*, Vol.30, Lawrence Livermore National Laboratory, Livermore, CA, 1991.
- [46] P P Kane, L Kissel, R H Pratt, and S C Roy. Elastic scattering of  $\gamma$ -rays and x-rays by atoms. *Phys. Rep.*, 140(2):75–159, 1986.
- [47] D E Cullen, M H Chen, J H Hubbell, S T Perkins, E F Plechaty, J Rathkopf, and J Scofield. Tables and graphs of photon-interaction cross sections from 10 eV to 100 GeV derived from the LLNL evaluated atomic data library (EADL). *Report UCRL-50400*, Vol.6, rev.4, Lawrence Livermore National Laboratory, Livermore, CA, 1989.
- [48] H Nettelbeck, G J Takacs, and A Rosenfeld. Effect of transverse magnetic fields on dose distribution and RBE of photon beams: comparing PENELOPE and EGS4 Monte Carlo codes. *Phys. Med. Biol.*, 53:5123–5137, 2008.
- [49] W H Bostick. Possible techniques in direct-electron beam tumour therapy. *Phys. Rev.*, 77:564–565, 1950.

- [50] C C Shih. High energy electron radiotherapy in a magnetic field. *Med. Phys.*, 2(1):9–13, Feb. 1975.
- [51] D P Whitmore and D L Bernard. Magnetic enhancement of electron dose distribution in a phantom. *Med. Phys.*, 4(2):127–131, Mar.–Apr. 1977.
- [52] D P Whitmore and D L Bernard. Magnetic modification of the electron-dose distribution in tissue and lung phantoms. *Med. Phys.*, 5(5):409–417, Sep.–Oct. 1978.
- [53] A F Bielajew. The effect of strong magnetic fields on dose deposition from electron and photon beams. *Med. Phys.*, 20(4):1171–1179, Jul.–Aug. 1993.
- [54] E Nardi and G Barnea. Electron beam therapy with transverse magnetic fields. *Med. Phys.*, 26(6):967–973, Jun. 1999.
- [55] D Jette. Magnetic fields with photon beams: Dose calculation using electron multiple scattering theory. *Med. Phys.*, 27(8):1705–1716, Aug. 2000.
- [56] D Jette. Magnetic fields with photon beams: Monte Carlo calculations for a model magnetic field. *Med. Phys.*, 27(12):2726–2738, Dec. 2000.
- [57] M C Lee and C M Ma. Monte carlo characterization of clinical electron beams in transverse magnetic fields. *Phys. Med. Biol.*, 45:2947–2967, 2000.
- [58] X A Li, L Reiffel, J Chu, and S Naqvi. Conformal photon-beam therapy with transverse magnetic fields: A Monte Carlo study. *Med. Phys.*, 28(2):127–133, Feb. 2001.
- [59] D W Litzenberg, B A Fraass, D L M<sup>c</sup>Shan, T W O’Donnell, D A Roberts, F D Becchetti, A F Bielejew, and J M Moran. An apparatus for applying strong longitudinal magnetic fields to clinical photon and electron beams. *Phys. Med. Biol.*, 46:N105–N115, 2001.

- [60] B W Raaymakers, A J E Raaijmakers, A N T J Kotte, D Jette, and J J W Lagendijk. Integrating a MRI scanner with a 6 MV radiotherapy accelerator: dose deposition in a transverse magnetic field. *Phys. Med. Biol.*, 49:4109–4118, 2004.
- [61] Y Chen, A F Bielajew, D W Litzenberg, J M Moran, and F D Becchetti. Magnetic confinement of electron and photon radiotherapy dose: A Monte Carlo simulation with a nonuniform longitudinal magnetic field. *Med. Phys.*, 32(12):3810–3818, Dec. 2005.
- [62] A J E Raaijmakers, B W Raaymakers, S van der Meer, and J J W Lagendijk. Integrating a MRI scanner with a 6 MV radiotherapy accelerator: impact of the surface orientation on the entrance and exit dose due to the transverse magnetic field. *Phys. Med. Biol.*, 52:929–939, 2007.
- [63] C Kirkby, T Stanescu, S Rathee, M Carlone, B Murray, and B G Fallone. Patient dosimetry for hybrid MRI-radiotherapy systems. *Med. Phys.*, 35(3):1019–1027, Mar. 2008.
- [64] W R Nelson, H Hirayama, and D W O Rogers. *The EGS4 Code System*. SLAC-265 [Online: <http://www.slac.stanford.edu/pubs/slacreports/slac-r-265.html>], 1985.
- [65] R Mohan, C Chui, and L Lidofsky. Energy and angular distributions of photons from medical linear accelerators. *Med. Phys.*, 12(5):592–597, Sep.–Oct. 1985.
- [66] D Sheikh-Bagheri and D W O Rogers. Monte carlo calculation of nine megavoltage photon beam spectra using the BEAM code. *Med. Phys.*, 29(3):391–402, Mar. 2002.
- [67] D Jette. Magnetic fields with photon beams: Use of circular current loops. *Med. Phys.*, 28(10):2129–2138, Oct. 2001.
- [68] B Grosswendt. Formation of ionization clusters in nanometric structures of

- propane-based tissue-equivalent gas or liquid water by electrons and  $\alpha$ -particles. *Radiat. Environ. Biophys.*, 41:103–112, 2002.
- [69] G P Van Der Schans. Gamma-ray induced double-strand breaks in DNA resulting from randomly-inflicted single-strand breaks: Temporal local denaturation, a new radiation phenomenon? *Int. J. Radiat. Biol.*, 33(2):105–120, 1978.
- [70] J F Ward. Some biochemical consequences of the spatial distribution of ionizing radiation-produced free radicals. *Radiat Res.*, 86:185–195, 1981.
- [71] D T Goodhead. Radiation effects in living cells. *Can J Phys.*, 68:872–886, 1990.
- [72] W A Bernhard, S Purkayastha, and J R Milligan. Which DNA damage is likely to be relevant in hormetic responses? *Dose Response*, 6(2):184–195, 2008.
- [73] International Commission on Radiation Units and Measurements. *Microdosimetry (ICRU report 36)*. ICRU, Maryland, 1983.
- [74] G W Barendsen. Responses of cultured cells, tumours and normal tissues to radiations of different linear energy transfer. *Curr. Top. Radiat. Res.*, 4:293–356, 1968.
- [75] P Mayles, A E Nahum, and J C Rosenwald. *Handbook of Radiotherapy Physics: Theory and Practice*. Taylor & Francis, London, 2007.
- [76] B R Paliwal, A L Wiley, B W Wessels, and M C Choi. Magnetic field modification of electron-beam dose distributions in inhomogeneous media. *Med. Phys.*, 5(5): 404–408, Sep.–Oct. 1978.
- [77] A J E Raaijmakers, B W Raaymakers, and J J W Lagendijk. Integrating a MRI scanner with a 6 MV radiotherapy accelerator: dose increase at tissue-air interfaces in a lateral magnetic field due to returning electrons. *Phys. Med. Biol.*, 50:1363–1376, 2005.

- [78] D R Lide. *CRC Handbook of Chemistry and Physics*. Taylor and Francis, Boca Raton, FL, (Internet version) 88th edition, 2008.
- [79] F Salvat, J M Fernández-Varea, and J Sempau. *PENELOPE-2006: A Code System for Monte Carlo Simulation of Electron and Photon Transport*. OECD Nuclear Energy Agency, Barcelona, Spain, 2006.
- [80] P K Duffner, M E Cohen, M L Voorhess, M H Macgillivray, M L Brecher, A Panahon, and B B Gilani. Long-term effects of cranial irradiation on endocrine function in children with brain tumors a prospective study. *Cancer*, 56:1841–1846, 1985.
- [81] W Thomlinson, P Berkvens, G Berruyer, B Bertrand, H Blattmann, E Bräuer-Krisch, T Brochard, A M Charvet, S Corde, M Dimichiel, H Elleaume, F Estève, S Fiedler J A Laissue, J E Le Bas, G Le Duc, N Lyubimova C Nemoz, M Renier D N Slatkin, P Spanne, and P Suortti. Research at the European Synchrotron Radiation Facility medical beamline. *Cell. Mol. Biol.*, 46(6):1053–63, Sep. 2000.
- [82] F A Dilmanian, T M Button, G Le Duc, N Zhong, L A Pena, J A L Smith, S R Martinez, T Bacarian, J Tammam, B Ren, P M Farmer, J Kalef-Ezra, P L Micca, M M Nawrocky, J A Niederer, F P Recksiek, A Fuchs, and E M Rosen. Response of rat intracranial 9L gliosarcoma to microbeam radiation therapy. *Neuro Oncology*, 4(1):26–38, 2002.
- [83] D N Slatkin, P O Spanne, F A Dilmanian, J O Gebbers, and J A Laissue. Subacute neuropathological effects of microplanar beams of x-rays from a synchrotron wiggler. *Proc. Natl. Acad. Sci.*, 92:8783–8787, 1995.
- [84] H J Curtis. The use of deuteron microbeam for simulating the biological effects of heavy cosmic-ray particles. *Radiat. Res. Suppl.*, 7:250–257, 1967.
- [85] J Stepanek, H Blattmann, J A Laissue, N Lyubimova, M Di Michiel, and D N Slatkin. Physics study of microbeam radiation therapy with PSI-version of Monte

- Carlo code GEANT as a new computational tool. *Med. Phys.*, 27(7):1664–1675, Jul. 2000.
- [86] E A Siegbahn, E Bräuer-Krisch, J Stepanek, H Blattmann, J A Laissue, and A Bravin. Dosimetric studies of microbeam radiation therapy (MRT) with Monte Carlo simulations. *Nucl. Instrum. Meth. Phys. Res. A*, 548:54–58, 2005.
- [87] I Orion, A B Rosenfeld, F A Dilmanian, F Telang, B Ren, and Y Namito. Monte Carlo simulation of dose distributions from a synchrotron-produced microplanar beam array using the EGS4 code system. *Phys. Med. Biol.*, 45:2497–2508, 2000.
- [88] A Niroomand-Rad, C R Blackwell, B M Coursey, K P Gall J M Galvin W L McLaughlin, A S Meigooni, R Nath, J E Rodgers, and C G Soares. Radiochromic film dosimetry: recommendations of AAPM Radiation Therapy Committee Task Group 55. *Med. Phys.*, 25(11):2093–2115, Nov. 1998.
- [89] Christopher G. Soares. Radiochromic film dosimetry. *Radiation Measurements*, 41:S100 – S116, 2006.
- [90] A Holmes-Siedle. The space-charge dosimeter general principles of a new method of radiation detection. *Nucl. Instrum. Meth.*, 121:169–179, 1974.
- [91] L Adams and A Holmes-Siedle. The development of an MOS dosimetry unit for use in space. *IEEE Trans. Nucl. Sci.*, NS-25:1607–1612, 1978.
- [92] T Kron, L Duggan, T Smith, A Rosenfeld, M Butson, G Kaplan, S Howlett, and K Hyodo. Dose response of various radiation detectors to synchrotron radiation. *Phys. Med. Biol.*, 43:3235–3259, 1998.
- [93] G Ensell, A Holmes-Siedle, and L Adams. Thick oxide pMOSFET dosimeters for high energy radiation. *Nucl. Instrum. Meth. A*, 269(3):655–658, 1988.
- [94] R Freeman and A Holmes-Siedle. A simple model for predicting radiation effects in MOS devices. *IEEE Trans. Nucl. Sci.*, NS-25-6:1216–1225, 1978.

- [95] G Sarrabayrouse, A Bellaouar, and P Rossel. Electrical properties of MOS radiation dosimeters. *Rev. Phys. Appl.*, 21:1283–1287, 1986.
- [96] A B Rosenfeld. MOSFET dosimetry in modern radiation oncology modalities. *Rad. Prot. Dosim.*, 101:393–398, 2002.
- [97] A B Rosenfeld, M G Carolan, G I Kaplan, B J Allen, and V L Khivrich. MOSFET dosimeters: role of encapsulation in mixed gamma-neutron and megavoltage X-ray fields. *IEEE Trans. Nucl. Sci.*, 42(6):1870–1877, 1995.
- [98] A B Rosenfeld, G I Kaplan, T Kron, F A Dilmanian, I Orion, B Ren, M L F Lerch, and A Holmes-Siedle. MOSFET dosimetry of an X-ray microbeam. *IEEE Trans. on Nucl. Sci.*, 46(6):1774–1780, Dec. 1999.
- [99] M Renier, T Brochard, C Nemoz, and W Thomlinson. A white-beam fast-shutter for microbeam radiation therapy at the ESRF. *Nucl. Instrum. Methods A*, 479:656–660, 2002.
- [100] A B Rosenfeld, M L F Lerch, T Kron, E Bräuer-Krisch, A Bravin, and A Holmes-Siedle. Feasibility study of on-line, high spatial resolution MOSFET dosimetry in static and pulsed X-ray radiation fields. *IEEE Trans. on Nucl.Sci.*, 48(6):2061–2068, 2001.
- [101] M J Berger, J S Coursey, M A Zucker, and J Chang. *ESTAR, PSTAR, and ASTAR: Computer Programs for Calculating Stopping-Power and Range Tables for Electrons, Protons, and Helium Ions (version 1.2.3)*. [Online: <http://physics.nist.gov/Star>], National Institute of Standards and Technology, Gaithersburg, MD, 2005, .
- [102] I Orion, F A Dilmanian, Z Zhong, A B Rosenfeld, A Henn, I Sagi, and L Pena. Simulations for x-ray synchrotron beams using the EGS4 code system in medical applications. *Proceedings of the Monte Carlo 2000 Conference in Lisbon*, pages 93–98, 2001.

- [103] J C Crosbie, I Svalbe, S M Midgley, N Yagi, P A W Rogers, and R A Lewis. A method of dosimetry for synchrotron microbeam radiation therapy using radiochromic films of different sensitivity. *Phys. Med. Biol.*, 53(23):6861–6877, 2008.
- [104] Radiation Products Design. *Gafchromic HD-810 radiochromic dosimetry film and D-200 pre-formatted dosimeters for high-energy photons*. [Online: [http://www.online1.ispcorp.com/\\_layouts/Gafchromic/content/products/hd810/pdf/conspefo.pdf](http://www.online1.ispcorp.com/_layouts/Gafchromic/content/products/hd810/pdf/conspefo.pdf)]. Accessed 18 November, 2008.
- [105] S.Dutta and D. S.Ray. Magnetic field induced pattern formation in reactive membranes. *Phys. Rev.*, 75:016205 1–7, 2007.
- [106] I C Smith and H C Jarrell. Membrane surface orientation and motion of glycolipids:  $^2\text{H}$  NMR investigations. *Pure & Appl. Chem.*, 63:529–534, 1991.
- [107] K Chang and C Weng. The effect of an external magnetic field on the structure of liquid water using molecular dynamics simulation. *J. Appl. Phys.*, 100:043917–1–043917–6, 2006.
- [108] E K Vozny, M Y Byakhov, A I Gorb, E V Krivenko, V D Chkhikvadze, L A Alipchenko, and I A Agrinskaya. The combined magnetoradiotherapy of breast cancer. *Voprosy Onkologii*, 38(7):823–828, 1992.
- [109] H Nettelbeck, G J Takacs, M L F Lerch, and A Rosenfeld. Microbeam radiation therapy: a Monte Carlo study of the influence of the source, multislit collimator, and beam divergence on microbeams. *Med. Phys.*, 36(2):447–456, Feb. 2009.
- [110] D W Archer. U.S. Patent No. 5771270, 23 June 1998.
- [111] P Coan, E Pagot, S Fiedler, P Cloetens, J Baruchel, and A Bravin. Phase-contrast X-ray imaging combining free space propagation and Bragg Diffraction. *J. Synchrotron Rad.*, 12:241–245, 2005.



- [112] J Sempau, J M Fernández-Varea, E Acosta, and F Salvat. Experimental benchmarks of the Monte Carlo code PENELOPE. *Nucl. Instrum. Meth. B*, 207:107–123, 2003.